The Mediterranean Outflow Water: Transformations and Pathways into the Gulf of Cádiz

Marc Gasser i Rubinat

Doctoral thesis as a compilation of publications

September 2018

Advisor: Josep Lluís Pelegrí Llopart

Thesis submitted to the
Civil and Environmental Engineering Department,
Marine Sciences Program,
Universitat Politècnica de Catalunya
in partial fulfillment of the requirements for the degree of

Doctor of Philosophy

Abstract

The Mediterranean Outflow Water (MOW) is a dense (ρ>1028.5 kg/m^3), saline (38.5 g/kg) ocean stream originated in the evaporative Mediterranean basin flowing westward past Espartel Sill as a fast (>1 m/s) and often unstable (as indicated by its gradient Richardson number) gravity current. During its descense into the Gulf of Cadiz, the MOW entrains the overlying North Atlantic Central Water (NACW), until the density difference between both water masses vanishes, and reaches its equilibrium depth. Inertia, Coriolis and frictional forces (both internal and with the bottom), as well as pressure gradients (associated with both seafloor slope and density gradients), play varying roles throughout the MOW's trajectory. In particular, bathymetric steering due to contouritic, turbiditic and diapiric structures controls the early trajectory of the outflow. Using both historic and current hydrographic data, and a new high-resolution bathymetry of a critical region west of Espartel Sill, we examine the hydrographic characteristics of the MOW and the mechanisms that set its pathway. Our study is complemented with the proposal of simple models that help explain pbservations of vertical mixing in the Strait of Gibraltar and the behavior of the MOW as a gravity current within the Gulf of Cádiz, as well as with a new tool, based on water tributaries methods, that assesses the relative impact of both seafloor slope and Coriolis force in steering the outflow

La sortida d'aigua mediterrània (MOW) és un corrent oceànic dens (ρ>1028.5 kg/m3) i salí (38.5 lg/m3) originat en la conca evaporativa de la Mar Mediterrània que flueix passant la baixa d'Espartel en forma d'un corrent de gravetat molt ràpid (>1 m/s) i sovint inestable (tal i com indica el número de gradient de Richardson). Durant el seu descens al Golf de Cadis, la MOW incorpora les aigües atlàntiques (NACW) suprajacents fins que la diferència de densitat entre ambdues masses d'aigua desapareix i assoleix la fondària d'equilibri. Les forces d'inèrcia, Coriolis i de fricció (tan internes com amb el fons), així com els gradients de pressió (associats amb el pendent del fons i els gradients de densitat), juguen papers variables al llarg de la trajectòria del MOW. En particular, la canalització del flux gràcies a les estructures de tipus contourític, turbidites i diapirs controlen la trajectòria del corrent. Aquest treball examina les característiques hidrogràfiques del MOW i els mecanismes que determinen la seva trajectòria usant dades històriques i modernes, així com una nova batimetria d'alta resolució d'una regió critica a l'oest de la baixa d'Espartel. L'estudi es complementa amb les propostes de models senzills que ajuden a explicar les observacions de barreja vertical a l'Estret de Gibraltar i el comportament de la MOW com un corrent de gravetat al Golf de Cadis, així com una nova eina, basada en metodologies per aigües tributàries, que permet valorar la importància relativa del pendent del fons i la força de Coriolis en la conducció del flux

Keywords

Mediterranean outflow water; Strait of Gibraltar; Gulf of Cádiz; Contourites; Turbidites; Bathymetric steering; Gravity current; Entrainment; Cold-water event; Drainage basin

Paraules clau

Flux de sortida d'aigua mediterrànea; Estret de Gibraltar; Golf de Càdiz; Contourites; Turbidites; Canalització pel fons; Corrent de gravetat; Incorporació; Episodi d'aigües fredes; Conca de drenatge.

Preface

The aim of this dissertation is to describe the trajectory and changes in the physical properties of the Mediterranean Outflow Water (MOW) as it flows west of the Strait of Gibraltar. In particular, we will investigate the relevance of bathymetric steering, mixing with overlying water masses, bottom and interfacial friction and Coriolis forces. For this purpose we use data (salinity, temperature and velocity measurements) obtained during several oceanographic cruises (Gibraltar Experiment 1988, CANIGO 1997-99, MEDOUT 2009 and MEDOUT 2011) plus recent, high-resolution bathymetry of the Gulf of Cadiz (Zitellini et al. 2009, MEDOUT 2011). Additionally, we will explore how the Mediterranean outflow is transformed within the Strait itself as a result of mixing with the entering Atlantic flow.

The origin of the MOW is the imbalance between evaporation and precipitation in the Mediterranean Sea, implying a replenishing net mass flow from the Atlantic through the Strait of Gibraltar. Underlying this Atlantic input, an output of denser, saltier Mediterranean Water (MW) is observed. Once it abandons the Gulf of Cádiz, the MW branches into several directions either as a coherent poleward current or as lenticular structures called meddies. This MW contributes to the formation of highly dense water in the subpolar North Atlantic Ocean, a process that constitutes the starting engine of the Global Conveyor Belt or Global Thermohaline Circulation (GTC); the salinity signal of the MW tongue is evident in the Atlantic, and several authors have postulated dynamical consequences for the MO such as being the origin of the Azores Current (Jia 2000, Özgökmen et al. 2001).

Although the general properties, dynamics and trajectory of the MOW have been studied by many authors (e.g. Armi and Farmer 1988, Ambar et al. 2002, Ambar and Howe 1979), the mechanisms causing the transformation of the MW and the branching of the MOW still remain poorly explored. A precise description of these processes in the Strait of Gibraltar and the Gulf of Cádiz still remains as a formidable challenge because of the high bathymetric complexity and the rapidly varying dynamics.

The Strait of Gibraltar and the Gulf of Cádiz are indeed morphologically very complex. As the MOW exits the Strait of Gibraltar and plummets towards the open sea as a gravity current, it follows an intricate network of canyons. Once the current diminishes its velocity, and the Coriolis force diverts it northwards, it encounters many other geomorphological accidents both parallel and normal to its direction of propagation. Bathymetric steering is one of several mechanisms postulated in order to explain the origin of the several MOW nuclei or cores observed by many authors (other mechanisms imply temporal variability originated, for

example, by tidal effects). Discerning between the alternative explanations for this branching or splitting of the MO is only possible through high-quality and high-resolution (both in time and space) hydrographic and bathymetric data, or using high-resolution numerical models. Recent advances in current velocity measurements (especially Lowered Acoustic Doppler Current Profilers, LADCP) are combined with a large historical CTD dataset plus recent oceanographic campaigns (especially MEDOUT 2009 and 2011) and precise high-resolution (up to 60 m) multibeam bathymetries.

Once the MOW enters the Gulf of Cádiz it experiences a series of physical processes (bottom friction, interfacial friction, shear instabilities and internal waves) that modify the core properties of the MW. These properties in turn determine the final equilibrium depth where, after sufficient mixing with the overlying fluid, the outflow reaches a final density equal to that of the surrounding waters. At this point the MOW abandons the bottom and starts flowing at mid-depth. The equilibrium depth and the final properties (temperature and salinity) of the MOW condition its ability to reach higher latitudes at relatively shallow layers, where it will mix with cold Arctic waters and will contribute to the formation of deep waters, the start of the Global Thermohaline Circulation (GTC). Any variation in these MOW parameters (due for example to a salinification of the Mediterranean Sea induced by Climate Change) may induce a non-linear response in the GTC.

Mixing and entrainment processes, although active during the entire trajectory of the MOW through the Strait of Gibraltar and Gulf of Cádiz, are particularly significant at certain discrete locations due to the existence of several major and minor sills and constrictions (such as Camarinal Sill and Spartel Sill) where the turbulent kinetic energy (TKE) dissipation rates are extremely high (with vertical diffusion coefficients up to 10^{-2} m^2 s^{-1}). Additionally, tidal and atmospheric-pressure forcing may cause these rates to be highly variable. Thus, in order to discern the precise spatio-temporal location of interfacial and bottom friction, we require a dense and repeated sampling of the study region. Such dense monitoring efforts are very costly so we must contend with the inference of information from data relatively sparse both in space and time, thus developing alternative strategies that include numerical models, satellite imagery and hydrological methods.

Acknowledgements

I would like to acknowledge the following people:

I would like to thank my fellow graduate students, UTM personnel and ICM administrative and research staff for all the help and support during the years I spent at the CMIMA.

I would like to thank the crew and technicians of the following research vessels: García del Cid, Sarmiento de Gamboa and BIO Hespérides.

I would like to thank my coauthors and the anonymous reviewers for my articles.

I would like to thank the members of my thesis committee: Simón Ruiz Valero, Manuel Grifoll Colls, Pedro Vélez Belchí, Manuel Espino Infantes and Elena Roget Armengol.

I would like to thank my UPC tutor Agustín Sánchez Arcilla Conejo.

And last but not least I would like to thank my thesis advisor Josep Lluís Pelegrí Llopart.

TABLE OF CONTENTS

LIST OF FIGURES

CHAPTER 1

CHAPTER 2

CHAPTER 3

CHAPTER 4

LIST OF TABLES

GLOSSARY AND ACRONYMS

ADCP: Acoustic Doppler Current Profiler
ASCII: American Standard Code for Information Interchange
CDS: Contouritic Depositional Systems
CTD: Conductivity Temperature Depth
DTM: Digital Terrain Model
Fr: Froude number
GTC: Global Thermohaline Circulation
LADCP: Lowered Acoustic Doppler Profiler
MATLAB: Matrix Laboratory, a high-level programming language
MO: Mediterranean Outflow
MOW: Mediterranean Outflow Waters
MW: Mediterranean Water
NACW: North Atlantic Central Water
Ri: Richardson number
Ro: Rossby number
SADCP: Ship Acoustic Doppler Profiler
SST: Sea Surface Temperature
TIN: Triangulated Irregular Network
TKE: Turbulent Kinetic Energy
XCP: eXpendable Current Profiler

CHAPTER 1: INTRODUCTION

1.1 MEDITERRANEAN WATER

The goal of this dissertation is the study of the pathways and transformations of the Mediterranean Water (MW) as it flows through the Strait of Gibraltar and into the Gulf of Cádiz, in what consitutes the Mediterranean Outflow Water (MOW). We must start therefore our introduction with a description of its origin and properties.

1.1.1 MEDITERRANEAN WATER CHARACTERISTICS

Salty (38.4) and relatively warm (12.8ºC) MW flows westward through the Strait of Gibraltar under fresher (36.2) and relatively colder North Atlantic Central Water (NACW) (Price 1993). Although flowing initially in a purely zonal (downslope) direction, it undergoes a gradual northwards turn in the region between 6.5 and 7ºW, constrained by the bathymetry of the Gulf of Cádiz (Fig. 1.1). Between 7 and 9ºW, the flow is again zonal and approximately parallel to the depth contours; additionally, the well-defined MOW branches or splits into at least two cores or nuclei, a northern and shallow (600 m) core and a southern and deep (900-1200 m) core. The origin and causes of the MOW branching can be located in the region between 6.5 and 7ºW, named the near field in the present study; this region also shows the largest decrease in MOW momentum due to interfacial and bottom stresses.

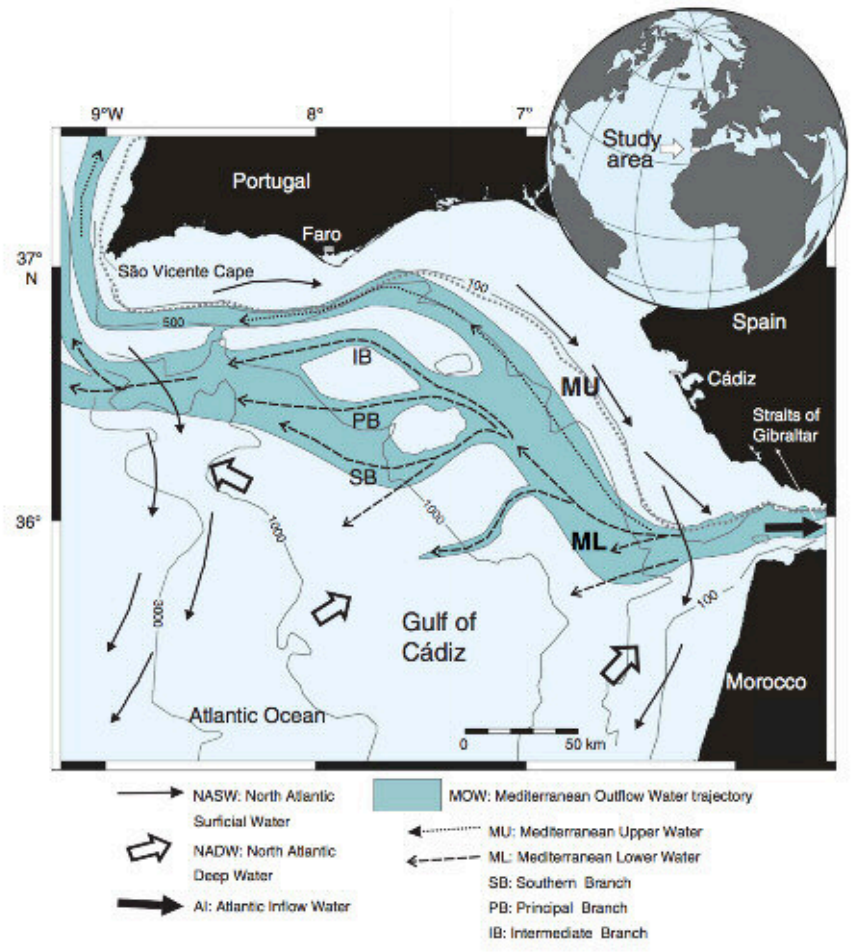

Fig. 1.1: General map and characteristics of the MOW (IODP 2012)

Fig. 1.2: A general view of the Mediterranean Sea showing the location of the Dardanelles, Bosphorus and Gibraltar Straits. From Wikimedia Commons.

The physical properties of the MOW are a consequence of mass, salinity and thermodynamic fluxes in the Mediterranean Sea. A brief discussion of these fluxes is thus necessary in order to understand the initial conditions of the MW in the Strait of Gibraltar and the impact of flux variations in the MOW characteristics (including those caused by human activities - agriculture, civil works, global warming or due to natural variability).

The Mediterranean Sea is a marine basin surrounded by the Eurasian and African continents, connected to the Atlantic Ocean through the Strait of Gibraltar and to the Marmara and Black Seas by the Dardanelles and Bosphorus Straits (Fig. 1.2). Mass, heat and salinity fluxes from the Atlantic Ocean and the Black Sea, from riverine inputs, and through air-sea thermodynamic fluxes control the Mediterranean Sea's salinity and temperature. We can write conservation equations for heat, mass and salinity as follows (Jordà et al. 2017):

$$\int_{V\,Med} \rho c_p \frac{\delta \vartheta}{\delta t} dV_{Med} = \int_{A\,Med} QH_{net}\, dA_{Med} + \int_{S\,Gib} \rho c_p \vartheta u ds ds_{Gib} + \int_{S\,Dard} \rho c_p \vartheta u ds ds_{Dard} + \sum \rho_{riv} Q_{riv} \vartheta_{riv} c_p$$

$$\frac{dV_{Med}}{dt} = \int_{A\,Med} (P - E) dA_{Med} + \int_{sGib} u\, ds_{Gib} + \int_{sDard} u\, ds_{Dard} + \sum Q_{riv} \qquad \text{(eq. 1.1)}$$

$$\int_{V\,Med} \frac{dS}{dt} dV_{Med} = \int_{sGib} Su\, ds_{Gib} + \int_{sDard} Su\, ds_{Dard}$$

where ρ is the density of seawater, ϑ the potential temperature, c_p the specific heat capacity, V_{Med} and A_{Med} are the Mediterranean volume and surface area, s_{Gib} and s_{Dard} are the section at the Gibraltar and Dardanelles Straits, u is the normal velocity through these sections, QH_{net} is the net heat flux through the surface and Q_{riv} is the river runoff, and the integrals are over elements of area (ds) and volume (dV).

Although seemingly simple, many parameters and terms in these equations are difficult to measure in practice. In addition, the size of every term is a function of the timescale considered during the measurement. For example, for a relatively long-term period (which is defined after careful consideration) the averaged time change is demonstrably of order 0 (which may not be true at time scales of days or thousands of years), thus simplifying the conservation equations.

1.1.2 SURFACE FLUXES

Total heat fluxes are the sum of evaporation (latent), precipitation and sensible heat, longwave and shortwave radiation fluxes and advective fluxes (Jordà et al. 2017). Air and sea temperature, sea level pressure, humidity, wind speed and cloud coverage are necessary in order to compute the former quantities, at an adequate spatial and temporal resolution. Nowadays, scarcity of high quality observational time series from in-situ instrumentation (meteorological buoys, surface vessels and radar) is the main obstacle for obtaining an accurate estimate for those parameters with adequate spatial and temporal resolution; experiments at sea usually only sample a limited range of conditions and satellite measurements and numerical models require in-situ data for sensor calibration and model validation. Additional difficulties arise from data integration between point (buoy and ship) measurements and relatively coarse data obtained from satellites or numerical models; due to the high variability of the atmosphere-ocean system, mesoscale and submesoscale processes remain oftern unresolved

Precipitation measurements are also notoriously difficult due to the inherent patchiness and intermittency of rain events; satellite measurements are becoming a possible alternative,

although still with substantial imitations in accuracy and spatio-temporal resolution.

Budget closure schemes at basin or sub-basin scales from advective fluxes at the Gibraltar and Dardanelles-Bosphorus Straits provide a complementary approach to direct measurements. Net volume and heat fluxes have been measured for the Strait of Gibraltar; a number of references providing an estimate of 0.065±0.033 Sv for the net volume flux (Jordà et al. 2017) and -5.2 ± 1.3 W m^{-2} for the net heat flux (McDonald et al. 1994). These results are close, within the error margin, to the averaged Mediterranean net heat flux of -3 ± 8 W m^{-2} provided by Sánchez et al. (2011).

1.1.3 BASIN EXCHANGE THROUGH THE STRAIT OF GIBRALTAR

The Strait of Gibraltar is the most important connection between the Mediterranean and the open Atlantic Ocean, and it constitutes the bulk of advective mass, salt and heat fluxes into or out of the Mediterranean. Understandably, this has generated much interest and many studies have tried to measure these variables. Difficulties derived from complex topography and strong tidal currents, introducing high variability in the net advection through the Strait, explain the uncertainty in the many estimates provided by several authors throughout the years.

Net fluxes through the Strait of Gibraltar can be ascertained either from inverse models (e.g. using sea-surfaces combined with hydraulic and energy considerations), from direct observations or from numerical models. The models require actual measurements in order to calibrate and validate the implicit assumptions and limitations; these observations are not easy due to the extraordinary technical challenges behind the required spatio-temporal resolution in such a harsh environment.

The volume transport or net flow through a certain section is defined as the area integral of the velocity vector crossing the section; it is thus uniquely computed once the bathymetry and velocity field are known. In the Strait of Gibraltar, it constitutes a small difference between two large terms (the inflow of Atlantic water into the Mediterranean and the MOW); thus, small errors in any of these larger terms compound into a large relative error in the net quantity.

Regarding volume estimates, the recent study by Sammartino et al. (2015) gives a net value of -0.85 Sv at Espartel Sill section. Tidal fluctuations at time scales of the order of hours account for a variability of ± 0.39 Sv; longer time-scale variability is due to atmospheric forcing (±0.15 Sv) and the seasonal cycle (±0.08 Sv). Interannual variability drops to ±0.03 Sv (based in ten years of observations), and shows no significant trend (Jordà et al. 2017).

Heat and salt fluxes are similarly derived using direct measurements (Jordà et al. 2017):

$$QH_i = \int_{LS}^{US} \rho c_p \vartheta u ds$$
$$QS_i = \int_{LS}^{US} \rho S u ds \quad \text{(eq. 1.2)}$$

where the area integrals range from the lower (L, the seafloor) to the upper (U, the interface) limits fo the MOW. Difficulties arise from the temporal and spatial variability of the temperature, salinity and velocity fields, which require adequately long time series resolving tidal effects in a region of complex bathymetry. Tidal dynamics induce non-linearities in the heat and salt fluxes due to cross-correlation between the velocity and property fields; this results in a non-zero mean transport despite either the velocity or heat/salt fluxes may have a section-averaged zero or near-zero value. Although continuous measurement of the velocity field is feasible (using a bottom-mounted Acoustic Doppler Current Profiler ADCP), heat and salt fluxes are a different matter. Ship measurements are usually discrete in time and lack in synopticity, while moorings are difficult to install and impractical in such a traffic-intensive region.

Numerical models constitute a third approach to describe the fluxes of properties; the physical constraints here translate in the necessity of high-resolution horizontal, O(500 m), and vertical, O(10 m), discretization and the adequate parameterization of the tidal forcing (Jordà et al. 2017). Non-hydrostaticity can be relevant for certain processes but it is usually of no concern if our goal is to obtain long-term flux estimates. Jordà et al. (2017) provides a table summarizing the results of one of such efforts.

1.1.4 BASIN EXCHANGE THROUGH THE DARDANELLES AND BOSPHORUS STRAITS AND RIVERINE INPUTS

The Mediterranean Sea is connected to the Black Sea through the Marmara Sea, an intermediate basin. Water flows between the Mediterranean and the Marmara Seas through the Dardanelles Strait, and between the Marmara and Black seas through the Bosphorus Strait. Mass, heat and salinity fluxes between the Mediterranean and the Marmara and Black Seas through the Dardanelles and Bosphorus Straits are much smaller than through Gibraltar; they will be considered here only for completeness. Longer and narrower than the Gibraltar Straits, the Dardanelles support a hydraulically-controlled (maximal exchange) regime, with very intense bidirectional flow. Turbulence and mixing is prevalent through the water column. All the

considerations described before apply to the Dardanelles case with the exception of the tide role, which is negligible due to its small amplitude, O(10 cm).

The total freshwater input into the Black and Marmara Seas is positive (about 10,000 m^3/yr) implying a positive mass contribution into the Mediterranean equivalent to 110 ± 24 mm/yr (Jordà et al., 2017). We must take into account that instantaneous fluxes can be up to 2-3 times larger than yearly averages. Using measured values for the Dardanelles and Mediterranean water temperatures and salinities, heat and salt fluxes can also be estimated. For T_d = 14ºC, T_m = 16ºC, S_d = 35 psu and S_m = 39 psu (values observed at the Dardanelles Straits, where the d subscript indicates the upper layer of Black Sea water flowing into the Mediterranean and the m subscript corresponds to the Mediterranean underlying water), the volume transports translate into a heat gain for the Mediterranean of 0.10 ± 0.16 W m^{-2} and a salt gain of 0.20 ± 0.22 x 10^6 kg, much smaller than those through the Strait of Gibraltar.

The drainage basin for the Mediterranean Sea covers about 8 × 10^6 km^2 and it is about 3 times as large as the sea itself. It contains some of the largest rivers of the World, such as the Nile and the Danube; the mass and heat fluxes from this source can be potentially significant. We must take into account that the Mediterranean is a heavily populated area; agriculture uses about 80% of the net rainfall in the Southern shore of the Mediterranean Sea (Margat 2008) and many rivers are strongly controlled for this or other purposes. Due to this strict supervision, one could think that riverine discharges to the sea are accurately measured and known. This is not true due to several reasons, some of them technical (flow measurements are not trivial in deltas, for example) but many of them political and economical. Jordà et al. (2017) discusses in detail the Nile case, where the CEFREM (Centre de Formation et de Recherche sur les Environnements Mediterraneens) has estimated that the total freshwater input to the Mediterranean and Black Sea has ranged between 710 and 780 km^3/yr for the last 60 years.

Heat flux from riverine origin is even a more complex case than volume influx, because of the lack of river temperature data for the Mediterranean basin. Some first approximations suggest a long-term annual-average heat contribution from riverine input of the order of 0.6 ± 0.4 W m^{-2} (Jordà et al. 2017).

1.2 MEDITERRANEAN OUTFLOW WATER

1.2.1 MORPHOLOGICAL DESCRIPTION OF THE GULF OF CÁDIZ

The area of study overlies structures generated by tectonic processes: the Gloria transform zone which constitutes the African-Eurasian plate boundary and the Gibraltar Arc. The MOW transits this already complex domain with a high capacity to further modify the seafloor, resulting from sedimentary and erosive mechanisms associated with paleochanges in the MOW's erosive powe. This section discusses the general morphology of the Gulf of Cádiz.

A first distinction must be made between down-slope processes that create turbidite, debris or mixed mass-gravity depositional systems and along-slope sedimentary processes generating contourite depositional systems (CDS) (García et al. 2009, Hernández-Molina et al. 2003, Llave et al. 2007). Sea-bottom generated contourites can span hundreds of kilometers, have widths in the order of ten kilometers and depth of the order of 10-100 m (García et al. 2009, Hernández-Molina et al. 2003, Llave et al. 2007). The Gulf of Cádiz is unique in the sense that, besides the down-slope turbiditic processes characteristic of the eastern margin of the Atlantic Ocean, the existence of the MOW makes possible the existence of a extensive CDS.

The Gulf of Cádiz continental margin is divided (following the coast) into three different morphological regions: the South-Iberic Continental Margin (located offshore the Algarve coast, with a steep slope crossed by submarine canyons); the Guadalquivir Margin (no submarine canyons and characterized by a broad shelf) and the Betic domain continental Margin (steep slope and submarine canyons). The presence or absence of canyons determines the exchange processes between the continental shelf, the continental slope and the abyssal plain (see below) (Mulder et al. 2009).

The Gulf of Cádiz can be also divided into a continental shelf, a continental slope and abyssal plain. The continental shelf has a slope of 0.3-0.5º and a variable width (between 10 and 30 km). The shelf break is located between 120 and 140 m, it has a depth-gradient of 2º and a width of 7 km.

The continental slope has a very irregular relief and can be further sub-divided into upper, middle and lower slope. The upper slope is located between 130 and 400 m, has a depth-gradient between 1-3º and a width of 10-20 km. Submarine canyons are only well developed in the western area of the portuguese section.

The middle slope, located between 400 m and 1200 m, is much wider (100 km) and has a smaller depth-gradient (0.5-1º). The effects of the MOW are much evident in this region.

The lower slope is located between 1200 and 4000 m, has a depth-gradient of 2-4º and a width between 50 km and 200 km. An increase in the slope gradient marks the transition between the lower slope and the Horseshoe and Seine Abyssal Plains.

Following the trajectory of the MOW as it exits from the Strait of Gibraltar, we can describe its imprint into the sedimentary record. The first sector is located in a region that represents the encounter of the Strait of Gibraltar and the Gulf of Cádiz. It shows an abrasive surface and erosive scours at depths between 300 and 1000 m due to the erosive effects of a fast (up to 2 m/s) MOW. Some sedimentary structures (longitudinal bedforms, sand ribbons and ripples) are observed in the northern margin of this sector. A second sector is located seaward from this region, characterized by large sand sedimentary lobes. Some furrows in a NE-SW orientation are also evident. These structures could be caused either by the detour of the MOW due to diapiric structures perpendicular to the flow or by the overflow of the densest portion of the MW.

A third sector can be defined between Cádiz and Faro, at depths between 800 and 1000 m. Nine contourite channels are described with lengths up to 100 km and widths up to 10 km, overlying a series of ancient contouritic sedimentary depositions and diapiric ridge structures. These channels are associated with the branching of the MOW: part of the outflow changes its direction towards the SW as it impinges the diapiric ridges. The contourite channels terminate abruptly once the MOW dettaches from the sea bottom.

The fourth sector is located in the middle slope of the central and NW Gulf of Cádiz, being also dominated by active contouritic structures.

Finally, a fifth sector located in the middle slope is characterized by downslope erosive features (canyons) with steep margins in a NE-SW orientation. Localized turbulence and internal waves are generated as the MOW travels across these structures.

1.2.2 MOW DYNAMICS: TOPOGRAPHIC STEERING, BOTTOM AND INTERFACIAL FRICTION, CORIOLIS FORCE AND HYDRAULIC CONTROL

As the MW exits the Strait of Gibraltar it encounters a somewhat cold, less salty NACW. The density difference between Mediterranean and Atlantic waters is the engine of the MOW's motion. As the NACW is entrained by the MOW, this density difference decreases until the MOW's density eventually becomes undistinguishable from that of its surrounding fluid. At this point the MOW reaches an equilibrium depth, dettaching from the bottom.

Mixing and entrainment processes determine the final density and equilibrium depth of the several nuclei of the MOW, hence their importance. Mixing is controlled by the density difference and the relative velocity between the Atlantic and Mediterranean layers. Most of this mixing takes place from less to more turbulent regions, in what constitutes a one-way transfer named entrainment. In the case of the MOW, the most turbulent region corresponds to the bottom layer so water is predominantly transferred (entrained) from the NACW to the MW layer. A good index for assessing the intensity of this mixing is the Richardson number (either gradient or bulk), its gradient definition being:

$$Ri = -\frac{g}{\rho}\frac{\frac{d\rho}{dz}}{\left\{\frac{\partial v}{\partial z}\right\}^2} \qquad \text{(eq. 1.3)}$$

where (u,v) are the horizontal velocity components. Away from the highly-turbulent regions other processes, such as double-diffusion, can locally modify the rate of mixing.

The density difference between the MW and the NACW is neither constant in space nor time. This is because of the transformations experienced by the MW but also because of NACW changes with depth. In opposition to the source MW type, which can be approximated by a single point in the T-S diagram, the NACW is represented by a nearly straight line, with temperature and salinity decreasing with depth. Consequently, as the MOW plunges into the Atlantic it encounters progressively colder, less salty and denser NACW. Hence, in the absence of mixing, as the MOW sinks the temperature and salinity contrast between the MW and NACW will increase but the density difference will diminish. However, mixing will cause that the MOW-NACW contrast diminishes in all three variables: temperature, salinity and density.

The location and intensity of mixing is a priori paramount to control the final density and equilibrium depth. If the mixing between MW and NACW happens at a shallow (deep) water

depth, the equilibrium depth will be also shallower (deeper) and the equilibrium density will be lighter (denser). However, due to the large initial MOW-NACW density difference, a fast gravity current is required in order to overcome the critical Richardson number. This is because the speed of a gravity current (neglecting bottom slope and friction) is directly proportional to the height of the moving layer and the density difference between the current and the surrounding fluid; thus speed, density difference and vertical mixing are inter-related factors. Interestingly, mixing in the MOW exhibits a negative feedback effect: variations in the initial conditions of the MW conduce to smaller than expected changes in the final output (Legg et al. 2009).

During its early stages, the MOW dynamics is controlled by the density difference between the MW and the surrounding NACW. The Mediterranean saline tongue follows the maximum depth-gradient pathway, crossing bathymetric contours in a near-perpendicular angle as a gravity current. MOW speed decreases gradually due to a combination of NACW entrainment and bottom friction. Once the Rossby number becomes sufficiently small, the Coriolis forces become significant and the outflow veers towards the North, following the bathymetric contours.

A more nuanced description of the outflow dynamics must take into account intra-flow small-scale processes. Coriolis forces play a significant role even near the Gibraltar Straits through the creation of an Ekman upper and bottom layers. A balance between friction and Coriolis forces is established in a relatively thin Ekman layer inside the MOW, creating a secondary circulation. An integrated transport towards the right in the upper layer and towards the left in the bottom layer introduces a clockwise (as seen following the MOW) motion and an increase in the flow helicity, defined as the projection of the vorticity vector in the direction of motion.

The secondary circulation impacts the MOW in two different ways. First, Ekman layers in conjunction with bathymetric irregularities give place to branching and splitting in the MO. Second, erosion and sediment deposition by this secondary circulation create contouritic structures, thus steering the main flow (contourites are commonly defined as sediments deposited by persistent bottom currents parallel to the batymetric contours, though its usage has widened to depict a series of structures originated by deep sea currents (Hernández-Molina et al. 2014).

Consider a gravity current flowing downslope as it impinges a small bottom irregularity or bump. Ekman layer dynamics generates a downslope bottom flow at the left of the mound and an upslope transport at the right. Downstream from the obstacle, the flow does no rejoin (as we would expect in the two-dimensional frictionless and irrotational case) but remains separated

and splits into two branches (Fig. 1.3). This branching mechanism could explain the formation of at least two well-differentiated MOW nuclei as it is observed near the Strait of Gibraltar.

The initial MOW direction is largely determined by the regional bathymetry. The down-slope flow directly erodes those regions under the swiftest waters. Additionally, the secondary MOW circulation in the MO erodes the sea bottom located right of the flow direction. Conversely, sediment deposition occurs in the left margin of the MOW. The creation of these so-called contouritic deposits modifies the bottom morphology, thus efecting the flow of MW.

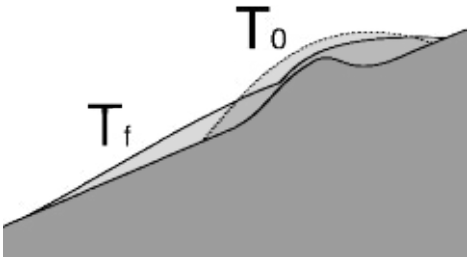

Fig. 1.3: MOW splitting mechanism caused by a mount in the seafloor. Flow is towards the page, shown as a cross-section. As the initial MOW (T_0) impinges a bump, the Ekman downslope flow elongates the initial cross section. After the bump, the MOW (T_f in the drawing) breaks into two branches that do not merge subsequently. Redrawn from Figure 7 in Borenas et al. (2002).

In addition to the above factors, we flow is hydraulically controlled when running over or through topographical sills and constrictions. At several points during its trajectory – most significant at the Espartel and Camarinal Sills – the MOW transits over shallow depths or through narrow canyons. At these constrictions, the flow turns from subcritical (stable) to critical conditions and subcritical again. This condition is traditionally assessed through the Froude number – essentially the squared root of the inverse bulk Richardson number – which defines a ratio between the flow velocity and the propagation speed of a perturbation:

$$Fr = \frac{v}{\sqrt{g'D}} \qquad \text{(eq. 1.4)}$$

where g' is the reduced gravity (see Section 1.3.4), v is the speed of the surrounding fluid, and D is the thickness of the perturbation. A hydraulic jump will develop when the Froude number reaches a critical value of one. As a consequence, velocity is uniquely controlled by the geometry of the strait, vertical mixing will be steered by this topography and so will happen with the flow of both layers. Generally, the flow will increase until the critical condition, a maximal state, beyond which the flow will again decrease; exchange acquires a maximum or optimal state (Sannino et al. 2009, Armi 1986, Dalziel et al. 1991). Several authors have studied the parameters necessary in order to achieve this maximal exchange for a hydraulically controlled flow in a strait including rotating, stratification and frictional effects (e.g. Pratt et al. 1991). However, observational confirmation in the Strait of Gibraltar has remained elusive due to the

high spatial and temporal variability of the velocity fields. In particular, tidal effects introduce fast changes in space and time, up to the point that locally the along-strait velocity can reach zero values or even reverse sign. As an example, Nash et al. (2012) observed characteristic values for velocity and Turbulent Kinetic Energy (TKE) dissipation that are consistent with the existence of hydraulic control in West Espartel, acknowledging the large variance of velocity measurements due to the tide.

The existence of locations where the flow is hydraulically controlled has a profound significance for the MOW and its effect on the North Atlantic. If the flow is maximal and largely a function of bottom-geometry considerations, any departure from the initial conditions will have a reduced impact on the downstream properties. In particular, changes in temperature and salinity of the MW exiting through the Strait of Gibraltar (due, for example, to climate change) may not correlate with changes in the final properties of the MOW once it reaches its equilibrium depth.

1.2.3 MEDITERRANEAN WATER IN THE NORTH ATLANTIC

A cursory view of the salinity distribution at intermediate depths (around 1000-1100 m) in the North Atlantic reveals a positive anomaly centered around the coast of Portugal and the Gulf of Cádiz (Candela 2001), reaching the East Coast of North America and the Nordic Seas and filling the entire subtropical North Atlantic Basin (Iorga and Lozier 1999a) (Fig. 1.4). This anomaly is the large-scale MW signature, generated due to the imbalance between evaporation and precipitation in this marginal basin and its posterior spreading into the North Atlantic Basin through the restricted Strait of Gibraltar (Price et al. 1994, Killworth 1983). This is probably one of the clearest examples of a local process having profound global consequences, acting as a preconditioner in the formation of North Atlantic Deep Waters (NADWs) and hence eventually controlling the intensity of the GTC.

Deep convection and water formation processes feed the GTC, with most of water filling the deep sea originating from very few marginal outflows (Price et al. 1994). Deep Convection occurs in the Atlantic Ocean in the Labrador, Greenland, Weddell and Mediterranean Seas. In the Mediterranean, deep convection has been extensively studied in the Gulf of Lions, ascertaining a certain temporal variability, but also in Rhodes, the Levantine Basin and the Adriatic Sea. The MOW helps maintain the high salinity of the Norwegian Sea, which in turn provides the source for the North Atlantic Deep Water (Reid 1979).

The MO provides an influx of saline, dense water, of between 0.6 and 1 Sv according to several estimates (see for example Ambar and Howe 1979). Part of this flux flows north following the

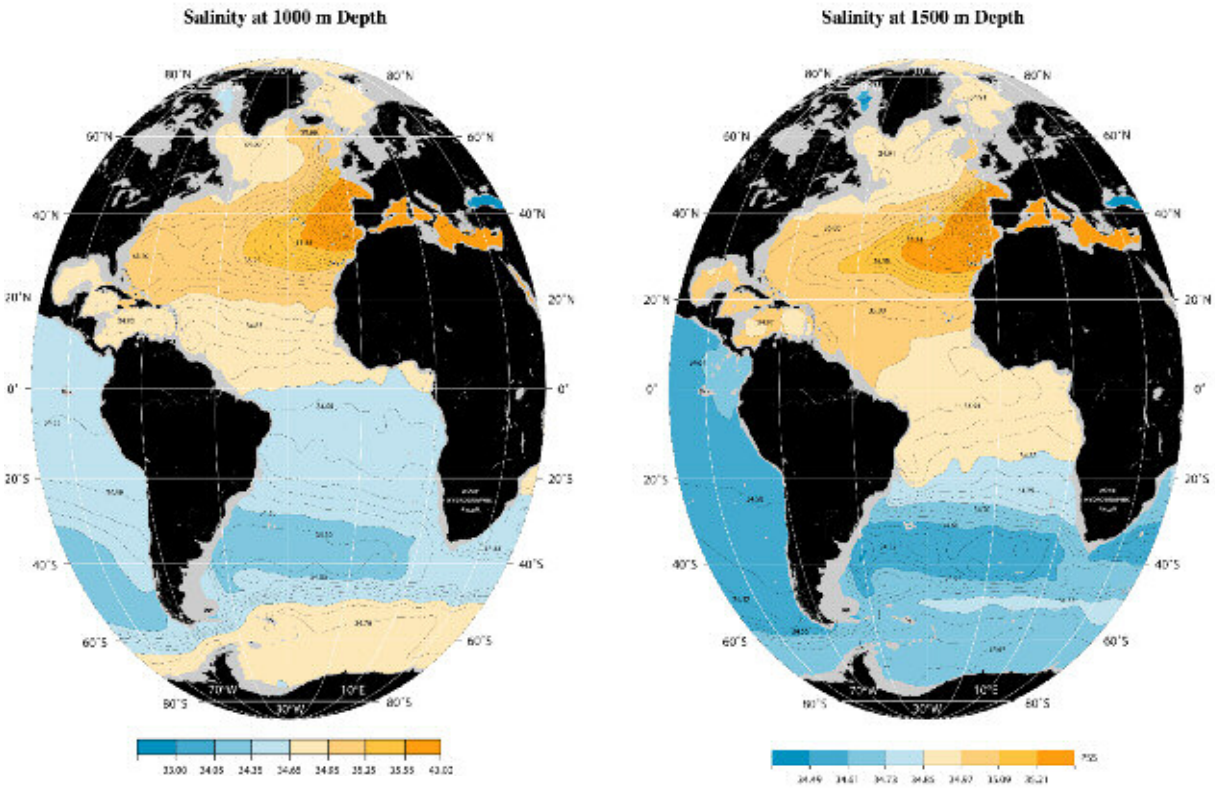

Fig. 1.4: (Top) Atlantic Ocean salinity distribution at 1000 m (left) and 1500 m (right). (Bottom) 25ºW Salinity section Retrieved from WOCE Atlas Volume 3: Atlantic Ocean (WOCE 2011).

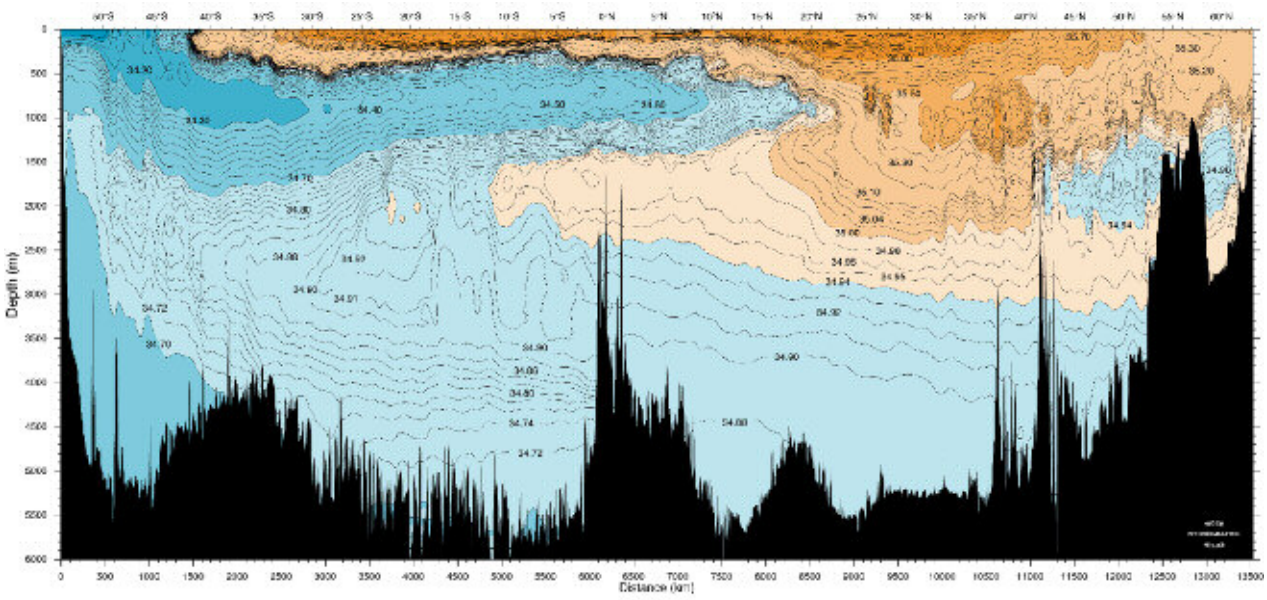

Iberian Coast; it bifurcates when it reaches the Galicia Bank and then turns eastward into the Bay of Biscay where some recirculation is observed. The flow turns northwards, strongly diluted, until around 50ºN (south of Porcupine Bank) where it no longer constitutes a well defined current but a weak salinity signal, according to observations (Iorga et al. 1999a, Reid 1970), though some numerical models still show a well defined poleward current (Iorga and Lozier 1999b). This signature reaches Iceland (in according to the dynamic topography and numerical models), and outcrops at the sea surface in the Labrador and Norwegian-Greenland Seas (Reid 1970).

Although the MW influx is relatively small, its high original salinity (38.4) and temperature (13ºC) allows following the path of the MOW until the Greenland Sea. There it continues as a western boundary undercurrent until the Shetland-Faroes Channel, where the isopycnal corresponding to the MW core rises from a depth of 1000-1200 m up to 400 m. This upwelling is supported by hydrographic observations (Reid 1970) and numerical models (Iorga and Lozier 1999b). The outcome is the cooling and mixing with Arctic waters in the Norwegian Current, generating the precursors of the NADW.

The MOW begins its Atlantic journey exiting the Gulf of Cádiz into the Tagus Basin, north of Cape Saint Vincent. The MOW flows west, past the Gorringe Bank, as two separate branches along its northern and southern flanks at least as far as 22ºW. Their weak signature may be detected as far as 30ºW but most data seems to suggest that the branches turn north in order to rejoin the poleward undercurrent (Iorga and Lozier 1999a). The existence of a direct westward advective pathway is neither supported by the hydrographic data nor by numerical models (e.g. Iorga and Lozier 1999a,b). The weak salinity signatures west of 20ºW suggest the predominance of either meddy activity or submesoscale diffusion, although a highly variable westward current cannot be ruled out. Some authors postulate that as much as 25-50% of the flux travels westward as meddies, large lenses of MW (20-100 km diameter, 200-1000 m thick) with a lifetime of 2-3 years (Iorga 1999a).

The spreading of the MOW into the Atlantic also explains that eastern NACWs are more saline than the western NACWs (Mauritzen et al. 2001). Central waters follow a very tight relationship in the T-S diagram, fairly well approximated by a straight line in the interval between (8ºC, 35.1) and (19ºC, 36.7). Salinity distributions along a constant sigma surface show that NACW located in the eastern boundary of the Atlantic Ocean can be up to 0.6 psu saltier than in the western boundary. NACW salinity anomaly contours follow the distribution of MW, suggesting that the zonal salinity change is due to the influence of the MOW (Fig. 1.5). Interestingly, NACW and MW are separated in the T-S diagram by a salinity minimum, hence direct diapycnal mixing

between both water masses cannot be the explanation for this zonal change. Alternative water masses have been proposed (none too convincingly) in order to solve this riddle, but other mechanisms are more plausible.

Most of the mixing between NACW and MW occurs in the first 80 km after the MOW exits the Strait of Gibraltar into the Gulf of Cádiz (Mauritzen et al. 2001). As explained above (section 1.2.2), it is also assumed that mixing involves an entrainment process, where Atlantic water is incorporated into the MOW thus lowering its salinity. An alternative detrainment mechanism was postulated by Mauritzen et al. (2001), wherein part of the MW would be incorporated into the Atlantic Water Mass through Kelvin-Helmholtz type instabilities and billow formation, as indicated by low (subcritical) Richardson numbers in the region between 6 and 7ºW. These instabilities were observed in a series of laboratory experiments, with the creation of secondary turbulent structures advecting MW at depths corresponding to the overlying NACW. The continuous salinity detrainment from the MOW into the overlying NACW would then increase the salinity of these layers.

The dilution mechanism is only plausible if the NACW, after undergoing this detrainment process, is not advected into the Mediterranean Sea: some fraction must recirculate towards the Atlantic Ocean through a westward net flow. Current measurements and inverse models from CTD data indeed suggest that this recirculation exists, as the velocity field for the shallow (<500 m) waters of the Gulf of Cádiz is much more complex than the simple eastwards advection of the Atlantic waters. A poleward current advecting continental slope waters from the Northwestern African Coast into the Gulf of Cádiz has also been described by observations and numerical models (e.g. Iorga and Lozier 1999a,b).

The MOW also influences the surface circulation of the North Atlantic: the general surface circulation model for the Subtropical North Atlantic Ocean shows a gyre spanning the whole basin width, i.e. the Gulf Stream and North Atlantic Current (Schmitz 1993, Worthington 1976). The western boundary of the gyre constitutes a well-defined current system – the poleward flowing Gulf Stream – while the eastern margin current system is much wider and the currents commonly much weaker and diffuse. Modifications and deviations from this simplified cartoon arise, among other factors, from the boundary conditions of the general circulation problem.

The Azores current is a zonal flow located between 32 and 35ºN that runs from between the Newfoundland Rise to the eastern Atlantic margin, reaching depths of about 1000 m, mean velocities of O(0.1 m/s) and a mean transport of 8-12 Sv (Özgökmen et al. 2001). Althougth its origin and causes are still unclear, numerical models and physical reasoning suggest a

relationship between the Azores Current and the MOW: due to the entrainment of NACW by the MO, the outflow acts as a localized sink of potential vorticity for the Atlantic Ocean, what has been named a "beta plume" effect (Jia 2000, Özgökmen et al. 2001).

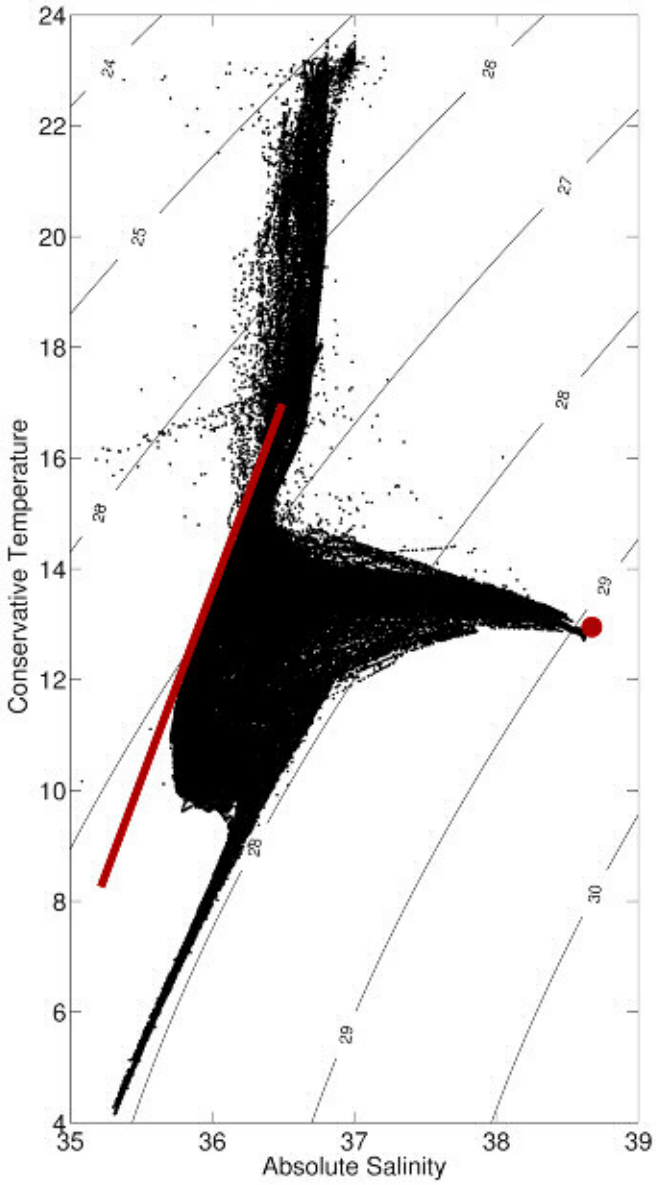

Fig. 1.5. Temperature-Salinity diagram using the data from this study. Eastern NACW is defined by the red line; MW is shown by the red circle. Water from mixing between these two water masses must be located inside the mixing triangle defined by the line and the point.

1.3 METHODOLOGICAL CONSIDERATIONS

1.3.1 BATHYMETRY FROM PROCESSED MULTIBEAM DATA

Raw multibeam data acquired during the 2011 cruise was processed using the CARIS software. Raw data is not suitable for direct conversion into a Digital Terrain Model (DTM), either TIN (Triangulated) or Gridded, requiring several previous steps. First, raw data are imported and converted, and vessel characteristics (such as instrument offset) are applied. Navigation data are subsequently filtered and checked for outliers. Swath editor tools are used in order to eliminate outliers and erroneous numbers, and data are corrected for tidal effects and sound velocity variations due to the temperature and salinity profiles. Once these corrections are computed, data are merged and edited manually using the subset editor. Finally, a BASE surface is created and exported to image and data (ASCII and MATLAB) formats.

1.3.2 VELOCITY MEASUREMENTS

The velocity of a water particle in the ocean can be determined using two methods (asides numerical modeling): it can be either directly measured using an adequate instrument, typically using drifters following water parcels or a moored current-meter, or it can be ascertained indirectly from salinity, temperature and sea surface height data through an inverse method.

Due to the highly complex fluid dynamics of the Gulf of Cádiz, it is likely that the approximations implicit in inverse models will lead to relatively high errors unless an equivalently complex model is used. On the other hand, there is already a large hydrographic and velocity dataset for this region. The methodologies and instrumentation for the several datasets are carefully described at the beginning of each chapter and will not be discussed in detail. In this section we only provide a general overview of the particularities of the data acquisition and the specific problems and limitations derived from the bathymetry and physiography of the Gulf of Cádiz.

The velocity measurements used in this study were obtained using eXpendable Current Profilers (XCP), Shipborne Acoustic Doppler Profilers (SADCP) and Lowered Acoustic Doppler Profilers (LADCP) during several hydrographic cruises in the area (see Chapters 3 and 4). These include novel velocity data acquired using SADCP and LADCP instruments during the MEDOUT 2009 and MEDOUT 2011 experiments; current meter data were also obtained during these cruises but these data will not be discussed in this study.

ADCPs use a sonic pulse or ping to calculate the velocity of a water parcel. This ping is reflected by the microorganisms or particulate matter present in all but the most clean fluid; assuming that these particles are moving with the same average velocity as the water parcel, the echo doppler effect provides us with a way to compute such velocity (Thurnherr 2010, Fisher and Visbeck 1993, Visbeck 2002). ADCPs can be integrated to a ship's hull (SADCP), deployed in conjunction with a CTD (LADCP) or integrated in a mooring.

SADCPs allow velocity measurements while the ship is underway, up to a range limited by the instrument's frequency (typically from a few tens of meters up to 700-800 m) thus providing near-synoptic measurements of a relatively small region. Velocity measurements near the bottom (in a layer 25-50 m thick) are not possible even within the instrument's range, due to interference from the fluid-solid interface. On the other hand, moored ADCPs and LADCPs measure the velocity in a given geographical position but have the ability to provide data for the full water column. By design, SADCP data will have greater data coverage than either LADCP or moored ADCP but it is unable to provide measurements for the water layer nearest to the bottom. In the first 200 km west of the Strait of Gibraltar the MOW propagates as a bottom gravity current, hence only coverage-limited LADCP data will be able to determine its velocity field. On the other hand, a detailed velocity field of the overlying Atlantic layer and the MO nuclei, once this has as they separated from the bottom, can be obtained using SADCP measurements.

Velocity error for SADCP measurements is mainly a function of instrument frequency and configuration, vertical resolution and sea conditions. Increasing the working frequency decreases velocity error but the depth range also diminishes. Decreasing the vertical resolution (increasing bin size) decreases the velocity error. Finally, rough sea conditions increase the error due to ship oscillations and bubble advection towards the ADCP.

LADCP errors are mostly due to unwanted bottom reflections, ship drift and rosette inclination. Bottom reflection may be a problem near the seafloor when the water depth exceeds about 1000 m and can be minimized using a staggered ping configuration for the LADCP script. Ship drift is a relevant problem in the Gulf of Cádiz, especially near the Gibraltar Straits, due to the strong surface currents generated by the inflow of NACW and the tides. It introduces a spurious barotropic component in the velocity profile. The most important error source in our study region is rosette inclination due to the strong current shear. If not heavily ballasted, velocity gradients tilt the ADCP package such that the beam cone axis is no longer vertical. This creates an error in the bin depth proportional to the cosine of the tilt angle. This error can be partly corrected except when the tilt angle exceeds 30º, beyond wich the algorithm will not generate a solution.

During the MEDOUT 2009, cruise extreme rosette tilt was observed due to the strong velocity gradients, only partially minimized through heavy ballasting.

A characteristic error for SADCP velocity measurements in our region is O(5 cm/s). LADCP errors can be of this same order in favorable conditions, up to 10 cm/s in the worst-case scenario. Due to the fact that current velocities are typically of 0.5-1.5 m/s, the relative error range is about 0.03-0.20.

1.3.3 DATA MERGING AND INTERPOLATION

Bathymetry data for the study region came from different sources and with different resolutions. Hence, a detailed approach was followed in order to merge the different datasets into a coherent and uniform product. Different methods have been used by several authors (e.g. Weatherall et al. 2015, Hell and Jakobson 2011) and only the main points will be treated in this section.

Several schemes have been developed in order to interpolate a set of soundings or multibeam data into a regular grid, including linear interpolation, krigging, cubic splines and splines-in-tension (Smith and Wessel 1990). Linear interpolation is the simplest exact interpolation method and has several beneficial properties, including the preservation of maxima and minima and the monotonicity of the data. By definition, the interpolated field is C1 continuous (first derivatives are discontinuous), which can produce a jagged or harsh appearance in the solution, a property undesirable for a representation of the ocean bottom surface.

Krigging is a well-known and widely used interpolation method in the context of geophysical sciences. It uses an estimate of the covariance function in order to provide the best-possible linear estimate of the real variable field. This method also provides an estimate of the interpolation error, hence its appeal for geophysicists. Its major drawback arises from the fact that it is very computationally intensive for more than a few hundred data points; it is also not efficient with highly colinear data, as it is the case with ship soundings along a straight line or CTD casts following a section.

Cubic-splines is an exact interpolation method using piecewise cubic (low order) polynomial. It has the advantage of being C2 continuous, at the expense of preserving the monotonicity and maxima/minima of the interpolated field. It has been widely used for the interpolation of geophysical fields, but it can generate method artifacts such as artificial heights/lows in regions

with steep gradients. This disadvantage can be critical in our study region, due to the abruptness and roughness of the sea bottom morphology in the Gulf of Cadiz.

The splines-in-tension method is based in the solution of the equation (Smith and Wessel 1990):

$$D\nabla^2(\nabla^2 z) - T\nabla^2 z = q \qquad \text{(eq. 1.5)}$$

The first term is the curvature of the interpolant function, z being the interpolant variable and D the flexural rigidity of the plate; T is a uniform isotropic tensile stress and the last term q is a vertical normal stress; 0ℂTℂ1. It can be shown that the method is analogous to a thin plate or membrane stretched over the data points. When T=0, we obtain a solution that minimizes the global curvature (at the expense of introducing large local oscillations). For T different than zero, a tension is introduced that relaxes the global constraint in order to parameterize shorter wavelengths with more accuracy.

Recent bathymetry compilations have used either cubic splines or splines-in-tension methods in order to interpolate ship sounding tracks and multibeam sweeps into a regular grid. Multiresolution methods such as remove-and-restore or stacked splines allow merging high and low resolution data, e.g. multibeam soundings with a resolution of tens of meters and altimetry data with a wavelength greater than 10 km. Open-source (e.g. Generic Mapping Tools) and license-based (e.g. MATLAB; D'Errico 2006) implementations for most (but not all) of these algorithms are available.

In our case, a modified remove-and-restore algorithm was custom-implemented in MATLAB (for efficiency and workflow related reasons). The algorithm successfully merges data with resolution from about 60 m up to 1 km (approximately); grid artifacts and dataset boundaries were satisfactorily eliminated or minimized (Fig. 1.6).

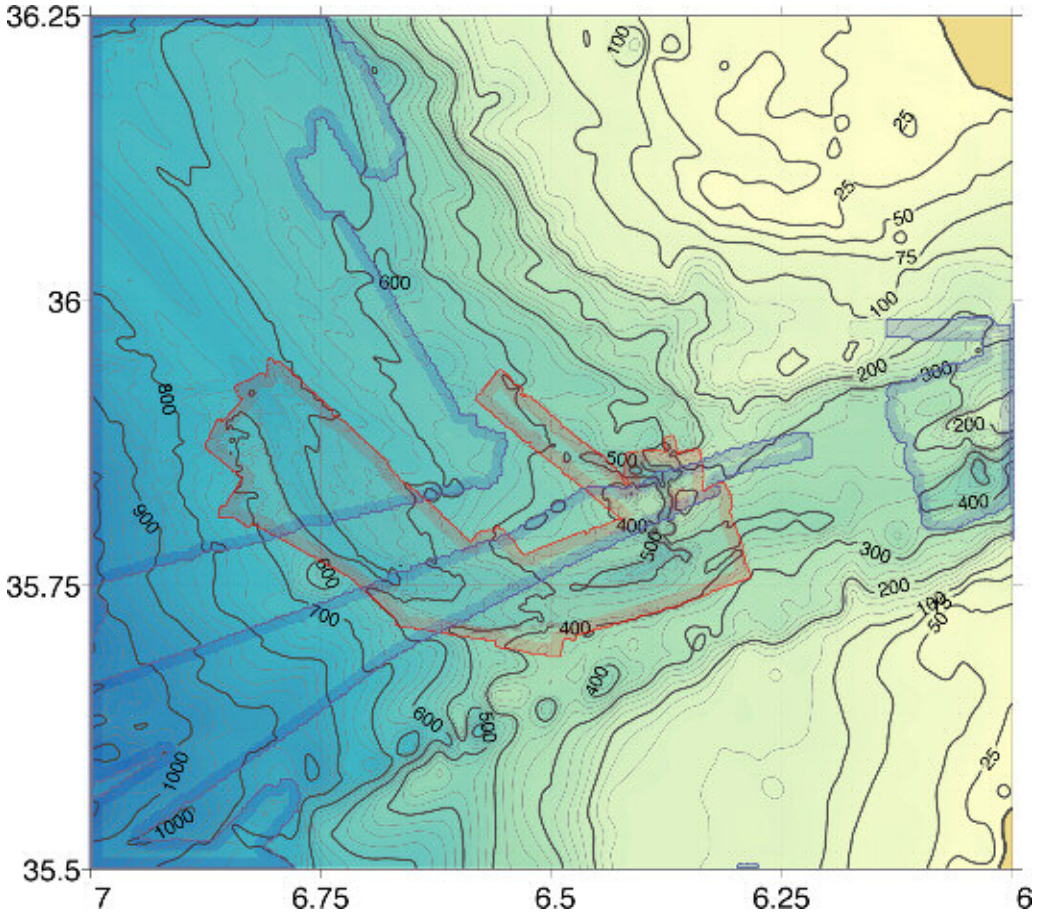

Fig. 1.6: Bathymetry of the region of interest (near field). This figure is a compilation of data from several sources with very different resolutions: MEDOUT 2011 high-resolution (up to 60 m) multibeam data (red), SWIM compilation multibeam data with a resolution of 250 m (Zitellini et al. 2009, blue contour) and SRTM30-plus bathymetry with a resolution between 1-12 km (Smith and Sandwell 1997).

1.3.4 HYDROLOGICAL AVENUES

For a pure gravity current, the fluid would follow the maximum slope trajectory, crossing the isobaths at a normal angle. During the initial stages of the MOW, we can approximate its behavior as that of a gravity current. The motion of this bottom flow would be calculated replacing gravity by a reduced gravity g':

$$g' = g\frac{\Delta\rho}{\rho_0} \qquad \text{(eq. 1.6)}$$

where Δρ is a characteristic density difference between the bottom layer and the environmental fluid, ρ_0 is the density of the ambien water and g is the gravity acceleration.

The idea of a down-slope flow allows establishing a strong analogy between the MOW and the behavior of tributaries above land. Hence, the possibility of using tools developed by hydrologists for land arises naturally, subject to the pertinent modifications. A useful concept is that of a drainage basin and the surface flow of tributaries.

In hydrology, we can loosely define a drainage basin as the land surface area where a river or a stream obtains its water supply. Standard techniques allow us to calculate, using a Digital Terrain Model (DTM), the trajectory of the different streams and rivulets that merge and coalesce in order to constitute a river following the pathway of maximum gradient (Schwanghart and Kuhn 2010). Of course, this is not the case in the ocean, due to the fact that a gravity current is not formed by the union of converging tributaries. Nevertheless, it is possible to obtain the expected trajectory of a gravity current from similar principles, once suitable modifications to the physics are allowed.

This description fails to take into account any effects derived from frictional and Coriolis forces. One possible way to incorporate the effect of the Earth's rotation is to introduce a Coriolis slope, $\delta h/\delta x$, using the approximation that the bottom flow is in geostrophic balance, with a velocity given by:

$$fv = g'\frac{\delta h}{\delta x} \qquad \text{(eq. 1.7)}$$

where f is the Coriolis parameter, g' is the reduced gravity as defined above and h is the ocean floor depth (Fig. 1.7).

A reduced slope can be defined as the vector sum of the topographic plus Coriolis slopes. Once the reduced slope is obtained, it is then trivial to apply the standard hydrological-avenue methodology to the reduced bathymetry (Fig. 1.7); for more details see Chapter 4. This approach, which relies on the cross-flow momentum balance being in geostrophic equilibrium, allows assessing the gross effects of rotational forces on the general trajectory of the flow, inferring what areas are under Coriolis control in opposition to those where bathymetric steering is the dominant factor.

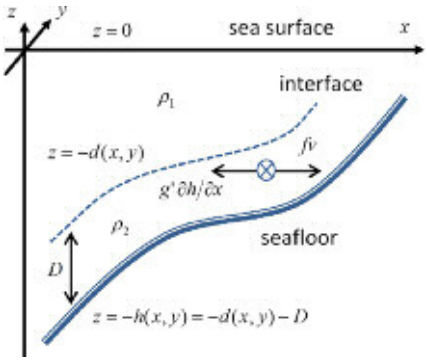

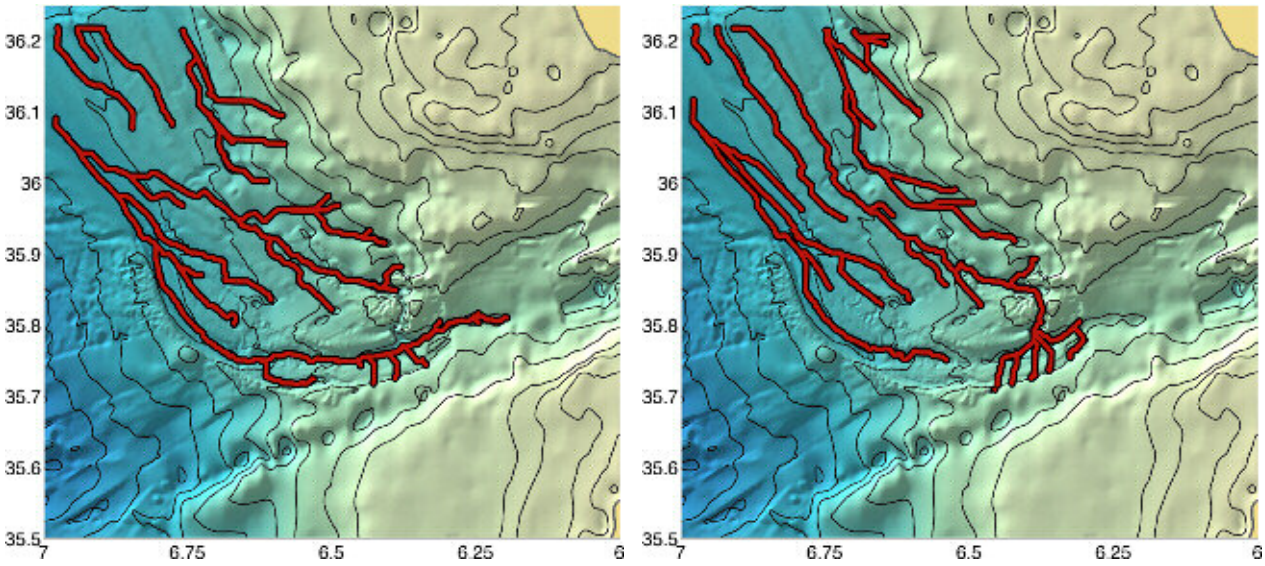

Fig. 1.7: (Top) Force balance in a gravity current (excluding friction and mixing). (Bottom left) Gravity current network with no rotation; (Bottom right) Gravity current network in cross-stream geostrophic balance using v = 1 m/s.

1.4 DISSERTATION LAYOUT

The following three chapters in this dissertation follow the MOW as it transits through the Strait of Gibraltar and enters the Gulf of Cádiz. Each chapter explores a different aspect of the transformation and/or pathway of the MOW: from the effect of vertical mixing within the Strait in Gibraltar to its rapid plunging downstream of a bottom discontinuity past West Espartel Sill to its final transformation and spreading within the Gulf of Cádiz.

A plausible mechanism for extensive upward entrainment in the Strait of Gibraltar, leading to the rapid cooling of the surface waters, is described in Chapter 2. Such events, which lead to a rapid decrease in sea surface temperature (SST) that lasts 5-10 days, are attributed to high frequency variations in atmospheric pressure over the western Mediterranean Sea. A simple 1.5-layer model is developed and its hindcast is compared with the real hydrographic and velocity observations; further, some simple energy arguments are used to explore the consistency of the entrainment hypothesis with the cooling episodes.

Chapter 3 deals with a detailed description of the MOW characteristics in the western end of the Strait of Gibraltar, what we name the Gibraltar Channel. We use data from the MEDOUT 2009 cruise to explore the dynamics of the MOW as it overcomes West Espartel Sill, at approximately 6º30'W, the last obstacle before finally plunging into the Gulf of Cádiz. As the flow overtakes the interface develops high billows and mixing and energy dissipation is very much enhanced. The development of instabilities, as related with the phase of the tide and the location along the channel, is discussed. We close the chapter with a theoretical discussion of the applicability of grabity current theory for the propagation of the MOW within the Gulf of Cádiz.

Finally, Chapter 4 will present a detailed description of the MOW trajectory into the Gulf of Cádiz, both near the western end of the Strait of Gibraltar and as it flows into the complex network of contouritic, turbiditic and diapiric structures and canyons in the upper slope of the Gulf of Cádiz. An improved bathymetry of the region of interest is presented, and a new hydrological tool is developed that allows assessing the relative impact of bathymetric steering and the Earth's rotation in the MOW's pathway. These tools are combined with an extensive dataset of hydrographic and velocity measurements in order to examine what are the principal mechanisms (bathymetry, Coriolis forces and mixing) that control the MOW's evolution.

CHAPTER 2: INTERMITTENT VERTICAL MIXING IN THE STRAIT OF GIBRALTAR

A. L. Aretxabaleta , J. L. Pelegrí, M. Gasser, F. J. Machín, A. Hernández-Guerra and P. Sangrà

Unpublished manuscript

Abstract

Satellite imagery shows that the Strait of Gibraltar displays intermittent mixing events, roughly about once per month and lasting for a few days, when the sea surface temperature (SST) of the entire domain decreases by several degrees. The hydrographic time series suggest that this decrease is accompanied by a deepening of the upper Atlantic layer, being consistent with upward entrainment of Mediterranean subsurface waters. We construct a simple gravity-reduced 1.5-layer unidimensional model, where the along-shore velocity is expressed in terms of the observed cross-strait sea-surface slope, forced by high-frequency changes (periods of 1-10 days) of sea-surface atmospheric pressure in the western Mediterranean, to diagnose when the two-layer Richardson number becomes subcritical and mixing takes place. The model is accompanied by simple mechanic-energy conserving arguments to predict the evolution of the upper layer density and velocity during the mixing events. The models are capable of reproducing the timing of the observed fluctuations while slightly overestimating their size. The results confirm that the observed mixing and sporadic SST decrease is due to shear-induced strait-wide vertical mixing, initiated through intermittent sea-surface low pressures in the western Mediterranean and possibly conditioned by the phase of the baroclinic tide.

.

2.1. INTRODUCTION

The Strait of Gibraltar connects the Mediterranean Sea and North Atlantic Ocean, with relatively fresh and warm Atlantic waters entering near the surface and relatively cold and salty Mediterranean waters exiting at deeper levels. The Strait is about 60 km long, comprised between Capes Espartel and Trafalgar to the west (43 km) and the Point Almina (east the city of Ceuta) and the Rock of Gibraltar to the east (23 km). The minimum width of the strait is 14 km, and its depth ranges between 280 m in Camarinal Sill, near the western end, and over 900 m near the Gibraltar-Ceuta section (Fig. 2.1). The Strait's dynamics has been extensively studied during the last five decades (e.g. Lacombe and Richez, 1962; Deacon, 1985; Farmer and Armi, 1988; Candela et al., 1989; Bryden and Kinder, 1991; Bryden et al., 1994; Candela, 2001; Vargas et al., 2006; García Lafuente et al., 2013). The research on the Strait was initially motivated by its geostrategic location and more recently because of its role controlling the conditions in the Mediterranean and Atlantic basins and, hence, its potential impact of the Earth's climate. The outcome of these studies has been the discovery of a variety of dynamic phenomena within and near the Strait, forced both locally and remotely, and a better appreciation of the Strait's role controlling the climate at regional and global scales. In this study, we examine one specific aspect that has not yet received proper attention: the intermittent appearance of cold surface waters that cover the entire Strait.

Several studies have previously described the appearance of cold patches of surface waters in the Strait of Gibraltar region, which have been attributed to upwelling, either tidally or wind induced, and to local mixing as the result of internal waves. La Violette and Lacombe (1988) proposed the depth of the interface between the Atlantic and Mediterranean waters to be controlled by tidally induced convergence in the lower layer and divergence in the upper layer, causing the cold lower-layer waters to intermittently reach the sea surface. The importance of tides in the generation of localized hydraulic jumps an mixing, mainly at Camarinal Sill, and internal bores that propagate along the Strait, has also been reported (Izquierdo et al., 2001; Bruno et al., 2002; Alonso del Rosario et al., 2003; Macías et al., 2006; Sanchez Garrido et al., 2008; Sannino et al., 2009; Bruno et al., 2013; García Lafuente et al., 2013). Additionally, Richez and Kermogard (1990) and Folkard et al. (1997) have suggested that strong easterly winds may drive upwelling in the southern margin of the Strait. Stanichny et al. (2005) found a high correlation between easterly winds and a decrease in sea surface temperature (SST). Peliz et al. (2009) added that the winds generate a coastal jet in the southern portion of the Strait, which drives the upwelled waters into the Atlantic coast, off NW Africa, as a cold filament.

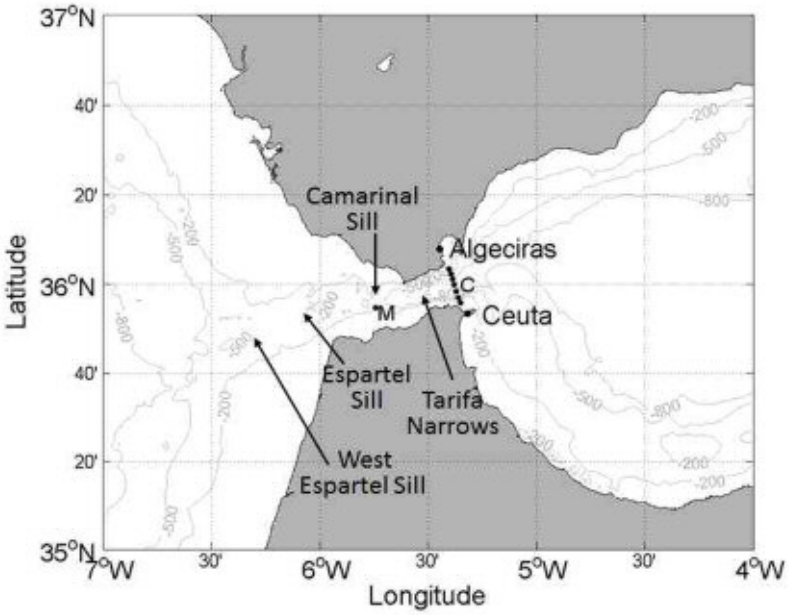

Fig. 2.1. The Strait of Gibraltar with the Gulf of Cadiz to the west and the Alboran Sea to the east, displaying the bathymetric contours in meters and the locations mentioned in the paper. The eastern section, with seven stations, runs between Algeciras and Ceuta, with station C as its central. On Camarinal Sill we find station M.

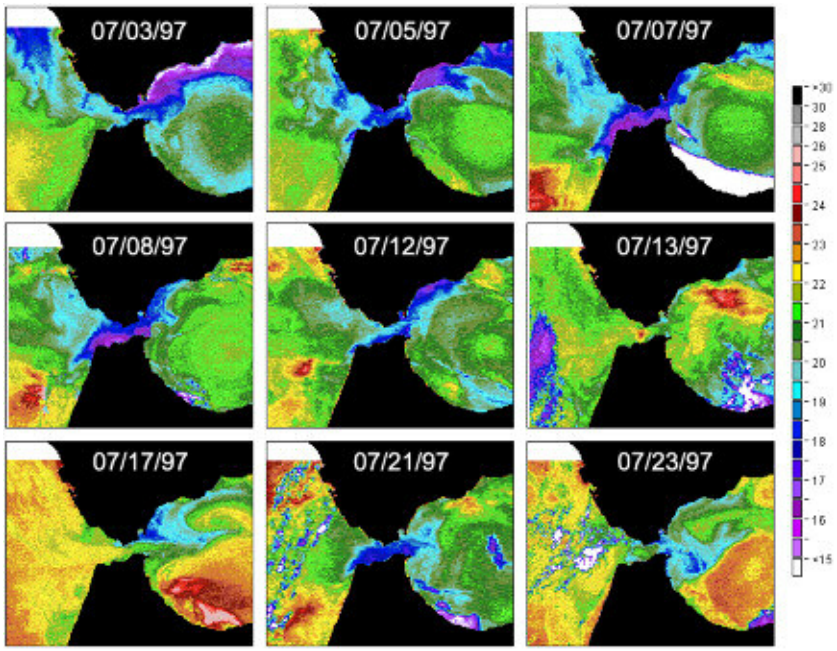

Fig. 2.2. SST sequences for the Strait of Gibraltar during July 1997. The top and centre rows illustrate a relatively long mixing and stratification event between 3 and 13 July. The bottom row illustrates a shorter event, between 17 and 23 July.

Both internal oscillations and wind vertical pumping appear capable of inducing localized upwelling. In particular, the hydraulic jump generated at Camarinal Sill and the propagating baroclinic tides are capable of producing rapid local oscillations in the depth and thickness of the interface, on time scales from tens of minutes to hours, respectively (Sannino et al., 2009; García Lafuente et al., 2013). However, they do not appear to be responsible for the occurrence of events that take place on time scales of days, where the entire surface Strait cools down, as shown by sequences of sea surface temperature (SST) imagery (Figs. 2.2 and 2.3). These events happen intermittently, with no clear daily or fortnightly periodicity, and thus appear to not be solely related to tidal dynamics. Furthermore, since the width of the Strait is similar to the internal radius of deformation of the two-layer system, it is difficult to envisage the wind raising deep cold waters over the entire Strait. During strong easterly winds, for example, surface Ekman transport would divert warm waters towards the opposite coast, something that is not consistently observed in SST images.

In this study, we explore the alternative hypothesis that generalized cooling of surface waters, typically lasting just a few days, is the result of widespread mixing between the Atlantic and Mediterranean waters. We idealize the Strait dynamics as a two-layer flow, with the velocity in the upper layer in geostrophic balance. The two-layer system experiences occasional transitions to a subcritical state, with one-way entrainment of the Mediterranean into the Atlantic layer (as in Turner, 1986). As a result, the surface layers cool down while the interface between both layers remains sharp.

These ideas are partly motivated by early works on two-layer hydraulic theory that examined the possibility of subcritical, critical or supercritical conditions inside the Strait of Gibraltar (Bryden and Stommel, 1984; Farmer and Armi, 1986, 1988; Armi and Farmer, 1987, 1988; Bormans and Garrett, 1989a,b; Garrett et al., 1990; Bryden and Kinder, 1991; Dalziel, 1991; García Lafuente et al., 2002a; Sannino et al., 2007, 2009); hereafter, we will refer to subcritical conditions as those corresponding to a dynamically unstable flow, characterized by a gradient Richardson numbers which is less than some critical value, $Ri < Ri_c$ (for a historic review, see Van Gastel and Pelegrí, 2004). These studies indicate that the stability of the flow within the Strait will depend on the existence of one or more hydraulic, and whether these controls may or may not apply to both layers. For example, if there are two control points on both layers, then the interior of the Strait will be isolated from the neighbouring reservoirs. However, if there is only one control point (or if the second control point affects only one layer) then the information from one reservoir could propagate along the unconstrained layer into the interior of the Strait.

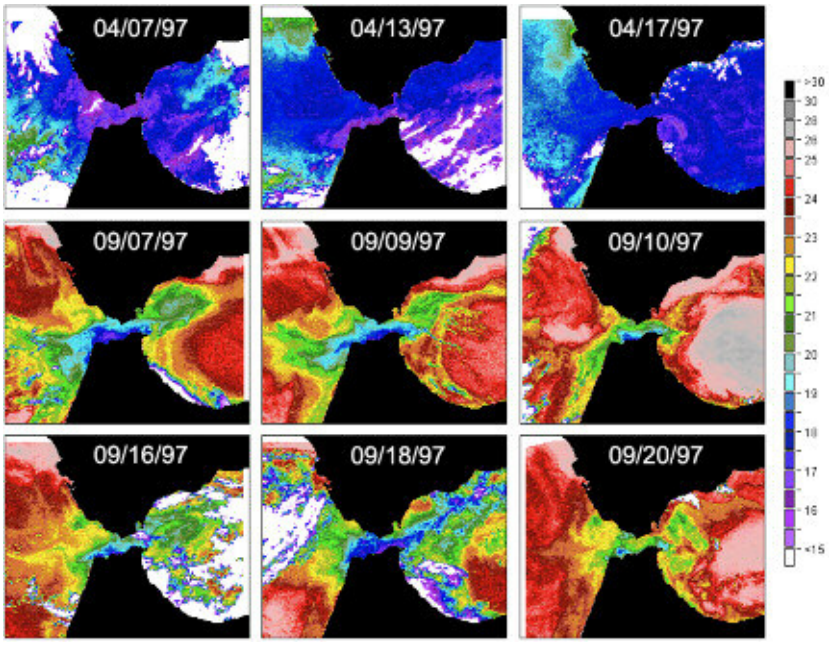

Fig. 2.3. SST sequences for the Strait of Gibraltar during April and September 1997. The centre and bottom rows illustrate one stratification event between 7 and 10 September, followed by a rapid mixing and stratification event between 16 and 20 September.

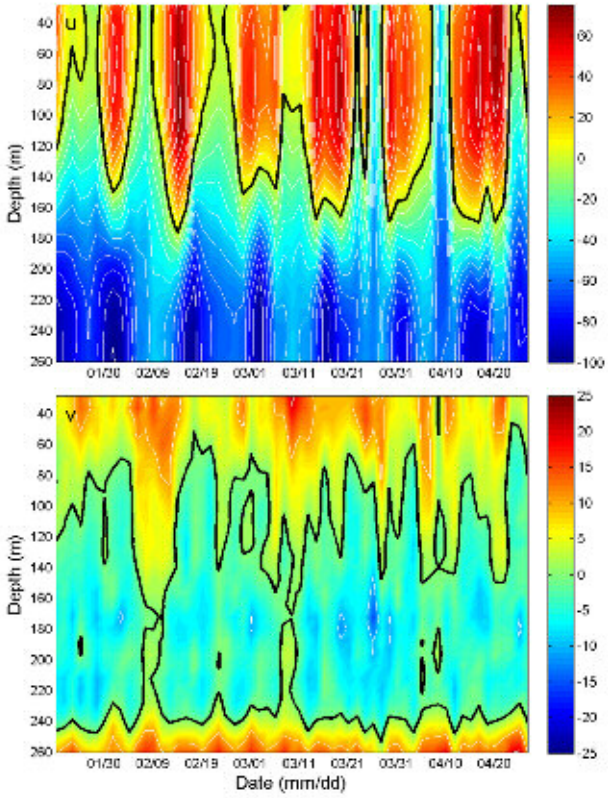

Fig. 2.4. Time series between 19 January and 28 April 1997 of the (top) along-strait and (bottom) cross-strait velocities (cm s^{-1}) at station M, after projecting the velocity data to the axis of maximum variance.

Most studies on the Strait of Gibraltar have considered the existence of two control points, Camarinal Sill and Tafira Narrows, and possibly a third one, Espartel Sill; in some works even a fourth control point, West Espartel Sill, has been proposed (Armi and Farmer, 1988; Farmer and Armi, 1988). In these circumstances, the idealized hydraulic theory (steady-state and frictionless) indicates that the region between these controls will be connected by subcritical flow. Armi (1986) and Armi and Farmer (1986), however, have shown that a sill affects directly the lower layer and only indirectly the upper one. Further, Camarinal, Espartel and West Espartel Sills are found in the region where the Strait opens widely and it is fair to question how much they can control the flow of the upper layer. If there is no complete control on the upper layer, the Strait and Atlantic waters of the upper layer may indeed be connected despite the existence of a hydraulic control on the lower layer.

The dynamic stability of the flow is likely to change with time. Bormans and Garrett (1989a,b) and Garrett et al. (1990) have shown the alternation between maximal (the flow is critical and the water exchange is maximum) and submaximal conditions in the course of the year, at unknown frequencies. Garret et al. (1990) actually proposed the existence of a seasonal cycle in the exchange at the Tafira Narrows, with maximal conditions following deep-water formation early in the year, but with a large degree of uncertainty. During submaximal conditions the Mediterranean reservoir could also influence the flow conditions within the Strait. A time-dependent barotropic current could also be responsible for the occasional loss of one of the hydraulic controls (Armi and Farmer, 1986; Farmer and Armi, 1986). This current could either be at tidal or subinertial frequencies, the latter forced through pressure differences between both adjacent basins (Crepon, 1965; Garret, 1983; Candela et al., 1989; García Lafuente et al., 2002a) or by wind and pressure-difference pulses over the Strait (Candela et al., 1989; García Lafuente et al., 2002a,b).

In this study, we investigate the occurrence of widespread mixing events within the Strait of Gibraltar, either forced locally or remotely by the conditions in both neighbouring basins. Our objectives are, first, to identify the characteristic spatial and temporal scales of these mixing events and, second, to examine whether these events may be predicted using a simple reduced-gravity subinertial model, where the only external force is the atmospheric pressure at both ends of the Strait and the along-strait velocity is diagnosed from the sea-level data (assuming a cross-strait geostrophic balance). In particular, the model allows us to determine if a rapid deepening of the surface layer is associated with transitions between stable and unstable flow states, as expressed in terms of a two-layer Richardson number.

The organization of the manuscript is as follows. We first present the data sets (section 2.2) and use them to illustrate the occurrence of strait-wide mixing events during one particular year

(section 2.3). The relevance of the oscillations in the Mediterranean sea-surface pressure, creating along-strait forces at periods between 1 and 10 days, is examined in section 2.4. We then develop an idealized 1.5 layer reduced-gravity model (section 2.5) and examine whether, during mixing events, the changes in kinetic energy are consistent with predictions on the change in potential energy (section 2.6). We later present the numerical results for different values of the tuning parameters (section 2.7) and discuss the relevance of the various forcing mechanisms (section 2.8). We close the paper with some concluding remarks (section 2.9).

2.2 DATA SET

We have selected an 11-month period, from 1 December 1996 to 31 October 1997, when a substantial amount of hydrographic and current velocity data was obtained as part of the CANIGO (Canary Islands, Azores and Gibraltar Observations) project (Parrilla et al., 2002). In particular, during this period there were eight hydrographic cruises that included a cross-strait section (Algeciras-Ceuta) with repeated sampling carried out in its mid-point (station C, Figure 2.1). Additionally, between 19 January and 28 April 1997, a mooring with a bottom-mounted acoustic Doppler profiler (ADCP) was located in the Camarinal Sill (280 m, station M in Figure 2.1), sampling most of the water column, between about 260 m and 20 m.

The data was complemented with hourly sea-surface elevations and daily mean values of sea-surface atmospheric pressure. The sea-surface elevations corresponded to Ceuta and Algeciras, in the African and Iberian margins of the strait, which are part of the tide-gauge network maintained by the Spanish Institute of Oceanography (Fig. 2.1). For the sea-surface atmospheric pressure we have looked at two data sources. First, the forecasts by the Spanish National Institute of Meteorology at two individual locations, (36ºN, 4ºW) and (36ºN, 8ºW), separated by a distance of 261 km and chosen as characteristic of the Atlantic and Mediterranean sides of the Strait of Gibraltar. Second, the mean reanalysis values obtained by the U.S. National Centers for Environmental Prediction (NCEP) for different regions in the northeastern Atlantic Ocean and western Mediterranean Sea; specifically, we have considered one first case with relatively large domains, (30-40ºN, 10-20ºW) and (35-45ºN, 0-10ºE), and a second case with much smaller domains, (35.0-37.5ºN, 5.0-7.5ºW) and (35.0-37.5ºN, 2.5-5.0ºW). It turns out that the pressures from the individual locations are very similar to the average values from the 2.5º latitude-longitude boxes, while averaging over 10º generally results in a smoothing of the time series (not shown).

Finally, we have examined daily SST images from NOAA satellites for the Strait of Gibraltar. The SST images were acquired through a local satellite receiving station located in Gran Canaria and processed using the methodology presented by Eugenio et al. (2001).

2.3 OBSERVATIONS OF STRAIT-WIDE MIXING EVENTS

The SST imagery illustrates the existence of strait-wide mixing events lasting a few days. Cloud coverage usually prevents from properly appreciating the time evolution of most events, yet the analysis of the 11 months of SST images allows identifying several events when widespread mixing took place (see also the SST images in García Lafuente et al., 1998). The examples shown in Figures 2.2 and 2.3 are illustrative of mixing and restratification events, each of them occurring on time scales of 2-5 days, so that the entire development and disappearance of the cold water anomaly in the Strait of Gibraltar takes between about 5 and 10 days.

The decrease in SST implies the upward entrainment of subsurface cold water. This subsurface water not only is colder than the surface waters but also moves towards the Atlantic Ocean. Hence, such an upward entrainment would not only cool down the surface layers but would also reduce, or even arrest, the surface flow towards the Mediterranean. Hence, the time series of velocity at Camarinal Sill, as recorded between January and April 1997, can be used to investigate the occurrence of such events.

A previous step, however, is to identify the along-strait direction. For this purpose the original velocity time series is analysed searching for the angle of the current that leads to the maximum variance; we find that the angle between the current and the E-W axis increases counter-clockwise with depth, between about 0º in the top 100 m to 30º at 260 m, indicative of local bathymetric effects on the near-bottom flow. The original velocity time series is hence projected into this (depth-dependent) axis of maximum variance, and the time series for the along- and cross-strait velocity components are obtained (Fig. 2.4). As expected, the flow is aligned along the main axis of the strait, reflecting a dominant fortnightly variation: most of the time the top 100 m of the water column head towards the Mediterranean but about every two weeks this eastward flow weakens or ceases and, simultaneously, the subsurface near-bottom westward flow weakens. However, this variation is not regular: there are instances when the surface flow completely reverses, the most prominent example occurring between the 8 and 10 April, precisely when the SST images exemplified the occurrence of widespread surface cooling (top panels, Fig. 2.3).

The rapid mixing of the top 100-150 m of the water column, at time scales from hours to days, is also observed in the eastern end of the Strait (station C, at the mid-point in the Ceuta-Gibraltar section). A rapid interface deepening, of the order of 30-50 m and lasting no more than a few hours, took place on 11, 14 and 15 April 1997 (Fig. 2.5). However, on 16 April 1997 there was a much stronger and longer event, where the mixed layer deepened by about 50 m during 40

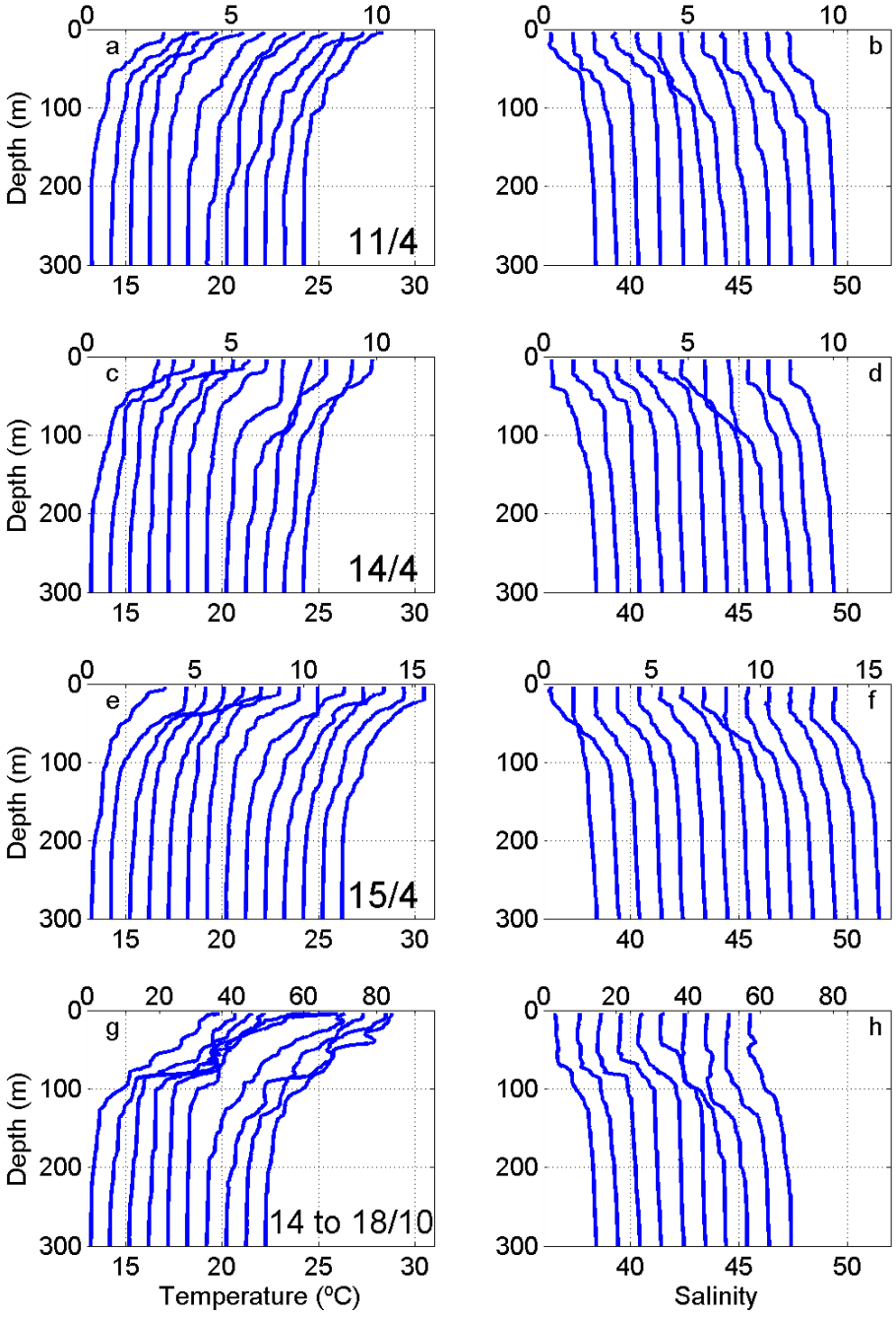

Fig. 2.5. Short-term evolution of the (left panels) temperature and (right panels) salinity stratification in station C during (top row) 11 April 1997, (second row) 14 April 1997, (third row) 15 April 1997, and (bottom row) 14 to 18 October 1997. The temperature and salinity scales correspond to the leftmost profile; subsequent profiles are displaced one unit to the right. The upper axis is indicative of the time interval between profiles.

hours and re-stratified during the following 40 hours; unfortunately, no simultaneous cloud-free SST images were available.

The flow and SST variability at any specific location, such as over Camarinal Sill or along the Ceuta-Algeciras section, is not necessarily indicative of strait-wide events. In particular, the Camarinal Sill is the site of hydraulic jumps that are generated during the intensification of the Atlantic tide, which propagate east as an internal bore on time scales not exceeding a few hours (Bruno et al., 2002; García Lafuente et al., 2013). During the spring phase of the fortnightly tidal cycle, the baroclinic tide and the internal bore reach maximum velocities and set the conditions necessary for localized mixing – yet there must be some other mechanism that is capable of causing strait-wide mixing, acting at time scales long enough to alter the near-geostrophic along-strait flow. The existence of substantial changes in the geostrophic flow of the upper layer is indeed reflected by the variations in the cross-strait tilting of the interface between the upper and lower layers, with times when it is strongly tilted (therefore an intense Atlantic inflow) and times when it remains much flatter (Fig. 2.6). In the following section we explore whether this mechanism is related to the sea-surface atmospheric pressure.

2.4 SEA-SURFACE ATMOSPHERIC FORCING

Several authors have pointed out the effects of the atmospheric pressure over the western Mediterranean Sea on the flow through the Strait of Gibraltar (Crepon, 1965; Garrett, 1983; Garrett and Majaess, 1984; Candela et al., 1989). In particular, Candela et al. (1989) carried out a principal mode analysis of six months of velocity data from three moorings in Camarinal Sill. They found that most of the variance (84%) was well correlated with fluctuations of the sea-surface atmospheric pressure in the western Mediterranean Sea, and only 12% of the variance was related to the spring-neap tidal cycle. In this study, we use our sea-surface atmospheric pressure and sea surface elevation data to explore these relationships between December 1996 and October 1997. We focus on the following variables: atmospheric pressure over the western Mediterranean and eastern North Atlantic (the average values for 2.5º latitude-longitude boxes, section 2.2) and their difference (the along-strait pressure gradient), sea surface residual elevation at Algeciras and Ceuta and their difference (proportional to the along-strait geostrophic flow), and the time derivative of these cross strait gradients (the along-strait acceleration).

Our first step is to conduct a harmonic analysis of the hourly sea-surface elevation data from Algeciras and Ceuta, and to calculate the difference between the observations and predictions (Fig. 2.7). The sea-surface elevation residuals at these locations are daily averaged and compared with the sea-surface atmospheric pressure at either the Atlantic or Mediterranean side of the Strait. In general, the atmospheric pressure at both locations evolves similarly in time, and so do the tidal residuals. The oscillations of the along-strait pressure difference are much smaller than the oscillations of the pressure on either the Mediterranean or Atlantic sides and, similarly, the oscillations in the cross-strait change in residual elevation are much smaller than the oscillations of the residual elevation in either Algeciras or Ceuta (Fig. 2.7).

The time series in Figure 2.7 also show that the pressure and residual elevations are anti-correlated, but only at relatively low frequencies: those oscillations with temporal scales of a few days do not exhibit such phase opposition. Scattered plots of the filtered time series confirm that the low (periods longer than 30 days) and intermediate (periods of 10-30 days) frequencies are anti-correlated but not so the high frequencies (periods of 1-10 days) (Fig. 2.8).

Finally, we consider whether the along-strait geostrophic flow is indeed related to the pressure fluctuations in the western Mediterranean (Candela et al., 1989). We hypothesize that only those pressure oscillations at (relatively) high frequencies (periods between 1 and 10 days) are not compensated through the inverted-barometer effect and, hence, cause subinertial pressure

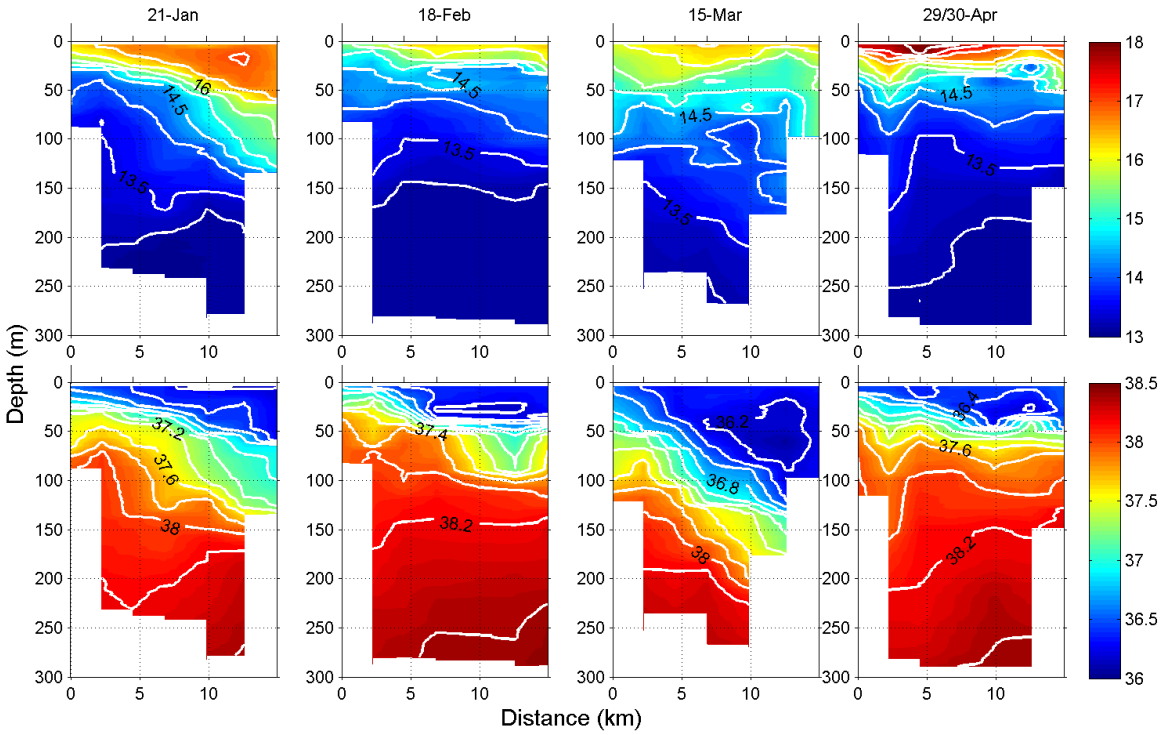

Fig. 2.6. Monthly distributions of (top panel) temperature, (centre panel) salinity, and (bottom panel) potential density, from January to April 1997, along the hydrographic section between Ceuta (to the right) and Algeciras (to the left).

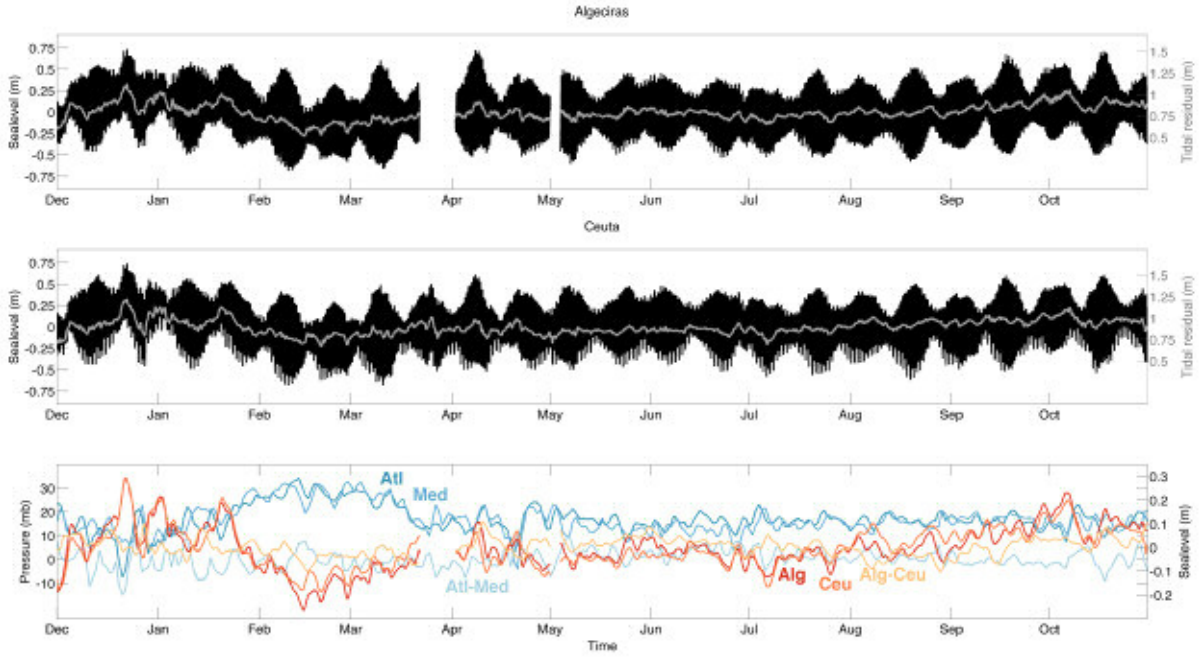

Fig. 2.7. (Top and centre panels) Hourly tidal elevations (black line) and daily tidal residuals (grey line) in Algeciras and Ceuta. (Bottom panels) Tidal residuals in Algeciras and Ceuta (grey solid and dashed lines, respectively) and sea-surface atmospheric pressure in the Atlantic (35.0 to 37.5ºN, 7.5 to 10.0ºW) and Mediterranean (35.0 to 37.5ºN, 2.5 to 5.0ºW) (black solid and dashed lines, respectively).

forces that can drive the along-strait flow. For this purpose we compute the cross-strait difference in tidal residuals (proportional to the along-strait geostrophic flow) and the daily change of this cross-strait difference (proportional to the geostrophic acceleration). A scatter plot of the first variable (the geostrophic velocity) as a function of the atmospheric pressure in the Mediterranean shows no significant correlation; however, if we choose the second variable (the geostrophic acceleration) the correlation becomes significant (Fig. 2.8). Thus, high-frequency sea-surface atmospheric pressure oscillations (with periods between 1 and 10 days) in the western Mediterranean appear as capable of driving substantial subinertial accelerations in the along-strait surface flow. In the following section we propose a simple model that considers these pressure fluctuations to investigate the development of subcritical conditions that result in strait-wide mixing.

2.5 DIAGNOSTIC 1.5 LAYER REDUCED GRAVITY MODEL

2.5.1 MODEL FORMULATION

As we are interested in predicting the evolution of the pycnocline between the Atlantic and Mediterranean waters, we idealize the Atlantic inflow and Mediterranean outflow as a two-layer flow, with *x* and *y* as the along- and cross-strait coordinates (positive directions towards the East and North), respectively, and *z* the vertical coordinate (positive upwards) (Fig. 2.9). All variables are depth independent (except pressure) and refer to the upper layer: (u,v) are the horizontal velocities in the (x,y) directions, ρ is the density, *p* is the pressure, η is the free-surface elevation, and *h* is the depth of the upper layer.

In the case of the Strait of Gibraltar, the Atlantic and Mediterranean water transports differ by about 5% (Soto-Navarro et al., 2010) and the thickness of the Mediterranean layer is generally several times greater than the depth of the Atlantic waters (except over the western sills). Hence, it turns out that the along-strait velocity of the Atlantic waters (upper layer) is typically much greater than that of the Mediterranean outflow (lower layer), which is therefore neglected. We also take the cross-strait velocity as zero, so the cross-strait momentum advection and along-strait Coriolis force are not considered. Further, following Crepon (1965), Garrett (1983) and Candela et al. (1989), we consider the subinertial flow fluctuations in the upper layer to be controlled by changes in atmospheric pressure and interfacial friction, so we neglect the effects of wind stress on the surface layer. The equation for the *x* (along-strait) component of the depth-integrated upper-layer momentum becomes

$$\frac{\partial\left[u\left(\eta+h\right)\right]}{\partial t}+\frac{\partial\left[u\,u\left(\eta+h\right)\right]}{\partial x}=-\frac{1}{\rho}\frac{\partial}{\partial x}\left(\int_{-h(x,t)}^{\eta(x,t)}p\,dz\right)+\frac{P_{sx}}{\rho}+\frac{P_{bx}}{\rho}-\frac{\tau_{bx}}{\rho} \qquad \text{(eq. 2.1)}$$

where P_{sx} and P_{bx} are the *x* component of the pressure forces acting on the upper and lower faces of the water column (Fig. 2.9c), and τ_{bx} is the interface stress between both layers, again in the *x* direction.

The upper-layer pressure is $p=p_{at}+\rho g\left(\eta-z\right)$, as obtained from the hydrostatic equation $\frac{\partial p}{\partial z}=-\rho g$ and the atmospheric pressure condition $p\left(z=\eta\right)=p_{at}$. Hence, after integrating over the upper layer, the along-strait pressure gradient is given by:

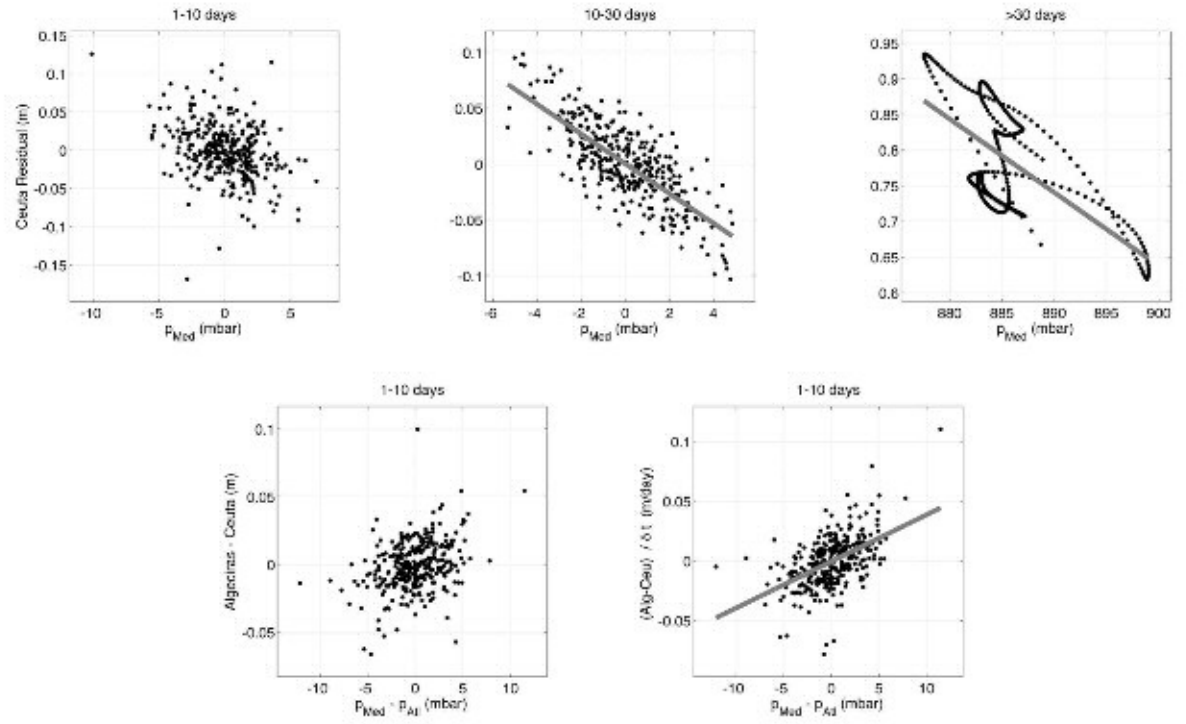

Fig. 2.8. (Top panels) Scattered plots of the daily tidal residuals in Algeciras as a function of the daily values of sea-surface atmospheric pressure in the western Mediterranean (36ºN, 4ºW); the tidal residuals and pressure data are decomposed in three different frequency bands: (left panel) 1-10 days, (middle panel) 10-30 days, and (right panel) longer than 30 days; the correlations are significant only at the intermediate and low-frequency bands. (Bottom panels) Results for the high-frequency band: (left panel) the cross-strait difference in residual elevations (Algeciras minus Ceuta) shows no significant correlation with the atmospheric pressure in the western Mediterranean but (right panel) its daily change does. The data in all panels corresponds to the period between 1 December 1996 and 31 October 1997).

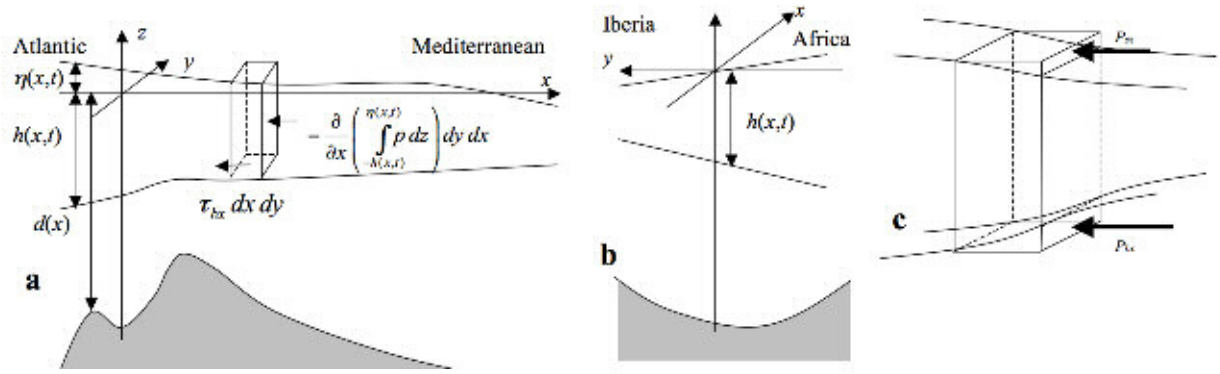

Fig. 2.9. Main elements of the one and a half layer model: (a) Lateral view from Africa with the surface forces acting on an upper-layer water column, (b) along-strait view from the Atlantic Ocean, and (c) detail of the pressure forces associated to the tilted free surface and interface.

$$\frac{\partial}{\partial x}\left(\int_{-h(x,t)}^{\eta(x,t)} p\,dz\right) = \frac{\partial\left[p_{at}(h+\eta)\right]}{\partial x} + \rho g(h+\eta)\frac{\partial(h+\eta)}{\partial x}$$

The frictional force between the upper and lower layers is commonly parameterized in terms of the velocity difference between both layers. Since we neglect the speed of the lower layer, the interface friction force (per unit area) becomes a linear function of the upper-layer velocity, i.e. $\tau_{bx} = r\rho uh$ (e.g., Csanady, 1976). Additionally, the *x* component of the pressure forces (per unit area) acting on the top and bottom faces of our control volume are $P_{sx} = p_{at}\,\partial\eta/\partial x$ and $P_{bx} = p_b\,\partial h/\partial x$, where $p_b \equiv p(z=-h) = p_{at} + \rho g(\eta + h)$ is the pressure at the interface between the upper and lower layers.

After these considerations, Equation (2.1) becomes

$$\frac{\partial\left[u(\eta+h)\right]}{\partial t} + \frac{\partial\left[u\,u(\eta+h)\right]}{\partial x} = -\frac{1}{\rho}\frac{\partial\left[p_{at}(h+\eta)\right]}{\partial x} - g(h+\eta)\frac{\partial(h+\eta)}{\partial x} + \frac{p_{at}}{\rho}\frac{\partial\eta}{\partial x} + \frac{\left[p_{at}+\rho g(\eta+h)\right]}{\rho}\frac{\partial h}{\partial x} - ruh \qquad \text{(eq. 2.2a)}$$

This last equation may be further simplified by neglecting those terms where the thickness of the surface elevation η is compared with the thickness of the upper layer *h*, leading to

$$\frac{\partial(uh)}{\partial t} + \frac{\partial(uuh)}{\partial x} = -\frac{h}{\rho}\frac{\partial p_{at}}{\partial x} - gh\frac{\partial\eta}{\partial x} - ruh \qquad \text{(eq. 2.2b)}$$

An additional simplification comes through the inverted-barometer approximation (Gill, 1982; Wunsch and Stammer, 1997). In the Atlantic Ocean, changes in atmospheric pressure imply vertical displacements of the free surface elevation that are accommodated through a rapid horizontal mass distribution (on the order of minutes to hours). However, if the size of the basin is comparable to the size of the atmospheric perturbation, as commonly occurs in the western Mediterranean Sea, the water mass redistribution has to take place through the constrictions between the basin and the surrounding ocean – in this case isostatic adjustment occurs over relatively long periods, on the order of days (Crepon, 1965; Garret, 1983; Garrett and Majaess, 1984; Candela et al., 1989; Le Traon and Gauzelin, 1997). Therefore, we may decompose both the sea-surface elevation and the atmospheric pressure into slowly (overbar variables) and rapidly (primed variables) changing contributions, $\eta = \overline{\eta} + \eta'$ and $p = \overline{p}_{at} + p_{at}'$, and assume that, no matter the size of the basin, the changes in atmospheric pressure will adjust isostatically only at sufficiently long time scales, $\partial\overline{p}_{at}/\partial x = -\rho g\,\partial\overline{\eta}/\partial x$.

In the case of the Strait of Gibraltar, the gradients in p_{at}' will not be directly related to the gradients in η' because at sufficiently short time scales (hours to a few days) the surface elevation in the Mediterranean side does not have enough time to respond to surface pressure. The elevation gradients may still exist, caused by other factors such as wind setup on one side of the Strait or by large-scale changes in the dynamics, but we cannot easily infer them. Hence, we assume that they are not substantial to the displacement of the interface during mixing events. Equation (2.2b) becomes

$$\frac{\partial(uh)}{\partial t} + \frac{\partial(uuh)}{\partial x} = -\frac{h}{\rho}\frac{\partial p_{at}'}{\partial x} - ruh. \qquad \text{(eq. 2.3)}$$

Let us temporarily ignore the advective terms in the above equation. Under this assumption, Equation (2.3) provides an explicit expression on the temporal evolution of the depth of the upper layer:

$$\frac{\partial h}{\partial t} = -\frac{h}{u}\left(\frac{1}{\rho}\frac{\partial p_{at}'}{\partial x} + \frac{\partial u}{\partial t}\right) - rh \qquad \text{(eq. 2.4)}$$

For the *y*-momentum component, we assume geostrophic balance, which means that the vertically integrated cross-strait velocity is zero and the effect of friction in this direction is neglected, i.e.

$$fu = -\frac{1}{\rho}\frac{\partial p}{\partial y} = -g\frac{\partial \eta}{\partial y} \qquad \text{(eq. 2.5)}$$

where the atmospheric pressure p_{at} is assumed to be independent of the cross-strait direction. Since the upper layer flows east (positive *u* values), the cross-strait geostrophic balance implies a negative cross-strait surface-elevation gradient, i.e. the surface elevation is higher along the coast of Africa.

Combining Equations (2.4) and (2.5), we get the following equation for the temporal evolution of the upper-layer interface:

$$\frac{\partial h}{\partial t} \cong \frac{f}{g}\frac{h}{\partial\eta/\partial y}\left[\frac{1}{\rho}\frac{\partial p'_{at}}{\partial x} - \frac{g}{f}\frac{\partial}{\partial t}\left(\frac{\partial \eta}{\partial y}\right)\right] - rh \qquad \text{(eq. 2.6)}$$

At this point it is convenient to briefly summarize how we have obtained such an explicit solution for the thickness of the upper layer. In a one-layer two-dimensional model, we would have three variables (*u*, *v* and *h*), its solution requiring three equations (the horizontal momentum equations and a volume conservation equation). Our assumptions (a one-dimensional flow, a 1.5 layer gravity-reduced model, and the interface stress between both layers being linearly proportional to the flow) have reduced the problem to only two active variables: *u* and *h*. Further, the assumption of cross-strait geostrophic balance allows expressing the along-strait flow of the upper layer inside the Strait of Gibraltar in terms of the change in sea-surface elevation across the Strait – a quantity that is available from tide gauge observations – so we are left with the solution for *h* in equation (2.6).

One limitation in Equation (2.6) comes from the neglect of the along-strait advective terms: for the upper layer these correspond to the surface flow continuously bringing the unaltered upstream Atlantic waters. On the contrary, Equation (2.6) assumes that all the changes in thickness of the upper mixed layer respond to processes taking place within the Strait, where instability and rapid mixing occurs; specifically, in Equation (2.6) there is no resetting mechanism to the upstream conditions, so *h* will likely drift in time towards unrealistic values. An apparent restoring mechanism is the $-rh$ term that appears to damp the thickness of the upper layer. However, from Equation (2.3) we see that this is more correctly interpreted to be a damping term on the velocity, i.e. $\partial u/\partial t = -ru$.

A true restoring mechanism for *h* would result from the eastward advection of Atlantic waters, which will take place in a characteristic time scale τ that depends on the speed U of the incoming water, i.e. $\tau = L/U = (AL)/Q$, where *Q* is the transport of Atlantic water, *A* is the cross-sectional area for the incoming flow within the Strait, and *L* is the length of the Strait. Under these assumptions, we introduce a simple modification to Equation (2.6) that leads to a restored solution h :

$$\frac{\partial(h-h_0)}{\partial t} \cong -\frac{(h-h_0)}{\tau} + F ,$$

where h_0 is the upper-layer thickness found west of the Strait of Gibraltar and *F* is the forcing term in the r-h-s of Equation (2.6). If we take h_0 as a constant reference upper-layer thickness, this equation becomes

$$\frac{\partial h}{\partial t} \cong -\frac{\left(h - h_0\right)}{\tau} + F \qquad \text{(eq. 2.7)}$$

The restoring mechanism in Equation (2.7) may be compared with the advective term neglected in Equation (2.3):

$$\frac{\partial\left(uh\right)}{\partial t} + \frac{\partial\left(u\,uh\right)}{\partial x} = u\left(\frac{\partial h}{\partial t} + \frac{\partial\left(uh\right)}{\partial x}\right) + h\left(\frac{\partial u}{\partial t} + u\frac{\partial u}{\partial x}\right) \qquad \text{(eq. 2.8)}$$

The first term in the r-h-s may be related to the volume conservation equation for the upper layer (again neglecting η as compared with *h*)

$$\frac{\partial h}{\partial t} + \frac{\partial\left(uh\right)}{\partial x} = w_e$$

where w_e is the entrainment velocity (actual lower-layer water that is incorporated into the upper layer) (Pelegrí and Richman, 1993); this term does not cancel precisely because $w_e \neq 0$. The second term in the r-h-s of Equation (2.8) is the material derivative of the along-strait velocity, du/dt. Hence, we see that one first effect of maintaining the advective term would be the turning of the temporal derivative $\partial u/\partial t$ in equation (2.4) into a material derivative.

A second effect would be the x-advection of x-momentum through the $\partial\left(uh\right)/\partial x$ term, which may be approximated in terms of the velocity and length scales of the upper layer as $\partial\left(uh\right)/\partial x \approx U\left(h - h_0\right)/L = \left(h - h_0\right)/\tau$, giving rise to the additional term introduced in Equation (2.7); in this expression τ is the characteristic time scale for the along-stream advection, $\tau \equiv L/U$. To neglect the spatial derivative of the along-strait velocity (i.e. $du/dt \cong \partial u/\partial t$) and to assume that the upper-layer thickness restores to a constant value with a time scale τ essentially presumes the incoming Atlantic water flow to remain steady.

2.5.2 TUNING PARAMETERS

Our simple model has four tuning parameters. One parameter is the interfacial friction coefficient, a widely used approximation for slab models. The other three parameters are set by the model approximations: one is related to the relevant period over which the pressure fluctuations are efficient in transmitting along-stream forces and the other two are related to the restoring effect of the far upstream unaltered conditions. Let us briefly revise what is a reasonable range of values for these parameters. A typical value for the linear interfacial friction

coefficient is r^{-1} = 4 day or, equivalently (for h = 83 m), to $r' \equiv r\,h = 2.4 \times 10^{-4}$ m s^{-1} (a value quoted by Gill, 1982). Lee et al. (2001) have shown that r' is related to the vertical eddy viscosity coefficient A_v through $r' = \left(A_v f/2\right)^{1/2}$, so that at 36ºN this would correspond to $A_v \approx$ 10^{-3} m^2 s^{-1}, a high-range reasonable value that corresponds to highly energetic conditions (Toole, 1998). For our analysis, however, it is important to realize that the main effect of interfacial friction is to transform kinetic into potential energy, through interfacial mixing and deepening of the upper layer. Only a minor fraction of interfacial friction is likely to directly dissipate along-strait momentum, uh. Hence, for our analysis we will set, as the base case $r^{-1} = 16$ day and consider two additional cases: $r^{-1} = 4$ day and $r^{-1} = 64$ day.

The second parameter is related to the time scale over which isostatic adjustment takes place. In practice, this is the time filter used to retain the fast pressure oscillations and to remove the slow ones, the latter assumed to be responsible for the isostatic changes in the free surface. As discussed before, the Atlantic is a large ocean, with horizontal extension greater than the perturbations that induce changes in the atmospheric sea pressure, so that changes in atmospheric pressure should rapidly adjust isostatically; in contrast, the Mediterranean needs sufficient time, on the order of one week, for water to exchange through the main constrictions before reaching isostatic adjustment. To explore the contribution caused by the changes in sea-level atmospheric pressure between both basins, we explore the following cases (Table 2.1): without the effect of atmospheric pressure at sea level; with daily atmospheric pressures in both basins; and with a constant sea-surface pressure in the Atlantic, equal to its annual-mean value, and the 1-10 days band-pass filtered values for the Mediterranean sea surface pressure. The sea-level atmospheric pressures at both sides of the Strait of Gibraltar are specified as discussed in Section 2.2.

The last two parameters set the advection of upstream characteristics. These are the restoring depth of the upper layer h_0 and the advection time τ. The restoring upper-layer depth is related, but not equal, to the depth of the upper layer west of the Strait of Gibraltar. As the Atlantic water enters the Strait, the dynamic regime changes and the balanced conditions may be different from the upstream conditions. Under these considerations, we have estimated h_0 from the yo-yo C stations in April and October 1997 (Fig. 2.5). García Lafuente et al. (2002a) found that, near section C, the zero-velocity contour corresponds to salinity values between 37.05 and 38.09, with a mean value of 37.74. Here we set the interface to correspond with the 37.5 isohaline (Candela et al., 1989, 1990; Bryden et al., 1994; García Lafuente et al., 2000)

and find that this corresponds to a depth of 80 ± 21 m. Hence we select as our base case h_0 =80 m but also examine the cases h_0 = 60 and 100 m.

Table 2.1. Parameters corresponding to the main numerical cases. The along-strait surface atmospheric-pressure gradient is calculated over a distance of 261 km, the advective time is τ = 2 days and, except for the non-restored cases, the upper-layer initial depth is equal to the restoring depth. The base-case conditions are indicated in bold.

Case	Interfacial friction, r^{-1} (day)	Upper layer restoring depth, h_0 (m)	Atlantic surface pressure	Mediterranean surface pressure
1	16	80	No pressure	No pressure
	16	Non-restored	No pressure	No pressure
2	16	80	No filter: daily values	No filter: daily values
	16	Non-restored	No filter: daily values	No filter: daily values
3	16	80	Constant and equal to the mean Atlantic pressure	Band-pass: 1-10 days
	16	Non-restored	Constant and equal to the mean Atlantic pressure	Band-pass: 1-10 days
	4	80	as above	as above
	64	80	as above	as above
	16	60	as above	as above
	16	100	as above	as above

The advection time $\tau = (AL)/Q$ depends on the eastward transport of Atlantic water through the Strait, and on the cross-sectional area *A* and the along-stream characteristic distance *L*. For the Atlantic water transport we choose a constant value of 1 Sv, which is not substantially different from observations (Candela, 2001; Soto-Navarro et al., 2010). The area depends on the width of the cross-section and also on the depth of the incoming water, i.e. $A = Wh$ where we set h = 80 m and select a width W = 22 km, or about the mean width of the Strait (section C is slightly narrower, about 16.5 km). The characteristic distance is selected to be large enough to extend beyond the region that undergoes rapid mixing: from the SST images we choose L = 100 km. This gives a characteristic time scale of 2 days, a value consistent with the re-stratification time observed from SST images.

Finally, the results of the model are moderately sensitive to our computation of the along-strait atmospheric pressure gradients. We have explored the solution using the surface pressure data at individual locations and over regions of different size, as explained in Section 2.2. For the numerical calculation, we show the results corresponding to the first case, with the atmospheric surface pressures in the western Alboran Sea (36ºN, 4ºW) and the Gulf of Cadiz (36ºN, 8ºW), or separated by a distance of 261 km. This is a compromise between the values being close enough to both ends of the Strait, yet being representative of regional basins.

2.6 ENERGY CONSERVATION MODEL

Equation (2.7) is a fully diagnostic expression, in the sense that the evolution of the upper-layer thickness depends on the along-strait velocities, which are inferred from the cross-strait gradients in surface elevation. This equation shows that the upper layer deepens as the cross-strait surface-elevation gradients decrease in magnitude (the gradient gets less negative and the along-strait geostrophic velocity decreases) but does not explain why it happens.

The natural explanation is that the upper layer deepening happens as a result of active mixing, with kinetic energy being transformed into potential energy. To verify this hypothesis, we propose a simple energy-conserving argument aimed at modelling those events when the thickness of the upper layer increases rapidly. The model uses an initial velocity and the temporal evolution of the upper-layer thickness to estimate the along-strait velocity at each time. This velocity may be compared with the geostrophic velocity, inferred from the cross-strait gradient in sea-surface elevation. If the patterns are analogous we may conclude that a rapid deepening of the upper layer is associated with exchanges between kinetic and potential energy as a result of mixing.

Consider the temporal evolution of the water column illustrated in Figure 2.10. We neglect dissipation and examine the time evolution of a material water column. The thickness of the upper layer is a function of time $h = h(t)$, starting from an initial condition h_i, and the lower (or deep) layer density is constant and equal to ρ_d. We consider the mechanic (potential plus kinetic) energy to remain constant in time:

$$\int_0^D \left(\rho g z + \frac{1}{2} \rho u^2 \right) dz = \text{constant} .$$

In particular, at any time during the mixing process the mechanic energy has to equal its initial value, characterized by the velocity and stratification conditions before shear-induced mixing

($Ri < Ri_c$) took place:

$$\int_0^{D-h} \rho_d g z dz + \int_{D-h}^{D} \left(\rho g z + \frac{1}{2} \rho u^2 \right) dz = \int_0^{D-h_i} \rho_d g z dz + \int_{D-h_i}^{D} \left(\rho_i g z + \frac{1}{2} \rho_i u_i^2 \right) dz \qquad \text{(eq. 2.9)}$$

In this last expression, we assume that only upward entrainment occurs, i.e. the deep layer, located between 0 and $D - h$, remains motionless and does not change its density. This is

consistent with the idea that all turbulence is restricted to the layer in motion and that mass and momentum are entrained from the non-turbulent to the turbulent domains (Turner, 1973, 1986).

Mass conservation implies

$$\rho = \frac{h_i \rho_i + (h - h_i)\rho_d}{h} \qquad \text{(eq. 2.10)}$$

so that $\rho_d - \rho = h_i \Delta / h$ and $\rho - \rho_i = (h - h_i)\Delta / h$, where $\Delta \equiv \rho_d - \rho_i$. With these expressions and defining $g' \equiv (\Delta / \rho) g$, Equation (2.9) reduces to

$$u^2 = \frac{h_i}{h}\left[g'(h_i - h) + \frac{\rho_i u_i^2}{\rho} \right] \qquad \text{(eq. 2.11)}$$

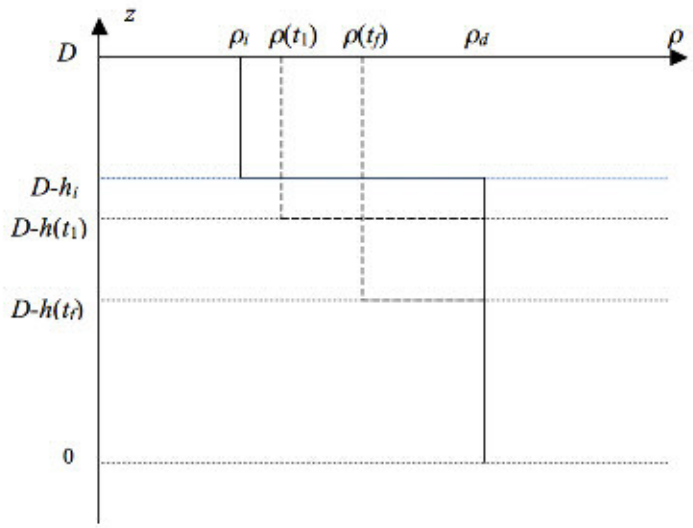

Fig. 2.10. Schematic of the upper-layer evolution during a mixing event illustrating the main elements used in the energy-conservation model.

Strictly speaking, Equations (2.10) and (2.11) are only pertinent during mixing periods. Nevertheless, both equations may also be interpreted as indicative that, after the mixing event, the density and thickness of the upper layer will return to their initial conditions – as Equation (2.7) brings h back to h_i, it happens that ρ returns to ρ_i and u gets back to u_i. Hence, Equations (2.10) and (2.11) can be used to obtain an energy solution for the entire time series, simply requiring a proper selection of the restoring density and velocity values. For the density, we choose a characteristic value of the upper Atlantic waters, ρ_i = 1026.8 kg m^{-3}, and for the velocity we select the mean geostrophic velocity (Equation 2.5) for the entire period of

measurements, u_i = 0.56 m s^{-1}; note that this velocity value is similar to the number we would obtain using realistic values of the upper-layer transport, depth and width (Q = 1 Sv, h = 80 m, W = 22 km), which justifies this approximation.

2.7 NUMERICAL CALCULATIONS

We have solved Equation (2.7) numerically, exploring many combinations of the atmospheric forcing, initial conditions and model parameters discussed in Section 2.4.2. Hereafter, we focus on the instances listed in Table 2.1, which are most representative of the full range of solutions. Those combinations labelled as Case 1 (no atmospheric pressure), Case 2 (full non-filtered atmospheric pressure) and Case 3 (mean atmospheric pressure in the Atlantic side, mean plus 1-10 day band-passed filtered pressure oscillations in the Mediterranean side) use our best estimates for friction coefficient and restoring depth. Considering our data analysis in Section 2.3, Case 3 is expected to be the optimal combination. A modification of Case 3, where the Atlantic surface pressure is chosen to be constant and equal to the mean Mediterranean value, shows only minor differences and is not shown. In all cases the along-strait surface atmospheric-pressure gradient is calculated over a distance of 261 km, and the advective time is taken to be τ = 2 days.

For the non-restored model (Equation 2.6), the depth of the upper-layer evolves towards unrealistic values for Case 1 (decaying to near-zero values in about four months) and Case 2 (giving both negative and positive values). The non-restored solution for Case 3 is not fully unrealistic, as the thickness remains always between 20 and 150 m; however, it displays about five transitions, all of them taking place after a rapid mixing event, when the oscillations revolve around a new thickness value (about 60, 80 or 100 m) – these transient mean values would represent a local anomaly, inconsistent with the arrival of Atlantic waters with a preset upper-layer thickness. Figure 11 shows these results for the model initialized with h_0 = 80 m but, after only a few days, the results are not sensitive to this initial choice.

In contrast, the restored solutions (Equation 2.7) show a suitable temporal evolution of the upper-layer thickness in all cases. The results again have little dependence on the initial depth (except for a few days at the start of the time series, not shown) but rely on the restoring depth. Therefore, and for simplicity, we select initial depths that are equal to the restoring values (Figure 2.11 corresponds to initial and restoring depths equal to 80 m). For the restored solutions, the thickness of the upper layer ranges between 40 and 120 m, with relatively small mean differences between the different cases – just a few meters deeper for Case 2 than for Cases 1 and 3.

All restored solutions exhibit intermittent oscillations in the depth of the upper layer, greater in magnitude for Case 3 than for Cases 1 and 2 (generally a difference of a few meters though in several cases it exceeds 10 m). These oscillations correspond to a deepening of the interface in 3-4 days, followed by a recovery in 2-3 days. Considering Case 3, during the 11-month period there are 25 such events where the interface deepened more than 10 m, 14 cases when this exceeded 20 m and five cases with changes greater than 40 m. Given the greater response of Case 3, and based on our earlier discussion of the potential relevance of the high-frequency pressure fluctuations in the western Mediterranean basin, we will focus on the results for Case 3 hereafter.

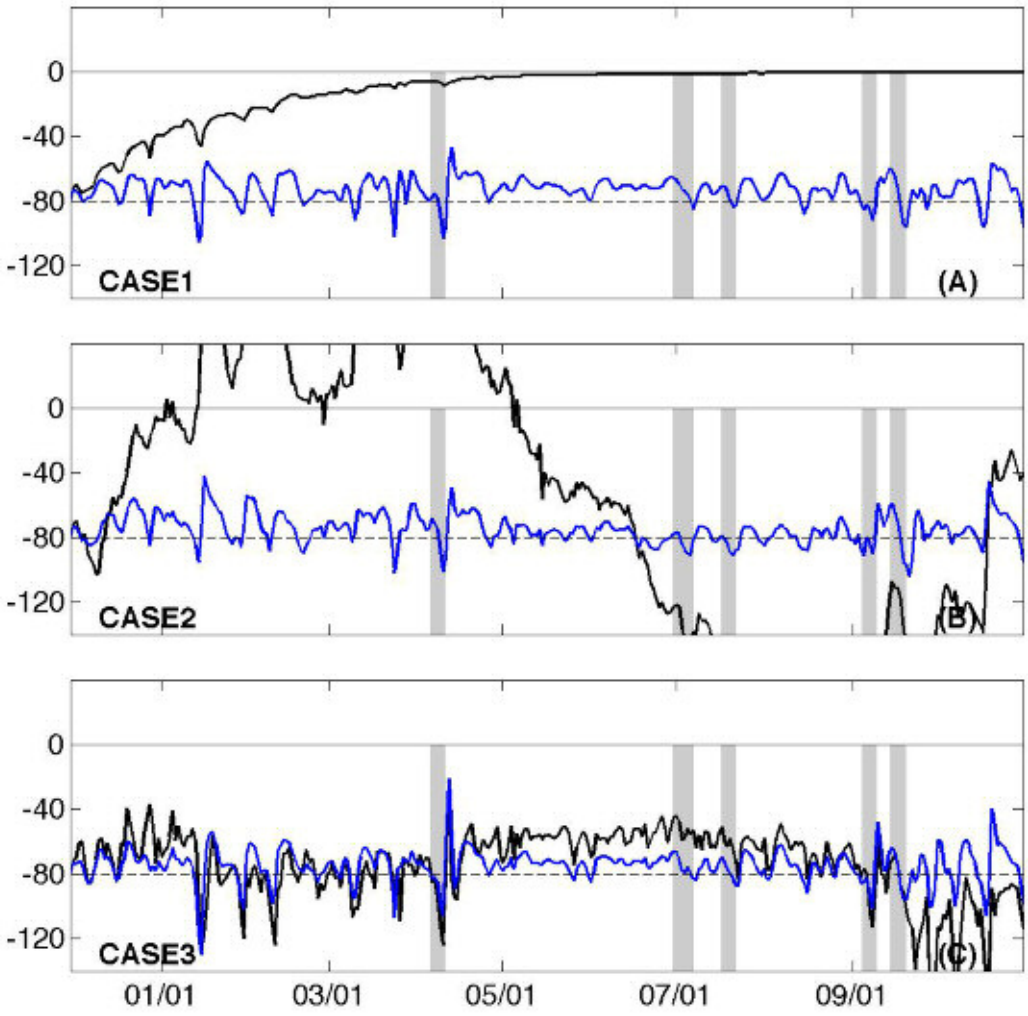

Fig. 2.11. Temporal evolution of the upper-layer thickness between 1 December 1996 and 31 October 1997 for Cases 1 (A), 2 (B), and 3 (C), with h_0 = 80 m and r^{-1} = 16 days. For each case we show the non-restored (black line, Equation 2.6) and restored (blue line, Equation 2.7) solutions.

The sensitivity of the model to the linear interfacial friction is explored by comparing the results for h_0 = 80 m and different values of the linear friction coefficient, r^{-1} = 4, 16 and 64 days (Figure 2.12a). The case with larger friction, r^{-1} = 4 days, leads to minimum upper-layer thicknesses. The other two cases, r^{-1} = 16 and 64 days, give fairly similar solutions, with the weaker friction causing slightly larger oscillations and smaller departures from the h_0 = 80 m reference level. Similarly, the response of the model to the restoring depth is examined using r^{-1} = 16 days and varying the upper-layer thickness, h_0 = 60, 80 and 100 m (Fig. 2.12b). It turns out that the shape of the solution is similar for all restoring depths though the size of the oscillations increases with restoring depth (Fig. 2.12b).

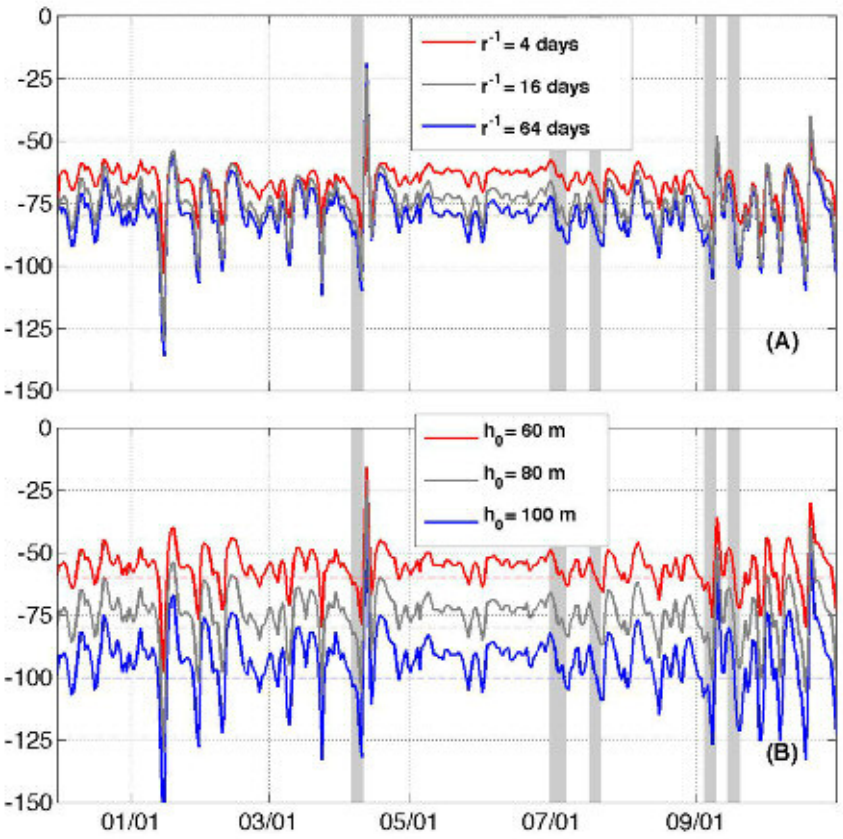

Fig. 2.12. Temporal evolution of the restored upper-layer thickness between 1 December 1996 and 31 October 1997 for Case 3. (A) Sensitivity to friction parameter, h_0 = 80 m with r^{-1} = 4, 16, and 64 days; (B) sensitivity to restoring depth, r^{-1} = 16 days with h_0 = 60, 80, and 100 m.

2.8 DISCUSSION

2.8.1 MOMENTUM BALANCE

Motivated by the results in Figures 2.11 and 2.12, let us revise the role of interfacial friction and restoring thickness on our solutions. Friction is a decaying term for the upper-layer momentum (the product of upper-layer velocity and thickness), which contributes to reducing the upper-layer thickness at a rate $\partial h/\partial t = -rh$ (Equation 2.6) – with no atmospheric pressure and no advection the solution tends to zero (Fig. 2.11a). Hence, the greater the friction (the shorter the associated time scale, r^{-1}), the faster the upper-layer thickness (as a contributor to the upper-layer momentum) will decay towards small values (Fig. 2.12a).

In contrast, setting a restoring depth not only brings the upper-layer thickness back to the target value in time scales of a few days but it is also responsible for influencing the size of the oscillations. This is a result of momentum conservation (Equation 2.3), $\partial(uh)/\partial t \cong 0$ means $\partial h/\partial t \cong -(h/u)\,\partial u/\partial t$, so that the changes in upper-layer thickness are opposite to the changes in velocity but amplified proportional to *h* itself. The restoring model is effective at returning the depth of the interface to a given depth level in times of the order of $\tau = (AL)/Q$, typically a few days (Fig. 2.12) However, the effectiveness decreases when the frictional time scale is comparable to the advective time scale (Fig. 2.12a).

We may analyse the magnitude of the different terms in the along-stream momentum balance, i.e. after combining Equations (2.6) and (2.7):

$$u\frac{\partial h}{\partial t} + h\frac{\partial u}{\partial t} + \frac{h}{\rho}\frac{\partial p'_{at}}{\partial x} + ruh + u\frac{(h-h_0)}{\tau} \cong 0\,, \qquad \text{(eq. 2.12)}$$

where the along-strait velocity is obtained using the geostrophic approximation (Equation 2.5). The analysis is done for July 1997 (Fig. 2.13), as the SST imagery suggests that at least two mixing events took place during this period (3-6 July and 18-20 July, Figure 2.3). The size of the different terms varies substantially in time, with the first and second terms in Equation (2.12) experiencing the largest oscillations and fundamentally compensating each other. The atmospheric pressure gradient term (3rd term), although smaller in magnitude than the other terms in the balance, appears to be important to the appearance of the mixing events. The thickening of the upper layer takes place after several days of reduced atmospheric pressure in the Mediterranean side (negative pressure gradients), concurrent with the acceleration of the Atlantic inflow. The frictional term (4th term) is relatively constant in time, as it is proportional to

the product of upper-layer velocity and thickness, which approximately balance each other $\partial(uh)/\partial t \cong 0$. The frictional term decreases slightly when the acceleration term is negative and increases with positive acceleration. The restoring term (5th term) is of similar magnitude to the frictional term but of opposite sign and exhibits larger fluctuations in time. The (negative) magnitude of the restoring term peaks at the early stages of the mixing events, simultaneous with the largest mismatch between the other terms, and returns to small values after the events.

In summary, before a mixing event the pressure decreases in the Mediterranean side of the Strait and the upper layer accelerates. The upper layer presumably turns subcritical and mixing ensues: the top layer thickens (1st term) and decelerates (2nd term) with nearly no temporal lag (at most one day); the mixing event ends by the time that both terms go to zero. Following the mixing event, the depth of the upper layer decreases to its restoring value (the 1st term decreases) and the velocity increases (2nd term).

2.8.2 ALONG-STRAIT VELOCITY

In the present study, we consider two independent velocity estimates. The first one is the geostrophic velocity along section C, calculated from the elevation residuals at Algeciras and Ceuta, which is available for the entire period of analysis (1 December 1996 to 31 October 1997). The second one is the ADCP measurements at station M, on Camarinal Sill, for the period between 19 January and 27 April 1997; recall these measurements are rotated to fit the axis of maximum variance (Fig. 2.4) so a mean value for the along-strait upper layer velocity is obtained from averaging all positive values.

A comparison of the two velocity estimates shows that the velocity at section C is substantially larger than at station M but the oscillations are generally well correlated, both in timing and direction (Fig. 2.14). This is an important result, as it strongly suggests that the geostrophic estimate in the eastern Strait does characterize the subinertial velocity all throughout the Strait, supporting our use of the geostrophic approximation to model the thickness of the upper layer. The difference in size between both estimates is caused by the different locations; there may be other reasons – the geostrophic velocity is a cross-strait average of the surface velocity while the ADCP estimate is a vertical average at the centre of the Strait – but these are probably less important as they tend to compensate each other.

The difference in location not only changes the amplitude of the velocity but also the depth of the upper layer. We may compare the upper-layer observations (Figs. 2.5 and 2.6) and estimates (Fig. 2.12) for the interface at section C (about 80 m) with the depth of the zero velocity contour at station M (Fig. 2.4). For the period between 19 January and 28 April 1997,

when the ADCP observations were available, the upper-layer depth was 111 ± 60 m; this value is similar, but slightly less, than reported by Candela et al. (1989) for the depth of the 37.5 isohaline interface along a section near M2 (119 to 169 m). If the dynamical regime at both locations remains unchanged then the currents between stations M and C would increase by 40-100%, which is consistent with the observations (Fig. 2.14).

We can use Equations (2.10) and (2.11), for mass and energy conservation during mixing events, to predict the evolution of the upper-layer velocity from an adequate initial condition and the upper-layer thicknesses. In Figure 2.14, we show this prediction for Case 3 during the 19 January to 28 April 1997 period, using the geostrophic velocity at section C as the initial condition. The energy-based upper-layer geostrophic velocities exhibit oscillations similar to the observations (Fig. 2.14). As discussed in Section 2.5, the energy-based velocity is strictly valid in a one-dimensional sense for relatively short time periods (less than 10 days), while the mixing event takes place. Nevertheless, the energy conservation argument restores the velocity back to its initial level (*u* speeds up) as the thickness of the upper layer decreases (*h* decreases towards h_i) (Equation 2.11). In Figure 2.14 we show two different solutions: one where Equations (2.10) and (2.11) are used throughout the entire simulation and another where the energy-based velocity is re-initialized each time we observe a substantial drop in velocity (a mixing event starts). The non-stop solution is generally larger than the geostrophic velocity except at times with a sharp drop in velocity, corresponding to potential mixing events, when the modelled velocity does a good job at simulating the geostrophic velocity. On the other hand, the re-initialized solution indeed matches the observed fluctuations most of the time and is usually capable of simulating fairly well the observations beyond the mixing event. The single exception during the modelled period corresponds to the peak velocities predicted for 11-12 April, which show limited skill. This departure occurs at the end of a mixing event, when the cross-strait gradient in the elevation residuals gets small (appearing in the denominator in the first term of Equation 2.6) and the local acceleration exceeds the along-strait atmospheric pressure gradient (the term in brackets in Equation 2.6 is negative), leading to a rapid decrease in the upper-layer thickness (Equation 2.6) and, consequently, to an increase in the energy-based velocity (Equation 2.11).

We can repeat the prediction for the 26 June to 31 July period, when two mixing events were observed through SST satellite imagery (Fig. 2.2) The modelled (Equations 2.10 and 2.11) and geostrophic (Equation 2.5) velocities decrease during both events (Fig. 2.15a): The agreement is poor during the first event, with the modelled solution decreasing much less than the geostrophic value, but it is excellent during the second mixing event. Figure 2.13 shows that the disagreement for the first event results from the large frictional and restoring terms, which

regulate the increase of *h* and, in consequence, do not allow *u* to decrease as fast as expected. During the second event these two combined terms are reduced by a factor of two, so the solution is more conservative, $\partial(uh)/\partial t \cong 0$, and the velocity decreases approximately proportional to the increase in upper-layer thickness.

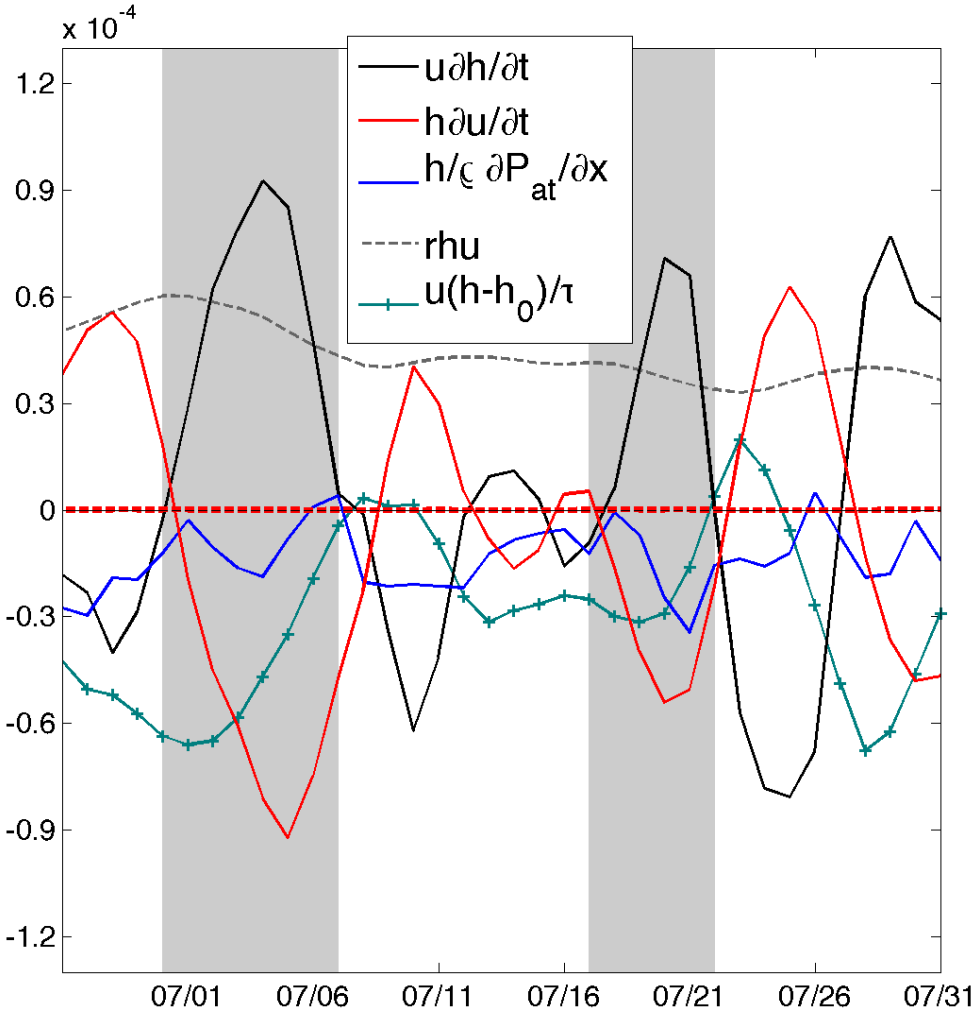

Fig. 2.13. Size of the different terms in the along-stream momentum balance (Equation 2.12) for the restored Case 3 with h_0 = 80 m and r^{-1} = 16 days, during July 1997.

2.8.3 THE GRADIENT RICHARDSON NUMBER

At any time, we may calculate the two-layer Richardson number as

$$Ri = \frac{\delta\rho}{\rho}\frac{g\,h}{u^2} \qquad \text{(eq. 2.13)}$$

where $\delta\rho \equiv \rho_d - \rho$ is the density difference between both layers. Subcritical conditions, i.e. $Ri < Ri_c \cong 1$ (Van Gastel and Pelegrí, 2004), correspond to large cross-strait slope of the free surface and/or to small thickness of the upper layer. For the calculation we take the density of the lower layer as constant and equal to the characteristic density of the outflowing Mediterranean water, $\rho_d = 1028.8$ kg m^{-3}. We use Equation (2.7) for the depth of the upper layer, while we have several options for the other upper-layer variables: for the density, we may either adopt a constant value, characteristic for the upper layer, or apply the mass conservation Equation (2.10); for the velocity, we may either use the geostrophic approximation (Equation 2.5) or the energy-based solution (Equation 2.11).

The temporal evolution of the Richardson number for the entire period of measurements is shown in Figure 2.16 for three sets of upper-layer variables: constant density and geostrophic velocity, variable density and geostrophic velocity, and variable density and energy-based velocity (one single run, with no restart). The solution for all cases exhibits large fluctuations, with a number of instances when the values approach critical conditions. Generally speaking, the oscillations appear to be robust as most of the time they have similar amplitude and appear simultaneously in all cases.

The *Ri* values obtained with the geostrophic velocity (Equation 2.5), with either constant or variable density, are fairly similar (Fig. 2.16); in particular, they display a significant reduction between May and June, with mean values between 1 and 2, corresponding to a time period of increased geostrophic velocities (not shown). The *Ri* solution arising from mass and energy conservation arguments (Equations 2.10 and 2.11) displays oscillations of relatively small amplitude and its mean value remains quite stable, close to 2 – this is because of the strongly restoring character of Equations (2.10) and (2.11). In several instances, however, the energy-based velocity results in low *Ri* values, much smaller than obtained from the geostrophic approximation: one such instance is during 11-12 April that corresponded with peak speeds (Fig. 2.14). These situations occur at times when the upper-layer thickness is predicted to be small so the energy-based velocity is enhanced (Equation 2.11); during these instances, the geostrophic-based *Ri*

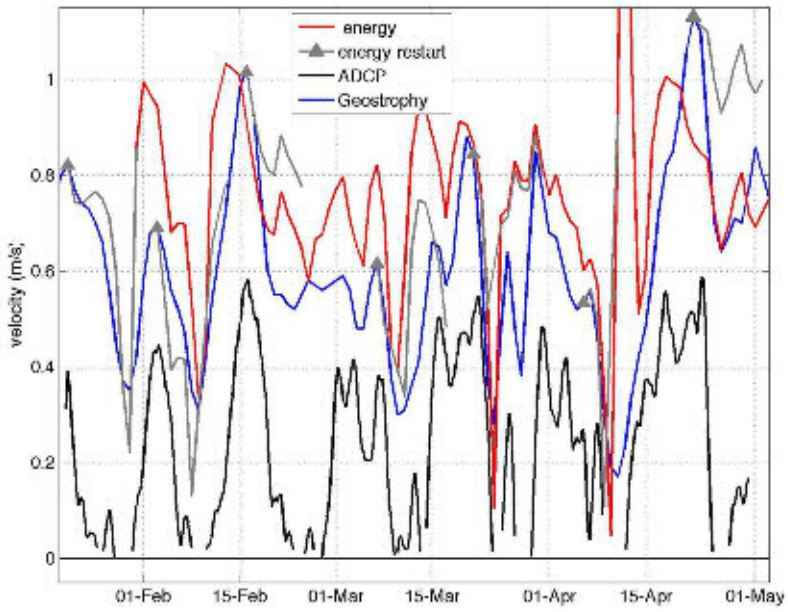

Fig. 2.14. Temporal evolution of the upper-layer velocity between 20 January and 27 April 1997 for Case 3 with h_0 = 80 m and r^{-1} = 16 days. We show the upper-layer mean ADCP velocity at station M (black line), the geostrophic velocity (blue line), and the energy conservation velocity (Equation 2.12) for the restored depth solution initialized at the beginning of the record (gray line) and restarted at times (red triangles) when a drop in velocity was observed (red line). The energy-based velocity might be more valid for relatively short time periods, so the restarted series shown extends 10 days at most.

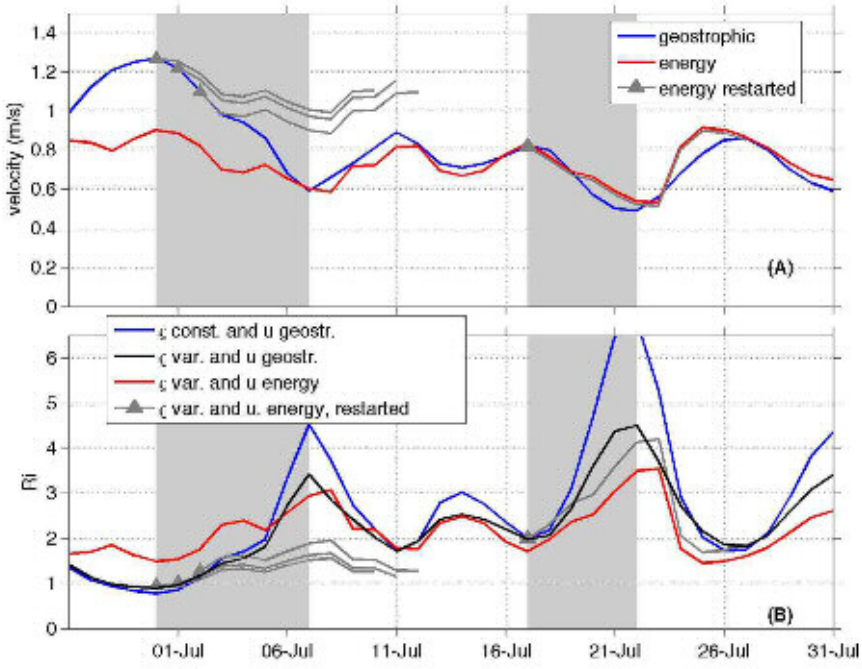

Fig. 2.15. (A) Temporal evolution of the upper-layer geostrophic (red) and energy conservation velocities initialized from the beginning of the record (blue) and restarted at times when a decrease of velocity was observed (black) between 26 June and 31 July 1997 for Case 3, with h_0 = 80 m and r^{-1} = 16 days. (B) Temporal evolution of the Richardson number (using the restored upper-layer thickness) for the same case and period. The difference in Richardson number using constant density (Equation 9, blue) and non-constant density difference $\delta\rho$ (Equation 2.11, red) is illustrated. Estimates of the Richardson number using the velocity from Equation 2.12 (black) are also provided. The shaded bands illustrate time intervals when the sea surface temperature in the Strait of Gibraltar is observed to decrease significantly, as illustrated in Fig.s 2.2 and 2.3.

solution differs because the decrease in thickness is accompanied by a decline in the velocity (through $\partial\eta/\partial y$).

A comparison of the *Ri* time series (Fig. 2.16) with the Case 3 solution for the upper-layer thickness (Fig. 2.12) shows good agreement in the timing of low *Ri* values immediately before the mixing events. This is better appreciated when focusing on the 26 June - 31 July period (Fig. 2.15b; recall that the low velocities correspond to large thickness, developing towards the end of the mixing event). When adopting the geostrophic approximation (Equation 2.5), the *Ri* estimates using a constant density match those for non-constant density (Equation 2.10), except towards the end of the mixing event as the non-constant density estimate gets smaller (and likely more realistic). On the other hand, the *Ri* estimates obtained following the mass and energy conservation approximations (Equations 2.10 and 2.11) do well for the second event but are not equally sensitive during the first event, because they do not capture well the decrease in upper-layer velocity (Fig. 2.15a).

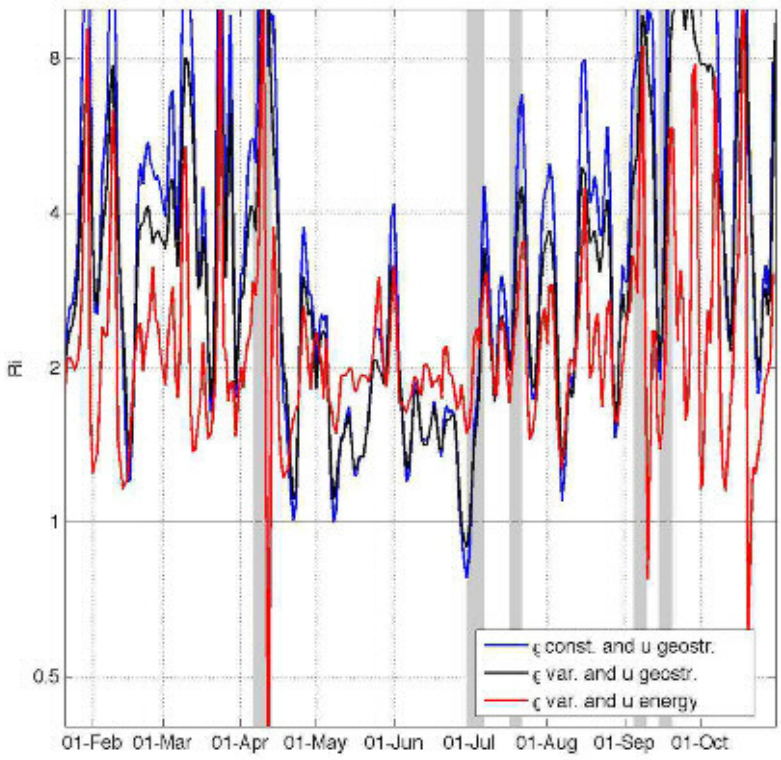

Fig. 2.16. Temporal evolution of the Richardson number (using the restored upper-layer thickness) between 1 December 1996 and 31 October 1997 for Case 3 with h_0 = 80 m and r^{-1} = 16 days. The Richardson number (blue) is calculated with a constant density (Equation 2.8) difference $\delta\rho$ = 2 kg m^{-3}. The Richardson numbers using evolving upper-layer density (Equation 2.11) for the geostrophic (black) and energy-derived velocities (red) are also included. The shaded bands illustrate time intervals when the sea surface temperature in the Strait of Gibraltar is observed to decrease significantly, as illustrated in Fig.s 2.2 and 2.3.

2.9 CONCLUDING REMARKS

Many works have reported the occurrence of localized mixing inside the Strait of Gibraltar, typically attributed to tidal mixing and wind-induced upwelling; in particular, tidal induced mixing appears to be a frequent phenomenon over sills and associated with eastward-propagating hydraulic jumps. In this work, however, we have focused on a much less studied phenomenon: strait-wide mixing events that are observable in SST imagery. Based on the analysis of SST and velocity data we estimate that these events occur about 10-15 times per year. The analysis of elevation data on both sides of the strait, together with the output from simple models, suggests that the mixing episodes are characterized by a deepening of the upper layer (the Atlantic inflow water), typically 20 to 30 m though it may be substantially larger, accompanied by a proportional decrease in the velocity. The time scale for such mixing is 5-10 days, followed by relatively fast surface capping (2-3 days), though the recovery of the initial conditions may take another 5-10 days.

The occurrence of strait-wide mixing is likely favoured by spring tides, yet our analysis and model results support the idea that its onset is the result of high-frequency (1-10 days) variability of the sea-surface atmospheric pressure in the Mediterranean side of the Strait. Before the mixing episode, atmospheric pressure decreases in the western Alboran Sea and the Atlantic flow speeds up. If the low pressure is intense enough, the flow becomes subcritical and mixing develops: as a result of the transformation of kinetic into potential energy, the top layer entrains lower layer water and decelerates. Following the mixing event, the Atlantic water is advected back into the Strait, the upper layer thins towards a characteristic value and the velocity increases.

The existence of strait-wide mixing does not alter the net exchange of water mass between the Atlantic and Mediterranean basins but affects the transport of each layer, with potential important consequences in the net salt and heat exchange through the Strait of Gibraltar. During the mixing episodes, relatively salty and cold Mediterranean waters are entrained into the Atlantic layer potentially leading to the salinization and cooling of the Mediterranean Sea. This also opens the question on how such changes may influence the development of the original agent responsible for the mixing events, i.e. the sea-surface atmospheric pressure patterns, and what might be the long-term impact of these processes on the state of the Mediterranean.

ACKNOWLEDGEMENTS

Hydrographic and velocity data used in this research was gathered in the frame of the CANIGO project (MAS-CT96-0060), funded by the European Union; tidal data in the Strait of Gibraltar comes from the tidal gauges maintained by the Spanish Institute of Oceanography, kindly provided by María Jesus García. We are also grateful to Jesús Cisneros for useful discussions during the early stages of this research. This research has been possible thanks to the support of the Spanish government through projects TIC-MOC (CTM2011–28867) and VA-DE-RETRO (CTM2014-56987-P). A. L. Aretxabaleta was supported by a Juan de la Cierva grant from the Spanish Government during the early stages of the study.

CHAPTER 3: TOPOGRAPHIC CONTROL ON THE NASCENT MEDITERRANEAN OUTFLOW

M. Gasser, J. L. Pelegrí , J. D. Nash, H. Peters, J. García-Lafuente
Published in Geo-Marine Letters, 2011, Vol 31, 301–314

Abstract

Data collected during a 12-day cruise in July 2009 served to examine the structure of the nascent Mediterranean Outflow Water (MOW) immediately west of the Espartel Sill, the westernmost sill in the Strait of Gibraltar. The MOW is characterized by high salinities (>37.0 and reaching 38.3) and high velocities (exceeding 1 m s−1 at 100 m above the seafloor), and follows a submerged valley along a 30 km stretch, the natural western extension of the strait. It is approx. 150 m thick and 10 km wide, and experiences a substantial drop from 420 to 530 m over a distance of some 3 km between two relatively flat regions. Measurements indicate that the nascent MOW behaves as a gravity current with nearly maximal traveling speed; if this condition is maintained, then the maximum MOW velocity would decrease slowly with distance from the Espartel Sill, remaining significantly high until the gravity current excess density is only a small fraction of its original value. The Sharp pycnocline between the Mediterranean and the overlying North Atlantic Central waters is dynamically unstable, particularly where the flow interacts with the 100 m decrease in bottom depth. Here, subcritical gradient Richardson numbers coincide with the development of large interfacial undulations and billows. The very energetic downslope flow is likely responsible for the development of a narrowV-shaped channel downstreamof the seafloor drop along the axis of the submerged valley, this probably being the very first erosional scour produced by the nascent MOW. The coincidence of subcritical gradient Richardson numbers with relatively high turbidity values above the cannel flanks suggests it may be undergoing upstream erosion.

3.1 INTRODUCTION

The Mediterranean Outflow Water (MOW) is born after the Mediterranean Water (MW) passes the Espartel Sill (360 m depth), the westernmost sill in the Strait of Gibraltar (e.g., Madelain 1970; Zenk 1975; Ambar and Howe 1979; Baringer and Price 1999; Habgood et al. 2003; Hernández-Molina et al. 2006; Zitellini et al. 2009; León et al. 2010). The MOW penetrates subsurface layers of the Gulf of Cadiz, driven by pressure gradients caused by the density excess of the intruding MW relative to the ambient North Atlantic Central Water (NACW). This nascent MOW is zonally channeled along the middle slope by the bottom bathymetry, in what constitutes the natural extension of the Strait of Gibraltar, until the channel opens widely into the Gulf of Cadiz. The plunging MOW is an excellent example of a two-way flow–bottom interaction process. The MOW is strongly influenced by the bottom topography, but it is also the principal actor in the development and maintenance of the complex contourite depositional system characterizing the continental slope in the northern gulf sector (e.g., Baraza et al. 1999; Nelson et al. 1999; Habgood et al. 2003; Hernández-Molina et al. 2006; García et al. 2009).

The flow is most intense shortly after exiting the Strait of Gibraltar, as the MW–NACW density difference is maximal here (Baringer and Price 1997a). It is in this energetic, and relatively small, region west of the Espartel Sill that the nascent outflow undergoes its most significant and fastest transformation (Baringer and Price 1997a). The large density-induced MW–NACW velocity difference is responsible for the entrainment of NACW into the MOW, leading to a substantial decrease in salinity and an increase in outflow transport. The mean MOW speed, however, is maintained quite far from this source region (Habgood et al. 2003; Hernández-Molina et al. 2006) because of the transformation of potential into kinetic energy. Therefore, the rate of density transformation of this nascent MOW determines where the current veers northward along the Iberian continental slope, and also its final equilibrium depth.

Paleo-changes in MW density and the depth of the Espartel Sill (relative to sea level) have likely resulted in different MOW paths into the North Atlantic Ocean (Bryden and Stommel 1984), as reflected by the presence of numerous erosional and depositional features of varied ages (Habgood et al. 2003; Hernández-Molina et al. 2006). The MOW erosive activity creates V-shaped downslope scours (Habgood et al. 2003), while the channeling effect helps maintaining high velocities. Increased erosion may locally modify the bottom slope, while accelerating the flow and increasing turbulence, which may lead to an unstable bottom equilibrium slope with an upslope retrogradation of the bottom profile.

Previous oceanographic studies in the region west of the Espartel Sill have paid little attention to the evolution of the MOW in its formation region. An exception is the work of Baringer and Price (1999), who examined the nascent MOWand its relation with depositional bed forms, although at poor spatial resolution (typically about 10 km). In fact, no high-resolution bottom data are available immediately west of the Espartel Sill, precisely where the MOW begins its downwelling path. Only Kenyon and Belderson (1973) characterized the erosional and depositional bed forms at this site, inferred from half a dozen side-scan sonar surveys.

The aim of the present study is to improve our knowledge of flow–bottom interaction along the main outflow channel of the nascent downsloping MOW, based on a novel set of combined oceanographic (CTD and velocity measurements) and bottom topography highresolution measurements west of the Espartel Sill.

3.2 PHYSICAL SETTING

3.2.1 OCEANOGRAPHIC SETTING

When the MOW passes the western Strait of Gibraltar through the Espartel Sill (360 m deep), it initially flows W-SW along the axis of the main channel toward the African continent, with a salinity of 38.3 and temperature of 13.3°C under NACW of salinity 36.3 and temperature 15.1°C. The 10-km-wide and 150-m-thick salinity wedge reaches a maximum speed of 1.5 ms^{-1}, associated with an excess density of $\Delta\rho$=1.9 kg m^{-3} (Ambar and Howe 1979; Mulder et al. 2003). The nascent MOW is driven by the downstream pressure gradient generated by this excess density relative to the surrounding fluid (Madelain 1970; Borenäs et al. 2002). Immediately west of the Espartel Sill the flow follows the main channel, but then splits rapidly into different branches (Baringer and Price 1997a), due either to the presence of seamounts or to mixing between MW and NACW. The initial mixing of the MOW is driven largely by local bathymetry-induced acceleration. The flow velocity rises as the bottom slope increases, enhancing vertical shear and favoring subcritical conditions. Shear mixing can result in the rapid formation of two or more layers of different densities (Pelegrí and Sangrà 1998), and these could propagate into the Gulf of Cadiz as distinct cores (Ambar and Howe 1979). Due to such mixing processes, the excess density has decreased enough beyond the 550 m isobath for the Coriolis force to become comparable to the inertial terms, and thus the MOW turns northwest onto the Iberian continental slope (Baringer and Price 1997b).

The distinct MOW cores eventually find their density levels in the northern Gulf of Cadiz (Madelain 1970; Zenk 1975; Ambar and Howe 1979; Ochoa and Bray 1991; Baringer and Price 1999; Borenäs et al. 2002; Serra et al. 2005). Two main cores have been reported. The upper core reaches Cape San Vicente at depths of 500–800 m, with an average speed of about 0.5 ms^{-1}, temperature of 13°C, and salinity of 36.2–36.5 (Ambar and Howe 1979; Ambar et al. 1999). The lower core constitutes the main path for MW transport, located at 800–1,200 m and with an average speed of about 0.25 ms^{-1}, temperature of 12°C, and salinity of 36.5 (Zenk and Armi 1990; Bower et al. 2002). At this late stage the MOW has lost its gravity current character, and has reached near-geostrophic equilibrium. The exact path along the Iberian slope, however, depends largely on those processes that have modified the outflow density.

3.2.2 MORPHOLOGIC SETTING

MOW impact on sedimentary structures in the northern Gulf of Cadiz has been the subject of many past studies (for review, see Hernández-Molina et al. 2006). The northeastern sector, located between Cádiz and the Strait of Gibraltar, is a high-velocity zone where multiple scours and sand ribbons have been reported (Baraza et al. 1999; Nelson et al. 1999; Habgood et al. 2003; Hernández-Molina et al. 2006; García et al. 2009), but the region west of the Espartel Sill remains poorly characterized. Here, the MOW flows west, confined by east–west channels (Baringer and Price 1999) and responsible for numerous incisions in the upper sector (400–600 m) of the middle slope (Habgood et al. 2003). In most of the Gulf of Cadiz, the contouritic systems have the erosional–depositional character of contour flows, or along-slope currents in oceanographic terminology (Baraza et al. 1999; Nelson et al. 1999; García et al. 2009). However, immediately west of the Espartel Sill the nascent MOW has a downslope direction within an east–west submerged valley, hereafter referred to as the Gibraltar Valley. The seafloor is characterized by several ridges acting as barriers and constraining the flow's path, thereby increasing its velocity and erosive potential (Kenyon and Belderson 1973). Habgood et al. (2003) proposed that this nascent downslope MOW is highly erosive, being responsible for the presence of downslope scour alignments, i.e., deep V-shaped channels, along the Gibraltar Valley.

3.3 MATERIALS AND METHODS

Data were collected during a 12-day cruise from 12 to 21 July 2009 on board the R/V García del Cid, in a study area centered at 35º85'N, 6º4'W immediately west of the Espartel Sill (Fig. 3.1). The cruise started 3 days after the 9 July neap tide and ended 2 days before the 23 July spring tide (Bonanza-Seville tide-recording station, Puertos del Estado, http://www.puertos.es). The study area spans 27 x 22 km, examined at 4.5 km resolution; a central area of 5 x 5 km was surveyed with an increased resolution of 1 km.

3.3.1 BATHYMETRY

The study area is only marginally covered by the high resolution (250 m) maps available in the compilation by Zitellini et al. (2009). Therefore, additional echo-sounder data were acquired at 1 s intervals with vessel speeds that ranged between 1.5 and 10 knots, and subsequently averaged over 1 min intervals. A gross estimation of the echo-sounder resolution, obtained by using an average ship speed of 6 knots and 1 min-averaged bottom depth data, gives a value of 185 m (square root of study area, 594 km2, divided by the duration of the cruise, 12 days).

The final dataset includes the Zitellini et al. (2009) data, the new echo-sounder data, and the 0.5° resolution General Bathymetric Chart of the Oceans (GEBCO). This set was post-processed and combined using Generic Mapping Tools software to obtain the bathymetry on a 0.1 min grid as shown in Fig. 3.1. Data density is highest near transects AS and CS (cf. below), and in a 7-km-wide band immediately north of these transects corresponding to the Zitellini et al. (2009) study area.

3.3.2 IN SITU MEASUREMENTS

A preliminary survey involving expendable bathythermographs served to determine the approximate path of the MOW. Salinity, temperature, and turbidity data were subsequently acquired at 1 m vertical resolution by means of a Seabird 911Plus CTD at 27 hydrographic stations spaced about 4.5 km apart (Fig. 3.1, Table 3.1). Higher resolution data were acquired in a smaller area in the central channel, and include five continuous fixed-position yo-yo profiles, as well as several short synoptic tow-yo alongstream (AS) and cross-stream (CS) transects repeated over a full tidal cycle and characterizing the phases before and after ebb tide, and before and after flood tide (Fig. 3.1, Table 3.1). In the present study, four along-stream and four cross-stream short transects are reported. Tow-yo surveys were carried out at very low ship speeds (1.5 knots) with a vertical cycle wavelength close to 1 km; the total length was 4 km for

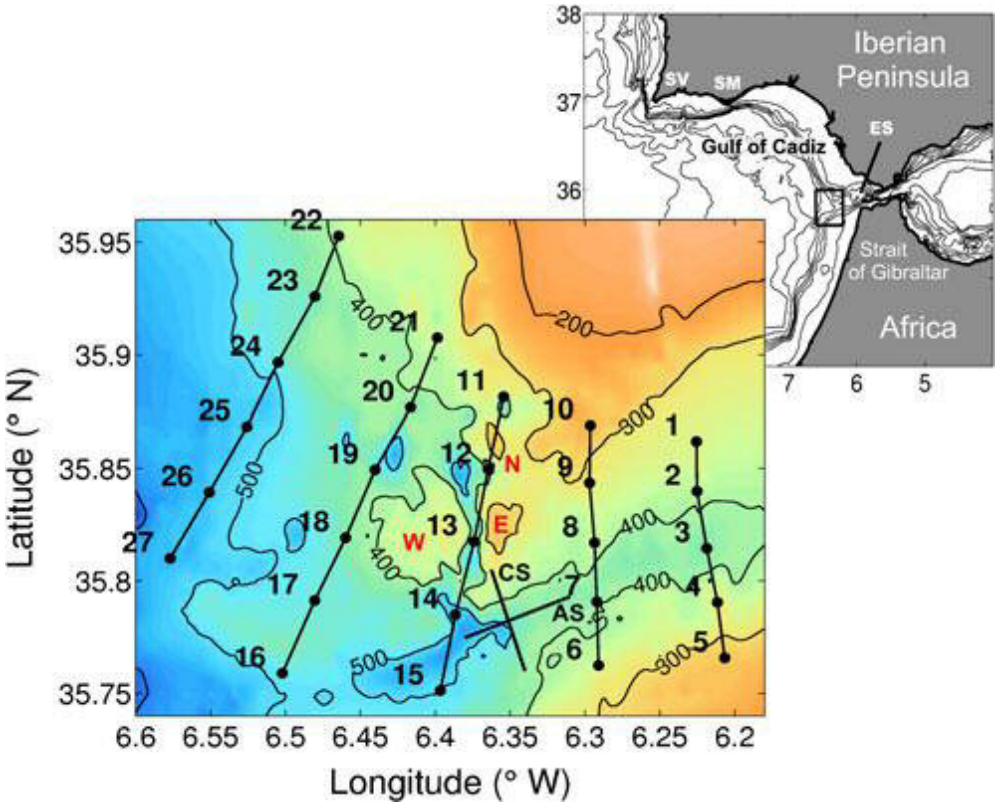

Fig. 3.1 Bathymetry based on combined data from the present study, GEBCO and Zitellini et al. (2009), with the locations of the 27 CTD stations and the short along-stream (AS) and cross-stream (CS) transects: W western morphological high, E eastern morphological high, N northern morphological high. The inset shows a map of the Gulf of Cadiz with bathymetric contours on a 1-min grid from the ETOPO1 database: SV Cape San Vicente, SM Cape Santa María, ES Espartel Sill, square study area

Table 3.1 Sampling times and locations for along- and across-stream tow-yo and CTD profiles. Dates correspond to July 2009

	Initial time (day, hour)	Final time	Initial position	Final position
CTD profiles 1–27	08, 17:22	09, 21:17	35°51.71′N, 6°13.53′W	35°48.60′N, 6°34.61′W
Along-stream tow-yo L1	09, 23:34	10, 00:27	35°47.09′N, 6°19.38′W	35°46.44′N, 6°20.88′W
Along-stream tow-yo L2	10, 01:50	10, 04:01	35°47.17′N, 6°18.48′W	35°45.91′N, 6°22.43′W
Along-stream tow-yo L3	10, 05:12	10, 07:32	35°47.41′N, 6°18.49′W	35°46.30′N, 6°22.11′W
Along-stream tow-yo L4	10, 08:40	10, 10:57	35°47.19′N, 6°18.37′W	35°46.22′N, 6°22.16′W
Across-stream tow-yo C1	12, 23:41	13, 01:34	35°45.07′N, 6°20.35′W	35°47.71′N, 6°21.49′W
Across-stream tow-yo C2	13, 02:57	13, 04:45	35°45.14′N, 6°20.42′W	35°47.92′N, 6°21.60′W
Across-stream tow-yo C3	13, 06:01	13, 07:43	35°45.21′N, 6°20.32′W	35°48.15′N, 6°21.68′W
Across-stream tow-yo C4	13, 08:43	13, 10:14	35°45.22′N, 6°20.33′W	35°48.09′N, 6°21.63′W

the cross-stream and 6 km for the alongstream transects, each being completed in less than 2h.

Continuous current velocities were simultaneously acquired during all surveys, using an RDI Ocean Surveyor 75 kHz acoustic doppler current profiler (ADCP) in Janus configuration with a theoretical maximum depth range of 750 m. In practice, reliable data reached depths of only about 350– 400 m, as near-bottom values were contaminated by sidelobe reflections. Tidal information for the central sector of the study area (near transects AS and CS in Fig. 3.1) was computed from the ADCP data obtained during the continuous yo-yo surveys covering full tidal cycles, using T-Tide MATLAB routines (Candela et al. 1990; Pawlovicz et al. 2002).

3.4 FLOW DYNAMICS

During its initial sinking the MOW is driven by the excess density of MW relative to the surrounding NACW, and so behaves as a gravity current. Under these conditions the MW layer is assumed to flow at the propagation speed of the gravity current head. In the absence of friction, and assuming a negligible slope, this velocity is (Benjamin 1968):

$$v_{gc} = C(g'd)^{1/2} \qquad \text{(eq. 3.1)}$$

where $g' = g\ \Delta\rho/\rho$ i.e. the reduced gravity acceleration, and

$$C = [(1-\delta)(2-\delta)\delta/(1+\delta)]^{1/2}$$

in which δ = h/d, i.e., the ratio between the wedge thickness h and the total water depth d. The maximum possible speed of this gravity current is $v_m = 0.53\ (g'd)^{1/2}$ for δ_m =0.35 (Benjamin 1968; Pelegrí 1988).

The gradient Richardson number (Ri) can be used to assess the dynamic stability of the MOW:

$$Ri = -\frac{g}{\rho}\frac{\frac{\partial\rho}{\partial z}}{\frac{\partial v^2}{\partial z}}\frac{N^2}{S^2} \qquad \text{(eq. 3.2)}$$

where ρ is the density, v the along-stream velocity, z the vertical coordinate, and g the gravity acceleration. The buoyancy frequency for an incompressible fluid is defined as

$$N = \left[-(g/\rho)\frac{\delta\rho}{\delta z}\right]^2 \qquad \text{(eq. 3.3)}$$

and the along-stream vertical shear as

$$S = \frac{\partial v}{\partial z} \qquad \text{(eq. 3.4)}$$

For Ri values below some critical value the interfacial waves may become unstable or, equivalently, the flow has enough kinetic energy to provide the required potential energy increase. Some studies argue that this critical value is 0.25, although more recent studies suggest it should be 1 (see Van Gastel and Pelegrí 2004 for a historical perspective).

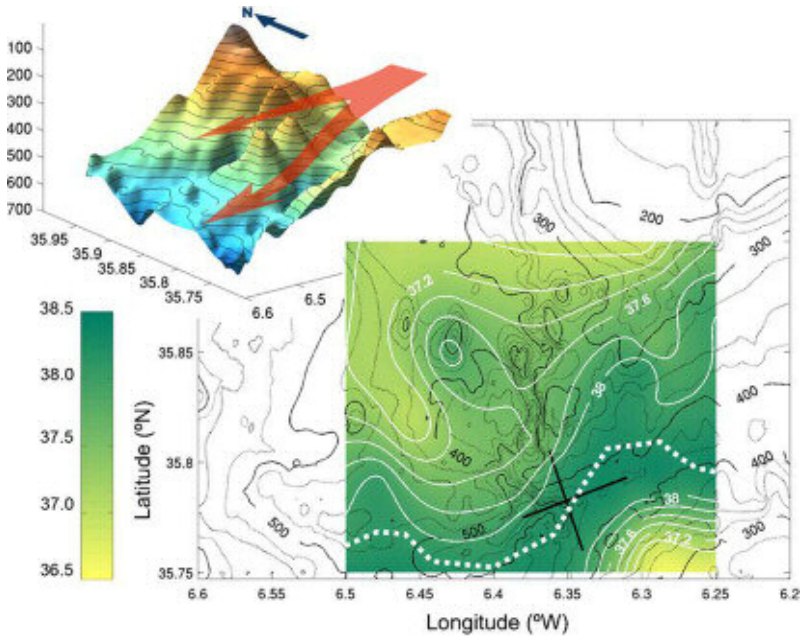

Fig. 3.2 Bathymetry (solid black contours, in meters) and salinity (solid white contours and green shading): dotted white line maximum salinity values, a proxy for the MOW core path; straight black lines locations of the tow-yo cross- and along-stream sections. The inset shows a three-dimensional view of the bottom topography, looking from the southwest: red arrows approx. MOW trajectory.

Fig. 3.3 Maximum values of salinity (dashed line) and bottom depth along the MOW core path (cf. dotted white line in Fig. 3.2)

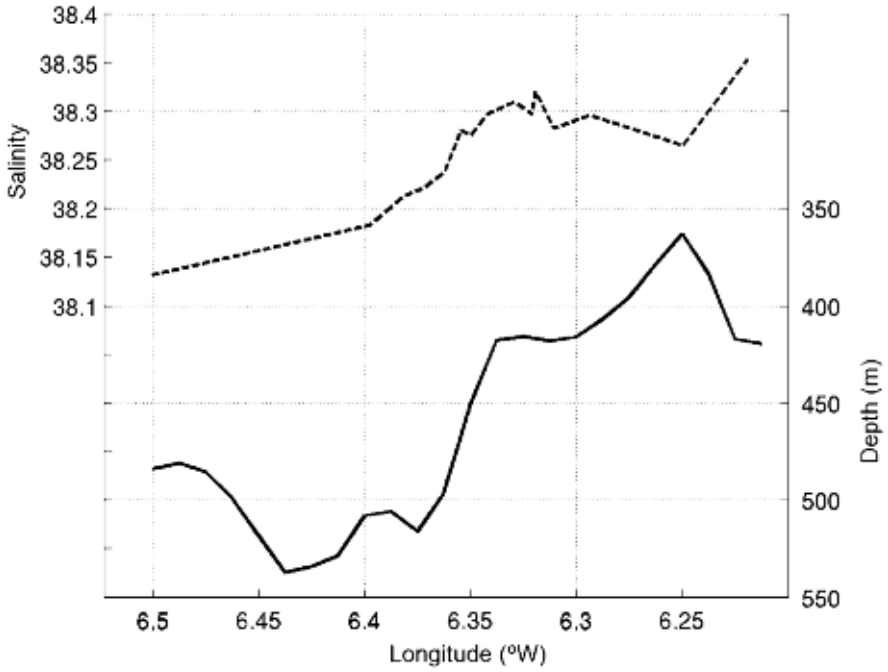

As mixing takes place, the MOW excess density decreases, so that the speed of the associated gravity current also decreases, and its width increases. The non-dimensional Rossby (Ro) number compares the acceler-ation and Coriolis force terms, and may be used to evaluate for how long the MOW behaves as a gravity current. Ro_y and Ro_x assess the cross-stream (y) and along-stream (x) force balances, respectively; values much less than 1 indicate that the flow is controlled by the Coriolis force:

$$Ro_x = \frac{U^2/L_x}{fV} = \frac{U}{fL_y} \qquad \text{(eq. 3.5)}$$

and

$$Ro_y = \frac{V^2/L_y}{fU} = \frac{U}{fL_y}\delta^2 \qquad \text{(eq. 3.6)}$$

where (L_x, L_y) and (U, V) are the characteristic length and velocity scales in the (x, y) directions; $\delta = L_y/L_x$, i.e., the width–length aspect ratio, and the Coriolis parameter is defined as $f=2\Omega\sin\theta$, where Ω is the angular velocity of the Earth and θ the latitude. The scale relation $U/L_x = V/L_y$ arises from a simple requirement of flow conservation in the horizontal plane.

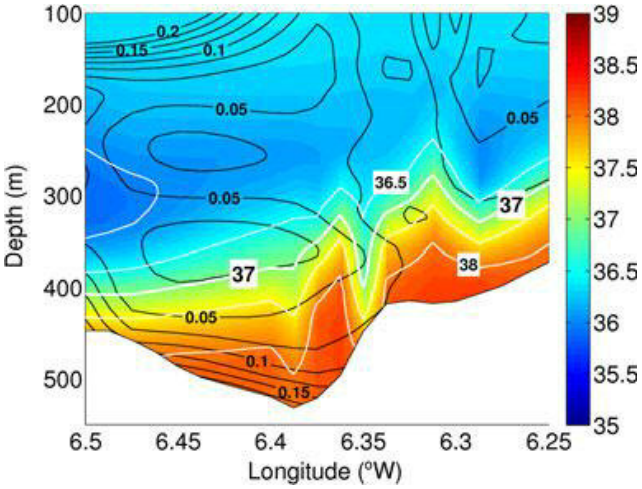

Fig. 3.4 Salinity (white contours and color) and turbidity (black contours, FTU units) distributions along the MOW core path (cf. dotted white line in Fig. 3.2)

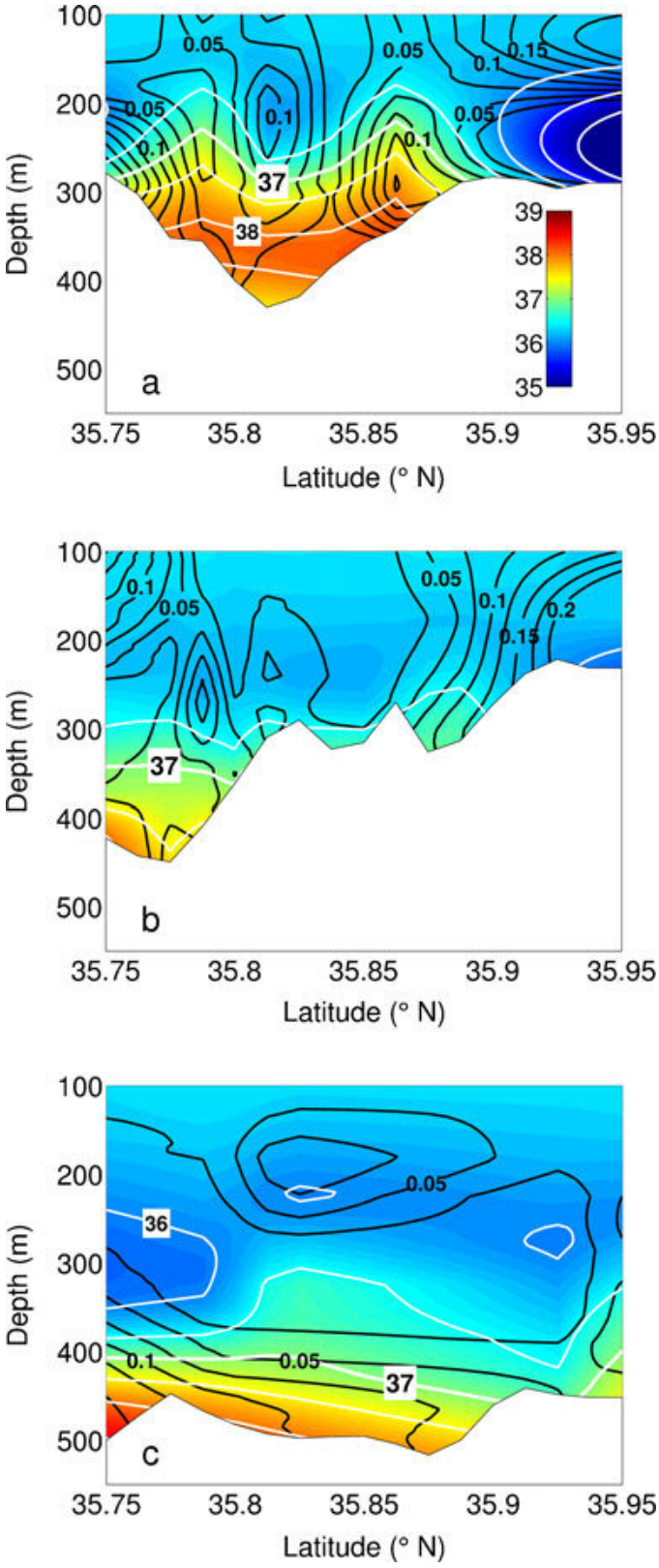

Fig. 3.5 Salinity (white contours and color) and turbidity (blackcontours, FTU units) distributions along the eastern, central, andwestern meridional large-scale transects at longitudes a 6.25°W, b6.35°W, and c 6.5°W

5 RESULTS

5.1 MORPHOLOGY

Depths in the study area are everywhere over 100 m (Fig. 3.1), even in the northern sector where nautical charts drawn in the 1970s by the Instituto Hidrográfico de la Marina indicated much shallower values. In the northeastern sector (at about 35.83°N, and 6º32'–6º44'W) there is a southward extension of the continental slope with depths of about 300 m, possibly diverting the flow toward the southern part of the study area. South of the continental slope there are three morphological highs with depths of 340 m (southwestern high), 375 m (southeastern high), and 370 m (northeastern high), respectively denoted W, E, and N in Fig. 3.1.

On the upper continental slope of the western Gulf of Cadiz, the Gibraltar Valley (10 km wide and 150 m deep) stretches approx. zonally from the Strait of Gibraltar until it branches into two main channels (Fig. 3.1). The northern channel reaches maximum depths of 600 m, with an entrance sill at 325 m. The southern channel increases in depth from 400 to 550 m toward the west, its steepest slopes being in the central sector; in the western part of the AS transect (Fig. 3.1), the bottom slope increases to 0.1 (seafloor gradient of 5°). The axis of the southern channel between 6º35' and 6º45'W displays a remarkably steep V shape; here, the channel is about 50 m deep and no more than 500 m wide.

3.5.2 HYDROGRAPHY

The temperature–salinity diagrams for all CTD records combined (not shown) reveal two well-differentiated water masses: the MW (temperature 13.5°C, salinity 38, potential density 1,030.0 kg m^{-3}), and the NACW (temperature 12.5–15°C, salinity 35.75–36.25, potential density 1,028.25 kg m^{-3}); the excess density between the MW and the NACW is then 1.75 kg m^{-3}. The horizontal distribution of maximum (near-bottom) salinity recorded during the large-scale CTD survey shows the main WSW path of the high-salinity MOW, as well as a flow diversion north of the morphologic low located at 35.8°N, 6.4°W (Fig. 3.2). The bottom depth increases westward along the MOW core path (cf. dashed white line in Fig. 3.2), with an abrupt change at about 6º35'W (Fig. 3.3). The maximum salinities display a general decrease with longitude, the largest change occurring simultaneously with the maximum increase in bottom depth (Fig. 3.3).

Contrasting with the large-scale difference in vertical salinity patterns between the MW and NACW, changes in turbidity are much more subdued (Figs. 3.4 and 3.5). The along-stream cross-section illustrates the existence of near-bottom high-salinity values in excess of 37.5

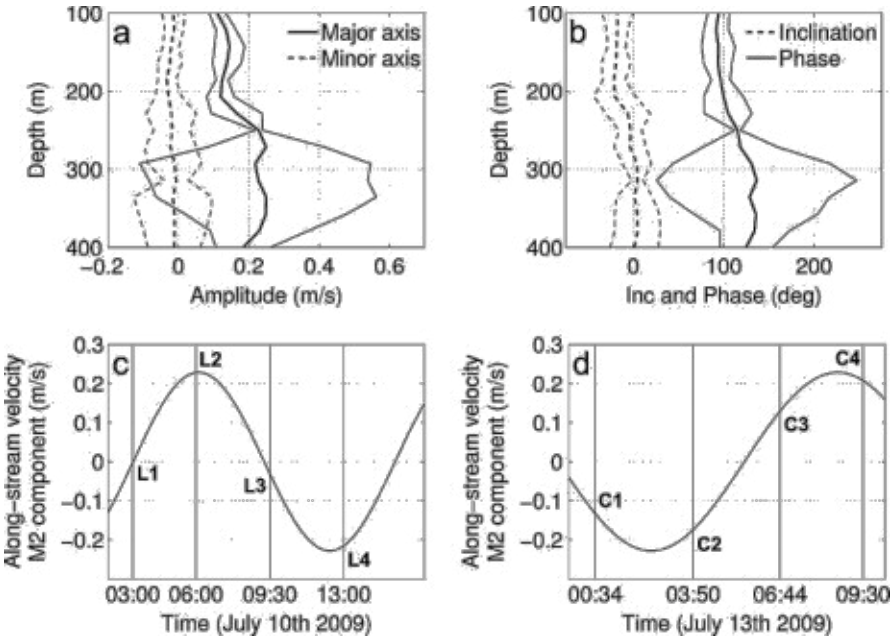

Fig. 3.6 M2 velocity tidal component. a) Depth profiles of along-stream (thick continuous line) and cross-stream (thick dashed line) velocity tidal components (thinner lines 95% confidence intervals). b) Greenwich phase (thick continuous line) and inclination (dotted line) of M2 tidal velocity ellipse. c) Vertically averaged M2 along-stream velocity component between 250–350 m during along-stream two-yos; L1–L4 middle time for each transect. d) Vertically averaged M2 along-stream velocity component from 250–350 m during cross-stream two-yos; C1–C4 middle time for each transect. Positive velocity values show flow toward the strait

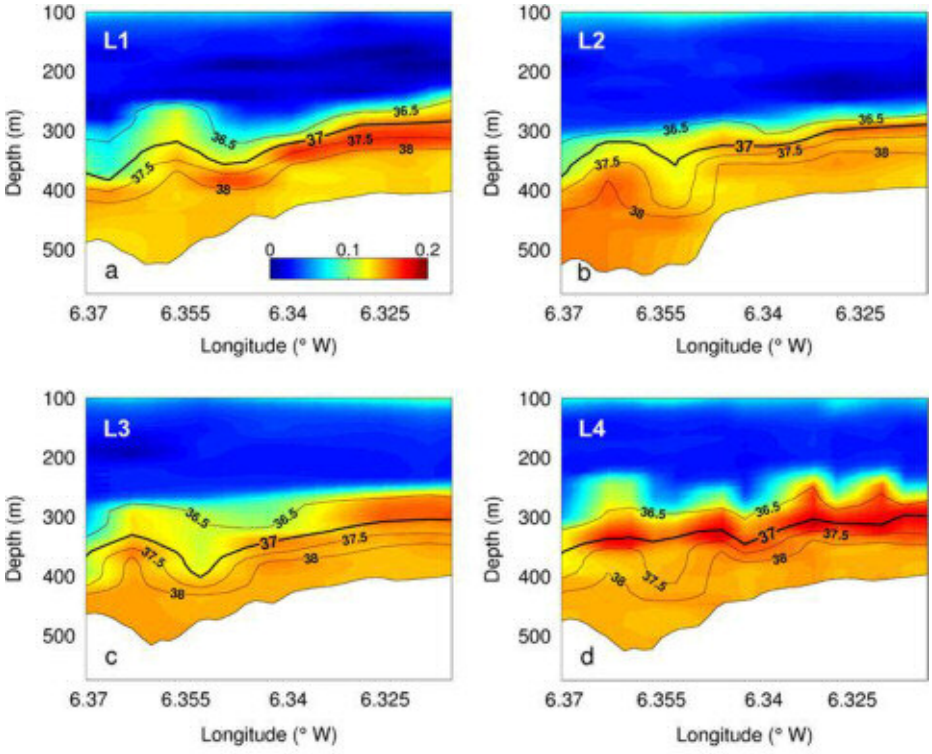

Fig. 3.7 Distributions of salinity (black contours) and turbidity (color, FTU units) on along-stream short transects at four different times of the tidal cycle (see Fig. 3.6). Thick solid line 37.0 isohaline, proxy for MW– NACW interface

associated to the MOW path (Fig. 3.4). The corresponding turbidity values generally increase away from the bottom, except immediately downstream of the abrupt change in bottom depth where a local maximum is present (Fig. 3.4). Three meridional cross-sections (at 6.225, 6.35, and 6.5°W) show that only the easternmost one captured the whole width (10 km) of the MOW (Fig. 3.5), emphasizing the V-shaped bottom profile and clearly defining the track of the high-salinity, low-turbidity MOW.

The M2 tidal velocity component is well aligned with the MOW trajectory (Fig. 3.6a, b). The tidal velocities are relatively weak (less than 0.2 ms^{-1}) within NACW, but increase in the MOW; in fact, the 95% confidence intervals are very large in the lower 150 m, suggesting a substantial tidal effect within the MOW. Figure 3.6c, d reveals strong temporal variation in the averaged M2 component of the along-stream velocity between 250–350 m over the tidal cycle; note that the duration of each short transect (typically 2 h) is substantially shorter than the characteristic period of the M2 tide (12.4 h).

Distributions of measured (temperature, salinity, turbidity, and velocity) and inferred (buoyancy frequency and gradient Richardson number) parameters on all short transects show large-scale patterns that remain invariable during the different phases of the tidal cycle. In Figs. 3.7, 3.8, and 3.9 depicting the trends for each along-stream transect, L2 and L4 correspond to ebb (out of the strait) and flood conditions, respectively, and L1 and L3 to phases with weaker tidal currents after ebb and flood tide, respectively (cf. Fig. 3.6). High salinity and turbidity values characterize the MOW, although maximum turbidity is associated to the MW–NACW interface (Fig. 3.7). Figure 3.8 shows the corresponding along-stream velocity contours for each but the last along-stream transect, where these data are lacking. There is a depth reversal in the flow direction, whereby the surface layers flow east and the swift MOW heads west, although no data are available for the deepest 50 m. Low gradient Richardson numbers are associated to the highly stratified (large buoyancy frequency) MW–NACW interface (Fig. 3.9); again the last transect is lacking, and Richardson numbers below 350–400 m are not shown because of ADCP contamination.

In Figs. 3.10, 3.11, and 3.12 depicting the flow properties for each across-stream transect, C1 and C2 correspond to conditions shortly before and after ebb tide, respectively, and C3 and C4 to before and after flood tide, respectively (cf. Fig. 3.6). The MOW has high salinity and turbidity values, although maximum turbidity occurs on either side of the V-shaped channel (Fig. 3.10).

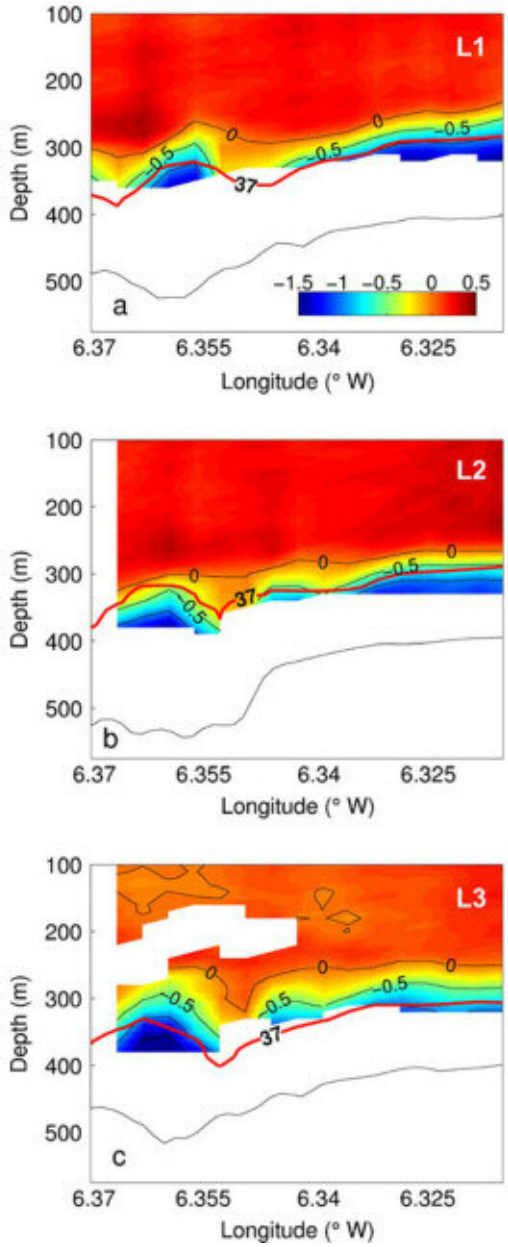

Fig. 3.8 Along-stream velocity (black contours and color) on along-stream short transects at three different times of the tidal cycle (see Fig. 3.6). Thick solid line 37.0 isohaline, proxy for MW–NACW interface. Positive velocities show flow toward the strait

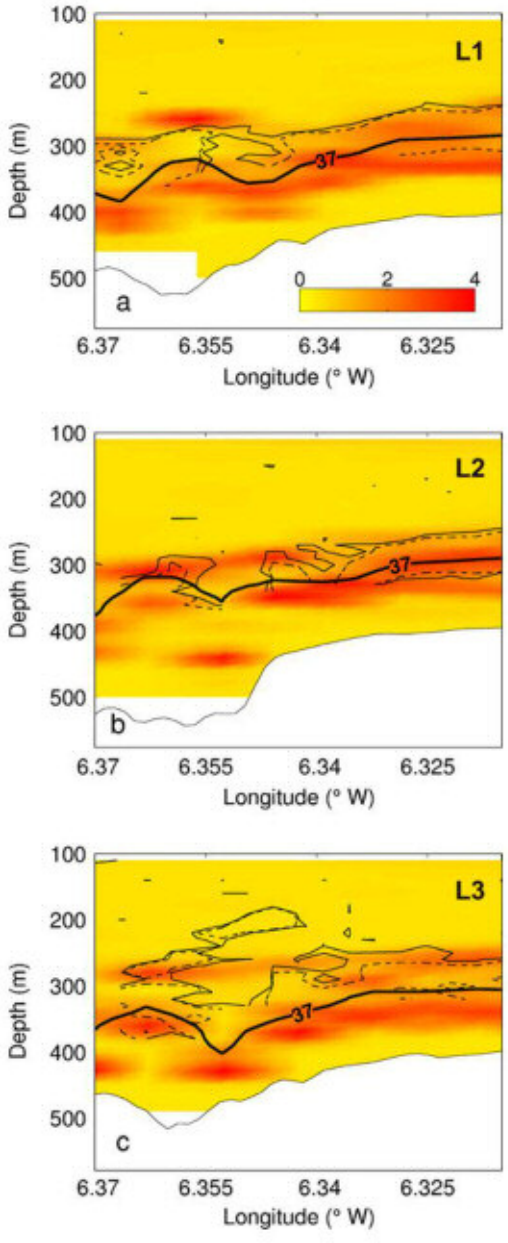

Fig. 3.9 Distributions of gradient Richardson number (solid line Ri=1, dashed line Ri=0.25) and squared buoyancy frequency (color, 10^{-4} cycles per hour) on along-stream short transects at three different times of the tidal cycle (see Fig. 3.6). Thick solid line 37.0 isohaline, proxy for MW–NACW interface

The along-stream velocity field illustrates the reversal of flow with depth, most clearly along the northern margin of the channel (and despite the absence of good-quality data near the seafloor; Fig. 3.11). The MW–NACW interface is characterized by maximum buoyancy frequencies, except after flood (C4) when high stratification in the center of the channel reaches down to the seabed (Fig. 3.12).

The isohalines roughly follow the bathymetry at all times (cf. individual cross-stream short transects), although there is also some tidal modulation of the location of the salinity maximum (Fig. 3.10). At times C1 and C2 after maximum westward tidal velocities, the MOW wedge thins and widens, particularly toward the northern margin. At time C4 after maximum eastward velocities, the high-salinity wedge is thicker and located in the center of the channel.

The cross-stream velocity field has no clear pattern (not shown). In contrast, the along-stream flow is of a two-layer type, with the MOW reaching values exceeding 1 ms^{-1} (although only along the northern margin of the channel), and the NACW flowing eastward with values locally reaching 0.3 ms^{-1}. The along-stream velocity contours closely follow the salinity field (Figs. 3.10 and 3.11), and the flow becomes unstable ($Ri < 0.25$) in the pycnocline, typically for depths below 300 m (Fig. 3.12). These subcritical values occur in the well-stratified interface.

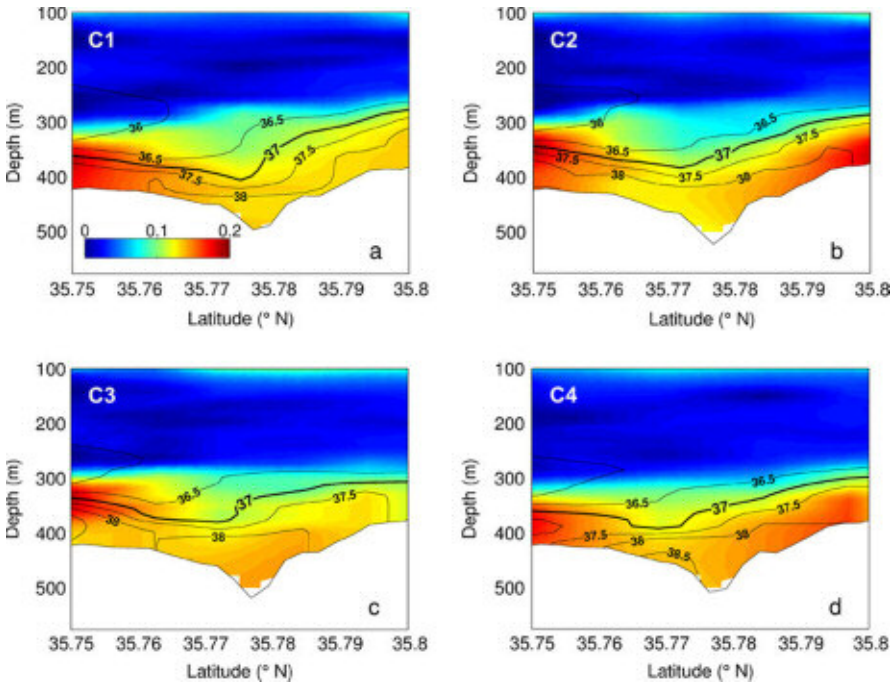

Fig. 3.10 Distributions of salinity (black contours) and turbidity (color, FTU units) on cross-stream short transects at four different times of the tidal cycle (see Fig. 3.6). Thick solid line shows the 37.0 isohaline, proxy for MW– NACW interface.

Fig. 3.11 Along-stream velocity (black contours and color) on cross-stream short transects at four different times of the tidal cycle (see Fig. 3.6). Thick solid line 37.0 isohaline, proxy for MW–NACW interface. Positive values show flow toward the north.

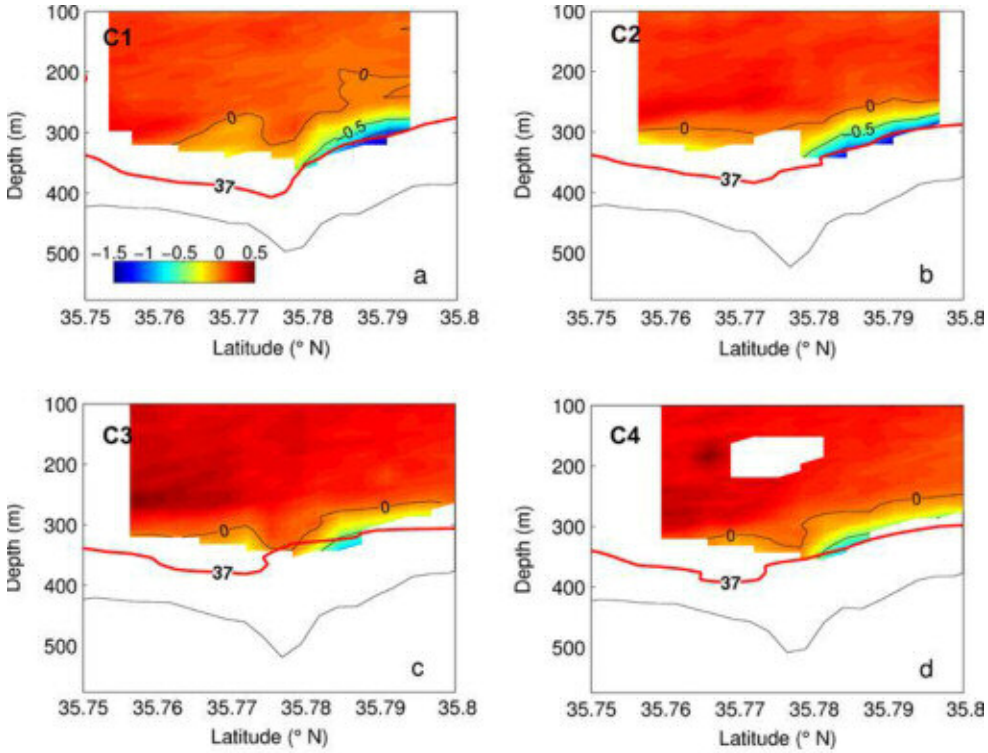

3.6 DISCUSSION AND CONCLUSIONS

3.6.1 MOW CHARACTERISTICS

The results presented above convincingly demonstrate that the bathymetry west of the Espartel Sill is responsible for both steering the MOW and determining specific sites where MOW kinetic energy becomes redistributed. The maximum salinity values (38.3) indicates that the MOW initially follows the Gibraltar Valley oriented WSW, but at 6.35°W bifurcates along two main channels, mostly the southern channel and less the northern channel (Fig. 3.2). Using the 37.0 isohaline as a proxy for the interface between the NACW and MW, the data reveal the sinking of the MOW as it flows toward the west following the bathymetry (Fig. 3.4); its thickness ranges between ca. 50 and 150 m, decreasing in those areas where the bottom slope increases rapidly, and reaching maximum values over the deepest part of the channel. The salinity field in the eastern section across the MOW is symmetric with respect to the channel axis, while in the western section the isohalines rise toward the south, as do the turbidity contours (Fig. 3.5), indicating that the MOW is centered south of this transect.

The marked decrease in salinity corresponding to the pronounced increase in bottom depth at 6.35°W (Figs. 3.2 and 3.3) suggests the occurrence of enhanced mixing between high-salinity MW and low-salinity NACW in this area. Observations for the AS transect indeed confirm that the local increase in bottom slope induces a flow acceleration that would explain the development of large billows, typically 50 m tall and 1 km long (Fig. 3.7). Actually, the along-stream irregular bottom profile becomes mirrored by undulations at the MW–NACW interface. Subcritical gradient Richardson numbers ($Ri<0.25$) are also related to this outflow acceleration (Fig. 3.8), so that vertical mixing develops in the undulated and well-stratified MW–NACW pycnocline (Fig. 3.9).

All along-stream short transects display a two-layer structure, with high-salinity near-bottom MOW propagating westward under the NACW. MW thickness decreases in association with the pronounced increase in bottom depth at 6.34–6.35°W. While the basic characteristics of the salinity field remain similar for each transect (Fig. 3.7), there is considerable tidal variability in the thickness, which fluctuates by 10–50 m depending on the isopycnals considered. The data also suggest the occurrence of intermittent instabilities strongly related to the tidal phase. During the maximum outflow tide (L4), the mixing of MW (cf. salinities exceeding 37.0) displays its maximum vertical extension.

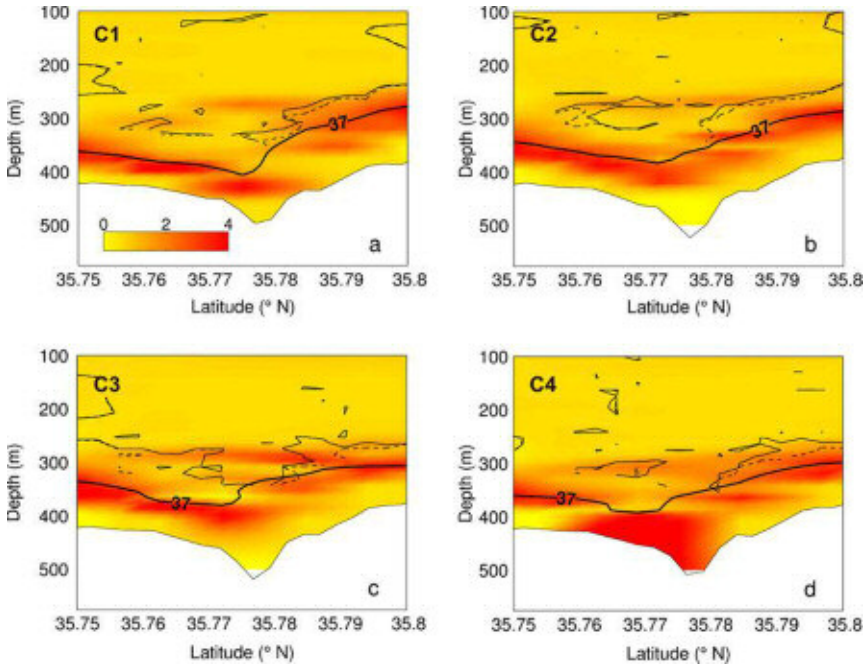

Fig. 3.12 Distributions of gradient Richardson number (solid line Ri=1, dashed line Ri=0.25) and squared buoyancy frequency (color, 10−4 cycles per hour) on along-stream short transects at four different times of the tidal cycle (see Fig. 3.6). Thick solid line 37.0 isohaline, proxy for MW–NACW interface.

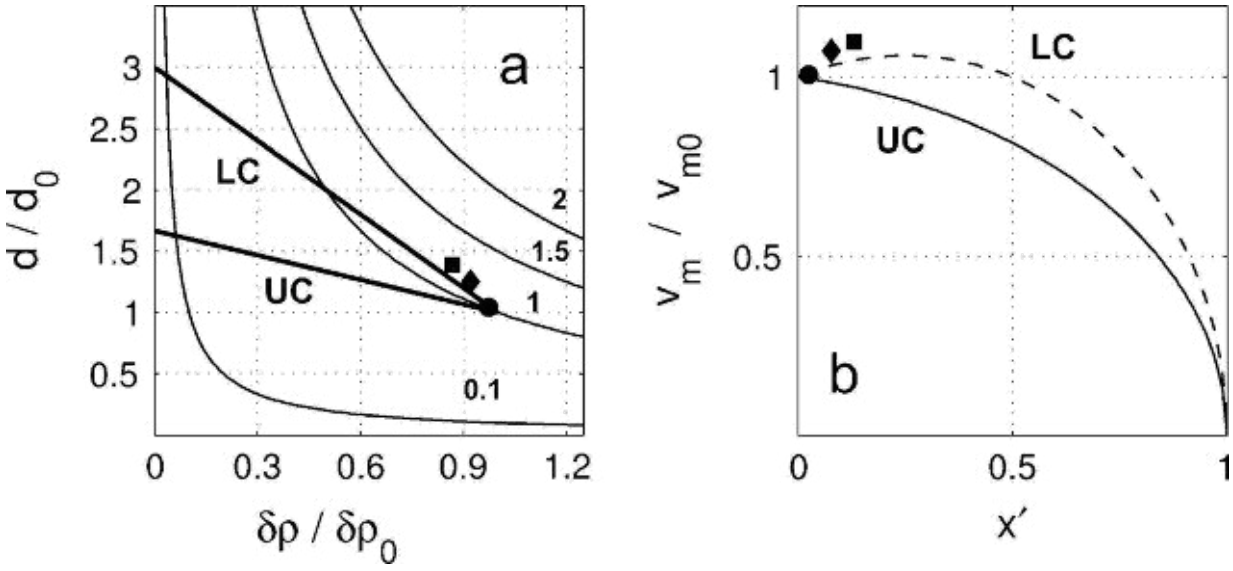

Fig. 3.13 a) Normalized maximum velocity v_m/v_{m0} (thin solid lines) in the $\Delta\rho/\Delta\rho_0$ vs d/d_0 space: thick solid lines possible path for the MOW's upper core (UC) and lower core (LC) from a position (1, 1) near the Espartel Sill to a final depth-stabilized position (0, d_f/d_0). b) Normalized maximum velocity v_m/v_{m0}, for both UC and LC, as a function of the normalized distance $x' \equiv x/L$ between the Espartel Sill and the final depth-stabilized position. Circle, diamond, square: Values calculated using cruise data along the MOW path for depths of 375, 450, and 500 m, respectively.

Cross-stream velocities are weak and do not exhibit any noticeable pattern along the MOW core path (not shown). In contrast, along-stream velocities closely follow the salinity pattern; MOW velocity remains negative (toward the west) during the complete tidal cycle, no MOW inversion having been observed during the cruise (Fig. 3.8). The gradient Richardson number is subcritical (smaller than 0.25) in large areas below 300 m, including the well-stratified interface between the MW and NACW (Fig. 3.9). Richardson numbers tend to be smaller west of 6.34°W, consistent with accelerated flow above the steep slopes there. High values of the buoyancy frequency occur slightly below the 37.0 isohaline, defining the sharp NACW–MW pycnocline (Fig. 3.9).

3.6.2 CORIOLIS AND CENTRIFUGAL FORCES

In addition to the pressure gradient, Coriolis and centrifugal forces modify the MOW. Considering the along-stream Rossby number Ro_x (Eq. 3.5), a characteristic MOW width L_y =10 km (cf. Figs. 3.2 and 3.5) and maximum velocity U= 1.4 m s^{-1} result in Ro_x = 1.7. Therefore, the Coriolis force is not a principal element controlling the along-stream MOW force balance during its initial plunging stage. Setting the critical value Ro_x =0.1 shows that the critical velocity for L_y =10 km would be 0.08 m s^{-1}. In fact, the MOW does not reach such low values in the Gulf of Cadiz (Ambar and Howe 1979; Baringer and Price 1999).

Since δ = L_y/L_x has a small value, Eqs. 3.5 and 3.6 indicate that Ro_y << Ro_x. This implies that the Coriolis force has a relevant role in the cross-stream force balance. It is difficult to meaningfully estimate δ, as the along-stream length scale should reflect the distance over which the dynamics remains basically unchanged, an unknown quantity. Therefore, the reverse exercise would be to set Ro_y =0.1, and then estimate δ for a given characteristic along-stream velocity and cross-stream distance. Specifically, for U=1.4 ms^{-1} and L_y =10 km, δ = 0.25 or L_y =4.1L_x. This means that the Coriolis force plays an important role in the cross-stream balance at a distance only about 4 times the width of the current; using the above widths, this would occur about 40 km west of the Espartel Sill, near the western limit of the study area.

In the cross-stream balance, it is possible that the acceleration term is dominated by the curvature of the flow's path. In this case the acceleration term is U^2/R, R being the flow's radius of curvature; Eq. 3.6 is replaced by $Ro_y = U\delta^2/fR$, and the cross-stream Rossby number decreases by a factor L_y/R. If the width of the MOW is smaller than the radius of curvature, as it happens in the study area, then the centrifugal term is negligible.

3.6.3 GRAVITY CURRENT BEHAVIOUR

A relevant question is whether the MOW behaves as a gravity current as it passes the Espartel Sill. Based on characteristic values reported in García Lafuente et al. (2007), Sánchez-Román et al. (2008), and García-Lafuente et al. (2009), a total water depth d=360 m and MOW thickness h = 170 m gives δ = 0.47; with density ρ = 1,029 kg m^{-3} and density anomaly ρ=1.9 kg m^{-3}, Eq. 1 predicts a speed of 1.32 ms^{-1}. This is close to the mean maximum value reported by Sánchez-Román et al. (2008) for the Espartel Sill, 1.25 ms^{-1}. When h decreases to 126 m (δ=0.35), the outflow would increase to a maximum speed of 1.37 m s^{-1}, provided the density anomaly remains unchanged. Therefore, as a first approximation, the condi-tion for maximum velocity is met by the MOW as it exits the Strait of Gibraltar at the Espartel Sill.

The rapid changes in bathymetry, and the perturbations of the interface associated with instabilities that develop at the MW–NACW interface, make it very difficult to estimate the mean thickness of the MOW layer from a single survey. In the central sector, however, the repeated short along-stream transects enabled meaningful approximations of d=400 m and MOW thickness h=100 m, so that δ=0.25, again consistent with maximal speed conditions. Therefore, the observed velocity remains close to maximum velocity conditions as the MOW crosses the study area. Using the hydrographic cruise data at 6.225°W (eastern sector), 6.35°W (central sector), and 6.5°W (western sector; Figs. 3.3 and 3.5) leads to d=375, 450, and 500 m, and ρ=1.85, 1.75, and 1.65 kg m^{-3}, respectively. The velocity at the three locations would be 1.32, 1.41, and 1.45 ms^{-1}, respectively. Such an increase shortly downstream of the Espartel Sill is consistent with the results of Price et al. (1993) and Baringer and Price (1997a, b), but does not account for any tidal modulation of the flow.

Consider now the argument that the outflow always maximizes its speed, i.e., δ = h/d remains constant and close to δ_m =0.35 (Eq. 3.1). The outflow speed varies with both the water depth and the density excess as

$$v_m - v_{m0}\left[\left(\frac{\Delta\rho}{\Delta\rho_0}\right)\left(\frac{d}{d_0}\right)\right]^{1/2} \qquad \text{(eq. 3.7)}$$

where v_{m0} is the initial maximum speed, taken to be the case for the MOW over the Espartel Sill, and $\Delta\rho_0$ and d_0 respectively are the MOW initial excess density and initial water depth that lead to v_{m0}. Figure 3.13 shows two possible linear paths for the MOW in the ($\Delta\rho/\Delta\rho_0$, d/d_0) space, one for each of its two main cores. The path goes from the initial (1, 1) point to a final (0, d_f/d_0) position, where d_f/d_0 =600 m/ 360 m=5/3 for the upper core (UC), and d_f/d_0 =1,080 m/ 360 m=3

for the lower core (LC). This simply presupposes that the density difference will decrease linearly with depth, until it becomes zero at the final point. Hence, the depth and density excess are related: d/d_0-5/3, (2/3)($\Delta\rho/\Delta\rho_0$) for the UC, and d/d_0-3, 2($\Delta\rho/\Delta\rho_0$) for the LC.

Consider now a linear decrease in the density excess with distance, i.e., x/L – (1 $\Delta\rho/\Delta\rho_0$), where L=200 km is the distance between the Espartel Sill and a final point near Cape San Vicente. These considerations lead to the following final expressions for the normalized velocity as a function of the distance along its path:

$$v/v_{m0} = \{(\Delta\rho/\Delta\rho_0)[5/3-(2/3)(\Delta\rho/\Delta\rho_0)]\}^{1/2} \text{ for the UC, and}$$
$$v/v_{m0} = \{(\Delta\rho/\Delta\rho_0)[3-2(\Delta\rho/\Delta\rho_0)]\}^{1/2} \text{ for the LC, where } \Delta\rho/\Delta\rho_0=1-x/L$$

It may be argued that the MW density excess should decrease ver rapidly during the early plunging stage as a result of more intense mixing, i.e., a more realistic nonlinear relation between x and ρ could be chosen. Furthermore, the instantaneous MOW speed may differ from the above calculated maximum values because of two factors: the bottom slope, and tides. Typical mean bottom slopes are small (tan α=0.01–0.1), so that they should lead only to minor changes in the pressure difference at the head of the gravity current. On the other hand, tidally induced flow is not negligible, with amplitudes exceeding 0.2 ms^{-1} (Fig. 3.6). Nevertheless, the cruise data do show good agreement with the lower-core predictions for water depth, density difference, and normalized velocity (cf. Fig. 3.13). In particular, the LC data predict an initial increase in velocity with distance from the Espartel Sill, consistent with the velocity data. This initial velocity increase also agrees with observations by Price et al. (1993) and Baringer and Price (1997a). Figure 3.13 indeed suggests that the two MOW cores will experience relatively small velocity changes until the density excess of the intruding current ρ approaches zero. At this late stage along the continental slope in the northwestern Gulf of Cadiz, the MOW would find its compensating depth and the flow dynamics would no longer be that of a density-driven flow.

3.6.4 VERTICAL MOTIONS AND ENERGY

The available potential energy of the dense MOW wedge that exits the Strait of Gibraltar at depths of 200–350 m is progressively converted into mean flow kinetic energy. This enables the outflow to maintain high velocities despite the large increase in water transport resulting from entrainment of the overlying NACW (Ambar and Howe 1979; Ochoa and Bray 1991; Baringer and Price 1997a, b; Xu et al. 2007). Not all the outflow energy is transformed into the kinetic energy of the increased transport. Some energy is dissipated through turbulence in the boundary and interfa-cial layers (Johnson et al. 1994), and some is transformed back into potential energy through the formation of an intermediate layer with MW–NACW mixed characteristics. Some energy may also be released without mixing through the production of radiating internal waves from the undulating interface.

In the study area the velocity difference between MW and NACW is so large that Kelvin-Helmholtz-like interface billows develop, as identified by the ship's echosounder. The condition for this to occur is that the flow near the MW–NACW interface has to be subcritical, i.e., the excess kinetic energy of a water parcel that moves up in the water column is greater than the excess potential energy necessary to make this displacement permanent. This necessary condition is satisfied by gradient Richardson numbers smaller than a critical value of 1 (see Figs. 3.9 and 3.12). These instabilities overturn and mix large water parcels, in a diffusive process with temporal memory (Pelegrí and Sangrà 1998). This process can lead to the creation of an intermediate layer on top of the less-diluted MW layer, this potentially being the initial breakdown of the MOW as two cores that propagate into the Gulf of Cadiz at different levels and with distinct densities. However, further data are needed to verify if this mixed zone remains downstream or if it disappears in the sheared flow. The cruise observations show that this intermediate layer is yet fresher (salinities about 36.5–37.0) and the deep layer saltier (salinities >38.0) than the lower and upper MOW cores near Cape San Vicente (salinities about 37.1 and 37.4, respectively), implying that substantial vertical mixing still remains to be performed along the MOW path.

The generation of undulations at the MW–NACW interface, with a vertical scale of 50 m and horizontal scale of 1 km, appears related to accidents in the bottom morphology and vertical inversions in the potential density field (Fig. 3.4). The temporal scale of these Kelvin-Helmholtz-type instabilities should depend on the stratification of the flow, specifically on the large density difference between MW and NACW. This timescale is of order N^{-1} (Holst et al. 1992; Pelegrí and Sangrà 1998), the buoyancy frequency being defined as in Eq. 3.3.

Using $d\rho/dz = \Delta\rho/\Delta z = 1.75$ kg/m ^{3} per 100 m indicates that those billows developing at the MW–NACW interface are of rather short duration, no more than a few minutes.

3.6.5 EROSIVE POTENTIAL

The joint effect of high near-bottom velocities (mean kinetic energy), energetic interfacial undulations (internal wave energy), and overturning billows (turbulent kinetic energy) may increase the energy available from the flow, and facilitate sediment erosion and transport. The energy supply necessary for erosion may be expressed as bottom stress (force per unit area) multiplied by velocity (distance per unit time) in the same direction as the bottom stress, i. e., work per unit area and time, or power per unit area. Since bottom stress is proportional to the squared velocity, it means that power per unit area is proportional to velocity cubed. This leads to intermittent, highly erosive events linked to the fastest MOW velocities. A major event would occur when the MOW accelerates by the joint effect of a subcritical mean flow (e.g., the MOW thins and accelerates following a substantial increase in the bottom slope) and the westward tide component of the velocity. The frequency and intensity of these events may be seasonally or inter-annually modulated by other factors such as the evaporation–precipi-tation balance in the Mediterranean basin, and meteorological forcing over and at both sides of the Strait of Gibraltar (Stanton 1983; García Lafuente et al. 2007; García-Lafuente et al. 2009).

The actual MOW erosive capacity, however, would not only be a function of its velocity but also depend on the grain size and cohesion of the sediments. In this area the maximum turbidity signal is located over the two margins of the channel, in areas of high speed but away from the absolute velocity maximum located immediately over the channel bed (Fig. 3.10). This turbidity distribution suggests the presence of different bottom grain sizes in these sectors: the high velocities may have removed all fine-grained sediments from the center of the channel, so that the channel progressively evolves out, eroding the margins where grains of relatively small size remain and causing upstream erosion.

Contour currents are traditionally considered to flow along-slope, in near-geostrophic equilibrium and giving rise to contourite drifts; in contrast, downslope processes have been usually related to turbidity-driven flows resulting in turbiditic architectures (e.g., Chapter 15 in Kennett 1982). The nascent MOW does not share the properties of a contour current, as it moves toward deep waters along the Gibraltar Valley. It is along this central axis that a downslope erosional scour has developed (Fig. 3.10), as proposed by Habgood et al. (2003). The top of this indented V-shaped scour is no more than 500 m wide and penetrates about

50 m. This active scouring takes place along the southern branch of this valley, but what may be a remnant scour is visible in the apparently less active northern branch (Figs. 3.1 and 3.2).

This southern main branch reaches the open ocean before it turns north, along the Iberian Peninsula, initially no deeper than about 600 m (Baringer and Price 1999). However, it is possible that related downslope channels may have reached deeper in past climates (Llave et al. 2006, 2007). This could have occurred as a result of changes in the water balance within the Mediterranean basin (changing MW salinity and density), and variations in the total water depth at the Espartel Sill. As the speed of a gravity current is proportional to the squared root of both the total water depth and the density excess of the intruding water (Eq. 3.1), a scenario of maximum depth penetration would correspond to a thin (low total water depth) and yet very dense MOW. The high-density anomaly guarantees the possibility of reaching far and deep, but this has to occur through a relatively slow (therefore thin) current that undergoes little vertical mixing.

In conclusion, the findings show that the MOW interacts with the underlying bottom topography in a complex manner. Through its slope and shape characteristics, the seabed is responsible for steering and mixing the MOW, thereby defining its three-dimensional trajectory. In turn, MOW characteristics—e.g., erosive potential—control the slow evolution of the bathymetry. This two-way interaction possibly results in a meta-stable system, the flow and bottom variables remaining within a limited range of values. Theoretical, observational, and numerical studies are required to further characterize the key parameters controlling the stability of this system.

ACKNOWLEDGEMENTS

The authors are deeply grateful to all aboard the R/V García del Cid, in particular Captain Eduardo Otal and technicians José Antonio Pozo, Maribel Lloret and Joaquín Salvador, as well as Mikhail Emelianov and Sam Kelly for their help in gathering data during the cruise. The authors are also very grateful to Gemma Ercilla and two anonymous reviewers for many useful comments. Funding for this work comes from the Ministerio de Ciencia e Innovación, Spain, through project MOC2 (CTM2008-06438-C02-01), project INGRES (CTM2006-02326), and two complementary actions (CTM2008-03422-E/MAR and CTM2009-05810-E/MAR); funding also comes from the US National Science Foundation (grants OCE-0825287 and OCE-0825297).

CHAPTER 4: TRACKING THE MEDITERRANEAN OUTFLOW IN THE GULF OF CÁDIZ

M. Gasser, J. L. Pelegrí, M. Emelianov, M. Bruno, E. Gràcia, J. Nash, M. Pastor, H. Peters, A. Rodríguez-Santana, J. Salvador, R. F. Sánchez-Leal
Published in Progress in Oceanography, 2017, Vol. 157, 47-71

Abstract

The Mediterranean Water leaves the western end of the Strait of Gibraltar as a bottom wedge of salty and warm waters flowing down the continental slope. The salinity of the onset Mediterranean Outflow Water (MOW) is so high that leads to water much denser (initially in excess of 1.5 kg m ^{3}) than the overlying central waters. During much of its initial descent, the MOW retains large salinity anomalies – causing density anomalies that induce its gravity current character – and relatively high westward speeds – causing a substantial Coriolis force over long portions of its course. We use hydrographic data from six cruises (a total of 1176 stations) plus velocity data from two cruises, together with high-resolution bathymetric data, to track the preferential MOW pathways from the Strait of Gibraltar into the western Gulf of Cadiz and to examine the relation of these pathways to the bottom topography. A methodology for tributary systems in drainage basins, modified to account for the Coriolis force, emphasizes the good agreement between the observed trajectories and those expected from a topographically-constrained flow. Both contour avenues and cross-slope channels are important and have complementary roles steering the MOW along the upper and middle continental slope before discharging as a neutrally buoyant flow into the western Gulf of Cadiz. Our results show that the interaction between bottom flow and topography sets the path and final equilibrium depths of the modern MOW. Furthermore, they support the hypothesis that, as a result of the high erosive power of the bottom flow and changes in bottom-water speed, the MOW pathways and mixing rates have changed in the geological past.

4.1 INTRODUCTION

The dense Mediterranean Water (MW) flows at depth along the Strait of Gibraltar with salinities in excess of 38.5 g/kg, underlying North Atlantic Central Water (NACW) with salinities ranging between 36.0 and 36.2 g/kg. After the MW overcomes the western sills of the Strait of Gibraltar, it plunges into the Atlantic Ocean as the Mediterranean Outflow Water (MOW). The most restrictive sill is Camarinal (35º55'N, 5º46'W; 290 m) although, further west (35º50'N, 5º58'W; 360 m), Espartel Sill has also great dynamic importance as it imposes permanent hydraulic control on the MOW (García Lafuente et al., 2002); at this longitude, the Majuan Ridge (35º53'N, 6ºW; 60 m depth) divides the outflow into a main channel, where Espartel is found, and a northern channel with a minimum depth of 150 m (Luján et al., 2011; Hernández-Molina et al., 2014a). A third and deeper topographic constriction is West Espartel Sill (32º47'N, 6º20'W; 420 m), located some 22 km down-stream of Espartel Sill (Armi and Farmer, 1988; Gasser et al., 2011; Nash et al., 2012). As the MOW overpasses this last sill, it undergoes a substantial increase in water depth, from 420 to 500 m in about 1 km, which accelerates the flow and causes instability and vertical mixing (Gasser et al., 2011; Nash et al., 2012).

The MOW progresses through the eastern/northern margins and the eastern middle slope of the Gulf of Cadiz, first through the ambient NACW and later into the North Atlantic Deep Waters (NADW). The salinity of the NACW decreases nearly linearly with depth, from about 36.6 g/kg at the sea surface to 35.5 g/kg at depths of about 600 m. Within the Gulf of Cadiz and the entire eastern subtropical North Atlantic Ocean, the transition from NACW to NADW takes place in an intermediate water stratum, between about 600 and 1400 m, with contributions of both Mediterranean and Antarctic waters. The MOW is the predominant water mass in the Gulf of Cadiz, introduced through the shedding of Mediterranean eddies (meddies) and the posterior diffusion from these lens-type pulses (Richardson et al., 2000) and as a result of lateral diffusion of salt and heat (Iorga and Lozier, 1999; Mauritzen et al., 2001). The slope waters off NW Africa, north of the Canary Islands and into the Gulf of Cadiz, are also influenced by a diluted form of Antarctic Intermediate Water, located immediately on top of the level of maximum MOW influence (Machín and Pelegrí, 2009, 2016; Louarn and Morin, 2011).

Beyond Camarinal Sill, the principal pathway for the MOW is towards the W-SW, along a valley that arises as an extension of the Strait of Gibraltar. In this valley, the MOW becomes a salty wedge about 5 km wide and 150 m thick with time-averaged speeds near 1.5 m/s (Ambar and Howe, 1979) and instantaneous values as large as 3 m/s (Mulder et al., 2003). During its initial descent, the westward MOW is driven by pressure gradients arising from its excess density

relative to the ambient NACW, and its path is constrained by the bottom topography. Eventually the MOW reaches the continental slope and propagates into the Gulf of Cadiz in approximate geostrophic equilibrium, splitting into at least two main branches or cores centered at depths of about 600 m and 1000 m, respectively (Madelain, 1970; Zenk, 1975; et al., 1993; Baringer and Price, 1997a, 1999; Ambar et al., 2002; Borenäs et al., 2002). The upper branch flows along the base of the upper slope (depths between 500 and 800 m) until Cape São Vicente, with average speed about 0.5 m/s, temperature 13.7 ºC and salinity 37.1 g/kg (Madelain, 1970; Zenk, 1975; Ambar and Howe, 1979; Ambar et al., 1999; García et al., 2009). The lower branches are located further south – at depths 800–1200 m, with average speed about 0.25 m/s, temperature 13.6 ºC and salinity 37.4 g/kg (Madelain, 1970; Zenk, 1975; Zenk and Armi, 1990; Bower et al., 2002). These lower branches detach from the seafloor in the western Gulf of Cadiz, constituting the main path for MOW transport into the open ocean (Iorga and Lozier, 1999; Mauritzen et al., 2001).

Numerical models have also depicted the MOW as an along-bottom plume, widening with multiple velocity streams that eventually settle at two principal depths (Borenäs et al., 2002; et al., 2008; Xu et al., 2007). Papadakis et al. (2003) and Legg et al. (2009) endorsed that environment NACW is entrained by the turbulent MOW, therefore creating a layer of intermediate properties that leads to a second MOW core. However, Jungclaus and Mellor (2000) emphasized the relevance of the bathymetry for splitting the flow, pointing at relatively small canyons (widths less than 5 km) as the plausible responsible for routing the bottom waters. Peliz et al. (2013) and Barbosa Aguiar et al. (2015) used a 2-km horizontal-resolution model (though substantially smoothed) and observed two velocity cores but one single salinity core along 8.5º W, all them at different latitudes; however, these results depend largely on the intensity of vertical mixing.

It seems likely that the different cores arise from both topography and mixing acting together, with diapycnal mixing changing the vertical structure of density and speed in such a way that leads to differential topographic steering of the bottom and intermediate layers. Independently of the exact mechanism, in order to position these cores, models require a high resolution of the short-scale bottom topography, as either local intense mixing or the flow diversion through narrow canyons depend on structures of the order of 1 km or less (Gasser et al., 2011; Nash et al., 2012). This is substantially less than the grid size for all of the above models, with typical resolution of 10 km or even less after horizontal numerical smoothing.

The Iberia-Biscay-Irish (IBI) operational model of Sotillo et al. (2015, 2016) deserves special mention. It has 50 vertical levels and a horizontal resolution of 1/36º, or about 2–3 km for the

region under consideration, which implies some substantial smoothing of its 30-s resolution GEBCO08 seafloor topography (Becker et al., 2009). The IBI model is forced with 3-h atmospheric fields, includes tides and river discharges, and assimilates several datasets (altimetry, sea surface temperature and data from the Argo program). A data subset from 1 June to 31 August 2016 (downloaded from the Copernicus Environment Monitoring Service) has been used to produce the near-bottom distribution of temperature, salinity, density and velocity fields (Fig. 4.3). Near the Strait of Gibraltar, the model displays one single salinity-velocity core that, as it enters the Gulf of Cadiz, diverges into two cores, one along the continental slope and one single core in the open waters of the Gulf of Cadiz.

Several of the above oceanographic studies have indeed pointed at the relevance of the eastern and central Gulf of Cadiz bathymetry in driving the path and branching of the MOW (Madelain, 1970; Zenk, 1975; Baringer and Price, 1997a, 1999). The strong interaction between bottom flow and seafloor has also been progressively recognized by bathymetric and stratigraphic studies of the Gulf of Cadiz. Nelson et al. (1993, 1999) pointed out the relevance of diapiric ridges blocking the propagation of the MOW, and thus forcing the current to run along the ridges generating erosive moats and accumulating contourite deposits on their side. Hernández-Molina et al. (2003, 2006) produced a morpho-sedimentary map of the contourite depositional system of the Gulf of Cadiz, and Llave et al. (2006, 2007, 2011) examined the relation of this depositional system with both erosional and tectonic processes during the Quaternary. García et al. (2009) placed the emphasis on the erosive features, proposing a bottom flow scheme that combines along-slope excavation of contourite moats and channels with down-slope erosion of valleys and furrows. Hernández-Molina et al. (2014a,b), using high-resolution bathymetry, described contouritic channels in the eastern Gulf of Cadiz that suggest an early partition of the MOW into two branches. These authors also stressed the relevance of both erosional and depositional processes in the contourite systems and the abundance of erosive scours downslope, located at different depths and distances from the western end of the Strait of Gibraltar. All these studies, using sedimentary and chronostratigraphic data, support the idea that the different valleys and scours in the slope of the SW Iberian margin respond to current and/or previous MOW paths (Nelson et al., 1993, 1999; Llave et al., 2006, 2007, 2011; Rogerson et al., 2005; Hernández-Molina et al., 2014a,b).

Despite these numerous studies, we still lack a detailed understanding of the main MOW pathways in the Gulf of Cadiz: its early plunging and partition into different streams in the eastern Gulf, the steering of these streams through a complex network of channels over the middle slope in the eastern and central Gulf, the way these streams lead to several cores of distinct water properties, and the MOW final departure from the seafloor as neutrally-buoyant

veins in the western Gulf. The available schemes are either based on detailed descriptions of depositional-erosional features together with a limited analysis of hydrographic data (Nelson et al. 1993, 199; Maestro et al., 2007; García et al., 2009; Hernández-Molina et al., 2006, 2014a; Hernández-Molina et al., 2014b), or on more comprehensive hydrographic and velocity data accompanied by a restricted characterization of the subjacent bathymetry (Madelain, 1970; Zenk, 1975; Ambar and Howe, 1979; Price et al., 1993; Baringer and Price, 1997a; Ambar et al., 2005). A step forward has been recently done by Hernández-Molina et al. (2014a), combining geomorphological and stratigraphic data with hydrographic data to propose current and past pathways for the MOW in the eastern Gulf of Cadiz, although using a very limited oceanographic dataset.

The study of morphological and oceanographic interactions was limited by the lack of publicly-available high-resolution bathymetry data. Fortunately, Zitellini et al. (2009) provided such a bathymetry for most of the Gulf of Cadiz, with only some gaps in the shelf and upper slope areas. This dataset has been recently complemented with very high-resolution bathymetry data from a cruised carried out between 37ºW and Espartel Sill (Section 4.2.2). The availability of a high-resolution bathymetry for the entire Gulf of Cadiz represents an important step towards an improved understanding of the interaction between bottom flows and seafloor topography. This comes out very clear in the studies by Gasser et al. (2011) and Nash et al. (2012), which illustrate the relevance of local processes: following a depression immediately downstream of West Espartel Sill, the flow accelerates and leads to instabilities that generate something alike an intermediate layer between the NACW and MOW strata, in what could be considered as a vertical splitting of the MOW.

Our main objective is to use these high-resolution bathymetry data, combined with a comprehensive oceanographic dataset, to identify the relation between the MOW pathways and the seafloor topography in the eastern and central Gulf of Cadiz. We first present the bathymetric and hydrographic-velocity datasets (Section 4.2) and explain how these two different datasets have been integrated and analyzed (Section 4.3). Then, we move to a description of the location and characteristics of the MOW streams in the near (Section 4.4) and far (Section 4.5) fields, with special emphasis on their interaction with the seafloor. We continue with a discussion on what we have learned by combining the different approaches (Section 4.6) and conclude with some remarks on the crucial role of bathymetry on density-driven near-bottom flows (Section 4.7).

4.2 DATA SETS

4.2.1 BATHYMETRY DATA

We have built the Gulf of Cadiz bathymetry (Fig. 4.1) using a combination of three different datasets. The first two are the United States Geological Survey 30-s GTOPO data (GTOPO, 2013) (about 500 m resolution) and the Zitellini et al. (2009) data (250 m resolution). They are complemented with multibeam echosounder data west of Espartel Sill, obtained using an Elac Seabeam 1050D operating at 50 kHz during the MEDOUT-11 cruise, carried out in July 2011 onboard the R/V García del Cid. The new bathymetry data is of high resolution (between 40 and 80 m) and corresponds to an irregularly shaped band (about 8 km wide and 50 km long) that follows the main path of the MOW inside a rectangular domain of about 50 25 km, between 35º42'N and 35º57'N and between 6º19'W (some 3 km east of West Espartel Sill) and 6º51'W (Fig. 4.2).

For the purpose of this study, the path of the MOW is examined over the near and far fields. The near field corresponds to a region located immediately west of Espartel Sill, until about 7ºW. It includes a 70-km long irregular trough that is the natural extension of the Strait of Gibraltar, hereafter named as the Gibraltar Channel (Gasser et al., 2011), as well as the region between this valley and the SW Iberian shelf, where a shallower and less defined along-slope pathway is identified (Fig. 4.4b). We will see later that this near field is dynamically characterized by a very energetic MOW, which is substantially denser than the environment fluid and closely follows the contourite channels. The far field provides a larger, and obviously less detailed, view of the entire north-eastern and central Gulf of Cadiz, including the upper, middle and lower continental slope of the Atlantic margin SW of the Iberian Peninsula (Fig. 4a). The MOW extends over large areas of the middle slope yet the direction of the flow remains greatly influenced by the topography of the seafloor through numerous downslope erosive valleys. In this large domain we will be able to appreciate how the MOW positive density anomaly decreases progressively until it eventually disappears.

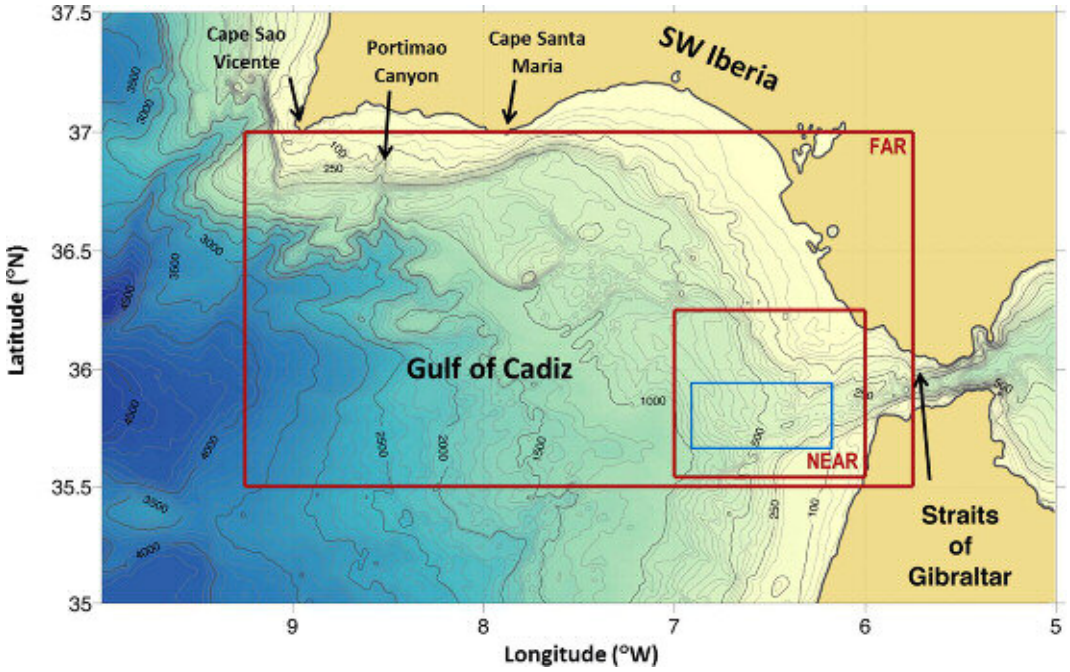

Fig. 4.1. Bathymetry (m) of the Gulf of Cadiz plotted with a resolution of 250 m. The blue rectangle corresponds to the area where the MEDOUT-11 data was gathered (Fig. 4.2) and the red rectangles indicate the MOW far- and near-field regions as defined in this study (4.4). The upper slope corresponds approximately to the band between the 200 and 500 m isobaths; the middle slope plateau extends over the area between the 500 and 1250/700 m isobaths al latitudes 36º/36º30' N.

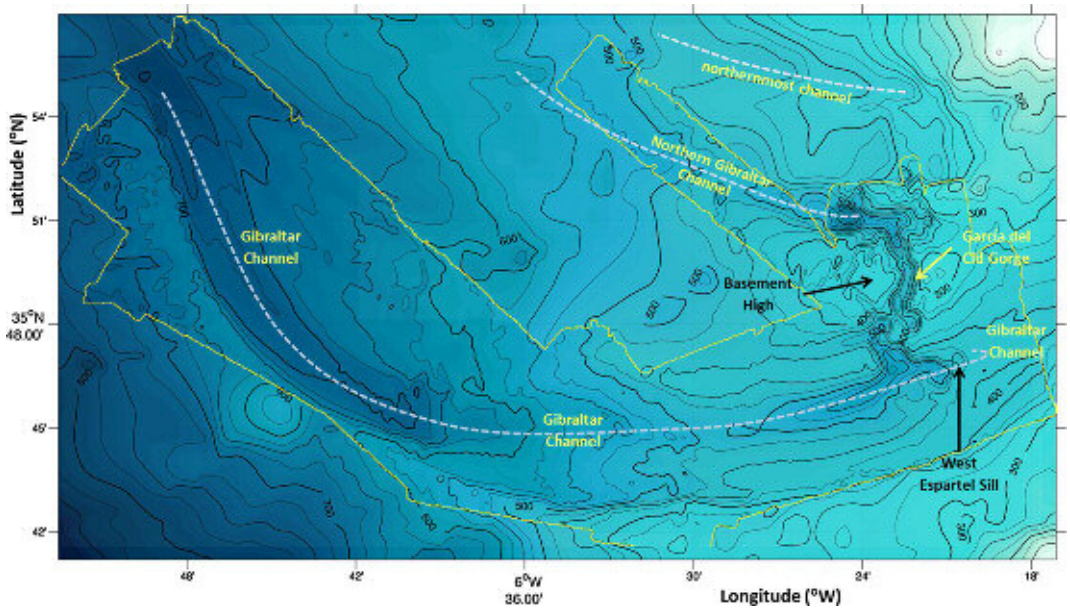

Fig. 4.2. Bathymetry (m) for the system of channels west of the Strait of Gibraltar, corresponding to the area inside the blue box in Fig. 1. The yellow line comprises the region studied during the MEDOUT-11 experiment, with the inner bathymetry as collected during the cruise; outside this region, the bathymetry comes from the GTOPO (2013) and Zitellini et al. (2009) data. The principal morphological features are shown, with the axis of the main contourite channels shown as dashed white lines.

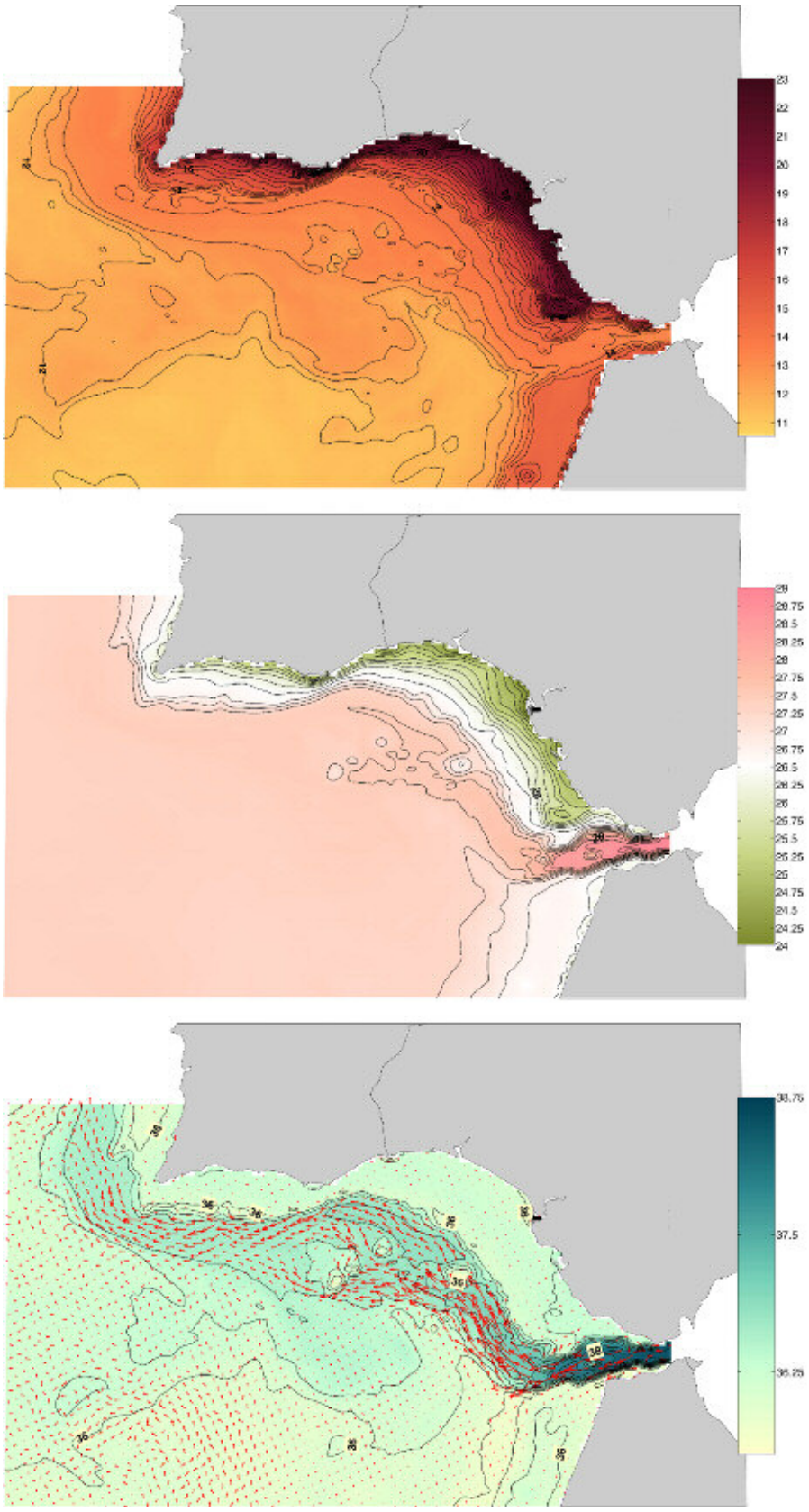

Fig. 4.3. (a) Property distributions at 800 m or the seafloor when shallower, for the far field. The results show the averaged IBI model outputs for the 1 June to 31 August 2016 period. Top panel: temperature (ºC). Middle panel: potential density anomaly (kg m^{-3}). Bottom panel: salinity (g kg^{-1}) and velocity (vectors).

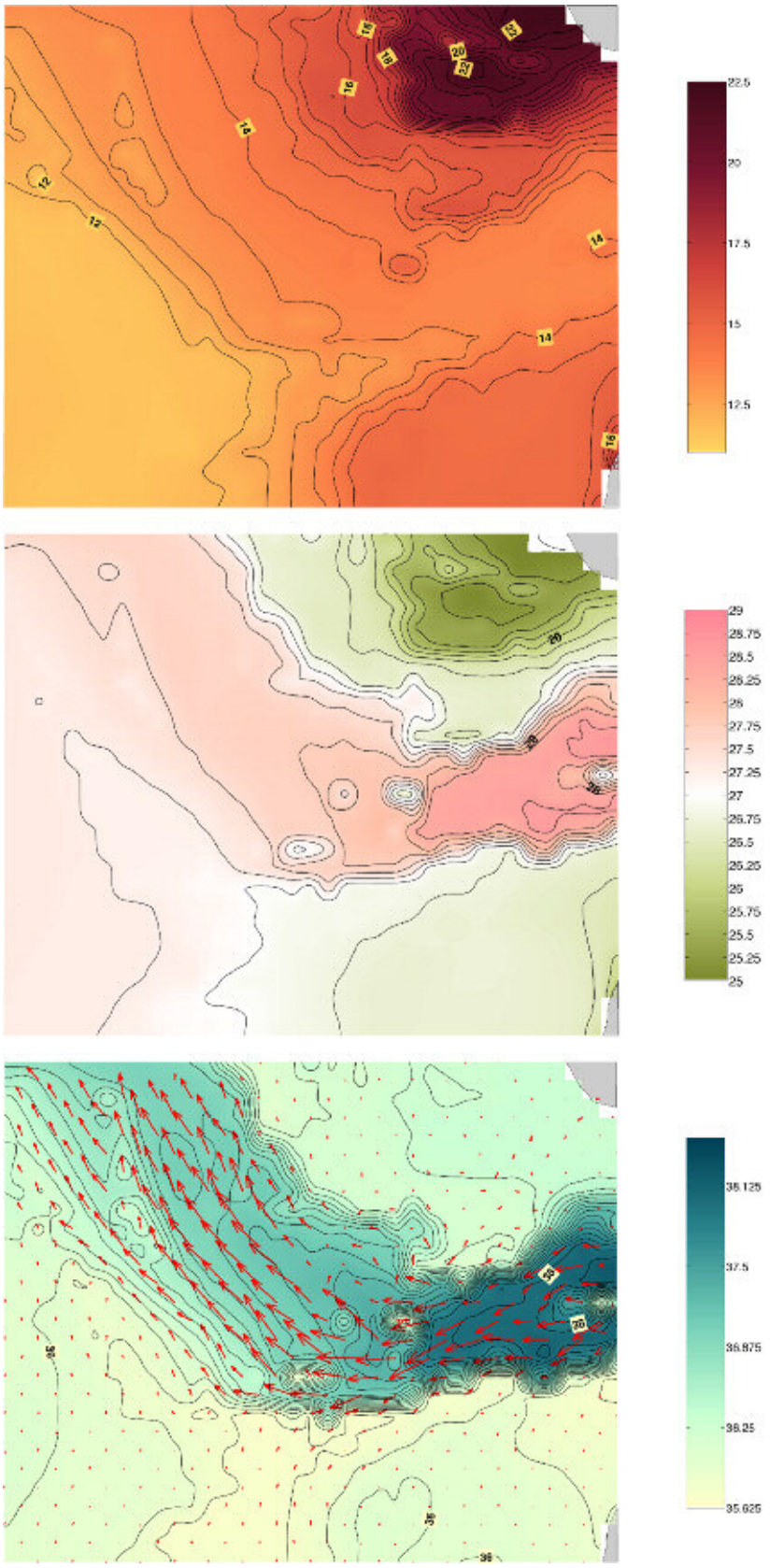

Fig. 4.3a. (continued): Property distributions at 800 m or the seafloor when shallower, for the near field. The results show the averaged IBI model outputs for the 1 June to 31 August 2016 period. Top panel: temperature (ºC). Middle panel: potential density anomaly (kg m^{-3}). Bottom panel: salinity (g kg^{-1}) and velocity (vectors).

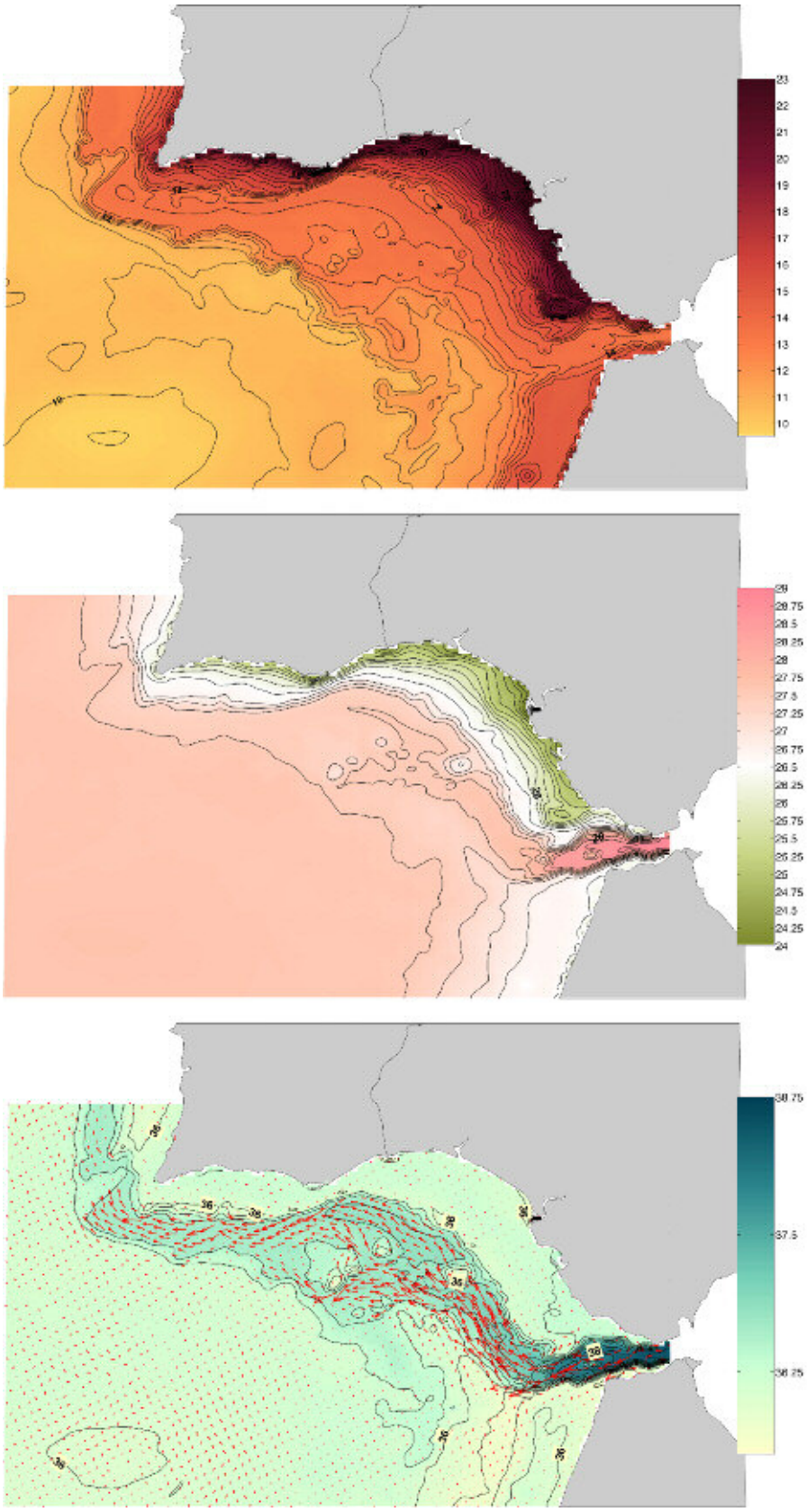

Fig. 4.3. (b) Property distributions at 1200 m or the seafloor when shallower, for the far field. The results show the averaged IBI model outputs for the 1 June to 31 August 2016 period. Top panel: temperature (ºC). Middle panel: potential density anomaly (kg m^{-3}). Bottom panel: salinity (g kg^{-1}) and velocity (vectors).

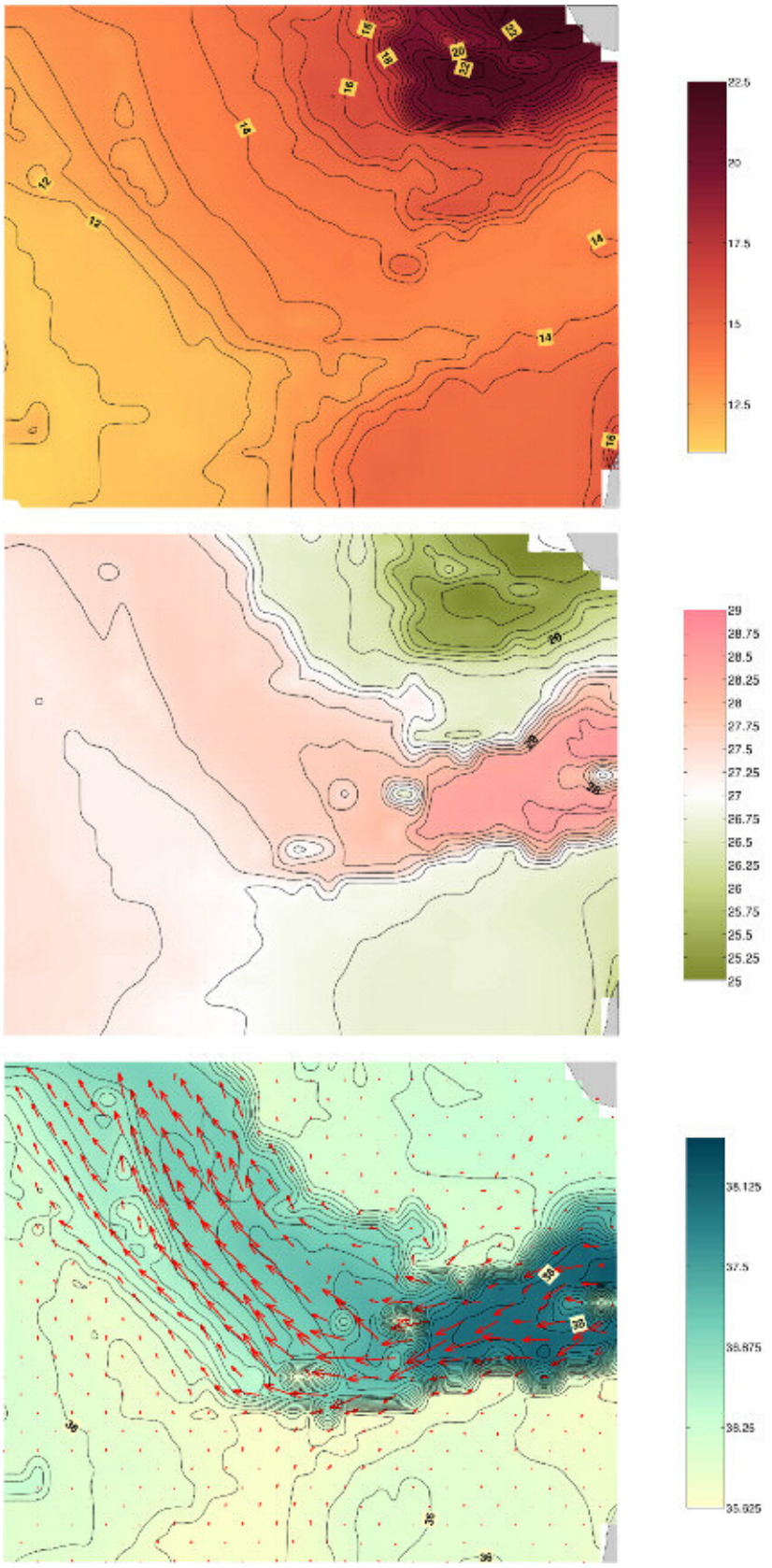

Fig. 4.3b. (continued): Property distributions at 1200 m or the seafloor when shallower, for the near field. The results show the averaged IBI model outputs for the 1 June to 31 August 2016 period. Top panel: temperature (ºC). Middle panel: potential density anomaly (kg m^{-3}). Bottom panel: salinity (g kg^{-1}) and velocity (vectors).

4.2.2 HYDROGRAPHY AND VELOCITY DATA

For the water-column analysis, we use four main sets of conductivity-temperature-depth (CTD) and/or velocity data. Three of these datasets are briefly described next, as they have been examined elsewhere: the 1988 Gulf of Cadiz Experiment (GCE) (Price et al., 1993; Baringer and Price, 1997a,b; Baringer and Price, 1999), the 1997–1999 CANIGO measurements (Ambar et al., 1999; Borenäs et al., 2002; Johnson et al., 2002), and the MEDOUT-09 cruise (Gasser et al., 2011; Nash et al., 2012). The fourth dataset corresponds to the MEDOUT-11 cruise, a yet unpub-lished experiment, which is described in detail at the end of this section. The CTD positions of all four datasets are shown in Fig. 4.5.

The GCE was completed in September 1988 on board the R/V Oceanus. It included a total of 98 CTD and 54 eXpandable Current Profilers (XCP), with every XCP approximately collocated to a CTD cast (Fig. 4a). The CTD-XCP stations were taken along the Strait of Gibraltar and 10 cross-slope sections (A to J) between Espartel Sill and off Cape São Vicente (9ºW).

The observations in the frame of the CANIGO (Canary Islands Azores Gibraltar Observation) project were carried out by the R/V Thalassa in September 1997 and by the R/V Coornide de Saavedra in January 1998 and February 1999. In this study we will use all available CTD data east of Cape Santa Maria, for a total of 238 stations (Fig. 4.5a); no velocity data comes from this dataset.

The MEDOUT-09 cruise was carried out in July 2009 onboard the R/V García del Cid. The region of study was west of Espartel Sill, approximately between 35º42’ and 35º54’N and between 6º15’ and 6º33’W, corresponding to an area of about 27 km x 22 km. Velocity data was continuously recorded during the entire cruise using an on-board Acoustic Doppler Current Profiler (ADCP) (Gasser et al., 2011) and was measured at the CTD stations with a Lowered ADCP (LADCP) system mounted to the rosette-CTD frame (Nash et al., 2012); the on-board ADCP data was used to constrain the LADCP solution. Fig. 4.5b shows the location of the 418 CTD and LADCP sta-tions; 27 were full-depth stations, taken along five sections approximately normal to the axis of the MOW, while most of the remaining stations sampled the lower part of the water column in a small region (6 km x 4 km) just downstream from West Espartel Sill.

Finally, a new dataset was gathered during the MEDOUT-11 experiment, from 12 to 25 July 2011 onboard the R/V García del Cid. The region of study was similar to the one sampled during MEDOUT-09 but with increased areal coverage (50 km 25 km rectangular domain shown in Fig. 4.2). During the first phase of the cruise, a total of nine zig-zag sections were carried out,

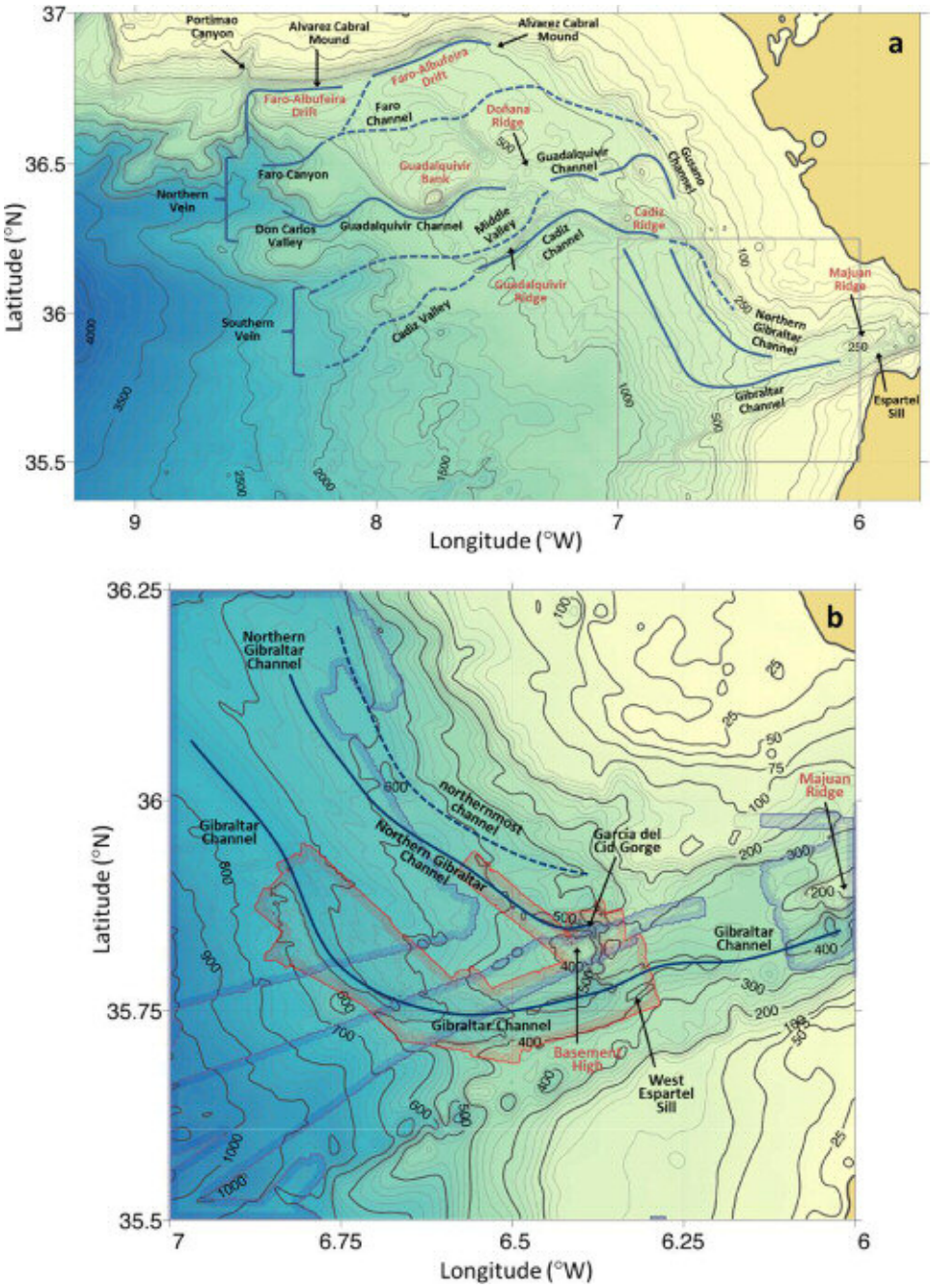

Fig. 4.4. (a) Bathymetry (m) of the far field plotted with 250-m resolution; the gray rectangle indicates the near-field region. (b) Bathymetry (m) of the near field plotted at 80-m resolution; the thin red and blue lines respectively indicate the area covered by the MEDOUT-11 and Zitellini et al. (2009) bathymetries, elsewhere the bathymetry data comes from GTOPO (2013). The principal morphological features and selected isobaths (m) are shown, with the axis of the main contourite channels as blue lines; the solid lines indicate those portions of channels reported in García et al. (2009) and Hernández-Molina et al. (2014a) that appear as current MOW pathways, while the dashed lines represent active connections revealed in this study.

crossing the axis of the MOW as determined from the previous MEDOUT-09 measurements; these sections represented 130 full-depth CTD stations. During the second phase of the cruise, additional along- and across-stream sections were carried out, some of them extending further north to cover the slope region, up to a total of 292 additional stations; most of these stations were in tow-yow mode over the outflow water, from about 100 m over the MOW to some 10 m above the seafloor (Fig. 4.5b). The CTD data was collected using a Seabird 911Plus System (pressure Seabird 9Plus, temperature Sea-bird 3Plus, conductivity Seabird 4Plus, oxygen Seabird 43Plus) with all sensors calibrated shortly before the cruise. Velocity data was continuously recorded throughout the cruise with a 75 kHz RDI on-board ADCP, with bottom-tracking enabled; unfortunately, due to bottom interference, the velocity data in the lowermost 50 m of the water column could not be recovered.

4.3. METHODS

4.3.1. MAP VIEWS AND PERSPECTIVE PLOTS

Throughout this paper we use the bathymetric data presented in last section to provide map views (Figs. 4.1–4.5) and thre-dimensional (3D) representations (Fig. 4.6) of the bottom topogra-phy, with an 80-m grid for the near field and a 250-m grid for the far field. We also present horizontal and perspective views of temperature and salinity (with the 2010 thermodynamic equation of seawater, TEOS-10) as well as of horizontal speed on top of these bathymetries.

By using the combined hydrography and velocity dataset we are implicitly accepting the MOW is stationary, a premise that deserves special consideration. Sammartino et al. (2015) estimated the MOW at Espartel Sill to change no more than ca. 5% with the tide; this result is consistent with the good fit between velocity outputs from a non-tidal model (Peliz et al., 2013) and observations in the eastern Gulf of Cadiz. Further, several authors have documented the flow at Espartel Sill to have relatively small variations at seasonal and inter-annual scales, ca. 8% and 5% respectively (García Lafuente et al., 2007; García-Lafuente et al., 2009; Sánchez-Román et al., 2009; Peliz et al., 2013), although it is recognized that larger changes may appear because of events such as the eastern and western Mediterranean transients (Peliz et al., 2013).

The major source of MOW variation is likely related to the warming and salinification of MW. According to Millot et al. (2006) and Fusco et al. (2008), during the last 50 years the MOW has warmed and salinificated at decadal rates of about 0.15 ºC and 0.03 g/kg. These rates are similar to those in a region west of the Gulf of Cadiz – defined as the North Atlantic MOW reservoir (Potter and Lozier, 2004) – and larger than the trends observed for the environment NACW (Levitus et al., 2000). However, Fusco et al. (2008) and Legg et al. (2009) have shown that the MOW product is quite insensitive to these changes, because the two factors com-pensate in density and the entrained transport largely exceeds the initial MOW output. Indeed, Bozec et al. (2011) have shown that most of the variations in the MOW reservoir respond to circulation changes within the North Atlantic rather than to changes in MOW characteristics.

Here we use data from one single dataset when showing vertical sections in 3D perspective plots and employ the entire dataset only for the horizontal representations. The vertical sections represent synoptic views of the water properties on top the bathymetry, with the MOW anomalies showing up independently of their tem-poral changes. The horizontal ensembles, on

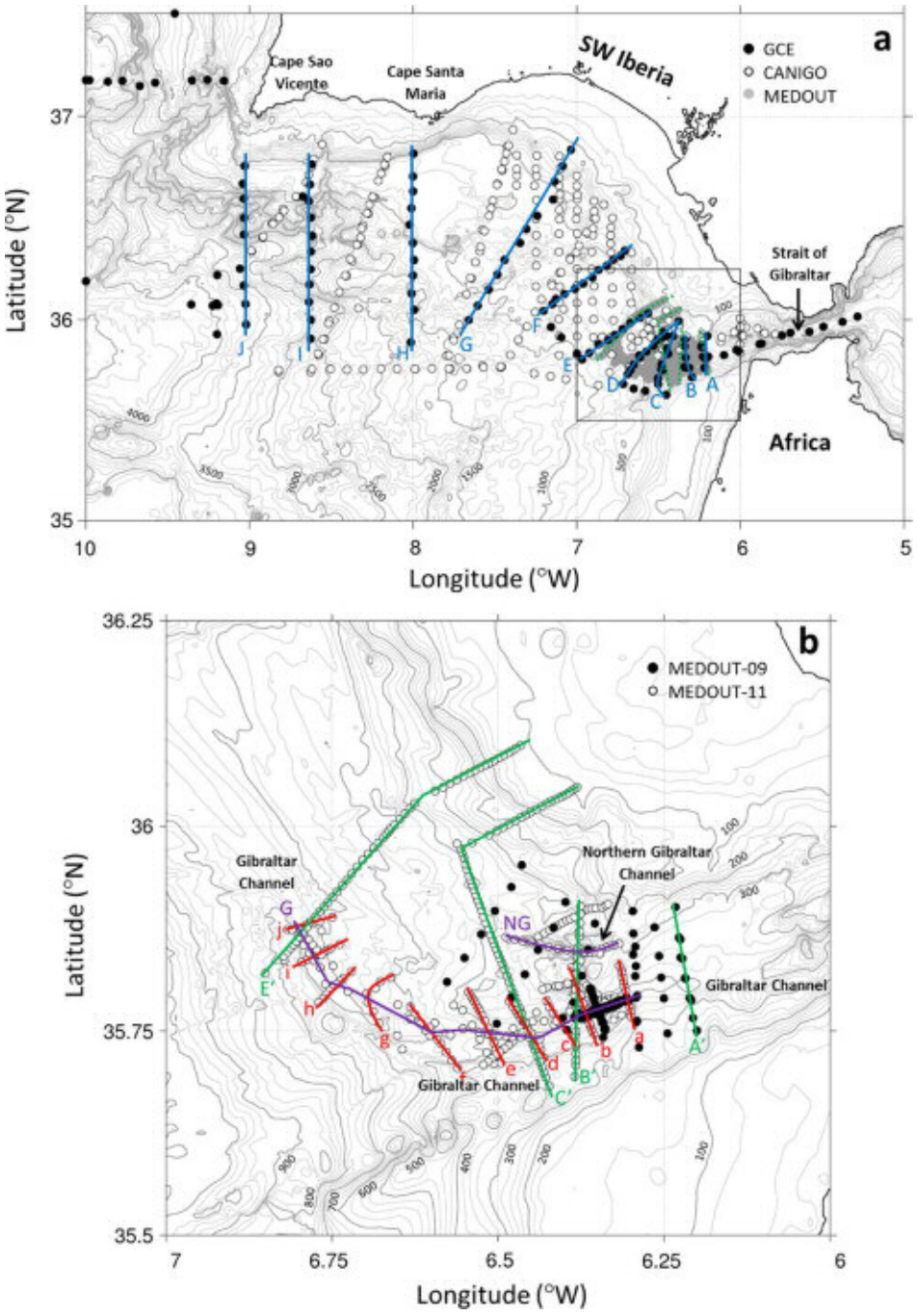

Fig. 4.5. Hydrographic stations and sections, the latter labeled as explained in the main text; the velocity sections are not shown as they are always close to a hydrographic section. (a) Far-field stations and sections during GCE (black circles), CANIGO (white circles), and both MEDOUT-09 and MEDOUT-11 (gray circles). (b) Near field stations and sections (labeled) during MEDOUT-09 (black circles) and MEDOUT-11 (white circles). Several principal morphological features are indicated and some selected isobaths are shown (m).

the other hand, may indeed be affected by the temporal variations, particularly near the Strait of Gibraltar; however, because the MOW anomaly near origin is much larger than the changes occurring over the 23 years of data (1988–2011), we anticipate that they will be good indicators of the predominant pathways for some prevailing mean steady state. Therefore, throughout this work we assume the MOW to be stationary, i.e. the outflow through Camarinal and Espartel Sills remains constant and unaffected by potential variations in either the source water or the open ocean, so that the velocity fields and property distributions characterize the streamlines over the eastern and central Gulf of Cadiz.

For the vertical sections we use the GCE, MEDOUT-09 and MEDOUT-11 cruises, as they have both hydrographic and velocity data. For the GCE dataset we follow the nomenclature in Baringer and Price (1997a), where 10 vertical sections are num-bered using capital letters, from A (closest to the Strait) to J (the farthest one) (Fig. 4.5a). We also use the MEDOUT-09 and MEDOUT-11 datasets to produce a total of 14 cross-stream and two along-stream sections in the near field (Fig. 4.5b). Four of these cross-stream sections are relatively long: sections A^0 and B^0 are similar to sections A and B; section C^0, located between sections C and D, and section E^0, very close to section E, are longer than their GCE counterparts as they extend into the continental shelf of the Iberian margin. The other 10 cross-stream sections, named a-j, are relatively short sections, cutting cross the Gibraltar Channel (Fig. 4.5b). Additionally, the high-density data allows us to draw two along-stream sections, approximately running along the Gibraltar and Northern Gibraltar Channels, respectively named G and NG (Fig. 4.5b).

4.3.2 UPPER AND LOWER MOW CORES

The horizontally gridded data can be used to identify the paths for the upper and lower MOW cores or branches during their transit over the middle slope and beyond. To position the path of the upper core, at each longitude we look for the location of the subsurface salinity maximum at depths between z_1 and z_2; likewise, to locate the lower core we simply search for the maximum salinity between z_2 and the seafloor. An upper boundary, z_1, is necessary to distinguish the upper MOW core from the high salinity surface NACW layers; this is particularly important as we move away from Espartel Sill and the MOW salinity-signal dilutes, becoming comparable with that of the surface NACW. The intermediate boundary, z_2, considers the vertical separation of the two cores, set after visual inspection of all individual vertical sections. After several trials we have selected a simple algorithm where we let z_1 and z_2 increase linearly with longitude: z_1 changes between 200 m near Espartel Sill and 400 m at 7ºW (remaining constant farther west) and z_2 changes between 500 m at 6º30'W and 800 m at 7º30'W (staying constant beyond).

4.3.3. MOW HYDROLOGICAL AVENUES

Under the approximation that the bottom currents are solely driven by gravity, we appraise the possible paths for the MOW with the help of a topographic analysis method, which is commonly used to draw the water tributaries in a drainage basin (Schwanghart and Kuhn, 2010). In this method, water spreads over land following the topographic gradients (weighted according to slope) and streams of different importance are identified. The extension of the method to the MOW is straightforward, with the bathymetric gradients driving the anomalous dense bottom waters. This tributary system represents the steady-state dense-water pathways – for steady state coinciding with streamlines – hereafter indistinctly named pathways, avenues or streams; we will continue using cores or branches to identify how these avenues are organized geographically and will refer to the neutrally buoyant cores as veins.

The paths of bottom dense water calculated with the topographic method completely ignore the Coriolis force. We may estimate its role by, first, equating the cross-stream Coriolis force to a cross-slope pressure gradient and, second, calculating the slope of the seafloor that would produce such a pressure gradient (4.6). For dense flow departing from the Strait of Gibraltar and running along the southwestern Iberian margin, this approach decreases the cross-slope bottom gradient and hence reinforces the contourite-type pathways.

The Coriolis-equivalent bottom slope is easily estimated for a two-layer ocean with the following approximations: (a) the anomalous dense water covers the bottom with a layer of constant thickness, (b) the sea surface remains flat, and (c) the lower layer flows along isobaths (Fig. 4.6). With these assumptions, the equivalent bottom slope is given by $dh/dx = -fv/g'$, where x refers to the cross-stream coordinate (taken to coincide with the cross-slope axis, with positive values in the up-slope direction), h is the sea-bottom depth, f is the Coriolis parameter, v is the along-stream velocity, and $g' = g\,(\delta\rho/\rho)$ is the reduced gravity, with $\delta\rho$ the water-density anomaly and ρ the environment water density. For our calculations we set $\delta\rho/\rho = 10^{-3}$ and use velocity values of 0.5 and 1.0 m/s, so that we get dh/dx ranging between 3.6×10^{-3} and 7.3×10^{-3}.

The slope calculated using the above procedure is mainly set to oppose the cross-slope bottom-depth gradient, effectively reducing the bottom slopes in the eastern and northern Gulf of Cadiz and hence favoring contourite-type flows. The procedure actually provides an upper limit estimate because the water usually does not flow along isobaths, i.e. the Coriolis force does not fully oppose the bottom depth gradient. Additionally, rather than using actual bottom velocities we employ characteristic values for the near and far fields. Despite these simplifications, the method retains in a simple way the two main forces driving the MOW – density-driven pressure

gradient and Coriolis force – and turns out to be very useful to identify plausible MOW pathways.

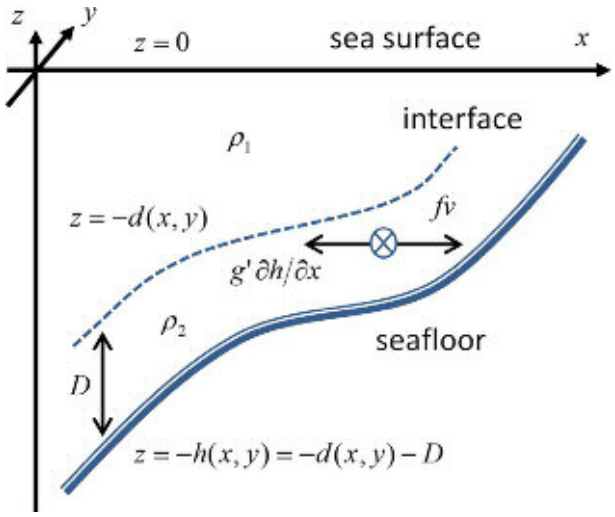

Fig. 4.6. Schematics of the force balance used to estimate the Coriolis-equivalent bottom slope, dh/dx.

4.4 THE MOW NEAR FIELD

4.4.1 DRAINAGE BASIN FOR THE NASCENT MOW

Hernández-Molina et al. (2014b) reported the existence of two channels west of Camarinal Sill – the southern and northern channels – that extend into the north-eastern Gulf of Cadiz along two upper-slope terraces. The southern channel is a deep valley that follows along the lowest of these terraces, constituting the natural extension of the Strait of Gibraltar, what Gasser et al. (2011) named the Gibraltar Valley or Channel (Fig. 4.2). The northern channel is less defined and runs along the upper terrace. According to Hernández-Molina et al. (2014a), this northern channel is the same one found north of Majuan Ridge, centred at about (35º53'N, 6ºW), although the channel appears discontinuous in their charts. In the following analysis we refer to this northern channel, at latitudes west of (35º51'N, 6.22^{0}W), as the North Gibraltar Channel (Fig. 4.2).

After surpassing Camarinal Sill (290 m), the Gibraltar Channel follows W-SW with a general U-shape and moderate slope until it encounters Espartel Sill (360 m), located immediately to the south of Majuan Ridge. Between Espartel and West Espartel (420 m) Sills, the Gibraltar Channel transits through a relatively large basin (40 20 km and depths of 350–400 m), with water depths gently increasing from 360 to 420 m in 40 km. Immediately downstream of West Espartel Sill, at (32º47'N, 6º20'W), the valley narrows due to the presence of a basement high that blocks its northern half (Hernández-Molina et al., 2014a) and the depth increases abruptly, from 420 to 550 m in a distance of about 1 km, nearly resembling a V-shaped waterfall (et al., 2011; Nash et al., 2012) (Fig. 4.2). Just after this waterfall, there is a depth maximum (580 m) that coincides with a narrow gorge that runs northwards, crossing the basement high until depths as shallow as 250 m, where it continues westwards in what constitutes the North Gibraltar Channel (Fig. 4.2). We will refer to this northward gorge as the García del Cid Gorge, as it was first reported from data collected during the MEDOUT-09 experiment onboard the R/V García del Cid (Gasser et al., 2011). In the next subsection we will see that most of the MOW follows the Gibraltar Channel although some spills northwards through the García del Cid Gorge to later continue westwards along the North Gibraltar Channel.

Between 6^{0}28'W and 6º37'W, the Gibraltar Valley is again relatively wide (ca. 10 km) and deepens smoothly (from 500 to 600 m); at 6º37'W the axis of the valley starts turning NW, now as a 4-km wide and 50-m deep U-shaped waterway along the SW Iberian continental slope (Fig. 4.2). Between West Espartel Sill and 6º51'W, in a distance slightly over 30 km, the axis of the Gibraltar Channel has deepened from about 420 to 750 m (Fig. 4.2). During this stretch,

asides the abrupt plunging immediately downstream of West Espartel Sill, there are other locations where the channel's depth increases substantially and, therefore, the MOW is prone to experience significant accelerations. It is plausible that each of these sites may be undergoing an upslope retrogradation of the seafloor profile, resembling the processes that led to the opening of the Strait of Gibraltar about 5.33 Ma ago (e.g. Blanc, 2002; Loget and Van Den Driessche, 2006).

A 3D view identifies the Gibraltar Valley as the main MOW path and also illustrates the existence of the relatively wide basin located immediately downstream of West Espartel Sill, which is connected north to the Iberian shelf through the García del Cid Gorge (4.7b). It also hints at the existence of a shallow avenue that runs parallel to the shelf edge, the North Gibraltar Channel, deepening from about 250 m (north of West Espartel Sill) to some 550 m over a distance of about 50 km.

The MOW hydrological avenues reveal the seafloor drainage pattern, becoming a useful tool to identify the preferential pathways of dense water in the near field (4.8). As explained in Section 4.3.3, the underlying assumption is that the bottom flow is solely driven by the seafloor relief; for our calculations we have used the unaltered gridded bathymetry as well as several modified bathymetries that incorporate the effect of the Coriolis force for different bottom velocities (Fig. 4.8). The major MOW avenue corresponds to the Gibraltar Channel, always clearly visible west of 6º30W. The connection with the Strait of Gibraltar is apparently lost east of 6ºW, because of sills and basins within the channel that locally change the sign of the seafloor slope. For zero bottom velocity (Fig. 4.8a), i.e. without the Coriolis force, the MOW avenue continues along the Gibraltar Channel fed by tributaries that run across the continental slope into this channel. In particular, there are two pathways which start very close to the North Gibraltar Channel, at the latitude of the northern mouth of the García del Cid Gorge – the northernless following the North Gibraltar Channel (35º51'N, 6º22'W) and the northernmost along a shallower channel (35º55'W, 6º24'W) (Fig. 4.2) – and eventually end into the Gibraltar Channel at about 6.48^0W (4.4c and 4.8c).

For intense but realistic bottom velocities (0.5 and 1.0 m/s), the simulated MOW pathways show two remarkable modifications (4.8b,c). First, immediately downstream of West Espartel Sill, the flow gets diverted northwards into the García del Cid Gorge and connects to the North Gibraltar Channel (Fig. 4.4b), as also endorsed by the salinity fields (next subsection); notice also the rupture of the pathway along the Gibraltar Channel near 6º30'W, suggesting that momentum advection is here possibly more important than the slope-induced pressure gradient. The second important change refers to the two MOW avenues starting near the northern mouth of

the García del Cid Gorge. For a bottom water velocity of 0.5 m/s these northern pathways become significantly modified, with the northernless path following the Northern Gibraltar Channel during nearly 50 km and combining with the northernmost path before joining the Gibraltar Channel beyond 36ºN (Figs. 4.2, 4.4b, 4.8b). If we raise the bottom velocity to 1 m/s, the northern end of the García del Cid Gorge and the channel immedi-ately to the north become the starting points of two distinct pathways running approximately parallel to the Gibraltar Channel (Figs. 4.2, 4.4b, 4.8c). The northernless pathway follows the Northern Gibraltar Channel, slowly crossing the isobaths (500 to 800 m) and ending in the northwestern end of the near field, at (36º20'N, 7ºW). The northernmost path goes along the base of the upper slope, crossing the isobaths even more slowly (500 to 700 m) (Figs. 4.2, 4.4b, 4.8c). Notice that these two northern pathways get very close to each other at (36ºN, 6º40'W) (4.8c), corresponding to a location where the Northern Gibraltar Channel is poorly defined – see Fig. 1 in Hernández-Molina et al. (2014a).

4.4.2 TEMPERATURE, SALINITY AND VELOCITY FIELDS

The relatively high temperature and, particularly, high salinity of the MOW allows tracking its trajectory. The temperature-salinity diagrams illustrate the mixing between the MW type, characterized by salinity of 38.5 g/kg and temperature of 12.8 ºC, and the NACW, characterized by temperatures and salinities decreasing almost linearly with depth (4.9). East from West Espartel Sill, where the water depth is about 400 m, a straight line joins the MW type (occupying the 350–400 m range) and the NACW immediately on top of the MOW wedge, at depths of about 300 m and with salinity and temperature values of (36.4 g/kg, 15.5 ºC). On its westward motion, the MOW progressively sinks so that this water mixture starts combining with NACW found at greater depths, drawing a characteristic asymmetric V-type curve that progressively reaches towards lower temperatures and salinities (Fig. 4.9). These diagrams could be carefully analyzed to provide additional information on the transformations experienced by the MW, as well as on the mechanisms that lead to these changes, but this is not the objective of our study. Instead, here we use the warm and salty signature of the MOW to identify its predominant paths – first travelling along the seafloor and below the NACW and later leaning on the continental slope or following an open ocean path, partly or entirely embedded in NADW.

To illustrate the MOW propagating over the seafloor, we present several sets of perspective plots, where vertical sections of temperature, salinity and speed are drawn on top of the seafloor topography. Since our objective is to stress the MOW signature, we plot absolute speed, i.e. the module of the velocity vector, but use a color code to emphasize the change in

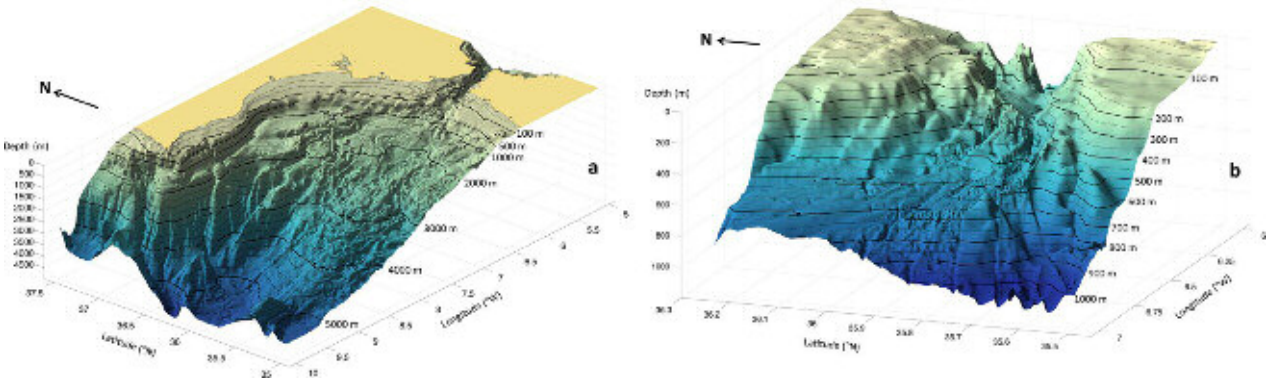

Fig. 4.7. Three-dimensional view of (a) the far field, plotted at 250-m resolution, and (b) the near field, plotted at 80 m resolution.

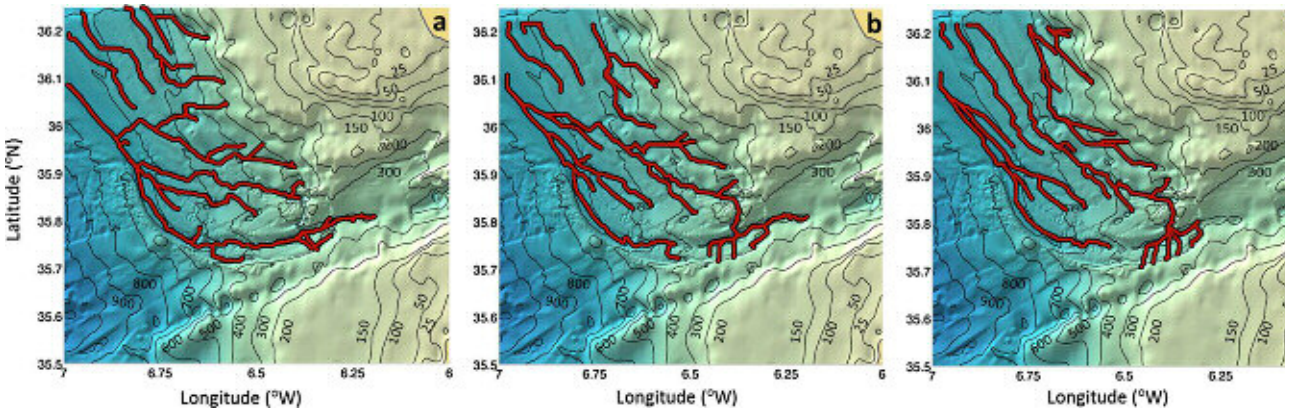

Fig. 4.8. MOW avenues for the near field, obtained using (a) the original bottom topography and (b and c) the modified bottom topography for along-slope velocities of 0.5 and 1.0 m/s, respectively. Several selected isobaths are shown (m).

direction between the westward flowing MOW and the eastward flowing NACW. In these plots the topography is drawn using either 80 m (near field) or 250 m (far field) grid-size resolution. The vertical sections corre-spond to individual realizations during different field experiments (Fig. 4.5), as explained in Section 2.2. The MOW signature is best observed through the salinity distribution, yet it also shows up well in the temperature and speed fields.

The first two sets of plots display sections A^0, B^0, C^0 and E^0 (Figs. 4.5b and 4.10) and sections A-E (Figs. 4.5a and 4.11), across the near field channels (the domains for Figs. 4.10 and 4.11 are very similar, only slightly larger in 4.11). The plots show the course of the MOW, first westwards and later turning clockwise to the N-NW. Section B^0, which runs along the García del Cid Gorge, reflects the northward propagation of salty MOW along this canyon. Sections C^0, D, E^0 and E show the signature of salty-warm MOW water, ending sharply on the offshore side of

the Gibraltar Channel but spreading out upslope, with the main stream located on top the Gibraltar Channel and a secondary one over the Northern Gibraltar Channel. The next set of plots corresponds to cross-stream sections crossing the width of the Gibraltar Valley: sections a-e (Figs. 4.5b and 4.12) and sections f-j (Figs. 4.5b and 4.13). Fairly undiluted MOW – for all sections with maximum salinities in excess of 37.5 g/kg – flows along the seafloor with a typically thickness of 50–70 m. As the U-channel veers north-westwards, the high-salinity MOW remains inside, overlaid by a 150-m thick intermediate layer of diluted characteristics (salinities between 36.5 and 37.5 g/kg); this intermediate layer is thicker than the valley's depth, initially overflowing to both margins and, after the MOW's clockwise veering, spilling only towards the northern margin. During its westward motion past West Espartel Sill and posterior northward heading, the along-stream speed of the MOW remains fairly close to 1 m/s.

The drainage avenues (Fig. 4.8) and perspective plots (Figs. 4.10 – 4.13) show how the MOW changes its propagation from SW to NW over distances of about 30–40 km. For a flow with speed 1 m/s this represents a turn in 8–11 h or about half an inertial period (20.5 h) – rather than the expected one-quarter period if the veer-ing was inertial – confirming that the northward turn is topographically induced and has nothing to do with inertial motions.

The final set of plots corresponds to along-stream sections designed to follow the Gibraltar and North Gibraltar Channels (Figs. 4.5b and 4.14). The sections along both channels exhibit the salty-warm-westward MOW bottom signature. The signature is most intense along the Gibraltar Channel, displaying flow acceleration and large interfacial undulations downstream of those locations where the bottom depth increases rapidly (Gasser et al., 2011; Nash et al., 2012). These locations resemble hydraulic control points where the outflow shifts from subcritical into supercritical, with profound topographic scours downstream of the depth change that suggest the existence of remounting erosion. These instabilities have the potential of producing a transitional layer ca. 150 m thick, where the salinity decreases from maximum bottom values to the minimum concentrations that characterize the deepest undisturbed NACW (Fig. 4.9)

4.5 THE MOW FAR FIELD

4.5.1 CHANNELS NETWORK IN THE CONTINENTAL MIDDLE SLOPE

The eastern and northeastern margins of the Gulf of Cadiz are characterized by an abrupt upper slope that reaches down to 500 m followed by a gentle middle slope that stretches westwards until about 7º30'W at latitudes ca. 36ºW (down to 1200 m) and 8ºW at latitudes ca. 36º30'N (down to 750 m) (Fig. 4.4a). Further west the slope becomes quite abrupt, so that at 8º30'W the seafloor is at about 2500 m.

The eastern upper slope has numerous along-slope avenues, the most prominent one positioned at its base, and a few cross-slope (often disconnected) channels and valleys, all them located east of 6º48'W – within 100 km of the clockwise veering of the Gibraltar Channel. The eastern middle slope, in contrast, is characterized by many more cross-slope contourite channels and erosive valleys, oriented zonally and relatively deep (Hernández-Molina et al., 2006; García et al., 2009). At the western end of the middle slope, at longitudes between 7º30' and 8º30'W, we find again major zonal canyons along ca. 36º10', 36º25' and 36º40'N.

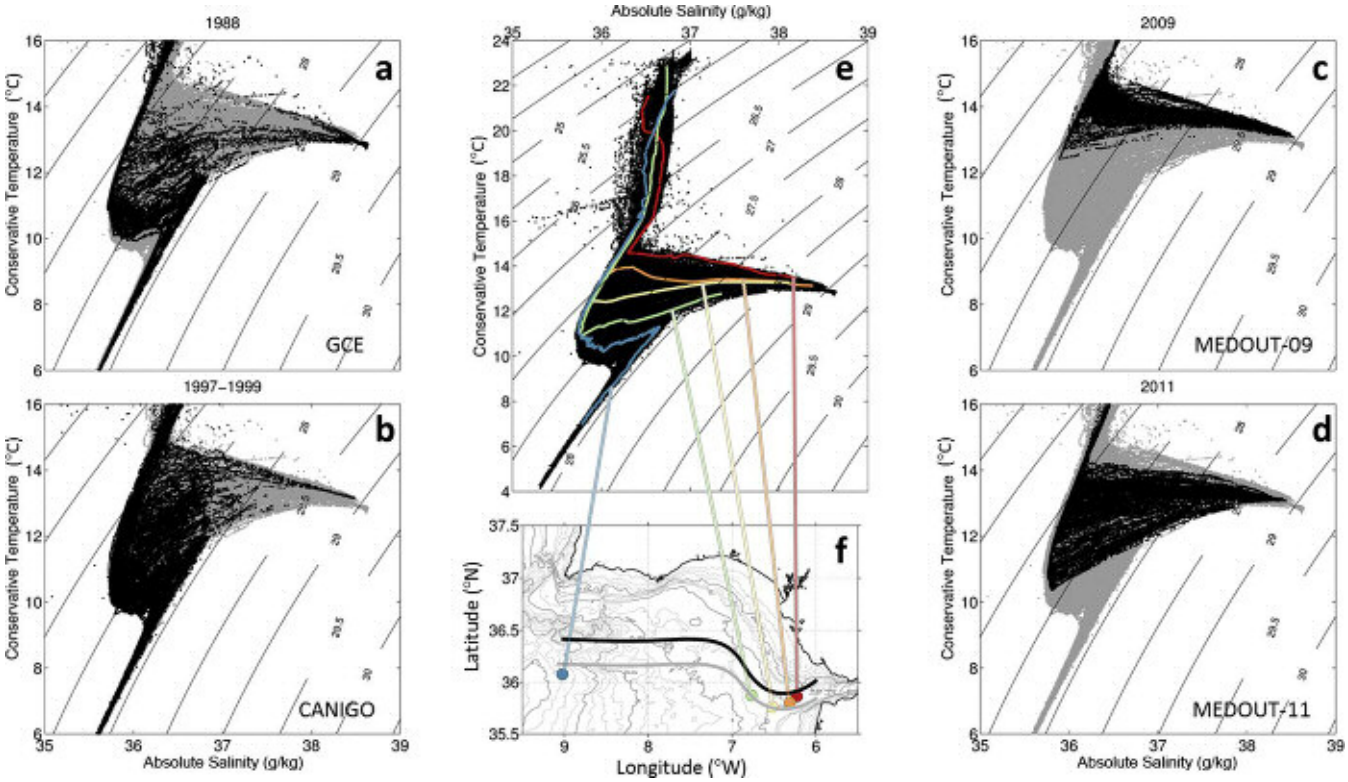

Fig. 4.9. Temperature-salinity diagrams for each individual dataset (temperature in LC and salinity in g/kg): (a) GCE, (b) CANIGO, (c) MEDOUT-09 and (d) MEDOUT-11; panel shows the diagram for all datasets together with five selected individual profiles that are positioned in panel (f), together with sketch lines for the northern and southern MOW cores

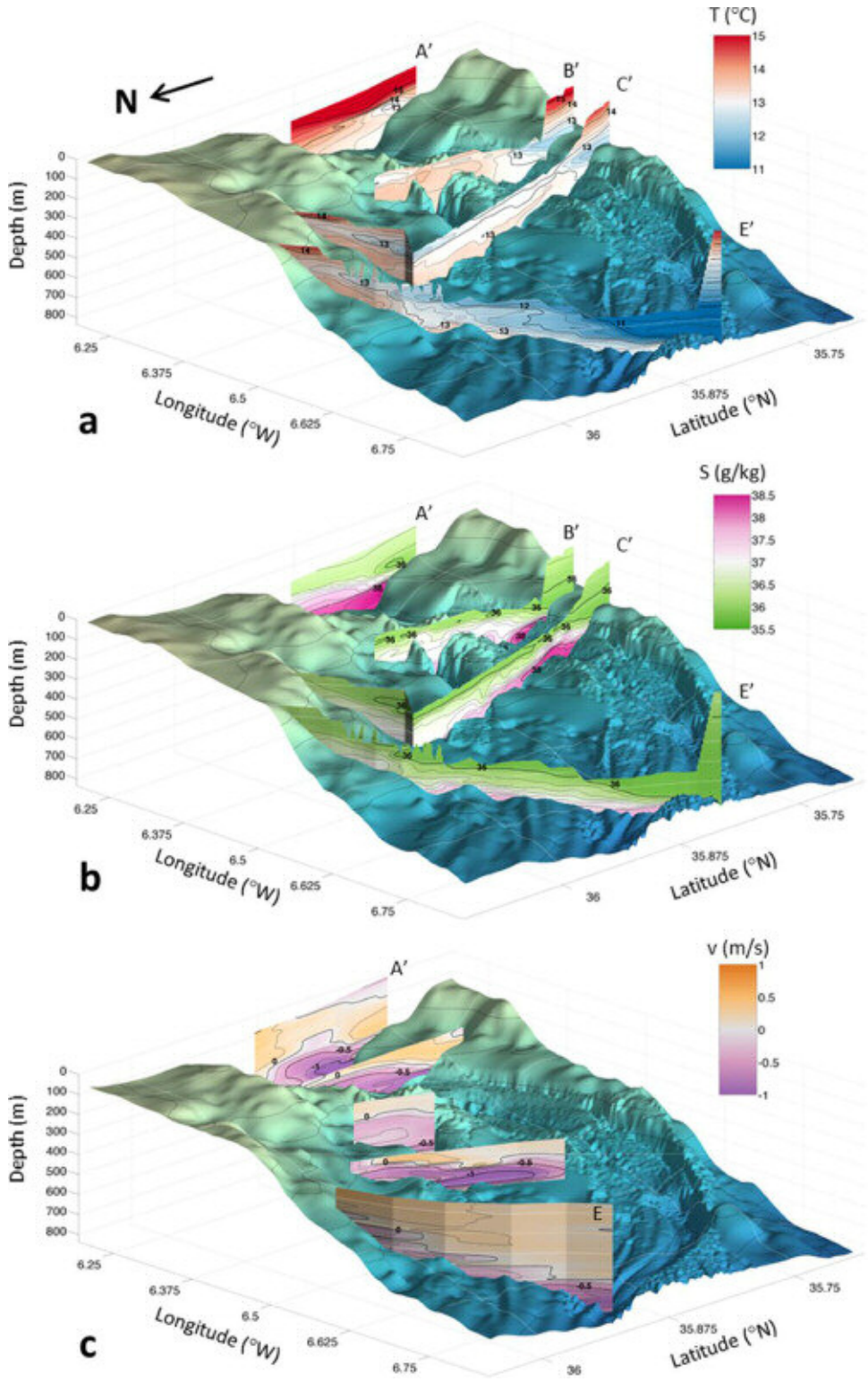

Fig. 4.10. (a) Temperature (ºC), (b) salinity (g/kg) and (c) speed (m/s) cross-stream sections in the near field. The hydrography comes from MEDOUT-11 (sections A^0, B^0 , C^0 and E^0 in Fig. 4b) while the speed fields are from MEDOUT-09 (black circles in Fig. 4.5b) except section E that comes from GCE (Fig. 4.5a); positive/negative speeds correspond to eastward/westward flows. Notice that most of the hydrographic stations do not sample the entire water column, approximately running from 100 m above the MOW to the seafloor.

The easternmost meridional canyon is Portimao Canyon (8º30'W), of tectonic origin (Lopes et al., 2006).

A 3D view of the northern Gulf of Cadiz helps visualize the relation between the set of near-parallel contour avenues found immediately NW of the near field and the numerous cross-slope channels and valleys along 7ºW, between 35º40' and 36º50'N (Fig. 4.7a). The contour avenues generally follow the isobaths between 600 and 1200 m, with a relatively small downslope component, until they find the V-shaped cross-slope valleys. The high-resolution bathymetry endorses the idea that contour channels and erosive valleys probably reflect different MOW paths, changing over time scales spanning the glacial-interglacial cycles and longer (Llave et al., 2006, 2007, 2011). These scours may possibly be linked to slope instability following tectonic activity, as proposed by Hernández-Molina et al. (2014b), but it is likely that they are reinforced through events of margin instability caused by the erosive power of the time-changing path of the MOW. In agreement with Mulder et al. (2003) and García et al. (2009), these changes would take place following variations in sea surface level and MW characteristics.

The far-field MOW hydrological avenues provide a complementary perspective of the channel network (Fig. 4.15). It is remarkable the way the network of streams connects the upper-slope contour avenues and the zonal cross-slope contourite channels and erosive valleys in the eastern Gulf of Cadiz, the precise connections depending on the speed of the flow (Fig. 4.15), getting to cover most of the middle-slope plateau. A comparison of this hydrological-like system with the detailed physiographic description in Hernández-Molina et al. (2006) and García et al. (2009) helps identify the most relevant bottom structures.

One relevant feature are the avenues that run along the base of most of the upper slope, alike to the Northern Gibraltar Channel in the near field; the contour-like character of these upper-slope north-eastern and northern avenues shows up when taking into consideration the Coriolis force (Fig. 4.15b,c). The avenues appear disconnected from each other but the separation between them is generally small, suggesting that water with intermediate characteristics, riding on top of the less diluted bottom MOW water, could likely link the different branches. In the northern Gulf, the along-slope avenue corresponds to the Alvarez Cabral contourite Moat, following the outer limit of the upper slope (depths of 600–700 m) and delimited offshore by the Faro-Albufeira Mounded Drift (García et al., 2009).

Taking into consideration the distribution of avenues in the western edge of the plateau, we identify two principal middle-slope MOW branches: southern and northern, respectively reach-

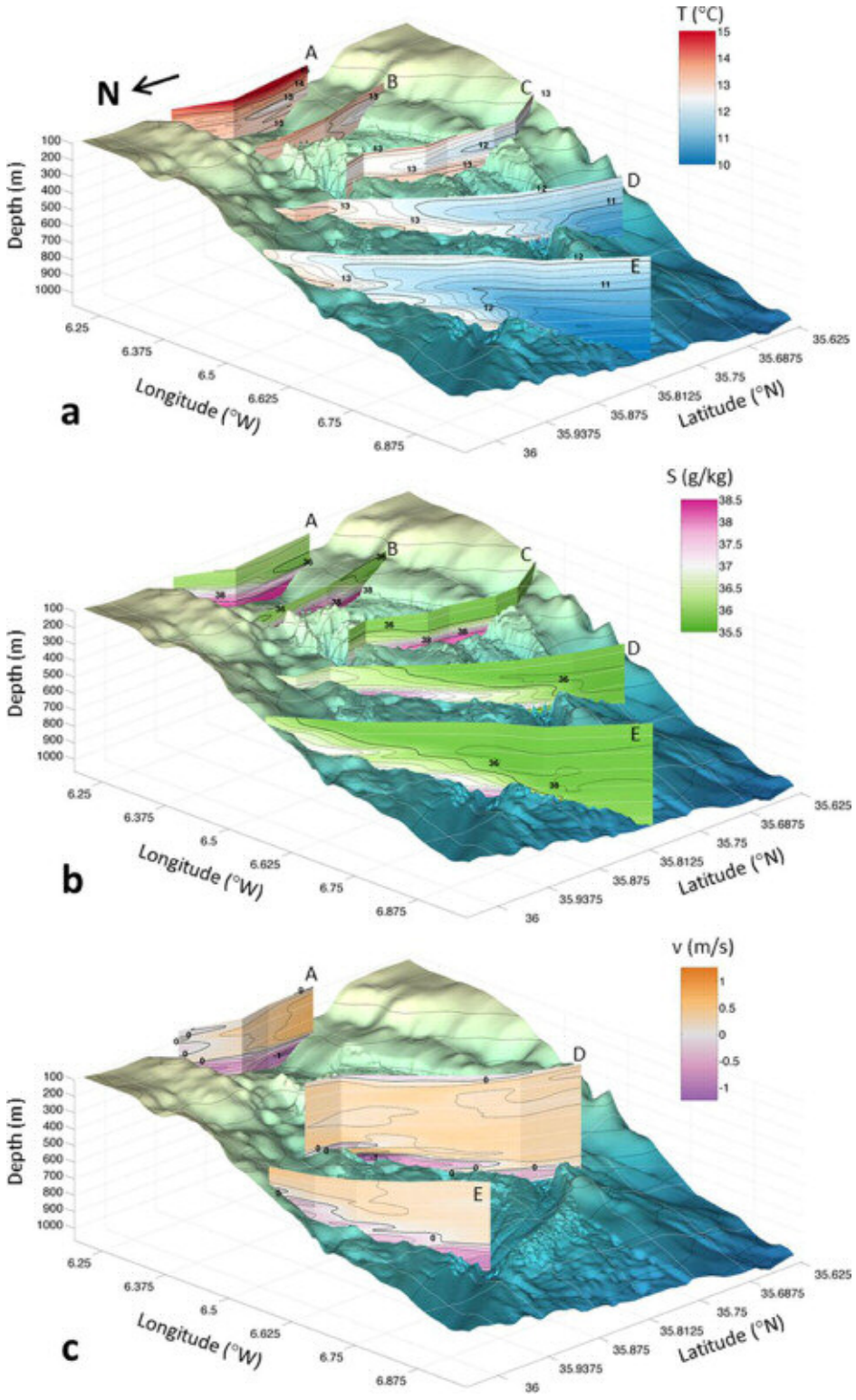

Fig. 4.11. (a) Temperature (ºC), (b) salinity (g/kg) and (c) speed (m/s) cross-stream sections in the near field. All data come from GCE: sections A, B, C, D and E for the hydrography and sections A, D and E for the water speed (labeled in Fig. 4.5b); positive/negative speeds correspond to eastward/westward flows. The original stations run all the way from the sea surface down to the sea bottom although in most instances the upper portion of the water column is removed to ease their representation.

ing the edge of the plateau at latitudes less and more than 36º15'N. Each of these branches consists in a set of channels and valleys, most of them identified by Hernández-Molina et al. (2006) and García et al. (2009). Generally speaking, these authors (see also Hernández-Molina et al., 2014b) point at a prevailing north-westward MOW over the middle-slope plateau. However, in many instances, the flow is connected not along one single channel or valley but interconnected between several of them, leading to net westward and even south-westward MOW transport.

Consider first the southern MOW branch. The southernmost contribution corresponds to the avenue that reaches the edge of the plateau at 36º5'N. It starts as an erosive channel ca. 36º15'N, at the base of the upper slope, which diverts westwards both the Gibraltar and Northern Gibraltar contourite Channels. This channel is precisely the rather wide Cadiz Channel, that runs immediately south of the Cadiz (7ºW) and Guadalquivir (7º20'W) diapiric Ridges (Figs. 4.4a and 4.15); as pointed out by García et al. (2009), these two ridges play a key role diverting the flow westwards, which then naturally results in an erosive valley. However, the actual pathway coincides with the Cadiz Channel only until (7º30'W, 36º5'N); from this point on, it continues south-westwards along what we have named the Cadiz Valley, directly towards the edge of the middle-slope (Figs. 4.4a and 4.15).

Further north, but still contributing to the southern branch, we find another erosive channel starting at about 36º25'N (Figs. 4.4a and 4.15). It begins as the Gusano Channel and continues first westwards as the Guadalquivir Channel (but only shortly, until about 7º30'W) and later south-westwards, limited now to the south by the same Cadiz and Guadalquivir Ridges – what García et al. (2009) identified as a marginal valley, hereafter the Middle Valley; after overpassing the Guadalquivir Ridge, the Middle Valley turns westwards, probably following the same westernmost path of the Cadiz Channel (García et al., 2009) (Fig. 4.4a). The Gusano part is barely visible for the cases of zero or weak Coriolis forces (Fig. 4.15a,b) but shows up when considering swift bottom flows (Fig. 4.15c): for non-Coriolis force, the Gusano Channel connects to the along-slope adjacent contourite channel while for moderate and fast flows the along-slope contourite channels get reinforced. For brevity, hereafter we will identify this complex pathway – which includes the Gusano Channel, Guadalquivir Channel and Middle Valley –simply as the Middle Channel (Fig. 4.4a).

Moving to the northern branch, there are two main contributions. Along 36º25'N and ca. 7º40'W, we find another channel that runs westwards, starting southwest of the Doñana diapiric Ridge and continuing south of the Guadalquivir Bank as the Guadalquivir Channel and then, between

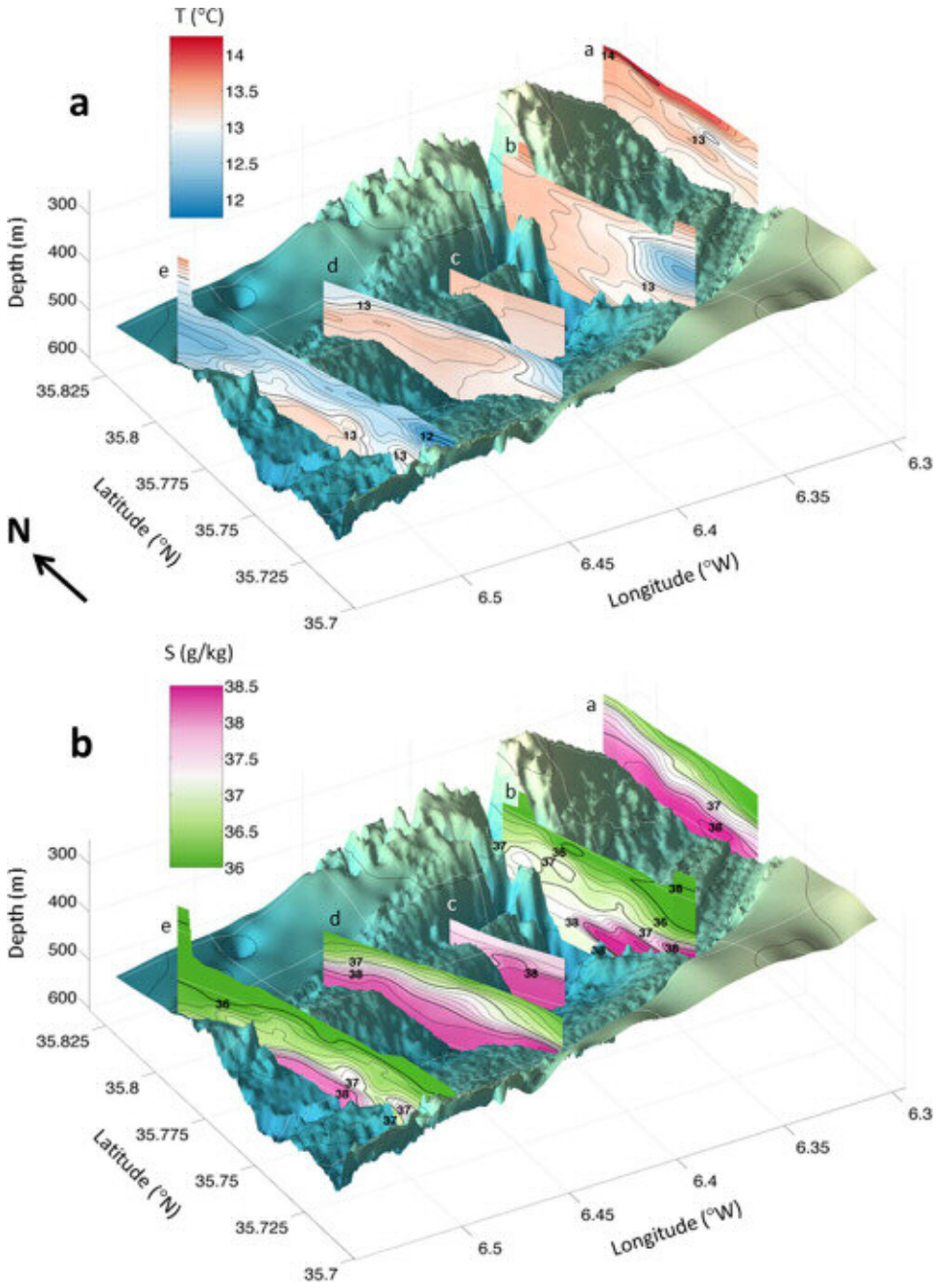

Fig. 4.12. (a) Temperature (ºC) and (b) salinity (g/kg) cross-stream sections in the eastern Gibraltar Channel. All data come from MEDOUT-11, with sections a, b, c, d and e labeled in Fig. 4b. Notice that most of the hydrographic stations do not sample the entire water column, approximately running from 100 m above the MOW to the seafloor.

the Portimao and Albufera Highs, into the Don Carlos Valley (García et al., 2009) (Figs. 4.4a and 4.15). Further north, we encounter one last channel that begins at the contourite mount along the north-eastern corner, at 36º35'N. This long channel – hereafter the Faro Channel – runs some 150 km separated from the upper slope, with a tributary that feeds from the Alvarez Cabral Moat ca. 8ºW, and discharges into the Faro Canyon (ca. 36º35'N) at the western edge of

the middle-slope plateau (García et al., 2009) (Figs. 4.4a and 4.15). Afterwards it joins with the Portimao Canyon from the north and the Don Carlos Valley from the south.

It is remarkable that all avenues start from eastern along-slope contourite moats and cross the middle slope plateau following zonal erosive contourite valleys, delimited by diapiric ridges and banks, until draining into canyons that connect to the deep ocean. We will see next that the MOW, after leaving the middle-slope plateau, finds an equilibrium depth between 800 and 1300 m; this implies that the avenues in the lower slope and continental rise (Fig. 4.15) do not constitute pathways for the actual MOW. Nevertheless, they raise the possibility that some of these deep canyons may have originated through slope instability, perhaps related to the cross-slope channelling of the MOW.

4.5.2. TEMPERATURE, SALINITY AND VELOCITY FIELDS

Moving from the near to the far field, we now provide two sets of perspective plots, respectively with two and three cross-slope sections of temperature, salinity and speed drawn on top of the seafloor topography. The first set has sections F and G, located in the north-eastern slope of the Gulf of Cadiz, which represent a continuation of the near field sections (Fig. 4.5a). Section F, located some 30 km downstream from sections E or E^0, reinforces the view of a main MOW path along the Gibraltar Channel, where the salin-ity still reaches values in excess of 37.5 g/kg, and a secondary path along the North Gibraltar Channel, where the maximum salinity is about 37.0 g/kg; in this section the Gibraltar Channel is found ca. 600 m while the Northern Gibraltar Channel is found at the base of the upper slope, ca. 450 m. The single velocity section in Fig. 4.16 approximately coincides with section F and illustrates two separated, but nearby, cores with westward velocities.

There is a prominent change in the character of the temperature and salinity fields between sections F and G (Fig. 4.16). The MOW cores are found close together in section F but stretch over a long cross-slope distance in section G: relatively high temperature and salinity values are still found at the base of the upper slope but the maximum values are located much deeper (ca. 800 m). Remarkably, this change takes place immediately west of a major feature detected by the hydrological avenues, as ca. 36º15N the course of the Gibraltar Channel is drastically interrupted by the Cadiz contourite Channel (Figs. 4.4a and 4.15). The maximum bottom salinities in section G are found along the axis of this channel but relatively high values now stretch all the way until the base of the upper slope, covering the entire middle plateau (Fig. 4.16b). In Fig. 4.17 we present the last set of plots, with sections H, I and J running normal to

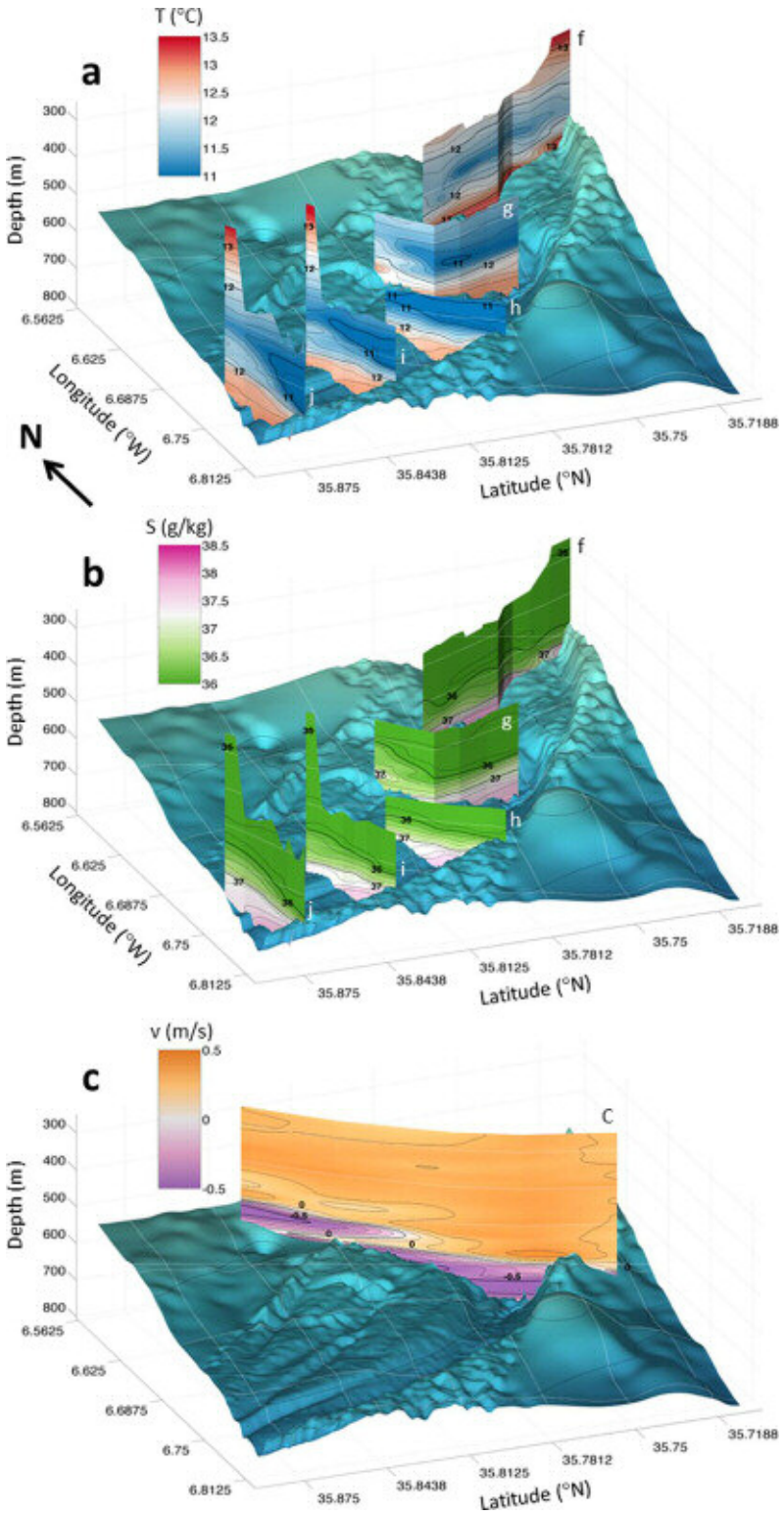

Fig. 4.13. (a) Temperature (ºC), (b) salinity (g/kg) and (c) speed (m/s) cross-stream sections in the western Gibraltar Channel. The hydrography comes from MEDOUT-11 (sections f, g, h, i and j in Fig. 4.5b) and the speed fields comes from MEDOUT-09 (section C in Fig. 4.5a); positive/negative speeds correspond to eastward/westward flows. Notice that most of the hydrographic stations do not sample the entire water column, approximately running from 100 m above the MOW to the seafloor.

the northern coast of the Gulf of Cadiz. The property fields in section H (along 8ºW) appear as the natural continuation of section G, with high salinity and temperature bottom values stretching some 70 km over the entire middle slope: from a shallow core (ca. 600 m) flowing along the Alvarez Cabral contourite Mount at the base of the upper slope to three deep cores (ca. 750, 1100 and 1300 m) that are approximately collocated with the Faro (ca. 36º35'N), Guadalquivir (ca. 36º25'N), and Cadiz and Middle (ca. 36º10'–36º20'N) Channels (Figs. 3a and 14). In section H we find, for the first time, a tongue of salty and warm waters detaching from the seafloor: it corresponds to the southern and deepest core, approximately on top the westward extension of the Cadiz and Middle Channels (Fig. 4.4a and 4.15).

In sections I and J, the middle slope narrows rapidly and some salty-warm water remains along the base of the upper slope, at depths of 600– The MOW follows two main pathways: the main Gibraltar Channel – cutting through the middle slope as the natural extension of the Strait of Gibraltar – and a shallower Northern Gibraltar Channel – a contour avenue that lies at the base of the upper-slope. The two channels progressively deepen as they flow westwards (till about 6º30'W) and turn northwards (between 6º30' and 6º45'N) until reaching about 36º15'N. The main Gibraltar Channel deepens from about 420 m at West Espartel Sill to some 900 m at about 36º15'N, appearing as a spectacular 80-km long, 4-km wide and 50-m deep U-shaped highway that clearly sustains the idea of a topographically-driven flow but also raises the view that the road itself is the result of the geological erosion of the swift MOW. The Northern Gibraltar Channel begins at depths of about 400 m immediately north of the García del Cid Gorge and reaches some 700 m at 36º15'N.

The clockwise turn of the MOW is driven by the Coriolis force associated to its own speed, causing these bottom waters to stretch until the base of the upper slope. Nevertheless, a remarkable change in the character of the MOW takes place as first the Cadiz Channel (ca. 36º10'N) and later the Gusano Channel (ca. 36º30'N) break down the northward path of both the Northern and main Gibraltar Channels (Figs. 4.16 and 4.17). Northwest of these crossing points, in the northeastern end of the Gulf of Cadiz, only a limited amount of the MOW continues along the base of the upper slope, prone to subsequent diversions either from the east by the Faro Channel (ca. 36º45'W) or later directly from the northern margin; these channels eventually find their way to the western Gulf of Cadiz via the Don Carlos Valley and Faro Canyon (Figs. 4.4a and 4.15). The network of zonal channels and valleys covers the entire middle plateau, dominated by the Cadiz and Middle Channels to the south and the Guadalquivir and Faro Channels to the north (Figs. 4.4a and 4.15).

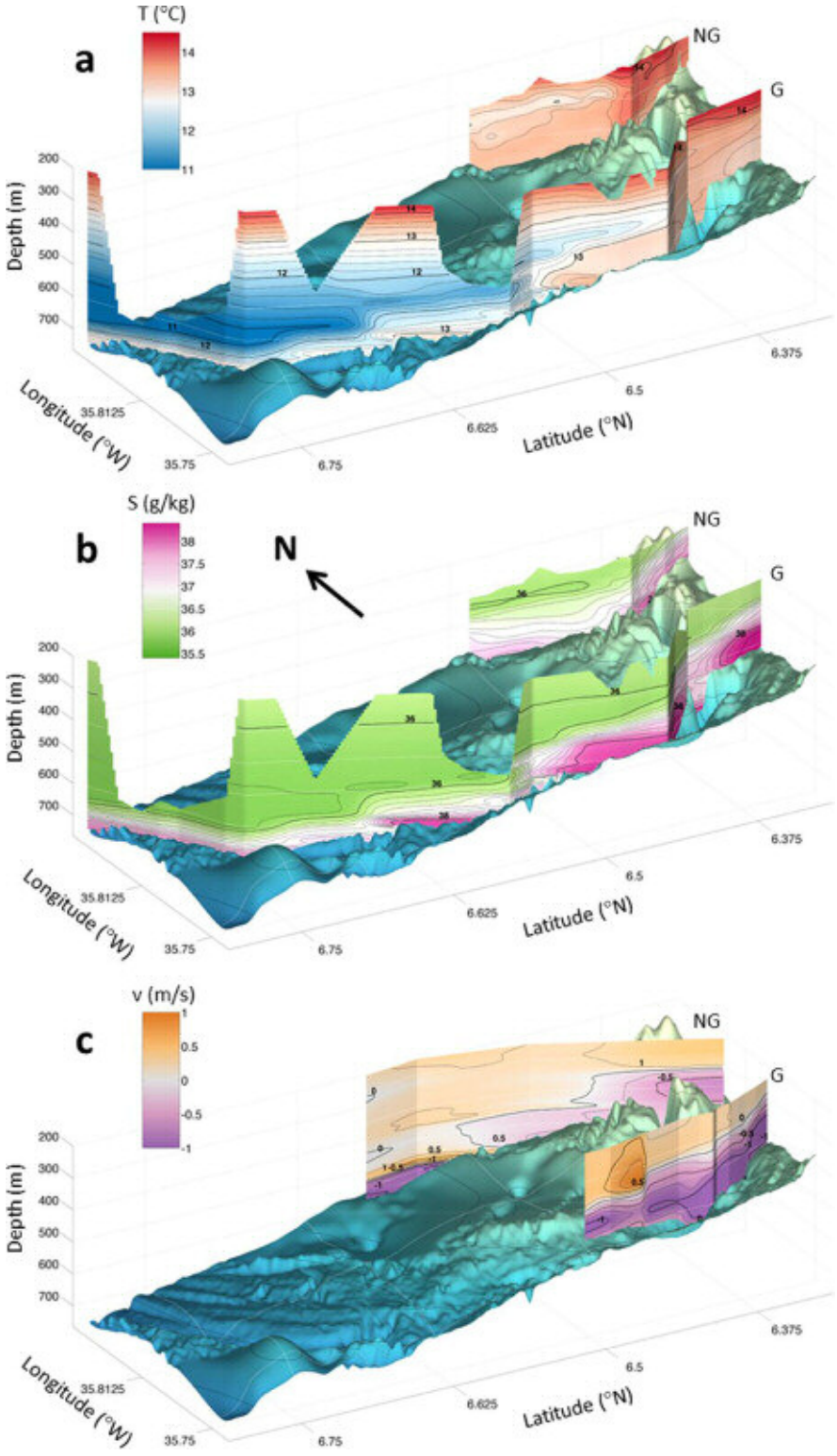

Fig. 4.14. (a) Temperature (ºC), (b) salinity (g/kg) and (c) speed (m/s) sections along the Gibraltar (G) and Northern Gibraltar (NG) Channels. The hydrography comes from MEDOUT-11 while the speed fields come from MEDOUT-09 (Fig. 4.5b); positive/negative speeds correspond to eastward/westward flows. Notice that most of the hydrographic stations do not sample the entire water column, approximately running from 100 m above the MOW to the seafloor.

The spreading of salty-warm bottom waters over the middle-slope plateau suggests a generalized westward MOW partly focalized by the zonal canyons and valleys connecting the middle-slope plateau with the deep ocean (Figs. 4.15-4.17). Indeed, in the perspective plots we find salty and warm MOW stretching all over the plateau but we identify two (ca. 36º10'N and 36º20'N; section G, Fig. 4.16) or three (ca. 36º15'N, 36º25'N and 36º35'N; section H, Fig. 4.17) streams that remain topographically-restricted as far as about 7º30'W (Figs. 4.16 and 4.17). The middle-slope plateau is quite wide in the eastern Gulf of Cadiz but narrows towards the west, totally disappearing ca. 8ºW; further, its western edge shallows to the north, 1200 m deep ca. 36ºN but only 700 m near 36º35'N (Figs. 4.4a and 4.15). Shortly after the MOW overpasses the middle-slope plateau, it becomes neutrally buoyant and detaches from the seafloor, settling as two separate veins centered at depths ca. 1300 and 800 m. This large difference in parking depth responds to the decrease in the MOW's density as it moves from the southern to the northern vein, from ca. 27.75 and 27.5 kg m^{-3}, reinforced by the latitudinal rise of the isopycnals in the eastern North Atlantic subtropical gyre, by as much as 200 m per degree of latitude (Iorga and Lozier, 1999; Machín et al., 2006).

Two subsurface high-salinity cores may also be detected using the methodology described in Section 4.3. The precise pathway for each core depends on the selected dataset and on the algorithm used to define them, with the results in Fig. 4.18 being an example obtained with the GCE data. Nevertheless, in all outputs we identify two principal middle-slope cores or branches: an upper branch flowing ca. 36º30'N and eventually settling at depths of about 800 m, and a lower branch located ca. 36º10'N and finally stabilizing at depths near 1300 m. Additionally, there is the shallow core going along the base of the upper slope, roughly following the 600-m isobath (Fig. 4.18)

It is worth comparing these observations with the model outputs mentioned in the Introduction, and particularly with the 800 m, but most of the high salinity and temperature signature is found deeper, detached from the seafloor, at latitudes where the middle-slope channels reach the western end of the plateau. Two separate offshore salinity veins are identified, settling at depths decreasing with latitude: the southern vein is found ca. 1300 m near 36º15'N and the northern one ca. 800 m around 36º35'N (Fig. 4.17). The velocity fields, ca. sections H and I, show that the westward flow remains intense in the northern vein, with values close to 0.5 m/s, but suggest that the southern vein does not display a conspicuous westward flow (Fig. 4.17c).

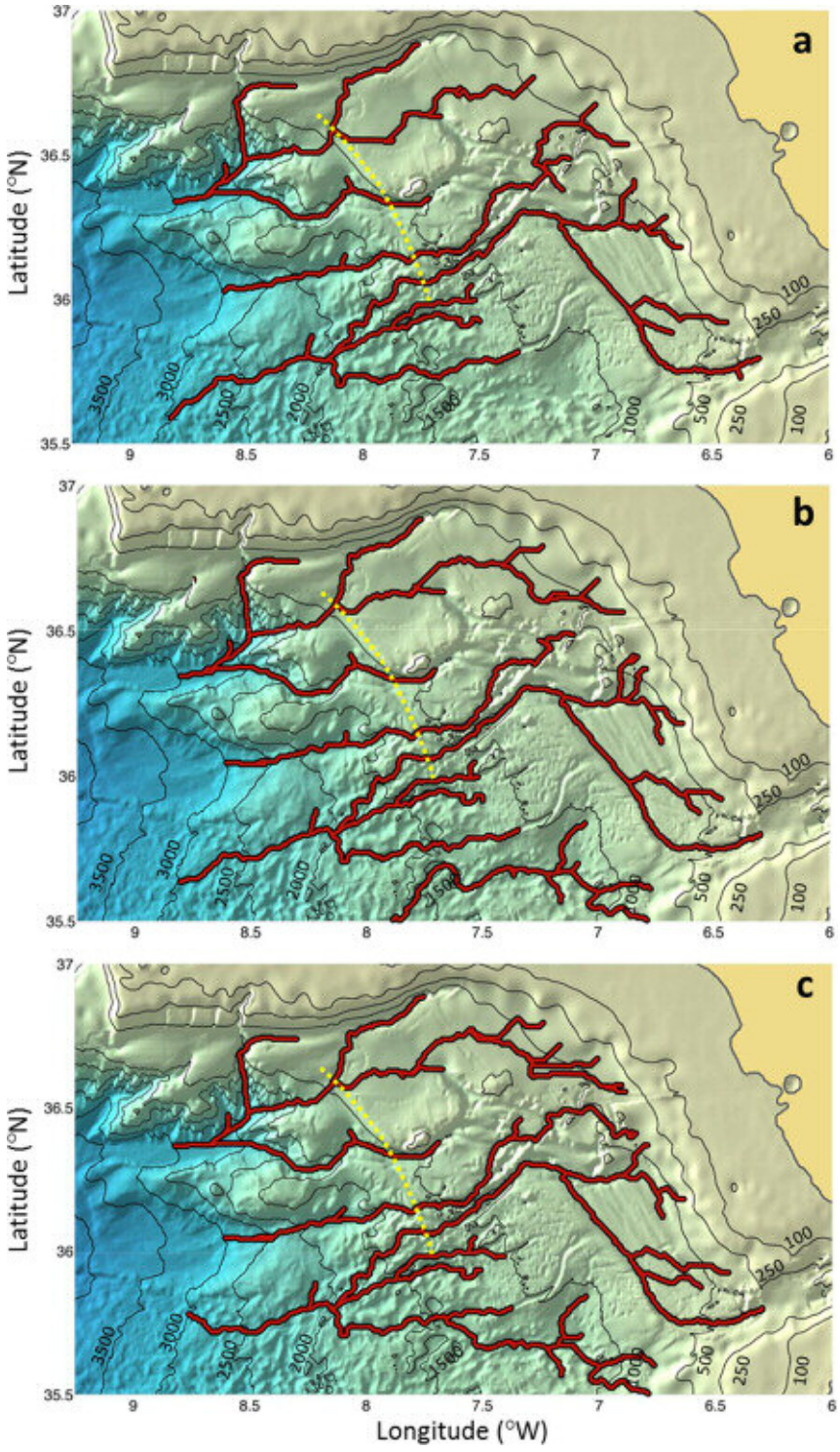

Fig. 4.15. MOW avenues for the far field as obtained using (a) the original bottom topography and (b and c) the bottom topography modified for along-slope velocities of 0.5 and 1.0 m/s, respectively. Selected isobaths are shown (m); the dashed line outlines the western limit of the middle-slope plateau.

4.6. DISCUSSION

4.6.1 MOW KINEMATICS

The MOW exits the Strait of Gibraltar passing round Majuan Ridge (35º53'N, 6ºW). The southern side of this ridge, through Espartel Sill, is the preferential pathway but individual sections from either CANIGO or GCE suggest that a significant fraction of the MOW overcomes the sill through the shallower northern side, probably influenced by the piling effect of the Coriolis force towards the Iberian margin; this is in agreement with the model outputs in Sammartino et al. (2015). After surpassing Espartel, the MOW joins in a relatively wide basin and follows primarily to West Espartel Sill. Immediately downstream of West Espartel, the water accelerates and most of the flow continues along the main Gibraltar Channel; however, some water penetrates northwards through the García del Cid Gorge and reaches the Northern Gibraltar Channel (Fig. 4.2), reinforcing the more limited water input that may be arriving to this channel directly from the east.

The perspective plots, drawn on top of the high-resolution bathymetry, emphasize how the seafloor topography sets the path of the MOW in the eastern margin of the Gulf of Cadiz (Figs. 4.10-4.14). The MOW follows two main pathways: the main Gibraltar Channel – cutting through the middle slope as the natural extension of the Strait of Gibraltar – and a shallower Northern Gibraltar Channel – a contour avenue that lies at the base of the upper-slope. The two channels progressively deepen as they flow westwards (till about 6º30'W) and turn northwards (between 6º30' and 6º45'N) until reaching about 36º15'N. The main Gibraltar Channel deepens from about 420 m at West Espartel Sill to some 900 m at about 36º15'N, appearing as a spectacular 80-km long, 4-km wide and 50-m deep U-shaped highway that clearly sustains the idea of a topographically-driven flow but also raises the view that the road itself is the result of the geological erosion of the swift MOW. The Northern Gibraltar Channel begins at depths of about 400 m immediately north of the García del Cid Gorge and reaches some 700 m at 36º15'N.

The clockwise turn of the MOW is driven by the Coriolis force associated to its own speed, causing these bottom waters to stretch until the base of the upper slope. Nevertheless, a remarkable change in the character of the MOW takes place as first the Cadiz Channel (ca. 36º10'N) and later the Gusano Channel (ca. 36º30'N) break down the northward path of both the Northern and main Gibraltar Channels (Figs. 4.16 and 4.17). Northwest of these crossing points, in the north-eastern end of the Gulf of Cadiz, only a limited amount of the MOW continues along the base of the upper slope, prone to subsequent diversions either from the

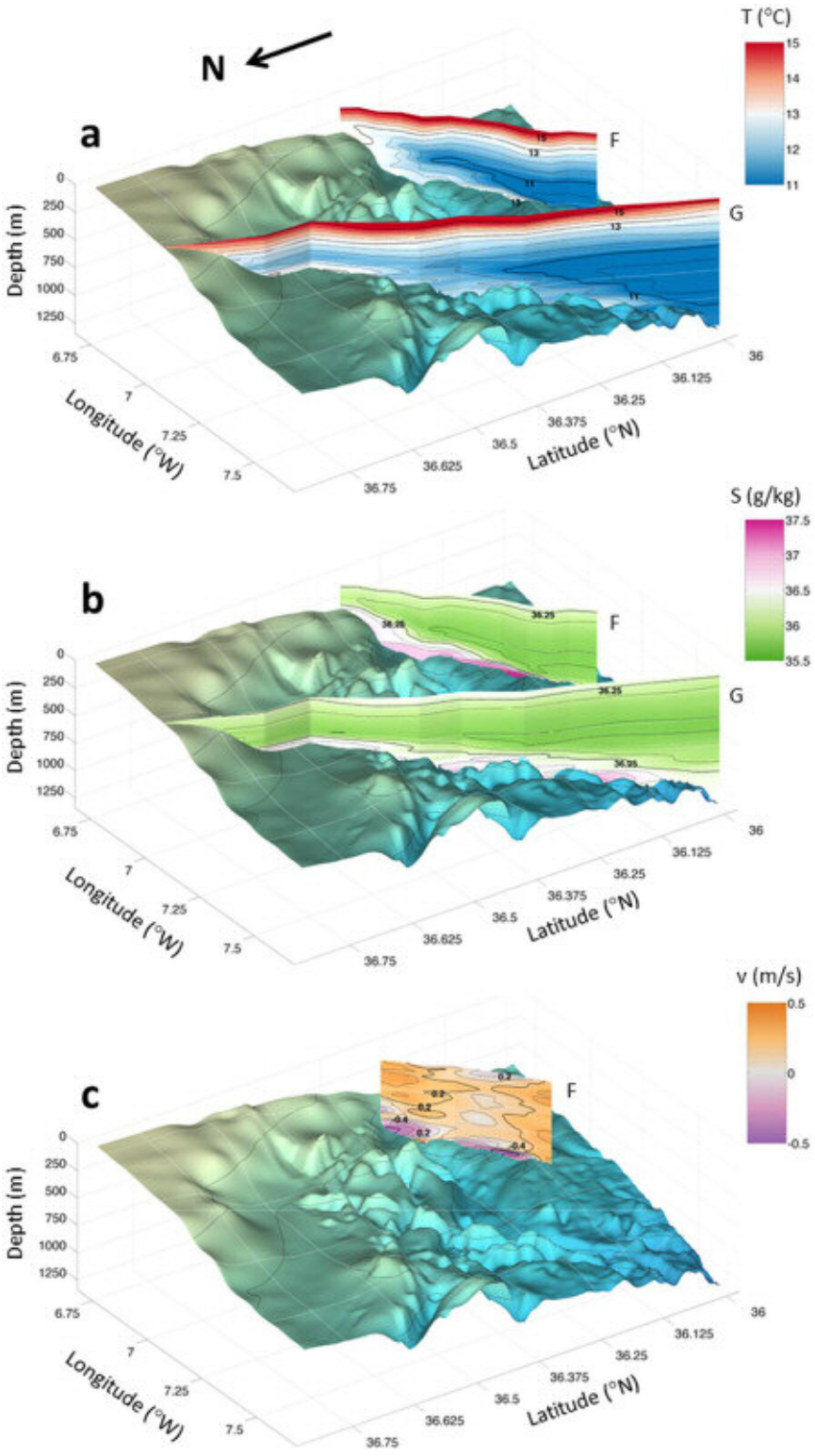

Fig. 4.16. (a) Temperature (ºC), (b) salinity (g/kg) and (c) speed (m/s) cross-stream sections in the far-field. All data come from GCE: sections F and G for the hydrography and section F for the water speed (labeled in Fig. 4.5a); positive/negative speeds correspond to eastward/westward flows. The original stations run all the way from the sea surface down to the sea bottom although in most instances the upper portion of the water column is removed to ease their representation.

east by the Faro Channel (ca. 36ª45'W) or later directly from the northern margin; these channels eventually find their way to the western Gulf of Cadiz via the Don Carlos Valley and Faro Canyon (Figs. 4.4a and 4.15). The network of zonal channels and valleys covers the entire middle plateau, dominated by the Cadiz and Middle Channels to the south and the Guadalquivir and Faro Channels to the north (Figs. 4.4a and 4.15).

The spreading of salty-warm bottom waters over the middle-slope plateau suggests a generalized westward MOW partly focalized by the zonal canyons and valleys connecting the middle-slope plateau with the deep ocean (Figs. 4.15 and 4.17). Indeed, in the perspective plots we find salty and warm MOW stretching all over the plateau but we identify two (ca. 36º10'N and 36º20'N; section G, Fig. 4.16) or three (ca. 36º15'N, 36º25'N and 36º35'N; section H, Fig. 4.17) streams that remain topographically restricted as far as about 7º30'W (Figs. 4.16 and 4.17). The middle-slope plateau is quite wide in the eastern Gulf of Cadiz but narrows towards the west, totally disappearing ca. 8ºW; further, its western edge shallows to the north, 1200 m deep ca. 36ºN but only 700 m near 36º35'N (Figs. 4.4a and 4.15). Shortly after the MOW overpasses the middle-slope plateau, it becomes neutrally buoyant and detaches from the seafloor, settling as two separate veins centered at depths ca. 1300 and 800 m. This large difference in parking depth responds to the decrease in the MOW's density as it moves from the southern to the northern vein, from ca. 27.75 and 27.5 kg m^{-3}, reinforced by the latitudinal rise of the isopycnals in the eastern North Atlantic subtropical gyre, by as much as 200 m per degree of latitude (Iorga and Lozier, 1999; Machín et al., 2006).

Two subsurface high-salinity cores may also be detected using the methodology described in Section 4.3. The precise pathway for each core depends on the selected dataset and on the algorithm used to define them, with the results in Fig. 4.18 being an example obtained with the GCE data. Nevertheless, in all outputs we identify two principal middle-slope cores or branches: an upper branch flowing ca. 36º30'N and eventually settling at depths of about 800 m, and a lower branch located ca. 36º10'N and finally stabilizing at depths near 1300 m. Additionally, there is the shallow core going along the base of the upper slope, roughly following the 600-m isobath (Fig. 4.18).

It is worth comparing these observations with the model outputs mentioned in the Introduction, and particularly with the results from the IBI model as shown in Fig. 4.3. In the near field, the IBI-model outflow shows a single path displaced towards the Northern Gibraltar Channel (Fig. 4.3); in contrast, the hydrographic data show at least two well-defined pathways, with the local salinity maximum following the main Gibraltar Channel (Figs. 4.10-4.14).

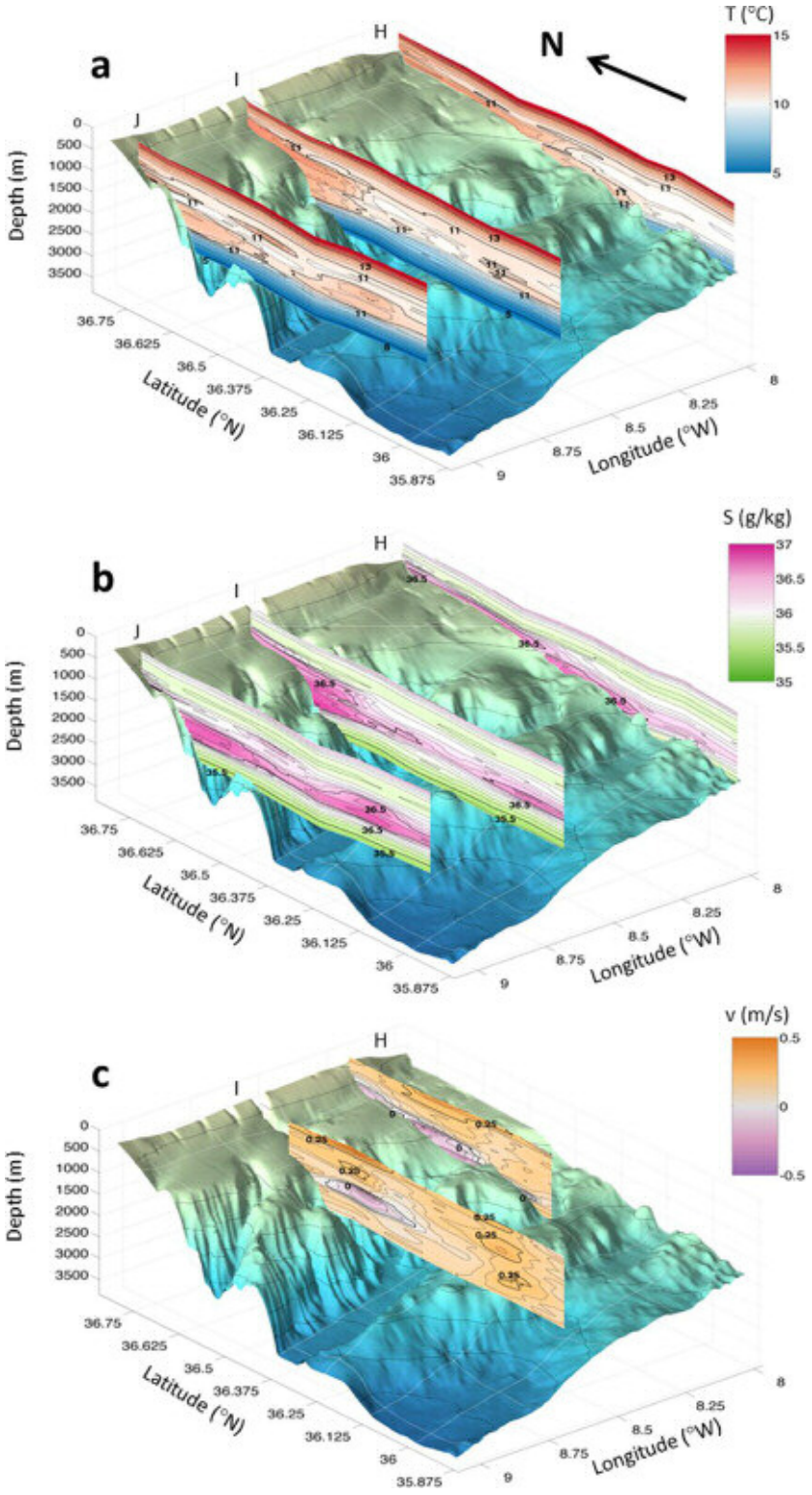

Fig. 4.17. (a) Temperature (ºC), (b) salinity (g/kg) and (c) speed (m/s) cross-stream sections in the far field. All data come from GCE: sections H, I and J for the hydrography and sections H and I for the speed (labeled in Fig. 4.5a); positive/negative speeds correspond to eastward/westward flows. The original stations run all the way from the sea surface down to the sea bottom although in most instances the upper portion of the water column is removed to ease their representation.

Similarly, for the far field, the IBI model displays a well-defined salinity maximum following the continental slope and a second core that separates momentarily at 7º5'W but rejoins the main flow near Portimao Canyon; in contrast, the CTD data point at the existence of at least two additional cores, with the southernmost reaching 36º25'N (Figs. 4.16 and 4.17).

Other than identifying the individual MOW-core pathways, we may produce time-averaged fields of hydrographic properties at two different levels: the minimum salinity surface, characteristic of the deepest undisturbed NACW, and the maximum salinity surface, which typifies the level of maximum MOW influence. For this purpose we use the entire data interpolated on a 1-km grid. The minimum salinity field identifies the upper limit of those waters with MOW influence, located at about 300 m over the upper slope and 500 m in the open ocean (Fig. 4.19a,b). The associated temperatures and salinities change quite linearly with depth, reaching minima ca. 35.75 g/kg and 12 ºC at depths of about 500 m (Fig. 4.19c-f).

The property distributions at the maximum salinity level expose the MOW spreading in the Gulf of Cadiz (Fig. 4.20). A comparison of the depth field (Fig. 4.20a,b) with the bathymetry (Fig. 4.3) reveals that maximum salinities take place along the upper slope in the near field and eastern Gulf of Cadiz and follow along the middle slope plateau until latitudes about 7º30'W but, thereafter, they detach from the seafloor (see next section). The temperatures at the maximum salinity values (Fig. 4.20c,d) cannot reflect the MOW's course, as these temperatures are dominated by the asso-ciated change in depth, but the actual maximum salinity field (Fig. 4.20e,f) is indeed informative of the mean MOW path. In the near field there are two bands of salinity maxima, associated to the Northern and main Gibraltar Channels, while in the far field there is a relatively wide band of high-salinity values, in excess of 36.6, that progresses westwards between ca. 36º10' and 36º35'N (Fig. 4.20e,f).

The ubiquity of the upper and lower MOW pathways is endorsed by the general good agreement between the position of the salinity maxima (Figs. 4.18 and 4.19e,f) and the location of the hydrological MOW avenues (Figs. 4.8 and 4.15). For along-slope velocities of 1 m/s, similar to observed values, the main Gibraltar and Northern Gibraltar Channels are the predominant avenues in the near field (Fig. 4.8). The results show that the Coriolis force indeed helps disconnect the shallow avenues from the main Gibraltar Channel. In the far field, in contrast, most of the MOW avenues depend barely on the flow velocity (Fig. 4.15). As discussed in Section 4.5.1, we may combine these avenues into southern and northern middle-slope branches, reaching the western edge of the middle plateau at latitudes less and more than 36º15'N, respectively (Figs. 4.4a and 4.15).

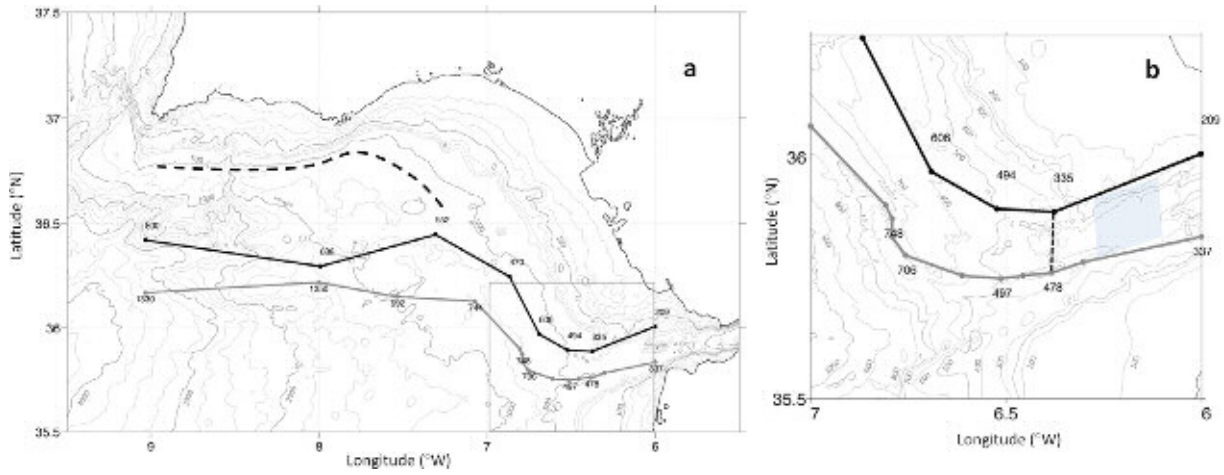

Fig. 4.18: Location of the upper (thick black line) and lower (thick gray line) salinity veins, as deduced from the subsurface salinity maxima, using data from the GCE experiment; the numbers indicate the depth of propagation. (a) In the far field, the dashed line represents the shallow pathway, along the base of the upper slope. (b) In the near field, the dotted line represents the connection through the García del Cid Gorge and the shaded area denotes the relatively flat basin between Espartel and West Espartel Sills. Selected isobaths are shown (m).

The southern branch consists of water initially collected by the Cadiz and Gusano, after diverting part of the flow along the Gibraltar and Northern Gibraltar Channels (Figs. 4.15 and 4.16). The northern branch starts as contour avenues at the base of the upper slope, in the northeastern and northern Gulf of Cadiz, which feed to the Faro Channel. The Guadalquivir Channel and Don Carlos Valley help collect MOW left in the middle-slope plateau, bringing it close to the northern branch (Fig. 4.4a). An inspection of the perspective plots (Figs. 4.10-4.14, 4.16, 4.17), the subsurface maximum-salinity pathways (Fig. 4.18) and the hydrological avenues (Figs. 4.8 and 4.15) shows how the MOW branches remain attached to the seafloor over the middle slope plateau but detach shortly after reaching its western edge (latitudes between 7º5’ and 8ºW).

The method used to calculate the modified MOW avenues has several assumptions. One limitation is related to the way it incorporates the Coriolis force, simply looking for the gradient of the bottom depth at each point. This is fine when the flow follows the contours of the Iberian Peninsula but could produce unex-pected results along valleys as it may reduce the slope of the surrounding ridges; however, in our analysis of the far-field avenues, we only see minor differences in the pathways over the middle slope (Fig. 4.15). Another limitation of the method is its inability to track waters of intermediate density, flowing away from the seafloor. These layers form at locations undergoing intense mixing, such as downstream of West Espartel Sill (Gasser et al., 2011). This is probably one way the salty and warm MOW continues along the base of

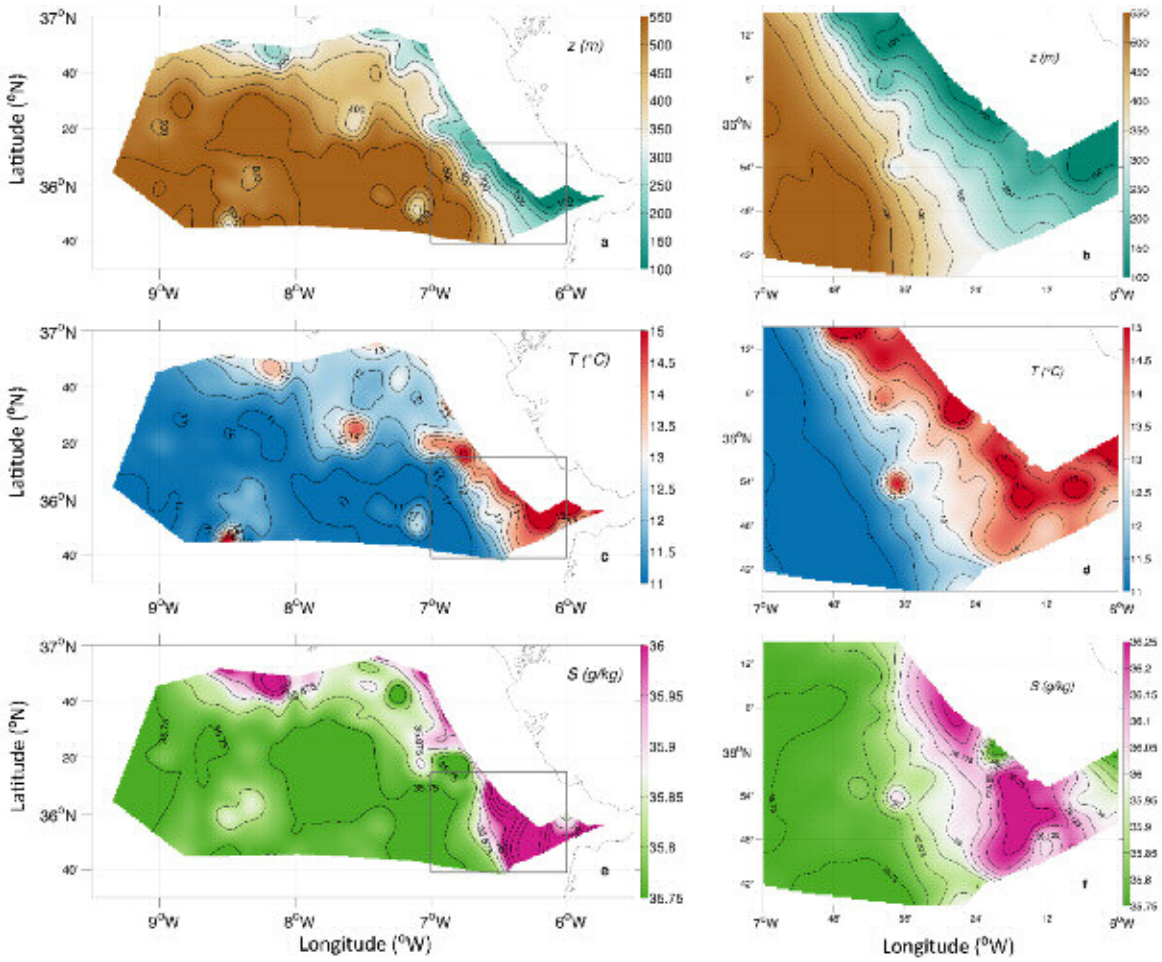

Fig. 4.19: (a,b) Depth (m), (c,d) temperature (ºC) and (e,f) salinity (g/kg) distributions at the minimum salinity level for the far and near fields (left and right panels, respectively). The color bars are saturated at the specified values; notice the change in the color scale between the left and right panels.

the upper slope, as shown by the perspective plots, despite the rupture of the contour avenue in a strict hydrological (slope-driven) sense (Fig. 4.15). An analogous bottom overfilling may also occur in the complex near-field channel network, particularly between the Espartel and West Espartel Sills and the García del Cid Gorge, and over the entire middle-slope plateau in the eastern Gulf of Cadiz.

A related issue is the dependence of the water speed with depth, e.g. for gravity-type currents the velocity maximum is usually located at some distance from the seafloor. In the near field, the vertical stratification of density and velocity could cause that adjacent vertical layers follow different paths, so that the saltiest waters may move along or across the channel depending on the vertical position of the maximum velocity. It could actually happen that the densest and swiftest waters, running close to the sea bed, get locally deflected upslope while the slower overlying waters, i.e. a mixture of MOW and NACW, follow contour avenues. Despite these limitations, the modified hydrological avenues emerge as a valuable tool for studying density-driven bottom flows.

4.6.2 CROSS ISOBATH MOW DYNAMICS

The analysis of the extensive datasets has provided substantial insight on the principal forces acting over the MOW. A phenomenological dynamical discussion is provided next, emphasizing the interaction between flow and bathymetry.

At any given density, the MOW is warmer and saltier than the NACW. This causes that the density anomaly associated to the MOW is smaller than its salinity and temperature deviations. However, as long as the flow remains over the seafloor, either crossing towards deeper areas or following constant depths, we expect that there will be a density anomaly. A flow crossing the isobaths means that the density anomaly is large enough for its associated pressure gradient to exceed any restoring Coriolis force – restoring in the sense that it will bring the flow towards shallower layers; on the contrary, an along-slope flow implies that the Coriolis force can compensate the pressure gradient induced by the density anomaly. Notice that the centrifugal force may also be significant when the flow curves sharply, as during its clockwise turn along the Gibraltar Channel.

The cross-slope flow is the predominant situation in the near field and over most of the far field, either along the Gibraltar Channel or when deviated westwards by the Cadiz (ca. 36º15'N), Middle (ca. 36º20'N) and Faro (ca. 36º40'N) Channels. This is because of the high MOW density anomaly over the surrounding NACW. However, as the MOW gets away from the Strait of Gibraltar, this anomaly diminishes and the associated cross-isobath pressure gradient decreases, so the Coriolis force turns capable of balancing the pressure gradient. This requires the speed of the flow to remain large enough but this is always going to be the case if there is a substantial positive density-anomaly over a sloping bottom. Notice that the interfacial mixing is very effective at reducing the MOW positive density anomaly (Ochoa and Bray, 1991; Baringer and Price, 1997a) but it is not an efficient along-flow retarding force except near West Espartel Sill (Baringer and Price, 1997b). A cross-flow balance between the Coriolis force and the density-driven pressure gradient takes place generally at the base of the upper continental slope – along the Northern Gibraltar Channel or along the entire eastern and northern margin of the Gulf of Cadiz – either because the density anomaly is small, the water speed is large or both.

The situation changes when the density anomaly disappears, such as when the MOW sinks rapidly at the western edge of the middle-slope plateau (beyond about 7º30'–8ºW). In this case the density-driven pressure gradient disappears and the flow will be diverted northwards by the Coriolis force unless there is a compensating pressure gradient caused by the overlying water

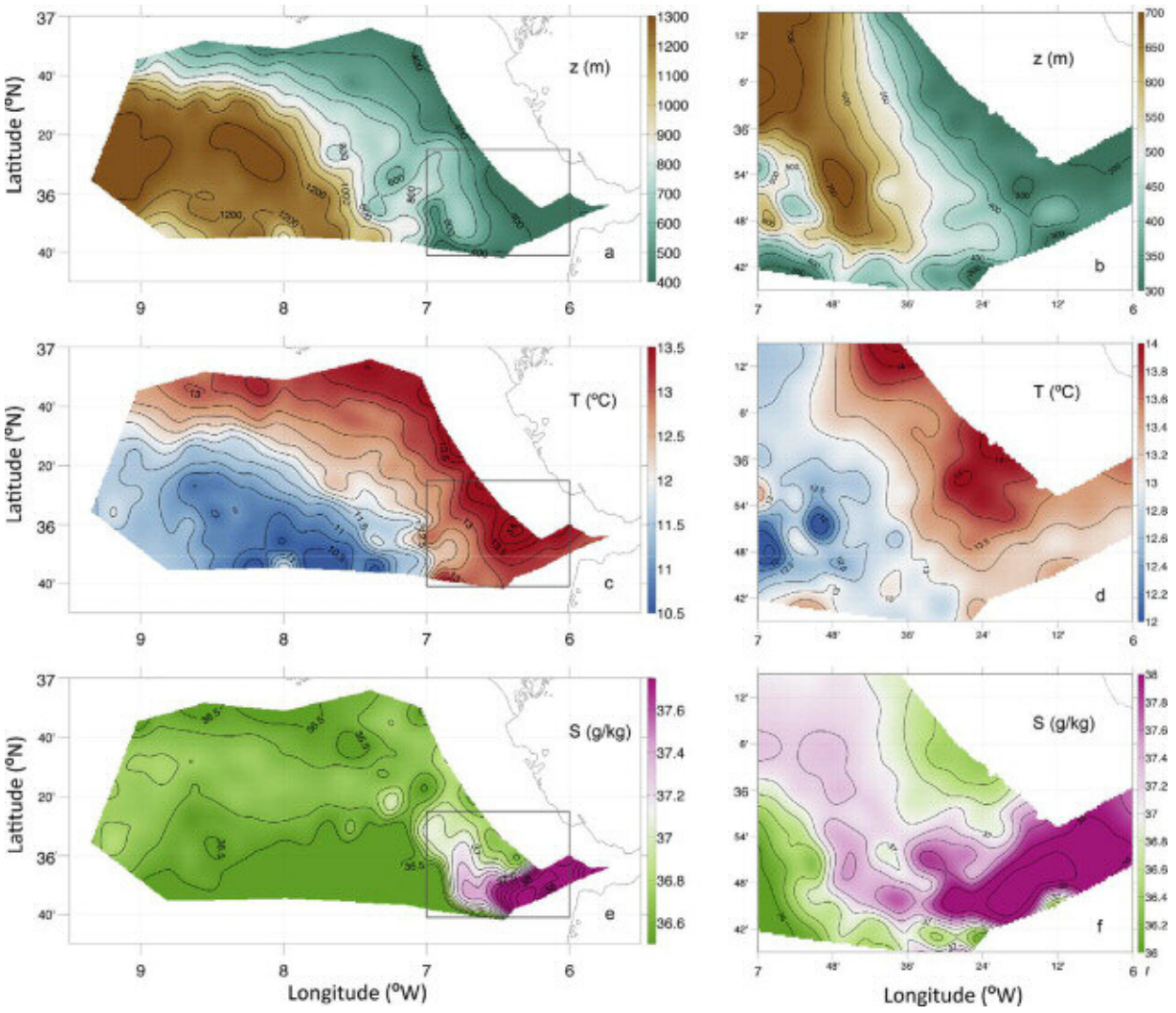

Fig. 4.20. (a and b) Depth (m), (c and d) Temperature (ºC) and (e and f) salinity (g/kg) distributions at the subsurface maximum salinity level for the far and near fields (left and right panels, respectively). The color bars are saturated at the specified values; notice the change in the color scale between the left and right panels. (For interpretation of the references to colour in this figure legend, the reader is referred to the web version of this article.)

column; this is the case in the Gulf of Cadiz, where the overlying isopycnals shallow towards the north (Iorga and Lozier, 1999; Machín et al., 2006), a reflection of the eastward flow of the NACW stratum (Peliz et al., 2007, 2009). Alternatively, a subsurface offshore MOW anomaly is still possible if its net westward velocity is very small.

In order to clarify these ideas we have constructed two final sets of plots (Fig. 4.21). In the first one (Fig. 4.21a,b), we show the depth difference between the level of propagation of the salinity maximum (Fig. 4.20a,b) and the bottom depth (Fig. 4.2). The distribution proves that the MOW core travels adjacent to the seafloor as it exits the Strait of Gibraltar and follows along the eastern margin of the Gulf of Cadiz, with depth differences less than 25 m (Fig. 4.21a). As the MOW continues along the middle-slope plateau in the eastern half of the Gulf of Cadiz, the depth difference remains most of the time less than 100 m, indicating some near-bottom

entrainment and dilution but evidencing that the MOW feels the bathymetry. As the MOW arrives to the western edge of this plateau (7º30'–8ºW), it follows the steeply sloping bottom until depths between ca. 800–1000 m to the north, adjacent to the northern continental slope, and 1300 m to the south (Fig. 4.21a). At these levels, the flow is neutrally buoyant and cannot sink further, propagating westwards as a tongue of intermediate waters far from the seafloor (Fig. 4.21a).

In the second set of plots, we present the potential density at the same subsurface maximum-salinity level (Fig. 4.21c,d). A posi-tive density anomaly shows up in the near field and the eastern Gulf of Cadiz, with densities in excess of 27.75 kg m^{-3} until 7ºW (Fig. 4.21d) and values greater than 27.6 kg m^{-3} along a zonal pathway (36.10^0–36º30'N) until the western edge of the

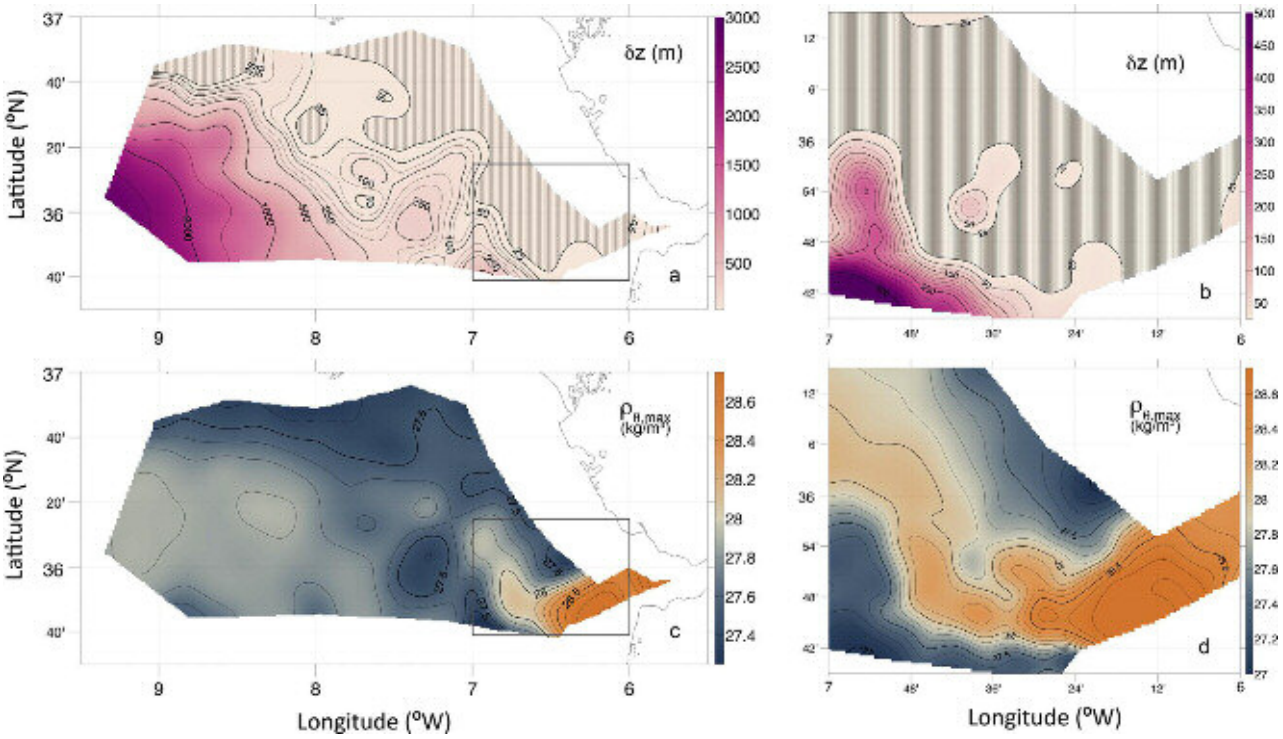

Fig. 4.21. (a and b) Distance from the seafloor (dz, in m; values less than 25 m are shaded) and (c and d) potential density ($q_{h,max}$, in kg m^{-3}) distributions at the subsurface maximum salinity level for the far and near fields (left and right panels, respectively). The color bars are saturated at the specified values; notice the change in the color scale between the left and right panels. (For interpretation of the references to colour in this figure legend, the reader is referred to the web version of this article.)

middle slope plateau, surrounded by values less than 27.5 kg m^{-3} (Fig. 4.21c). In contrast, as the MOW overpasses the middle slope plateau and detaches from the seafloor, it reaches an open-ocean region where the density values are fairly homogeneous, ca. 27.75 kg m^{-3}, as if a water tributary had finally arrived to the sea (Fig. 4.21c). In this final region the density decreases northwards, as expected since the northern MOW vein stabilizes at much shallower

waters (Fig. 4.21a); further, the final density values are slightly greater than those over the middle-slope plateau, indicative of mixing with the deeper and denser NADW.

4.7 CONCLUDING REMARKS

From its early stages after surpassing Espartel Sill to the moment it leaves the continental slope some 200 km later, the trajectory of the MOW results from a force balance between the pressure gradient associated to its excess density on a sloping bottom, the Coriolis force (and locally the centrifugal force) arising from its own speed, and the bottom/interfacial friction. The outcome is that the flow behaves, to a large extent, as a river flowing down a hydrological basin with a reduced bottom slope. Depending on the relative importance of these forces, we may idealize the MOW within the Gulf of Cadiz as belonging to either of three different regimes (Table 4.1).

Table 4.1. MOW regimes, corresponding scales and predominant momentum balances. The relevant scales are the cross-stream and along-stream length scales (L_x, L_y), the MOW excess density anomaly dq, and the along-stream velocity V. For steady state, the horizontal momentum balance is expressed as follows: momentum advection + Coriolis force = pressure gradient + bottom friction + interfacial friction (MA + CoF = PG + BF + IF). The pressure gradient has contributions caused by the density anomaly together with the shape of the interface (local PG, or LPG) and by the shape of the overlying isopycnals (environmental PG, or EPG); for curving flow, the cross-stream momentum advection turns into the centrifugal force (CeF). The bold terms show the dominant momentum contributions while the italicized terms denote relatively minor contributions that may become locally significant.

Regime	Scales				Along-stream momentum balance	Cross-stream momentum balance
	L_x (km)	L_y (km)	dq (kg m^{-3})	V (m/s)		
1. Density-driven current	10	10	1	1	MA = LPG + BF + IF	CeF + CoF = LPG + EPG + BF
2. Contour current	10	100	0.1	0.1–1	MA = BF	CeF + CoF = LPG + EPG
3. Buoyant vein	100	1000	0	0.01–0.1	MA = IF	CoF = EPG

In the first regime, the predominant along-stream MOW balance is between the downslope density-driven pressure gradient and bottom friction, although momentum advection and interfacial stress may locally peak up (Johnson et al., 1994; Baringer and Price, 1997b; Nash et al., 2012). In the cross-stream direction, the pressure-gradient dominates the momentum balance, with opposite contributions due to the upward bowing interface and the downward bowing overlying isopycnals. This regime takes place close to West Espartel Sill, when the density anomaly is high and the MOW finds itself in a channel with along-axis slope between moderate and large. However, we also find this regime in the channels that cross the eastern slope of the Gulf of Cadiz at about 36º15'N: the density-anomaly has reduced substantially but the steep zonal channels can still divert the direction of the flow.

A second MOW regime occurs when the density anomaly is small and/or the speed is large. This happens at the base of the upper continental slope along most of the Gulf of Cadiz, where

the flow follows a contour avenue with little along-axis slope. The predominant cross-flow balance is between the cross-slope density-driven pressure gradient and the Coriolis force, with significant centrifugal force contributions only near 6º40'W, when the flow turns northwards along the continental slope (Baringer and Price, 1997b; Gasser et al., 2011). Notice that bottom friction (which would cause downslope bottom Ekman transport) is likely small compared with the pressure gradients and the Coriolis force, as otherwise the dense MOW would be observed to spread down-slope; however, this is not the case, indicating that Ekman bottom transport is arrested (Garret et al., 1993). In contrast, in the along-flow direction, changes in along-stream momentum do occur mainly because of bottom friction (Johnson et al., 1994; Baringer and Price, 1997b). This regime may also happen downstream of West Espartel Sill, when the density anomaly is still very large but the flow is so fast that it becomes diverted through the García del Cid Gorge towards shallower waters.

The third MOW regime occurs after the density-driven topographic flow encounters an abrupt change in slope that reaches deep into the ocean. The flow will approximately follow the axis of the canyon as long as its density remains larger than the ambient density but it will naturally detach from the seafloor when the density anomaly becomes zero, becoming a buoyant water wedge (or vein) with distinct temperature and salinity values. This sort of river discharge into the open ocean occurs at latitudes of 36º10'– 36º35'N, shortly after the westward topographically-driven flow overpasses the edge of the middle-slope plateau (between 7º30' and 8ºW). In the cross-stream direction, the pressure gradient associated to the density anomaly is zero so, for non-stagnant waters, a non-local pressure gradient has to compensate the Coriolis force. This depth-integrated pressure gradient is caused by the rising of the NACW isopycnals towards the east and north. Our observations show that only the flow adjacent to the slope has significant westward speeds, consistent with the cross-slope rise of the isopycnals near the continental slope (Iorga and Lozier, 1999), while the offshore deep MOW core (discernible through its temperature and salinity anomalies) does not display perceptible velocities. In the along-stream direction, the along-stream momentum changes as a result of interfacial friction.

In summary, the MOW constitutes an extraordinary example of a density-driven current steered by both bottom topography and the Coriolis force. These processes play a key role in the modern MOW, setting the pathways within the continental slope and the eastern Gulf of Cadiz as well as fixing the density level where the MOW settles down as it reaches the western Gulf of Cadiz. Furthermore, our work clearly suggests that bathymetry and bottom currents must have interacted in diverse ways during past geological periods, with different settling depths in the deep ocean (Maestro et al., 2007). The high erosive power of the swift MOW is certainly capable of slowly shaping the bottom topography, and the paleo-changes in sea-surface level

and MW-NACW density differences must have led to different MOW mixing rates and pathways. The MOW, through its potentially high impact on the rate of deep water formation in the northern North Atlantic (Reid, 1979), is possibly the best example of a regional process influencing the climate of the entire Earth.

ACKNOWLEDGEMENTS

We are grateful to captain Eduardo Otal and the crew of the R/V Garcia del Cid for their exceptional work during the MEDOUT-09 and MEDOUT-11 cruises. We are thankful to Jim Price for making available the GCE dataset, Francisco Machín for assistance with the CANIGO dataset, and Jesús García Lafuente for logistic support during the MEDOUT-09 and MEDOUT-11 cruises. We are indebted to all scientists participating in the MEDOUT cruises: Aissa Benazzouz, Elisa Bruque, Jamal Chioua, Juan Jesús Gómiz, Samuel Kelly, Jonathan Nash, Mercedes Pozo, Antonio Jesús Sánchez, Jose Carlos Sánchez, Francisco Javier Soto and Agueda Vázquez. We also wish to sincerely thank Maribel Lloret, José Antonio Pozo and Cristina Alvarez for their technical support during the cruises, and Susana Díez for her assistance with the multibeam data processing. We thank Wolfgang Schwanghart for making available the topographic analysis functions through TopoToolbox. Finally, we are grateful to José Ochoa and an anonymous reviewer for a number of useful comments and suggestions, and to our editor, Enrique Curchitser, for the handling of the manuscript. This research has been carried out with the support of the Spanish government, through projects MOC2 (CTM2008-06438-C02-01), MED-OUTFLOW 2009 (CTM2008-03422-E/MAR), MED-OUTFLOW-2011 (CTM2010-11488-E) and VA-DE-RETRO (CTM2014-56987-P).

CHAPTER 5: SUMMARY AND CONCLUSIONS

SUMMARY AND CONCLUSIONS

This document analyzes the processes that control the salinity, temperature, density, velocity and trajectory of the Mediterranean Outflow Water (MOW) as it transits from the Strait of Gibraltar into the Gulf of Cádiz. For our analysis we use sea-surface elevation and hydrographic data in the Strait of Gibraltar, novel hydrographic and velocity data from two cruises (MEDOUT 2009 and MEDOUT 2011) in the Gulf of Cádiz adjacent to the Strait of Gibraltar, and an extensive historical dataset of hydrographic and bathymetric observations, which are then combined with simple models and methodologies in order to understand the principal processes that shape the trajectory and transformations of MW as it passages from the Strait of Gibraltar into the Gulf of Cádiz.

For our analysis we move from the description of mixing processes within the Strait of Gibraltar (Chapter 2) to the first intense transformations of the MOW as it exits the Strait of Gibraltar and overcomes the West Espartel Sill (Chpater 3) and its posterior evolution within the Gulf of Cádiz, largely influenced by a complex network of contouritic, turbiditic and diapiric structures (Chapter 4). In particular, we present an improved bathymetry of a key outflow region immediately west of the Strait of Gibraltar and develop and apply a new tool, based on hydrological methodologies, to assess the relevance of the Coriolis force on the MOW's trajectory.

The MOW is a dense (ρ>1028.5 kg/m^3), saline (38.5 g/kg) and relatively cold (13.3ºC) ocean current created by the evaporation imbalance in the Mediterranean Sea. After crossing the Strait of Gibraltar, it plunges westward with characteristic velocities of the order of 1 m/s underneath less dense North Atlantic Central Waters (temperatures 12-15ºC, salinities 35.7-36.5, characteristic density 1026.8-1027.2 kg/m^3) until it reaches the equilibrium depth, defined as the point where the density difference between the MW and the surrounding water reaches zero. As a positive salinity anomaly, its signature spans most of the North Atlantic Ocean and reaches polar latitudes, contributing to the formation of the cold and dense North Atlantic Deep Waters, one of the engines of the Global Thermohaline Circulation. The entrainment of NACW into the MOW is also credited as the origin, through a beta-plume mechanism, of the Azores Current

The MOW dynamics results from the interrelationship between many different forces: frictional forces between the current and the seafloor as well as internal friction associated with vertical mixing; inertia, Coriolis and centrifugal forces; pressure gradient due to both the sloping seafloor and the density difference between the MOW and the overlying waters; the intermittent and

often intense differences in atmospheric pressure between the Mediterranean Sea and the Atlantic Ocean; and the highly intermittent and localy very strong tidal forces. The temporal-variable forces are high within the Strait of Gibraltar and remain significant near its western exit, particularly in the northeastern Gulf of Cádiz. There are reports of interannual, seasonal and tidal frequencies accounting for up to 5%, 8% and 5% of the standard deviation in the MOW physical properties west of Espartel Sill, respectively, as well as of a decadal increase (up to 0.15ºC in temperature and 0.03 g/kg in salinity) in the initial MOW values. Despite this variability the final characteristics of the MOW at its equilibrium depth have remained relatively stable, hence suggesting the existence of substantial negative feedback processes.

Cold water events, defined as a sustained and significant drop in the sea surface temperature concomitant to an increase in the Atlantic layer depth, are observed in satellite images of the Strait of Gibraltar some 10-15 times per year, each lasting about 5-10 days. These events do not show an evident correlation with either tidal dynamics or wind-induced upwelling. An alternative possible explanation is the entrainment of deeper and relatively colder MW into the upper layer due to shear-induced instabilities resulting from high-frequency (1-10 days) pulses in the pressure differences between the Atlantic Ocean and the Mediterranean Sea, accounting for up to 84% of the outflow velocity variance. A simple 1.5-layer numerical model, developed in order to test this hypothesis, finds good agreement with hydrographic data, its results being also consistent with simple energetic considerations.

The evolution and trajectory of the MOW is inextricably linked to the complex bathymetry of the Gulf of Cádiz. Immediately west of the Strait of Gibraltar and Espartel Sill, the flow has thickness between 50-150 m and widths about 5 km, closely following the well defined Gibraltar Channel and the less distinct Northern Gibraltar Channel. In the West Espartel Sill the flow encounters abrupt topography changes and accelerates, turning unstable and developing large internal waves and billows with heights of about 50 m and wavelength of O(1 km) that likely have high erosive potential. This relatively small region shows the highest rates of energy dissipation and mixing, therefore largely controling the final properties of the MOW.

Once the MOW turns north, due to the Coriolis force, it is steered by a series of along slope contouritic-depositional and cross-slope erosive-turbiditic structures, including diapiric ridges and canyons aligned cross-slope that block and divert the flow. Although other alternative mechanisms have been suggested to be relevant, such as flow intermittency and tidal effects, the interaction of the flow with the seafloor relief suffices to explain the formation of at least two well defined main nuclei or branches, located at 500-800 m and 800-1200 m with mean temperatures of 13.7º and 13.6º and salinities of 37.1 and 37.4, respectively.

The MOW behaves largely as a gravity current, from its initial stages near the Strait of Gibraltar to its transiting in the upper slope of the northeastern Gulf of Cádiz. During the early plunging phases, the MOW has a density anomaly so large that it behaves essentially as a density-driven gravity current, so intense to shape the seafloor (often with cross-slope erosive structures) and bring about a natural combination of flow and relief. Further away from the Strait of Gibraltar, the density difference has decreased substantially but the flow largely retains its, now along-slope, gravity current behavior.

The behavior of the MOW as a gravity current allows applying methodologies and tools derived from the field of hydrology, in analogy with surface water tributaries. Through suitable modifications of pre-existing tools and methodologies, the effect of the Coriolis force is introduced in the description of the gravity current system. This tool defines differentiated stages in the trajectory of the MOW, as a function of the principal controlling force, and considers the effect of the diverse geological structures (e.g. canyons and ridges) on the trajectory of the outflow, until the flow becomes neutrally buoyant and separates from the seafloor. The addition of other physical mechanisms, such as interfacial or bottom friction, is possible but has not been included in our study.

The MOW is possibly the best example of local processes that have regional effects that eventually bring about global consequences. Here we have ensembled three different pieces of research that explore the sort of transformations that the MW, and the overlying NACW, experiences as it travels the Strait of Gibraltar and Gulf of Cádiz. We have used substantial amounts of data – although less than the recent works by Bellanco and Sánchez-Leal (2016) and Sánchez-Leal et al. (2017) – but our approach has focused mainly on the understanding of the mechanisms behind the observations. Despite the many advances produced by these and other studies, the full description and comprehension of the MOW remains as an extraordinary challenge both because of its beauty and its regional and global importance.

BIBLIOGRAPHY

Alonso del Rosario, J.J., Bruno Mejías, M., Vázquez-López-Escobar, A., 2003. The influence of tidal hydrodynamic conditions on the generation of lee waves at the main sill of the Strait of Gibraltar. Deep-Sea Res. 50:1005-1021.

Ambar, I., Howe, M.R., 1979. Observations of the Mediterranean outflow I. Mixing in the Mediterranean outflow. Deep Sea Res. 26:535–554.

Ambar, I., Armi, L., Bower, A., Ferreira, T., 1999. Some aspects of time variability of the Mediterranean Water off South Portugal. Deep-Sea Res. 46:1109–1136.

Ambar, I., Serra, N., Brogueira, M.J., Cabeçadas, G., Abrantes, F., Freitas, P., Gonçalves, P., González, N., 2002. Physical, chemical and sedimentological aspects of the Mediterranean outflow off Iberia. Deep Sea Res. 49:4163–4177.

Armi, L. 1986. The hydraulics of two flowing layers with different densities. J. Fluid Mech. 163:27-58.

Armi, L., Farmer, D.M., 1986. Maximal two-layer exchange through a contraction with barotropic net flow. J. Fluid Mech. 164:27-51.

Armi, L., Farmer, D.M., 1987. A generalization of the concept of maximal exchange in a strait. J. Geophys. Res. 92:14679-14680.

Armi, L., Farmer, D.M., 1988. The flow of Mediterranean water through the Strait of Gibraltar. Progr. Oceanogr. 21:1–105.

Baraza, J., Ercilla, G., Nelson, CH., 1999. Potential geologic hazards on the eastern Gulf of Cadiz slope (SW Spain). Mar. Geol. 155:191–215.

Barbosa Aguiar, A.C., Peliz, A., Neves, F., Bashmachnikov, I., Carton, X., 2015. Mediterranean outflow transports and entrainment estimates from observations and high-resolution modelling. Prog. Oceanogr. 131:33–45.

Baringer, M.O., Price, J.F., 1997a. Mixing and spreading of the Mediterranean outflow. J. Phys. Oceanogr. 27:1654–1677.

Baringer, M.O., Price, J.F., 1997b. Momentum and energy balance of the Mediterranean outflow. J. Phys. Oceanogr. 27:1678–1692.

Baringer, M.O., Price, J.F., 1999. A review of the physical oceanography of the Mediterranean outflow. Mar. Geol. 155:63–82.

Becker, J., Sandwell, D.T., Smith, W. H. F., Braud, J., Binder, B., Depner, J., Fabre, D., Factor, J., Ingalls, S., Kim, S-H., Ladner, R., Marks, K., Nelson, S., Pharaoh, A., Trimmer, R., Von Rosenberg, J., Wallace, G., Weatherall, P., 2009. Global bathymetry and elevation data at 30 arc seconds resolution: SRTM30_PLUS. Mar. Geodesy 32, 355–371.

Bellanco, M.J., Sánchez-Leal, R. F., 2016. Spatial distribution and intra-annual variability of water masses on the Eastern Gulf of Cadiz seabed. Cont. Shelf Res. 128:26–35.

Benjamin, T.B., 1968. Gravity current and related phenomena. J. Fluid. Mech. 31:209–248.

Blanc, P.L., 2002. The opening of the Plio-Quaternary Gibraltar Strait: assessing the size of a cataclysm. Geodin. Acta 15:303–317.

Borenäs, K.M., Wahlin, A.K., Ambar, I., Serra, N., 2002. The Mediterranean outflow splitting – a comparison between theoretical models and CANIGO data. Deep Sea Res. 49:4195–4205.

Bormans, M., Garrett, C., 1989a. The effect of rotation on the surface inflow through the Strait of Gibraltar. J. Phys. Oceanogr. 19:1535-1542.

Bormans, M., Garrett, C., 1989b. The effects of nonrectangular cross section, friction, and barotropic fluctuations on the exchange through the Strait of Gibraltar. J. Phys. Oceanogr. 19:1543-1557.

Bower, A.S., Serra, N., Ambar, I., 2002. Structure of the Mediterranean undercurrent and Mediterranean water spreading around the southwestern Iberian Peninsula. J. Geophys. Res. 107:3161–3179.

Bozec, A., Lozier, M.S., Chassignet, E.P., Halliwell, G.R., 2011. On the variability of the Mediterranean Outflow Water in the North Atlantic from 1948 to 2006. J. Geophys. Res. 116:C09033.

Bruno M., Alonso J.J., Cózar A., Vidal J., Ruiz-Cañavate A., Echevarría F., Ruiz J., 2002. The boiling-water phenomena at Camarinal Sill, the strait of Gibraltar. Deep-Sea Res. II 49:4097-4113.

Bruno, M., Chioua, J., Romero, J., Vázquez, A., Macías, D., Dastis, C., Ramírez-Romero, E., Echevarria, F., Reyes, J., García, C.M., 2013. The importance of sub-mesoscale processes for the exchange of properties through the Strait of Gibraltar. Progr. Oceanogr. 116:66-79.

Bryden, H. L., Stommel, H. M., 1984. Limiting processes that determine basic features of the circulation in the Mediterranean Sea. Oceanol. Acta 7:289-296.

Bryden, H.L., Kinder, T.H., 1991. Steady two-layer exchange through the Strait of Gibraltar. Deep-Sea Res. 38:445-463.

Bryden, H.L., Candela, J., Kinder, T.H., 1994. Exchange through the Strait of Gibraltar. Progr. Oceanogr. 33:201-248.

Candela, J., Beardsley, R.C., Limeburner, R., 1990. Removing tides from ship-mounted ADCP data, with application to the Yellow Sea. Proc IEEE 4th Working Conf Current Measurements. Institute of Electrical and Electronics Engineers, New York, 258–266

Candela, J., 2001. Mediterranean water and global circulation. Ocean Circulation and Climate. Academic Press, New York, 419–429.

Candela, J., Winant, C.D., Bryden, H.L., 1989. Meteorologically forced subinertial flows through the Strait of Gibraltar. J. Geophys. Res. 94:12667-12680.

Candela, J., Winant, C., Ruiz, A., 1990. Tides in the Strait of Gibraltar. J. Geophys. Res. 95 :7313-7335.

Crepon, M., 1965. Influence de la pression atmosphérique sur le niveau moyen de la Méditerranée Occidentale et sur le flux à travers le Détroit de Gibraltar. Présentation d'observations. Cahiers Océanographiques XVIII:15–32.

Csanady, G. T., 1976. Mean circulation in shallow seas. J. Geophys. Res. 81:5389–5399.

Dalziel, S. B., 1991. Two-layer hydraulics: A functional approach, J. Fluid. Mech. 223:135–163.

Deacon, M., 1985. An early theory of ocean circulation: J. S. von Waitz and his explanation of the currents in the Strait of Gibraltar. Prog. Oceanogr. 14:89-101.

D'Errico, J.R., 2006. Surface Fitting using gridfit.
https://www.mathworks.com/matlabcentral/fileexchange/8998-surface-fitting-using-gridfit

Dietrich, D.E., Tseng, Y.H., Medina, R., Piacsek, S.A., Liste, M., Olabarrieta, M., Bowman, M.J., Mehra, A., 2008. Mediterranean Overflow Water (MOW) simulation using a coupled multiple-grid Mediterranean Sea/North Atlantic Ocean model. J. Geophys. Res. 113:C07027.

Eugenio, F., Marcello, J., Hernández-Guerra, A., Rovaris, E., 2001. Methodology to obtain accurate sea-surface temperature from locally received NOAA-14 data in the Canary-Azores-Gibraltar area. Sci. Mar. 65:127–137.

Farmer, D., Armi, L., 1986. Maximal two-layer exchange over a sill and through the combination of a sill and contraction with barotropic flow. J. Fluid Mech. 164:53-76.

Farmer, L., Armi, L., 1988. The flow of the Atlantic water through the Strait of Gibraltar. Progr. Oceanogr. 21:1-105.

Fischer, J. and Visbeck, M., 1993. Deep velocity profiling with self-contained ADCPs. J. Atm. Oc. Tech. 10:764–773

Folkard, A.M., Davies, P., Fiúza, A.F.G., Ambar, I. 1997. Remotely sensed sea surface thermal patterns in the Gulf of Cádiz and the Strait of Gibraltar: variability, correlations, and relationships with the surface wind field. J. Geophys. Res. 102:5669-5683.

Fusco, G., Artale, V., Cotroneo, Y., Sannino, G., 2008. Thermohaline variability of Mediterranean Water in the Gulf of Cadiz, 1948–1999. Deep-Sea Res. I 55:1624–1638.

García, M., Hernández-Molina, F.J., Llave, E., Stow, D.A.V., León, R., Fernández-Puga, M.C., Díaz del Río, V., Somoza, L., 2009. Contourite erosive features caused by the Mediterranean outflow water in the Gulf of Cadiz: quaternary tectonic and oceanographic implications. Mar. Geol. 257:24–40.

García Lafuente J., Cano, N., Vargas, M., Rubín, J.P., Hernández-Guerra, A., 1998. Evolution of the Alboran Sea hydrographic structures during July 1993. Deep-Sea Res. 45:39-65.

García Lafuente, J., Vargas, J.M., Plaza, F., Sarhan, T., Candela, J., Bascheck, B., 2000. Tide at the Eastern section of the Strait of Gibraltar. J. Geophys. Res. 105:14197-14213.

García Lafuente, J., Delgado, J., Vargas, J.M., Vargas, M., Plaza, F., Sarhan, T., 2002a. Low-frequency variability of the exchanged flows through the Strait of Gibraltar during CANIGO. Deep-Sea Res. II 49:4051-4067.

García Lafuente, J., Delgado, J., Criado, F., 2002b. Inflow interruption by meteorological forcing in the Strait of Gibraltar. Geophys. Res. Lett. 29:1914.

García Lafuente, J., Sánchez Román, A., Díaz del Río, G., Sannino, G., Sánchez Garrido, J.C., 2007. Recent observations of seasonal variability of the Mediterranean outflow in the Strait of Gibraltar. J. Geophys. Res. 112:C10005.

García-Lafuente, J., Delgado, J., Sánchez Román, A., Soto, J., Carracedo, L., Díaz del Río, G., 2009. Interannual variability of the Mediterranean outflow observed in Espartel Sill, western Strait of Gibraltar. J. Geophys. Res. 114:C10018.

García Lafuente, J., Bruque Pozas, E., Sánchez Garrido, J.C., Sammartino, S., 2013. The interface mixing layer and the tidal dynamics at the eastern part of the Strait of Gibraltar. J. Mar. Syst. 117-118:31-42.

Garrett, C.J.R., 1983. Variable sea level and strait flows in the Mediterranean: a theoretical study of the response to meteorological forcing. Oceanol. Acta 6:79-87.

Garrett, C., Majaess, F., 1984. Nonisostatic response of sea level to atmospheric pressure in the eastern Mediterranean. J. Phys. Oceanogr. 14:656-665.

Garrett, C., Bormans, M., Thompson, K., 1990. Is the exchange through the Strait of Gibraltar maximal or submaximal? The Physical Oceanography of Sea Straits, NATO ASI Series, Kluwer, Boston 318:271-294.

Garret, C., Rhines, P., MacCready, P., 1993. Boundary mixing and arrested Ekman layers: rotating stratified flow near a sloping boundary. Ann. Rev. Fluid Mech. 25:291–323.

Gill, A.E., 1982. Atmosphere–Ocean Dynamics. Academic, N. Y., 662 pp.

Gasser, M., Pelegrí, J.L., Nash, J., Peters, H., García-Lafuente, J., 2011. Topographic steering of the early plunging Mediterranean outflow. Geo-Mar. Lett. 31:301– 314.

Habgood, EL., Kenyon, N.H., Masson, D.G., Akhmetzhanov, A., Weaver, P.P.E., Gardner, J., Mulder, T., 2003. Deep-water sediment wave fields, bottom current sand channels and gravity flow channel-lobe systems: Gulf of Cadiz, NE Atlantic. Sedimentology 50:483–510.

Hell, B., Jakobsson, M., 2011, Gridding heterogeneous bathymetric data sets with stacked continuous curvature splines in tension. Marine Geoph. Res. 32:493–501.

Hernández-Molina, J., Llave, E., Somoza, L., Fernández-Puga, M.C., Maestro, A., León, R., Medialdea, T., Barnolas, A., García, M., Díaz del Río, V., Fernández-Salas, L.M., Vázquez, J.T., Lobo, F., Alveirinho Dias, J.M., Rodero, J., Gardner, J., 2003. Looking for clues to paleoceanographic imprints: a diagnosis of the gulf of Cádiz contourite depositional systems. Geology 31:19–22.

Hernández-Molina, F.J., Llave, E., Stow, D.A.V., García, M., Somoza, L., Vázquez, J.T., Lobo, F.J., Maestro, A., Díaz del Río, V., León, R., Medialdea, T., Gardner, J., 2006. The contourite depositional system of the Gulf of Cadiz: a sedimentary model related to the bottom current activity of the Mediterranean outflow water and its interaction with the continental margin. Deep Sea Res. II 53:1420–1463.

Hernández-Molina, F.J., Llave, E., Preu, B., Ercilla, G., Bruno, M., Serra, N., Gomiz, J.J., Brackenridge, R.E., Sierro, F.J., Stow, D.A.V., García, M., Juan, C., Sandoval, N., Arnaiz, A.. 2014a. Contourite processes associated with the Mediterranean outflow water after its exit from the Strait of Gibraltar: global and conceptual implications. Geology 42:227–230.

Hernández-Molina, F.J., Stow, D., Alvarez-Zarikian, C., Acton, G., Bahr, A., Balestra, B., Ducassou, E., Flood, R., Flores, J.A., Furota, S., Grunert, P., Hodell, D., Jimenez-Espejo, F., Kim, J., Krissek, L., Kuroda, J., Li, B., Llave, E., Lofi, J., Lourens, L., Miller, M., Nanayama, N., Nishida, N., Richter, C.,

Roque, C., Pereira, H., Sanchez Goñi, M.F., Sierro, F.J., Singh, A., Sloss, C., Takashimizu, Y., Tzanova, A., Voelker, A., Williams, T., Xuan, C., 2014b. Onset of Mediterranean outflow into the North Atlantic. Science 344, 1244–1250.

Holst, S.E., Koseff, J.R., Ferziger, J.H., 1992. A numerical study of the evolution and structure of homogeneous stable stratified sheared turbulence. J. Fluid Mech. 237:499–539.

IODP, 2012. Mediterranean outflow: environmental significance of the Mediterranean Outflow Water and its global implications. IODP Preliminary Report, Integrated Ocean Drilling Program, Expedition 339.

Iorga, M.C., Lozier, M.S., 1999a. Signatures of the Mediterranean outflow from a North Atlantic climatology 1. Salinity and density fields. J. Geophys. Res. 104,:25985–26009.

Iorga, M.C., Lozier, M.S., 1999b. Signatures of the Mediterranean outflow from a North Atlantic climatology 2. Diagnostic velocity fields. J. Geophys. Res. 104:25985–26009.

Izquierdo, A., Tejedor, L., Sein, D.V., Backhaus, J.O., Brandt, P., Rubino, A., Kagan, B.A., 2001. Control variability and internal bore evolution in the Strait of Gibraltar: a 2-D two-layer model study. Est. Coast. Shelf Sci. 53:637-651.

Jia, Y., 2000. Formation of an Azores Current Due to Mediterranean Overflow in a Modeling Study of the North Atlantic, J. Phys. Ocean. 30:2342-2358.

Johnson, G., Sanford, T., Baringer, M., 1994. Stress on the Mediterranean outflow plume: Part I. Velocity and water property measurements. J. Phys. Oceanogr. 24:2072–2083.

Johnson, J., Ambar, I., Serra, N., Stevens, I., 2002. Comparative studies of the spreading of Mediterranean water through the Gulf of Cadiz. Deep Sea Res. II 49:4179–4193.

Jordà, G., Von Schuckmann, K., Josey, S.A., Caniaux, G., García-Lafuente, J., Sammartino, S., Özsoy, E., Polcher, J., Notarstefano, G., Poulain, P.M., Adloff, F., Salat, J., Naranjo, C., Schroeder, K., Chiggiato, J., Sannino, G., Macías, D., 2017. The Mediterranean Sea heat and mass budgets: Estimates, uncertainties and perspectives. Prog. in Ocean. 156:174-208.

Jungclaus, J.H., Mellor, G.L., 2000. A three-dimensional model study of the Mediterranean outflow. J. Mar. Syst. 24:41–66.

Kennett, J.P., 1982. Marine Geology. Prentice-Hall, Englewood Cliffs.

Kenyon, N.H., Belderson, R.H., 1973. Bed forms of the Mediterranean undercurrent observed with side-scan sonar. Sediment. Geol. 9:77–99.

Killworth, P. D., 1983. Deep convection in the World Ocean, Rev. Geophys. 21:1–26.

La Violette, P.E., Lacombe, L., 1988. Tidal-induced pulses in the flow through the Strait of Gibraltar. Oceanol. Acta 9:13–27.

Lacombe, H., Richez, C., 1962. The regime of the Strait of Gibraltar. Hydrodynamics of semi-enclosed seas, Elsevier Oceanogr. Ser. 34:13-73.

Legg, S., B. Briegleb, Y. Chang, E.P. Chassignet, G. Danabasoglu, T. Ezer, A.L. Gordon, S. Griffies, R. Hallberg, L. Jackson, W. Large, T.M. Özgökmen, H. Peters, J. Price, U. Riemenschneider, W. Wu, X. Xu, and J. Yang, 2009. Improving Oceanic Overflow Representation in Climate Models: The Gravity Current Entrainment Climate Process Team. Bull. Amer. Meteor. Soc. 90:657–670.

León, R., Somoza, L., Medialdea, T., Hernández-Molina, F.J., Vázquez, J.T., Díaz-del-Río, V., González, F.J., 2010. Pockmarks, collapses and blind valleys in the Gulf of Cádiz. Geo. Mar. Lett. 30:231–247.

Le Traon, P.Y., Gauzelin, P., 1997. Response of the Mediterranean mean sea level to atmospheric pressure forcing. J. Geophys. Res. 102:973-984.

Levitus, S., Antonov, J.I., Boyer, T.P., Stephens, C., 2000. Warming of the world ocean. Science 287:2225–2229.

Llave, E., Schönfeld, J., Hernández-Molina, F.J., Mulder, T., Somoza, L., Díaz del Río, V., Sánchez-Almazo, I., 2006. High-resolution stratigraphy of the Mediterranean outflow contourite system in the Gulf of Cadiz during the late Pleistocene: the impact of Heinrich events. Mar. Geol. 227:241–262.

Llave, E., Hernández-Molina, F.J., Stow, D.A.V., Fernández-Puga, M.C., García, M., Vázquez, J.T., Maestro, A., Somoza, L., Díaz del Río, V., 2007. Reconstructions of the Mediterranean Outflow water during the quaternary since the study of changes in buried mounded drift stacking pattern in the Gulf of Cadiz. Mar. Geophys. Res. 28:379–394.

Llave, E., Matias, H., Hernández Molina, F.J., Ercilla, E., Stow, D.A.V., Medialdea, T., 2011. Pliocene-Quaternary contourites along the northern Gulf of Cadiz margin: sedimentary stacking pattern and regional distribution. Geo-Marine Lett. 5:377–390.

Loget, N., Van Den Driessche, J., 2006. On the origin of the Strait of Gibraltar. Sed. Geol. 188–189:341–356.

Lopes, F.C., Cunha, P.P., Le Gall, B., 2006. Cenozoic seismic stratigraphy and tectonic evolution of the Algarve margin (offshore Portugal, southwestern Iberian Peninsula). Mar. Geol. 231:1–36.

Louarn, E., Morin, P., 2011. Antarctic intermediate water influence on Mediterranean Sea water outflow. Deep-Sea Res. I 58:932–942.

Luján, M., Crespo-Blanc, A., Comas, M., 2011. Morphology and structure of the Camarinal Sill from high-resolution bathymetry: evidence of fault zones in the Gibraltar Strait. Geo-Mar. Lett. 31:163–174.

Machín, F., Pelegrí, J.L., 2009. Northward penetration of Antarctic intermediate water off Northwest Africa. J. Phys. Oceanogr. 39:512–535.

Machín, F., Pelegrí, J.L., 2016. Interaction of intermediate water lenses with Antarctic Intermediate Water off northwest Africa. Scientia Marina 80:205–214.

Machín, F., Pelegrí, J.L., Láiz, I., Marrero-Díaz, A., Ratsimandresy, A.W., 2006. Near-surface circulation in the southern Gulf of Cadiz. Deep Sea Res. II 53:1161–1181.

Macías, D., García, C.M., Echeverría Navas, F., Vázquez-López-Escobar, A., Bruno Mejías, M. 2006. Tidal induced variability of mixing processes on Camarinal Sill (Strait of Gibraltar): A pulsating event. J. Mar. Syst. 60 :177-192.

Madelain, F., 1970. Influence de la topographie du fond sur l'ecoulement Mediterrraneen entre le Detroit de Gibraltar et le Cap Saint-Vincent. Cah. Océanograph. 22:43–61.

Maestro, A., Somoza, L., Díaz del Río, V., 2007. Reconstructions of the Mediterranean Outflow Water during the Quaternary based on the study of changes in buried mounded drift stacking pattern in the Gulf of Cadiz. Mar. Geophys. Res. 28:379– 394.

Mauritzen, C., Morel, Y., Paillet, J., 2001. On the influence of Mediterranean Water on the Central Waters of the North Atlantic Ocean. Deep-Sea Res. 48:347–381.

Millot, C., Candela, J., Fuda, J.L., Tber, Y., 2006. Large warming and salinification of the Mediterranean outflow due to changes in its composition. Deep-Sea Res. I 53, 655–666.

Mulder, T., Voisset, M., Lecroart, P., Le Drezen, E., Gonthier, E., Hanquiez, V., Faugères, J.-C., Habgood, E., Hernandez-Molina, F.J., Estrada, F., Llave-Barranco, E., Poirier, D., Gorini, C., Fuchey, Y., Voelker, A., Freitas, P., Lobo Sanchez, F., Fernandez, L.M., Kenyon, N.H., Morel, J., 2003. The Gulf of Cádiz: an unstable giant contouritic levee. Geo. Mar. Lett. 23:7–18.

Nash, J.D., Peters, H., Kelly, S.M., Pelegrí, J.L., Emelianov, M., Gasser, M., 2012. Turbulence and high-frequency variability in a deep gravity current outflow. Geophys. Res. Lett. 39:L18611.

Nelson, C.H., Baraza, J., Maldonado, A., 1993. Mediterranean undercurrent Sandy contourites, Gulf of Cadiz, Spain. Sed. Geol. 82:103–131.

Nelson, C.H., Baraza, J., Maldonado, A., Rodero, J., Escutia, C., Barber Jr., J.H., 1999. Influence of the Atlantic inflow and Mediterranean outflow currents on Late Quaternary sedimentary facies of the Gulf of Cadiz continental margin. Mar. Geol. 155:99–129.

Ochoa, J., Bray, N.A., 1991. Water mass exchange in the Gulf of Cadiz. Deep-Sea Res. 38:465–503.

Özgökmen, T.M., Chassignet, E.P., Rooth, C.G.H., 2001. On the Connection between the Mediterranean Outflow and the Azores Current. J. Phys. Ocean. 31:461-480.

Papadakis, M.P., Chassignet, E.P., Hallberg, R.H., 2003. Numerical simulations of the Mediterranean sea outflow: impact of the entrainment parameterization in an Isopycnic coordinate ocean model. Ocean Model. 5:329-256.

Parrilla, G., Neuer, S., Le Traon, P.-Y., Fernández-Suárez, E., 2002. Topical studies in oceanography: Canary Islands Azores Gibraltar Observations (CANIGO). Volume 2: Studies of the Azores and Gibraltar regions. Deep-Sea Res. II 49:3951–3955.

Pawlovicz, R., Beardsley, B., Lentz, S., 2002. Classical tidal harmonic analysis including error estimates in MATLAB using T_TIDE. Comput. Geosci. 28:929–937.

Pelegrí, J.L., 1988. Tidal fronts in estuaries. Estuar. Coast. Shelf. Sci. 27:45–60.

Pelegrí, J.L., Richman, J.G., 1993. On the role of shear mixing during transient coastal upwelling. Cont. Shelf Res. 13:1363-1400.

Pelegrí, J.L., Sangrà, P. 1998. A mechanism for layer formation in stratified geophysical flows. J. Geophys. Res. 103:30679–30693.

Peliz, A., Dubert, J., Marchesiello, P., Teles-Machado, A., 2007. Surface circulation in. the Gulf of Cadiz: model and mean flow structure. J. Geophys. Res. Oceans 112: C11015.

Peliz, A., Marchesiello, P., Santos, A.M.P., Dubert, J., Teles-Machado, A., Marta-Almeida, M., Le Cann, B., 2009. Surface circulation in the Gulf of Cadiz: 2. Inflow-outflow coupling and the Gulf of Cadiz slope current. J. Geophys. Res. Oceans 114:C03011.

Peliz, A., Boutov, D., Cardoso, R.M., Delgado, J., Soares, P.M.M., 2013. The Gulf of Cadiz-Alboran Sea sub-basin: model setup, exchange and seasonal variability. Ocean Model. 61:49–67.

Potter, R.A., Lozier, M.S., 2004. On the warming and salinification of the Mediterranean outflow waters in the North Atlantic. Geophys. Res. Lett. 31:L01202.

Pratt, L.J., Lundberg, P.A., 1991. Hydraulics of Rotating Strait and Sill Flow. Ann. Rev. Fluid Mech. 23:81-106.

Price, J.F., Baringer, M.O., Lueck, R.G., Johnson, G.C., Ambar, I., Parrilla, G., Cantos, A., Kennelly, M.A., Sanford, T.B., 1993. Mediterranean outflow mixing and dynamics. Science 259:1277–1282.

Reid, J.L., 1979. On the contribution of the Mediterranean Sea outflow to the Norwegian-Greenland Sea. Deep Sea Res. A 26:1199–1223.

Richez, C., Kermogard, C., 1990. Characteristic features occurring in the Strait of Gibraltar as seen through remote-sensing. The physical oceanography of sea straits., Kluwer Acad. Norwell, MA, 441-455.

Richardson, P., Bower, A., Zenk, W., 2000. A census of meddies tracked by floats. Prog. Oceanogr. 45:209–250.

Rogerson, M., Rohling, E.J., Weaver, P.P.E., Murray, J.W., 2005. Glacial to interglacial changes in the settling depth of the Mediterranean Outflow plume. Paleoceanography 20:PA3007.

Sammartino, S., Garcia Lafuente, J., Naranjo, C., Sánchez Garrido, J.C., Sánchez Leal, R., Sánchez Román, A., 2015. Ten years of marine current measurements in Espartel Sill, Strait of Gibraltar. J. Geophys. Res. Oceans 120:6309–6328.

Sánchez-Leal, R.F., Bellanco, M.J., Fernández-Salas, L.M., García-Lafuente, J., Gasser-Rubinat, M., González-Pola, C., Hernández-Molina, F.J., Pelegrí, J.L., Peliz, A., Relvas, P., Roque, D., Ruiz-Villarreal, M., Sammartino, S., Sánchez-Garrido, J.C., 2017. The Mediterranean Overflow in the Gulf of Cadiz: A rugged journey. Science Advances 3:eaao0609.

Sánchez Garrido, J.C., García Lafuente, J., Criado Aldeanueva, F., Baquerizo, A., Sannino, G., 2008. Time-spatial variability observed in velocity of propagation of the internal bore in the Strait of Gibraltar. J. Geophys. Res. 113:C07034.

Sánchez-Román, A., Criado-Aldeanueva, F., García-Lafuente, J., Sánchez, J.C., 2008. Vertical structure of tidal currents over Espartel and Camarinal sills, Strait of Gibraltar. J. Mar. Syst. 74:120–133.

Sánchez-Román, A., Sannino, G., García-Lafuente, J., Carillo, A., Criado-Aldeanueva, F., 2009. Transport estimates at the western section of the Strait of Gibraltar: a combined experimental and numerical modelling study. J. Geophys. Res. Oceans 114:C06002.

Sannino, G., Carillo, A., Artale, V., 2007. Three-layer view of transports and hydraulics in the Strait of Gibraltar: A three-dimensional model study. J. Geophys. Res. 112:C03010.

Sannino, G., Pratt, L., Carillo, A., 2009. Hydraulic criticality of the exchange flow through the Strait of Gibraltar. J. Phys. Oceanogr. 39:2779-2799.

Serra, N., Ambar, I., Kase, R.H., 2005. Observations and numerical modelling of the Mediterranean outflow splitting and eddy generation. Deep Sea Res. II 52:383– 408.

Schmitz Jr., W. J., McCartney, S., 1993. On the North Atlantic Circulation. Rev. Geophys. 31:29–49.

Smith, W.H.F., Sandwell, D.T., 1997. Global Sea Floor Topography from Satellite Altimetry and Ship Depth Soundings. Science 277:1956-1962.

Smith W.H.F, Wessel P., 1990. Gridding with continuous curvature splines in tension. Geoph., 55:293-305.

Soto-Navarro, J., Criado-Aldeanueva, F., García-Lafuente, J., Sánchez-Román, A. 2010. Estimation of the Atlantic inflow through the Strait of Gibraltar from climatological and in situ data. J. Geophys. Res. 115:C10023

Sotillo, M.G., Cailleau, S., Lorente, P., Levier, B., Aznar, R., Reffray, G., Amo-Baladrón, A., Chanut, J., Benkiran, M.,Alvarez-Fanjul, E. , 2015. The MyOcean IBI ocean forecast and reanalysis systems: operational products and roadmap to the future copernicus service. J. Oper. Oceanogr. 8:63–79.

Sotillo, M.G., Levier, B., Amo Baladrón, A., Cailleau, S., 2016. Product User Manual for Atlantic–Iberian Biscay Irish–Ocean Physics Reanalysis Product http:// cmems-resources.cls.fr/documents/PUM/CMEMS-IBI-PUM-005-001.pdf

Stanichny S., Tigny V., Stanichnaya R., Djenidi S., 2005. Wind driven upwelling along the Africa coast of the Strait of Gibraltar. Geophys. Res. Lett. 32:L04604.

Stanton, B.R., 1983. Low frequency variability in the Mediterranean outflow west of Gibraltar. Deep Sea Res 30:743–761.

Schwanghart, W., Kuhn, N.J., 2010. TopoToolbox: A set of Matlab functions for topographic analysis. Env. Model. & Softw. 25:6:770-781.

Thurnherr, A.M. 2010. A Practical Assessment of the Errors Associated with Full-Depth LADCP Profiles Obtained Using Teledyne RDI Workhorse Acoustic Doppler Current Profilers. J. Atmos. Ocean. Tech. 27: 1215-1227.

Toole, J. M., 1998. Turbulent mixing in the ocean. Ocean Modeling and Parameterization, NATO ASI Series, Springer 516:171-190.

Turner, J.S., 1973. Buoyancy effects in fluids. Cambridge University Press, Cambridge.

Turner, J.S., 1986. Turbulent entrainment: the development of the entrainment assumption, and its application to geophysical flows. J. Fluid Mech. 173:431-471.

Van Gastel, P., Pelegrí, J.L., 2004. Estimates of gradient Richardson numbers from vertically smoothed data. Sci. Mar. 68:459-482.

Vargas, J.M., García-Lafuente, J., Candela, J., Sánchez Román, A., 2006. Fortnightly and monthly variability of the exchange through the Strait of Gibraltar. Progr. Oceanogr. 70:466-485.

Visbeck, M. 2002. Deep velocity profiling using Lowered Acoustic Doppler Current Profilers: Bottom track and inverse solutions J. Atm. Oc. Tech. 19:794–807.

Weatherall, P., Marks, K. M., Jakobsson, M., Schmitt, T., Tani, S., Arndt, J.E., Rovere, M., Chayes, D., Ferrini, V., Wigley, R., 2015. A new digital bathymetric model of the world's oceans. Earth and Space Sci. 331-345.

WOCE, 2011. WOCE Atlas Volume 3: Atlantic Ocean https://doi.org/10.21976/C6RP4Z.

Worthington, L.V., 1976. On the North Atlantic Circulation. The Johns Hopkins Oceanographic Studies Number 6, Johns Hopkins University Press, Baltimore, MD, 110 pp.

Wunsch, C., Stammer, D., 1997. Atmospheric loading and the ocean "inverted barometer" effect. Rev. Geophys. 35:79-10.

Xu, X., Chassignet, E.P., Price, J.F., Ozgokmen, T.M., Peters, H., 2007. A regional modeling study of the entraining Mediterranean outflow. J. Geophys. Res. Oceans 112:C12005.

Zenk, W., 1975. On the Mediterranean outflow west of Gibraltar. Meteor Forschungsergebnisse A16:23–34.

Zenk, W., Armi, L., 1990. The complex spreading patterns of Mediterranean water off the Portuguese continental slope. Deep-Sea Res. 37:1805–1823.

Zitellini, N., Gràcia, E., Matias, L., Terrinha, P., Abreu, M.A., DeAlteriis, G., Henriet, J.P., Dañobeitia, J.J., Masson, D.G., Mulder, T., Ramella, R., Somoza, L., Diez, S., 2009. The quest for the Africa-Eurasia plate boundary west of the Strait of Gibraltar. Earth Planet. Sci. Lett. 280:13–50.